The Thermodynamic Properties and Structure of Alkali and Alkaline Earth Carbonate Melts

by

Sean M. Hurt

A dissertation submitted in partial fulfillment
of the requirements for the degree of
Doctor of Philosophy
(Earth and Environmental Sciences)
in the University of Michigan
2018

Doctoral Committee:

Dr. Aaron S. Wolf, Co-Chair
Professor Rebecca A. Lange, Co-Chair
Professor Edwin Bergin
Professor Jie Li
Professor Youxue Zhang

Sean M. Hurt

seanhurt@umich.edu

ORCID iD: 0000-0002-6611-855X

Dedication

For the greater glory of God, and to all my future students

Acknowledgements

First, I thank God for creating such a world, intelligible as it is and for creating me, a creature capable of comprehending it and imbuing me with the talents necessary to complete a Ph.D. program in the first place—thank you. Second, I thank my advisors Becky and Aaron for sharing with me their time, wisdom, amazing-talent, enthusiasm, love, devotion and all their whole selves—thank you. I owe you both a deep debt of gratitude. I would like to thank my family, my wife Jennifer and daughter Teresa for their moral support, the great many hours Jen has poured into house-keeping and baby-sitting and putting up with my long days at the office. I would like to thank the pastoral staff at St. Mary's Student Parish, St. Thomas the Apostle Catholic Church and Miles Christi for their spiritual and moral guidance, without which I could not have persevered through the most difficult parts of grad school. I thank our wonderful office staff here at the department on Earth and Environmental Sciences, especially Nancy Kingsbury, Anne Hudon, Stacy Wilkin and Paula Frank. I thank our wonderful faculty, especially my committee members Youxue Zhang, Jackie Li and Edwin Bergin. I owe a special thanks to Jackie who has always advocated for me and Youxue who has contributed many critiques and insights. I thank also all of my friends who gave me so much good counsel, moral support and many good laughs and good times, especially Will Bender, James Jolles, Spencer Washburn and many others. I also don't want to forget all the people that maintain the C.C. Little building, with all its labs and classrooms, namely the cleaning staff, building managers, maintenance and grounds-keeping staff. For all these people and many more, I owe a debt of gratitude. Thank you.

Table of Contents

List of Tables

List of Figures

Abstract

One of the most important liquid components of mantle-derived carbonate melts, $MgCO_3$, is also one of the most difficult to study experimentally due to its low decarbonation temperature at 1 bar. This dissertation offers constraints on the standard state thermodynamic properties of $MgCO_3$ liquid (and corresponding rough estimates for $FeCO_3$ liquid as well) through analysis of systematic property variations in alkali/alkaline carbonate liquids in combination with atomistic molecular dynamic (MD) simulations.

Chapter 2 presents new 1 bar density measurements on liquids in the Li_2CO_3-Na_2CO_3-K_2CO_3-Rb_2CO_3-Cs_2CO_3-$CaCO_3$-$SrCO_3$-$BaCO_3$ system. The partial molar volumes of all eight carbonate components increase linearly along two different trends, one for the alkali carbonates and another for the alkaline earth carbonates as a function of cation volume. The two trends yield two separate estimates for the partial molar volume of CO_3^{2-} in the melt, corresponding to coordination of the metal cation with the carbonate ion. The results permit the partial molar volume of $MgCO_3$ and $FeCO_3$ in multicomponent carbonate liquids to be calculated, if the oxygen and carbonate ion coordination with Mg^{2+} and Fe^{2+} are known. For example, if Mg^{2+} and Fe^{2+} are in 6-fold coordination with both oxygen and carbonate, the estimated partial molar volumes at 1100 K are 34.4(1), and 35.1(1) cm^3/mol, respectively, with a thermal expansion coefficient of 16.4(29) 10^{-5} K^{-1}. If Mg^{2+} and Fe^{2+} are in 4-fold coordination, their partial molar volumes are estimated at 40.0(6) and 40.4(6) cm^3/mol respectively with a thermal expansion of 22.1(17) $\cdot$ 10^{-5} K^{-1}.

Chapter 3 presents 1 bar sound speed measurements on liquids in the Li_2CO_3-Na_2CO_3-K_2CO_3-Rb_2CO_3-Cs_2CO_3-$SrCO_3$-$BaCO_3$ system using the ultrasonic frequency-sweep interferometer. The results were combined with those on Li_2CO_3-Na_2CO3-K_2CO_3-$CaCO_3$ quaternary liquids to estimate the partial molar compressibility and its temperature-dependence (i.e. $\bar{\beta}_T$ & $\frac{\delta\bar{\beta}_i}{\delta T}$) of each of the eight components. Liquid compressibility is positively correlated with ΔV_{fusion} (R^2 = 0.99). The trend among the alkaline earth carbonate liquids suggests that of the 1-bar compressibility for the $MgCO_3$ and $FeCO_3$ liquids at 1500 K are much higher (18 (±6) 10^{-2} GPa-1) than those obtained for the $SrCO_3$, $BaCO_3$ or $CaCO_3$ liquid components at 1500 K (5.4-8.8 10^{-2} GPa^{-1}).

Chapter 4 introduces an empirically-derived potential set model for classical mechanical molecular dynamic simulations of $MgCO_3$-$CaCO_3$-$SrCO_3$-$BaCO_3$ liquids. The potential set model is determined from the behavior of mineral solid structures and is applied to MD simulations of $CaCO_3$-$SrCO_3$-$BaCO_3$ liquids; simulated volumes are modeled with a temperature-dependent 3rd-order Birch-Murnaghan equation of state. The calculated thermodynamic properties of $CaCO_3$-$SrCO_3$-$BaCO_3$ melts show broad agreement with those determined experimentally in chapters 2 and 3. $CaCO_3$, $SrCO_3$, $BaCO_3$ liquids display a striking uniformity in their liquid structures with Ca^{2+}, Sr^{2+} and Ba^{2+} all in 6-fold coordination with carbonate groups.

In chapter 5, the potential set model is applied to molecular dynamic simulations of $MgCO_3$ melts. At 1 bar, $MgCO_3$ liquid assumes a novel topology, distinct from the other alkaline earths, characterized by a 4-fold coordination of Mg^{2+} with the carbonate molecule and oxygen ion. This novel topology results in a melt that is significantly more buoyant and compressible than previous estimates have suggested. The voluminous structure of the $MgCO_3$ liquid

component (and $FeCO_3$ liquid by proxy) may well drive up carbonate melt ascent rates and prevent iron-rich ferrocarbonatite melts from stagnating or sinking in the mantle.

Chapter 1 Introduction

Despite its relatively low concentration, carbonate liquid plays an important role in Earth's mantle. Carbonate, can dramatically lower the solidus of peridotite (e.g., Dasgupta and Hirschmann 2010) producing carbonatite liquids (e.g., Dalton and Wood, 1993) that drive mantle metasomatism (e.g., Green and Wallace 1988) and scavenge heat-producing trace elements (e.g., Blundy and Dalton 2000; Dasgupta and Hirschmann 2006). Mantle carbonate also plays a vital role in petrogenesis of silica-undersaturated alkaline rocks (e.g., Dasgupta et al. 2006), carbonatites (e.g., Harmer et al. 1998) and kimberlites (e.g., Weiss et al. 2011) as well as diamonds formation (e.g., Stachel and Harris 2009). A consideration of mantle carbonate is also integral to an understanding of the deep carbon cycle (e.g., Sleep and Zahnle 2001, Dasgupta et al. 2004, Dasgupta and Hirschmann 2010).

1.1 The fate of subducted carbonate in the mantle

There is much evidence for carbon in the mantle: e.g., carbonatites of unambiguous mantle origin (e.g., Harmer et al. 1998), carbon dioxide in mid-ocean ridge basalt glass (e.g., Wood et al. 1996) and diamond in mantle-sourced kimberlites (e.g., Bulanova et al. 2010). Estimates of carbon concentration in the mantle vary over a wide range. Trull et al. (1993) proposed a value of 50-250 ppm and certainly <500 ppm for the upper mantle on the basis of C/He^4 systematics. Wood et al. (1996) estimated upper mantle carbon concentration at 80 ppm on the basis of C concentration in mid-ocean ridge basalts but suggested that a relatively un-degassed lower mantle could contain 900-3700 ppm carbon.

Since carbon is insoluble in mantle silicate minerals it must be stored in accessory phases such as carbonate (e.g., Luth, 1999; Shcheka et al. 2006). Carbonate enters the mantle through subduction of hydrothermally altered oceanic crust (e.g., Staudigel et al. 1989; Rea and Ruff 1996) and sediment (e.g., Plank and Langmuir 1998). Most subducted carbonate is in the form of calcite ($CaCO_3$) but in the presence of mantle silicates it quickly reacts with Mg-perovskite or pyroxene to form magnesite establishing $MgCO_3$ as the predominant carbonate crystal phase in the mantle (Biellmann et al. 1993).

Many workers have attempted to estimate how much carbon is extracted from the down-going slab during subduction versus recycled into the convecting mantle. Experiments on decarbonation reactions in magnesite ($MgCO_{3magnesite} \rightarrow MgO + CO_{2gas}$) suggest that decarbonation in the subducting slab can remove significant amounts of carbon, but only at low pressures (i.e. in the forearc region) and only in the case of low subduction rates (Molina and Poli 2000). Other workers have attempted to constrain the fraction of subducted carbonate recycled into the convecting mantle by analyzing carbon fluxes at subduction zones (e.g., Gorman et al. 2006; Dasgupta and Hirschmann 2010; Johnston et al. 2011; Kelemen and Manning 2015). This kind of analysis has produced a wide range of estimates; e.g., Dasgupta and Hirschmann (2010) proposed that 20-80% of subducted carbon is returned to the mantle wedge while Kelemen and Manning (2015) concluded that nearly all carbon is extracted (but given the uncertainty on various carbon fluxes they allowed for as much as 80% of subducted carbon to be recycled into the mantle).

Carbonate that does escape decomposition and extraction in the subduction zone may be removed by partial melting throughout the upper mantle and transition zone. In order to constrain the solidus of carbonate-bearing mantled assemblage, many experimental phase equilibrium

studies have been carried out on a carbonated eclogite (e.g., Hammouda 2003; Yaxley and Brey 2004; Dasgupta et al. 2006; Litasov and Ohtani 2010), lherzolite (e.g., Dalton and Wood 1993; Dalton and Presnall 1998) and peridotite (Falloon and Green 1989; Dasgupta and Hirschmann 2006; Dasgupta and Hirshmann 2007; Brey et al. 2008; Ghosh et al 2009; Dasgupta et al. 2013) over a pressure range of 1.5 (Dalton and Wood 1993) to 32 GPa (Litasov and Ohtani 2010) (~50-800 km). The studies noted above unanimously conclude that the solidus liquid generated by low degree partial melting of variable carbonate mantle compositions is carbonatitic and composed mostly of $MgCO_3$, $CaCO_3$ and $FeCO_3$ components. Thomson et al. (2016) showed that the majority of pressure-temperature paths of a subducting slab would intersect the solidus of carbonated eclogite (representing carbonated oceanic crust) at ~300-700 km thus initiating low degree partial melting and generating carbonatitic melts. Given the ultralow viscosity of carbonatite melts (e.g., Dobson et al. 1996; Kono et al. 2014) and their relatively low dihedral angle (Hunter and McKenzie 1989) even small (0.02 %) carbonate melt fractions can separate from their residue. The ascent rates of carbonate melt through the mantle are extremely fast (i.e. meters per year) (Hammouda and Laporte 2000). Virtually any degree of carbonate melt will separate from a subducting slab and percolate throughout the upper mantle causing metasomatism (which is discussed in detail below). In this way, partial melting in the upper mantle and transition zone poses a significant barrier to carbonate entering the lower mantle.

The phase equilibrium studies noted above demonstrate that the solidus temperature of carbonate-bearing peridotite is generally below the average mantle geotherm throughout the upper mantle. Therefore, carbonate liquids generated by low-degree partial melting of a subducted slab could be stable throughout much of the upper mantle and transition zone. Some workers have posited that low volumes (0.1 %) of carbonate melts could be common throughout

the upper mantle based on the premise that the high electrical conductivity of carbonate melt may well explain the anomalously high conductivity of the oceanic asthenosphere 70-200 km beneath spreading ridges (Gaillard et al. 2008). Similarly, Low volumes of carbonate melt have been invoked to explain oceanic seismic low-velocity zones at 70-250 km depth (Presnall and Gudfinnsson 2005; Dasgupta et al. 2013).

If carbonate in a subducting slab escapes partial melting or reduction in the upper mantle/transition zone, it could enter the lower mantle. The possibility of carbonate liquids in the lower mantle is a question of special interest since it would hold important implications for the mobility and long-term storage of carbon in the mantle (Jones et al. 2013). Thomson et al (2016) concludes that the coldest subducting slabs could avoid partial melting in the transition zone and carry carbonate into the lower mantle. Carbonate inclusions in deep-sourced (lower-mantle) diamonds (e.g., Brenker et al. 2007; Kaminsky et al. 2009) seem to support this assertion. High-pressure experiments on the stability of magnesite at lower mantle conditions indicate that carbonate may very well be stable throughout the entire lower mantle possibly up to the core-mantle boundary (e.g., Katsura et al. 1991; Isshiki et al. 2003, Solopova et al. 2015).

1.2 Carbonate melt metasomatism in the mantle

Carbonate melts are effective agents of metasomatism (e.g., Green and Wallace 1988) owing to their high mobility (e.g., Hunter and McKenzie 1989) and ability to scavenge incompatible elements (e.g., Green et al. 1992). Carbonate melts produced by partial melting of carbonated eclogite or peridotite have low-TiO_2 contents and a high concentration of many incompatible elements, especially large ion lithophile elements (LILE), some high-field-strength elements (HFSE) (e.g., Nb, Ta, Zr) and light rare earth elements (LREE) (La-Sm) (e.g., Green and Wallace 1988; Green et al. 1992; Ionov et al. 1993; Rudnick et al. 1993; Blundy and Dalton

2000). Dasgupta et al. (2009) estimated that a carbonate liquid generated by a 0.1 % partial melt can extract 30-60% of highly incompatible elements from the residue. Interactions of carbonatite melt with mantle rocks can strongly enrich the host rock in LILE and impart a distinctive geochemical signature with only subtle changes to mineralogy (Brenan and Watson 1991). High CaO/Al_2O_3, Na_2O/Al_2O_3 ratios accompanied by extreme LILE enrichment with low concomitant TiO_2 enrichment are characteristic of carbonate melt metasomatism (e.g., Yaxley et al. 1991). On the basis of such distinct geochemical signatures, carbonate melts have been widely implicated as metasomatic agents for many metasomatized mantle xenoliths (e.g., O'Reilly and Griffin 1988; Wallace and Green 1988; Yaxley et al. 1991; Baker and Wyllie 1992; Rudnick et al. 1993; Ionov et al. 1993). The high mobility of carbonate melts, combined with its strong affinity for incompatible elements, establishes it as a key phase in considerations of mantle trace element geochemistry.

1.3 Thermodynamic modeling of partial melting of carbonated mantle

As noted above, the effect of carbonate on partial melting of the mantle has been extensively studied through phase equilibrium experiments. Phase equilibrium experiments are undeniably valuable for determining the location of the solidus of carbonate-bearing mantle in PT space, for identifying residual phases over a range of relevant temperatures and pressures and measuring melt fractions etc. However, the compositions of both the carbonate and silicate phases relevant to partial melting of carbonated mantle rocks are extremely heterogeneous. Even small variations in composition can lead to large differences in the location of the solidus (e.g., Dasgupta and Hirschmann 2010; Litasov et al. 2013). Furthermore, the range of pressures and temperatures at which partial melting may occur is extremely large. A phase equilibrium

experiment cannot be performed for every pertinent composition at every temperature and every pressure.

Thermodynamic modelling software such as pMELTS (Ghiorso et al. 2002) could offer a solution to the limitations of phase equilibrium experiments. However, in order to model partial melting of carbonate-bearing mantle lithologies, MELTS requires the standard state thermodynamic properties (e.g., molar volume, thermal expansion, compressibility, heat capacity and enthalpy of fusion) of the relevant carbonate components. Phase equilibrium experiments on partial melting of carbonated peridotite and eclogite indicate that $MgCO_3$, $CaCO_3$ and $FeCO_3$ are the most abundant and important carbonate components (e.g., Dalton and Wood 1993; Dalton and Presnall 1998; Hammouda 2003; Ghosh et al. 2009). Many of the standard state thermodynamic properties of the $MgCO_3$, $CaCO_3$ and $FeCO_3$ crystal phases have already been extensively studied. Full P-V-T equations-of-state for aragonite ($CaCO_3$) (e.g., Li et al. 2015; Litasov et al. 2017), magnesite ($MgCO_3$) (e.g., Ross 1997; Litasov et al. 2008) and siderite ($FeCO_3$) (Litasov et al. 2013) are available in the literature up to temperatures and pressures pertinent to the upper mantle and transition zone. Similarly, many of the requisite properties for calcite ($CaCO_3$) have also been previously determined: 1 bar molar volume and thermal expansion (e.g., Dove and Powell 1989; Markgraf and Reeder 1985; Antao et al. 2009; Ishizawa et al. 2013), compressibility (e.g., Redfern and Angel 1999; Zhang and Reeder 1999), K' (Redfern and Angel 1999) and heat capacity (Jacobs et al. 1981). However, the standard state thermodynamic properties for their respective liquid components are severely lacking due to relatively low decarbonation temperatures. $CaCO_3$, $MgCO_3$, $FeCO_3$ and the remaining alkaline earth carbonates all decompose into their respective oxide and CO_2 gas at a temperature lower than their respective 1 bar melting temperature making measurements on their pure, standard

state liquids impossible at ambient pressure. The 1 bar decomposition temperatures of $CaCO_3$, $MgCO_3$ and $FeCO_3$ are ~900 °C (e.g., Narsimhan 1961) ~500 °C (Hurst 1991) and ~450 °C (French and Rosenberg 1965) respectively. However, stable $CaCO_3$-bearing melts may be obtained at 1 bar by mixing $CaCO_3$ with alkali carbonates. The alkali carbonates all form stable melts at 1 bar. In the Li_2CO_3-Na_2CO_3-K_2CO_3 ternary, the eutectic composition $(Li_{.43}Na_{.32}K_{.25})_2CO_3$ melts at only 398 °C (Janz et al. 1962, 1979).

By mixing variable amounts of $CaCO_3$ (up to 50 mol. %) into the alkali ternary eutectic composition, Liu and Lange (2003) were able to generate stable $CaCO_3$-bearing melts at 1 bar and measure their densities via the Archimedean double-bob method. They found that an ideal mixing model recovers the molar volumes of their experimental liquids to within error. On this basis they concluded that the molar volumes of liquids in the Li_2CO_3-Na_2CO_3-K_2CO_3-$CaCO_3$ quaternary system mix ideally with respect to mol fraction and that the partial molar volume of $CaCO_3$ is a good proxy for the molar volume of pure $CaCO_3$ liquid at 1 bar. Using a similar strategy of mixing variable amounts of $CaCO_3$ with the alkali ternary eutectic mixture composition, O'Leary and Lange (2015) measured sound speeds in Li_2CO_3-Na_2CO_3-K_2CO_3-$CaCO_3$ liquids at 1 bar and high temperature (808-1323 K) using ultrasonic frequency-sweep interferometry (Ai and Lange 2004 a, b). Their sound speed data was used to calculate the isothermal compressibility (β_T) of each experimental liquid. They found that an ideal mixing model could recover the measured β_T data to within experimental error assuming its components mix ideally according to volume fraction. Thus, the partial volumetric β_T of $CaCO_3$ in the mixed $CaCO_3$-bearing liquids is an adequate proxy for the compressibility of pure $CaCO_3$ liquid at 1 bar.

1.4 The standard state thermodynamic properties of $MgCO_3$ liquid

Through the work of Liu and Lange (2003) and O'Leary and Lange (2015) the 1 bar molar volume, thermal expansion, isothermal compressibility and $\delta\beta_T/\delta T$ have been estimated for the $CaCO_3$ liquid component. $MgCO_3$ liquid is additionally a component of primary concern in considerations of partial melting of the mantle in the presence of carbonate. Could the same technique of mixing variable amounts of $MgCO_3$ into the alkali ternary mixture produce a stable $MgCO_3$-bearing melt at 1 bar? Unfortunately, the decomposition temperature of $MgCO_3$ is simply too low, making experiments on $MgCO_3$-bearing liquids nearly impossible—a novel approach is required. This work takes two approaches to constrain the standard state thermodynamic properties of $MgCO_3$ liquid: analysis of systematic variations in the properties of alkali and alkaline earth carbonate liquids and molecular dynamics simulations of alkaline earth liquids.

In the second chapter of this work, new measurements on the 1 bar densities of liquids in the Li_2CO_3-Na_2CO_3-K_2CO_3-Rb_2CO_3-Cs_2CO_3-$CaCO_3$-$SrCO_3$-$BaCO_3$ system are presented. The density data are combined with measurements from Liu and Lange (2003) on the Li_2CO_3-Na_2CO_3-K_2CO_3-$CaCO_3$ system. Molar volumes are calculated from the combined density dataset and the results are fitted with a linear mixing model to approximate the molar volumes of each of the pure components. By fully mapping out systematic trends in molar volume and thermal expansion among the alkali and alkaline earth carbonates, constraints can be placed on the volume and thermal expansivity of $MgCO_3$ and $FeCO_3$ liquid.

In the third chapter, a similar approach is taken to constrain the 1 bar compressibility of the pure $MgCO_3$ and $FeCO_3$ liquid components. Sound speed measurements were performed within the Li_2CO_3-Na_2CO_3-K_2CO_3-Rb_2CO_3-Cs_2CO_3-$CaCO_3$-$SrCO_3$-$BaCO_3$ system and combined with sound speed data from O'Leary et al. (2015) on the Li_2CO_3-Na_2CO_3-K_2CO_3-$CaCO_3$

quaternary. β_T was calculated for each liquid in the combined dataset and fitted with an ideal mixing model to approximate the β_T and $\delta\beta_T/\delta T$ of each of the pure components. Systematic trends between β_T and ΔV_{fusion} among the alkali and alkaline earth carbonate liquids were used to estimate the β_T of $MgCO_3$ and $FeCO_3$ liquid.

The fourth chapter introduces a new empirically-derived potential set for atomistic, classical-mechanic simulations of $MgCO_3$-$CaCO_3$-$SrCO_3$-$BaCO_3$ liquids. The model is applied to melts in the $CaCO_3$-$SrCO_3$-$BaCO_3$ ternary up to lower mantle PT conditions to test its ability to recover the known properties of $CaCO_3$, $SrCO_3$ and $BaCO_3$ liquid. The simulated volume data are fitted with a temperature-dependent 3rd order Birch-Murnaghan equation-of-state to estimate liquid properties that are currently unknown (e.g., K'). Isobaric simulations across a temperature range and simulations of pertinent crystal phases are also performed to provide estimates of isobaric heat capacity (C_P) and enthalpy of fusion (ΔH_{fusion}) for each liquid component. Mixing behavior and melt structure are also explored.

In the fifth chapter, the pair-potential model laid out in chapter four, is applied to simulations of pure $MgCO_3$ and mixed $MgCO_3$-bearing liquids. Simulations of pure $MgCO_3$ liquid are fitted with a temperature-dependent 4th order Birch-Murnaghan equation of state and the standard state thermodynamic properties (i.e. molar volume, thermal expansion, compressibility and its temperature and pressure dependence, heat capacity and enthalpy of fusion) of pure $MgCO_3$ liquid are calculated. The unique liquid structure of $MgCO_3$ liquid and its evolution with temperature and pressure are explored along with its unique mixing behavior. Finally, the model is applied to simulations of primary carbonate melts produced by partial melting of carbonate-bearing eclogite and peridotite to investigate their density and buoyancy in the mantle across a wide range of pertinent compositions, temperatures and pressures.

1.5 References

Ai Y., Lange R. A. (2004a) An ultrasonic frequency-sweep interferometer for liquids at high temperature: 1. Acoustic model. *J. Geophys. Res*. **109**, B12203.

Ai Y., Lange R. A. (2004b) An ultrasonic frequency-sweep interferometer for liquids at high temperature: 2. Mechanical assembly, signal processing, and application. *J. Geophys. Res.* **109**, B12204.

Antao M. and Hassan I. (2009) The orthorhombic structure of $CaCO_3$, $SrCO_3$, $PbCO_3$ and $BaCO_3$: linear structural trends. *Can. Mineral.* **47**, 1245–1255.

Baker M. B. and Wyllie P. J. (1992) High-pressure apatite solubility in carbonate-rich liquids: Implications for mantle metasomatism. *Geochim. Cosmochim. Acta* **56**, 3409–3422.

Biellmann C., Gillet P., Guyot F., Peyronneau J. and Reynard B. (1993) Experimental evidence for carbonate stability in the Earth's lower mantle. *Earth Planet. Sci. Lett.* **118**, 31–41.

Blundy J. and Dalton J. (2000) Experimental comparison of trace element partitioning between clinopyroxene and melt in carbonate and silicate systems, and implications for mantle metasomatism. *Contrib. to Mineral. Petrol.* **139**, 356–371.

Brenan J. M. and Watson E. B. (2002) Partitioning of trace elements between carbonate melt and clinopyroxene and olivine at mantle P-T conditions. *Geochim. Cosmochim. Acta* **55**, 1–12.

Brenker F. E., Vollmer C., Vincze L., Vekemans B., Szymanski A., Janssens K., Szaloki I., Nasdala L., Joswig W. and Kaminsky F. (2007) Carbonates from the lower part of transition zone or even the lower mantle. *Earth Planet. Sci. Lett.* **260**, 1–9.

Brey G. P., Bulatov V. K., Girnis A. V. and Lahaye Y. (2008) Experimental melting of carbonated peridotite at 6-10 GPa. *J. Petrol.* **49**, 797–821.

Bulanova G. P., Walter M. J., Smith C. B., Kohn S. C., Armstrong L. S., Blundy J. and Gobbo L. (2010) Mineral inclusions in sublithospheric diamonds from Collier 4 kimberlite pipe, Juina, Brazil: Subducted protoliths, carbonated melts and primary kimberlite magmatism. *Contrib. to Mineral. Petrol.* **160**, 489–510.

Dalton J. and Presnall D. C. (1998) Carbonatitic melts along the solidus of model lherzolite in the system CaO-MgO-Al_2O_3-SiO_2-CO_2 from 3 to 7 GPa. *Contrib. to Mineral. Petrol.* **131**, 123–135.

Dalton J. A. and Wood B. J. (1993) The compositions of primary carbonate melts and their evolution through wallrock reaction in the mantle. *Earth Planet. Sci. Lett.* **119**, 511–525.

Dasgupta R. and Hirschmann M. M. (2006) Melting in the Earth's deep upper mantle caused by carbon dioxide. *Nature* **440**, 659–662.

Dasgupta R. and Hirschmann M. M. (2007) Effect of variable carbonate concentration on the solidus of mantle peridotite. *Am. Mineral.* **92**, 370–379.

Dasgupta R. and Hirschmann M. M. (2010) The deep carbon cycle and melting in Earth's interior. *Earth Planet. Sci. Lett.* **298**, 1–13.

Dasgupta R., Hirschmann M. M., McDonough W. F., Spiegelman M. and Withers A. C. (2009) Trace element partitioning between garnet lherzolite and carbonatite at 6.6 and 8.6 GPa with applications to the geochemistry of the mantle and of mantle-derived melts. *Chem. Geol.* **262**, 57–77.

Dasgupta R., Hirschmann M. M. and Stalker K. (2006) Immiscible transition from carbonate-rich to silicate-rich melts in the 3 GPa melting interval of eclogite + CO_2 and genesis of silica-undersaturated ocean island lavas. *J. Petrol.* **47**, 647–671.

Dasgupta R., Hirschmann M. M. and Withers A. C. (2004) Deep global cycling of carbon constrained by the solidus of anhydrous, carbonated eclogite under upper mantle conditions. *Earth Planet. Sci. Lett.* **227**, 73–85.

Dasgupta R., Mallik A., Tsuno K., Withers A. C., Hirth G. and Hirschmann M. M. (2013) Carbon-dioxide-rich silicate melt in the Earth's upper mantle. *Nature* **493**, 211-222.

Dobson D. P., Jones A. P., Rabe R., Sekine T., Kurita K., Taniguchi T., Kondo T., Kato T., Shimomura O. and Urakawa S. (1996) In-situ measurement of viscosity and density of carbonate melts at high pressure. *Earth Planet. Sci. Lett.* **143**, 207–215.

Dove M. T. and Powell B. M. (1989) Neutron diffraction study of the tricritical orientational order/disorder phase transition in calcite at 1260 K. *Phys. Chem. Minerals* **16**, 503-507.

Falloon T. J. and Green D. H. (1989) The solidus of carbonated, fertile peridotite. *Earth Planet. Sci. Lett.* **94**, 364–370.

French B. M. and Rosenberg P. E. (1965) Siderite ($FeCO_3$) thermal decomposition in equilibrium with graphite. *Science* **147**, 1283-1284.

Gaillard F., Malki M., Iacono-Marziano G., Pichavant M. and Scaillet B. (2008) Carbonatite melts and electrical conductivity in the asthenosphere. *Science* **322**, 1363–1365.

Ghiorso M. S., Hirschmann M. M., Reiners P. W. and Kress V. C. (2002) The pMELTS: A revision of MELTS for improved calculation of phase relations and major element partitioning related to partial melting of the mantle to 3 GPa. *Geochemistry Geophys. Geosystems* **3**, 36.

Ghosh S., Ohtani E., Litasov K. D. and Terasaki H. (2009) Solidus of carbonated peridotite from 10 to 20 GPa and origin of magnesiocarbonatite melt in the Earth's deep mantle. *Chem. Geol.* **262**, 17–28.

Gorman P. J., Kerrick D. M. and Connolly J. A. D. (2006) Modeling open system metamorphic decarbonation of subducting slabs. *Geochemistry, Geophys. Geosystems* **7**.

Green D.H., Wallace M.E. (1988) Mantle metasomatism by ephemeral carbonatite melts. *Nature* **336**, 459–462.

Green T. H., Adam J. and Siel S. H. (1992) Trace element partitioning between silicate minerals and carbonatite at 25 kbar and application to mantle metasomatism. *Mineral. Petrol.* **46**, 179–184.

Hammouda T. (2003) High-pressure melting of carbonated eclogite and experimental constraints on carbon recycling and storage in the mantle. *Earth Planet. Sci. Lett.* **214**, 357–368.

Hammouda T. and Laporte D. (2000) Ultrafast mantle impregnation by carbonatite melts. *Geology* **28**, 283–285.

Harmer R. E., Lee C. A. and Eglington B. M. (1998) A deep mantle source for carbonatite magmatism: evidence from the nephelinites and carbonatites of the Buhera district, SE Zimbabwe. *Earth Planet. Sci. Lett.* **158**, 131–142.

Hurst H. J. (1991) The thermal decomposition of magnesite in nitrogen. *Thermochim. Acta* **189**, 91–96.

Hunter R. H. and McKenzie D. (1989) The equilibrium geometry of carbonate melts in rocks of mantle composition. *Earth Planet. Sci. Lett.* **92**, 347–356.

Ionov D. A., Dupuy C., O'Reilly S. Y., Kopylova M. G. and Genshaft Y. S. (1993) Carbonated peridotite xenoliths from Spitsbergen: implications for trace element signature of mantle carbonate metasomatism. *Earth Planet. Sci. Lett.* **119**, 283–297.

Ishizawa N., Setoguchi H. and Yanagisawa K. (2013) Structural evolution of calcite at high temperatures : Phase V unveiled. **8**, 9–11.

Isshiki M., Irifune T., Hirose K., Ono S., Ohishi Y., Watanuki T., Nishibori E., Takata M. and Sakata M. (2004) Stability of magnesite and its high-pressure form in the lowermost mantle. *Nature* **427**, 60–63.

Jacobs G. K., Kerrick D. M. and Krupka K. M. (1981) The high-temperature heat capacity of natural calcite ($CaCO_3$) *Phys. Chem. Miner.* **7**, 55–59.

Janz G. J., Neuenschwander E. and Kelly F. J. (1963) High-temperature heat content and related properties for Li_2CO_3, Na_2CO_3, K_2CO_3, and the ternary eutectic mixture. *Trans. Faraday Soc.* **59**, 841-845.

Johnston F. K. B., Turchyn A. V. and Edmonds M. (2011) Decarbonation efficiency in subduction zones: Implications for warm Cretaceous climates. *Earth Planet. Sci. Lett.* **303**, 143–152.

Jones A. P., Genge M. and Carmody L. (2013) Carbonate melts and carbonatites. *Rev. Mineral. Geochemistry* **75**. 289-322.

Kaminsky F., Wirth R., Matsyuk S., Schreiber A. and Thomas R. (2009) Nyerereite and nahcolite inclusions in diamond: evidence for lower-mantle carbonatitic magmas. *Mineral. Mag.* **73**, 797–816.

Katsura T., Tsuchida Y., Ito E., Yagi T., Utsumi W. and Akimoto S. (1991) Stability of magnesite under the lower mantle conditions. *Proc. Japan Acad. Ser. B-Physical Biol. Sci.* **67**, 57–60.

Kelemen P. B. and Manning C. E. (2015) Reevaluating carbon fluxes in subduction zones, what goes down, mostly comes up. *Proc. Natl. Acad. Sci.* **112**, E3997–E4006.

Kono Y., Kenney-Benson C., Hummer D., Ohfuji H., Park C., Shen G., Wang Y., Kavner A. and Manning C. E. (2014) Ultralow viscosity of carbonate melts at high pressures. *Nat. Commun.* **5**, 5091.

Li Y., Zou Y., Chen T., Wang X., Qi X., Chen H., Du J. and Li B. (2015) P-V-T equation of state and high-pressure behavior of $CaCO_3$ aragonite. *Am. Mineral.* **100**, 2323–2329.

Litasov K. D., Fei Y., Ohtani E., Kuribayashi T. and Funakoshi K. (2008) Thermal equation of state of magnesite to 32 GPa and 2073 K. *Phys. Earth Planet. Inter.* **168**, 191–203.

Litasov K. and Ohtani E. (2010) The solidus of carbonated eclogite in the system CaO-Al_2O_3-MgO-SiO_2-Na_2O-CO_2 to 32 GPa and carbonatite liquid in the deep mantle. *Earth Planet. Sci. Lett.* **295**, 115–126.

Litasov K. D., Shatskiy A., Gavryushkin P. N., Bekhtenova A. E., Dorogokupets P. I., Danilov B. S., Higo Y., Akilbekov A. T. and Inerbaev T. M. (2017) P-V-T equation of state of $CaCO_3$ aragonite to 29 GPa and 1673 K: In situ X-ray diffraction study. *Phys. Earth Planet. Inter.* **265**, 82–91.

Litasov K. D., Shatskiy A., Gavryushkin P. N., Sharygin I. S., Dorogokupets P. I., Dymshits A. M., Ohtani E., Higo Y. and Funakoshi K. (2013) P-V-T equation of state of siderite to 33GPa and 1673K. *Phys. Earth Planet. Inter.* **224**, 83–87.

Litasov K. D., Shatskiy A., Ohtani E. and Yaxley G. M. (2013) Solidus of alkaline carbonatite in the deep mantle. *Geology* **41**, 79–82.

Liu Q. and Lange R. A. (2003) New density measurements on carbonate liquids and the partial molar volume of the $CaCO_3$ component. *Contrib. to Mineral. Petrol.* **146**, 370–381.

Luth R. W. (1999) Carbon and carbonates in the mantle. In *Mantle Petrology: Field Observations and High Pressure Experimentation: A Tribute to Francis R. (Joe) Boyd* (eds. Y. Fei, C. M. Bertka and B. O. Mysen). The Geochemical Society, Houston. pp. 297-316.

Markgraf S. and Reeder R. (1985) High-temperature structure refinements of calcite and magnesite. *Am. Miner.* **70**, 590–600.

Molina J. F. and Poli S. (2000) Carbonate stability and fluid composition in subducted oceanic crust: An experimental study on H_2O-CO_2-bearing basalts. *Earth Planet. Sci. Lett.* **176**, 295–310.

Narsimhan G. (1961) Thermal decomposition of calcium carbonate. *Chem. Eng. Sci.* **16**, 7–20.

O'Reilly S. Y. and Griffin W. L. (1988) Mantle metasomatism beneath western Victoria, Australia : II . Isotopic geochemistry. *Geochim. Cosmochim. Acta* **52**, 449–459.

Plank T. and Langmuir C. H. (1998) The chemical composition of subducting sediment and its consequences for the crust and mantle. *Chem. Geol.* **145**, 325–394.

Presnall, D. C. and Gudfinnsson, G. H. (2005). Carbonate-rich melts in the oceanic low-velocity zone and deep mantle. In *Plates, Plumes and Paradigms. Geological Society of America, Special Papers* (eds. G. R. Foulger, J. H. Natland, D. C. Presnall and D. L. Anderson). The Geological Society of America, Boulder. pp. 297-316.

Redfern S.A.T. and Angel R.J. (1999) High-pressure behavior and equation of state of calcite, $CaCO_3$. *Contrib. to Mineral. Petrol.* **134**, 102–106.

Rea D. K. and Ruff L. J. (1996) Composition and mass flux of sediment entering the world's subduction zones: Implications for global sediment budgets, great earthquakes, and volcanism. *Earth Planet. Sci. Lett.* **140**, 1–12.

Ross N. L. (1997) The equation of state and high-pressure behavior of magnesite. *Am. Mineral.* **82**, 682–688.

Rudnick R. L., McDonough W. F. and Chappell B. W. (1993) Carbonatite metasomatism in the northern Tanzanian mantle: petrographic and geochemical characteristics. *Earth Planet. Sci. Lett.* **114**, 463–475.

Shcheka S. S., Wiedenbeck M., Frost D. J. and Keppler H. (2006) Carbon solubility in mantle minerals. *Earth Planet. Sci. Lett.* **245**, 730–742.

Sleep N. H. and Zahnle K. (2001) Carbon dioxide cycling and implications for climate on acient Earth. *J. Geophys. Res.* **106**, 1373–1399.

Solopova N. A., Dubrovinsky L., Spivak A. V., Litvin Y. A. and Dubrovinskaia N. (2015) Melting and decomposition of MgCOinf3/inf at pressures up to 84 GPa. *Phys. Chem. Miner.* **42**, 73–81.

Stachel T. and Harris J. W. (2009) Formation of diamond in the Earth's mantle. *J. Phys. Condens. Matter* **21**.

Staudigel H., Hart S. R., Schmincke H. U. and Smith B. M. (1989) Cretaceous ocean crust at DSDP Sites 417 and 418: Carbon uptake from weathering versus loss by magmatic outgassing. *Geochim. Cosmochim. Acta* **53**, 3091–3094.

Thomson A. R., Walter M. J., Kohn S. C. and Brooker R. A. (2016) Slab melting as a barrier to deep carbon subduction. *Nature* **529**, 76–79.

Trull T., Nadeau S., Pineau F., Polvé M. and Javoy M. (1993) CHe systematics in hotspot xenoliths: Implications for mantle carbon contents and carbon recycling. *Earth Planet. Sci. Lett.* **118**, 43–64.

Wallace M. E. and Green D. H. (1988) An experimental determination of primary carbonatite magma composition. *Nature* **335**, 343-346.

Weiss Y., Griffin W. L., Bell D. R. and Navon O. (2011) High-Mg carbonatitic melts in diamonds, kimberlites and the sub-continental lithosphere. *Earth Planet. Sci. Lett.* **309**, 337–347.

Wood B. B. J., Pawley A. and Frost D. R. (1996) Water and carbon in the earth's mantle. *Philos. Trans. Royal Soc. A* **354**, 1495-1511.

Yaxley G. M., Crawford A. J. and Green D. H. (1991) Evidence for carbonatite metasomatism in spinel peridotite xenoliths from western Victoria, Australia. *Earth Planet. Sci. Lett.* **107**, 305–317.

Yaxley G. M. and Brey G. P. (2004) Phase relations of carbonate-bearing eclogite assemblages from 2.5 to 5.5 GPa: Implications for petrogenesis of carbonatites. *Contrib. to Mineral. Petrol.* **146**, 606–619.

Zhang J. and Reeder R. J. (1999) Comparative compressibilities of calcite-structure carbonates: Deviations from empirical relations. *Am. Mineral.* **84**, 861–870.

Chapter 2 The density of Li_2CO_3-Na_2CO_3-K_2CO_3-Rb_2CO_3-Cs_2CO_3-$CaCO_3$-$SrCO_3$-$BaCO_3$ liquids: New measurements, ideal mixing, and systematic trends with cation coordination

2.1 Introduction

Despite its relatively low abundance in the mantle, carbonate plays a key role in the global carbon cycle and in the formation of mantle melts in various tectonic settings (e.g., Dasgupta and Hirschmann, 2010). Carbonate may be a major factor in deep (240-300 km) partial melting of the mantle beneath mid-ocean spreading ridges and intraplate settings (e.g., Dasgupta and Hirschmann, 2006), and it plays a critical role in the genesis of silica-undersaturated alkaline magmas (e.g., Dasgupta et al., 2006). Moreover, because carbonate melts are efficient scavengers of various incompatible elements (e.g., Blundy and Dalton, 2000), they are also are effective agents of mantle metasomatism (e.g., Dalton and Wood, 1993). Therefore, understanding the stability of carbonate melts under mantle conditions and incorporating it into thermodynamic models (e.g., p-MELTS; Ghiroso et al., 2002) is a major imperative. In order to extend thermodynamic models to include carbonate melts it is necessary to constrain their equation of state (P-V-T relation). The objective of this study is to expand the compositional range of carbonate liquids for which direct density measurements are known at 1-bar, with a focus on alkaline-earth components.

The three most abundant carbonate components in the mantle are $MgCO_3$, $CaCO_3$ and $FeCO_3$; however these three pure end-member liquids are not stable at one bar and decompose at temperatures below their melting temperatures. In previous studies, Liu and Lange (2003) and

O'Leary et al. (2015) showed that the $CaCO_3$ component could be added to low-temperature alkali carbonate liquids to form $CaCO_3$-bearing liquids that are stable at one bar. The same strategy is employed in this study, where $CaCO_3$, $SrCO_3$, and $BaCO_3$ are added in various proportions (≤ 50 mol%) to the eutectic in the Li_2CO_3-Na_2CO_3-K_2CO_3 ternary to permit density measurements of alkaline earth carbonate-bearing liquids to be obtained over as wide a range of composition and temperature as possible. In addition, the density of melts with 50-100% Rb_2CO_3 and Cs_2CO_3 are also measured. By expanding the compositional data set for which double-bob liquid density measurements are currently available from four to eight components (Li_2CO_3-Na_2CO_3-K_2CO_3-Rb_2CO_3-$Cs_2CO_3CaCO_3$-$SrCO_3$-$BaCO_3$), systematic variations with composition and temperature can be evaluated. This in turn allows constraints to be placed on the partial molar volume and thermal expansion of the $MgCO_3$ and $FeCO_3$ components in multicomponent carbonate liquids at 1 bar. Standard state thermodynamic property estimates on these critical components are necessary to extend thermodynamic models such as MELTS to carbonated mantle systems.

2.2 Materials and methods

2.2.1 Sample synthesis

Fifteen samples in the Li_2CO_3-Na_2CO_3-K_2CO_3-Rb_2CO_3-Cs_2CO_3-$CaCO_3$-$SrCO_3$-$BaCO_3$ system were used in this study (Table 2.1). For 13 of these samples, the eutectic composition in the Li_2CO_3-Na_2CO_3-K_2CO_3 ternary (referred to as T in Table 2.1) was combined with varying amounts of $CaCO_3$, $SrCO_3$, $BaCO_3$, Cs_2CO_3 and Rb_2CO_3. The remaining two samples are pure Rb_2CO_3 and Cs_2CO_3. The synthesized samples were made in 200 g batches from powdered or granular reagents with >99.5% purity. Before synthesis, the loss on ignition (LOI) of each reagent was determined and used to calculate the appropriate weight of each reagent to be poured

directly into the glass jar of an electric blender. The reagents were mixed at high speeds for several minutes to make a powdered sample with a homogenous composition.

2.2.2 Double-bob Archimedean method

The double-bob Archimedean method was used to determine the density of each experimental liquid over a 697 degree temperature interval (758-1455 K), following the methods described in detail in Lange and Carmichael (1987) and Liu and Lange (2003). Sufficient amounts of each sample (~75 g) were loaded into a Pt crucible to ensure a liquid depth of ~2.5 cm. The sample and Pt crucible were loaded into a Deltech vertical tube furnace and brought up to temperature under a constant stream of pure CO_2 gas.

A density measurement was made by suspending a Pt bob from a mass balance (with a precision of ±0.0001 g) above the surface of the sample liquid. The bob and sample were allowed at least thirty minutes to come to thermal equilibrium. The bob was weighed and then immersed in the sample liquid and weighed again to obtain buoyancy, B(T). The depth of immersion and volume of the bob that was immersed were measured, and used to calculate the density of the liquid:

$$\rho^{liq}(T) = \frac{B(T) + S(T)}{V(T)} \quad (2.1)$$

where ρ^{liq}(T) is the density of the liquid at the experimental temperature, B(T) is the buoyancy, S(T) is the surface tension effect from the liquid surface pulling on the stem of the bob, and V(T) is the volume of the bob immersed in the liquid. To eliminate the effect S(T), the procedure was repeated with a second bob of different size, which enables the density of the liquid to be calculated with the following equation:

$$\rho^{liq}(T) = \frac{B_L(T) - B_S(T)}{V_L(T) - V_S(T)} \quad (2.2)$$

where the L and S subscripts denote a large and small bob, respectively. The buoyancy measurements were repeated with two different large bobs (26.4 and 25.9 g) and two different small bobs (11.7 and 9.8 g), which allowed four different density measurements to be obtained at each experimental temperature, using Eq. 2.2. To further assess reproducibility, replicate density measurements were made on two different aliquots from the same synthesized sample batch in two cases (T-10%Sr and T-50%Ba), and the T-35%Ba sample was re-synthesized from scratch and its density re-measured. The $BaCO_3$-bearing liquids posed experimental difficulties not found for the other sample liquids, in which the platinum bobs were prone to adhering to the sides of the crucible as they were immersed during a buoyancy measurement.

Density measurements were made at three to four different temperatures, with the temperature interval bounded by the liquidus and decomposition temperature of each sample. For one sample (T-35%Ca; Table 2.1), liquid density was measured at only one temperature because the supply of CO_2 ran out and there was insufficient CO_2 in the furnace tube to prevent decarbonation (decomposition) of the sample. For the alkaline earth carbonate components, measurements were made over temperature intervals that ranged from 444 ($CaCO_3$), 697 ($SrCO_3$) and 407 ($BaCO_3$) K. For the Rb_2CO_3 and Cs_2CO_3 components, density measurements were made over temperature intervals of 392 and 355 K, respectively.

2.2.3 Temperature control

Determination of the experimental temperature during each density measurement was obtained with the following calibration. The Pt crucible was filled with alumina (Al_2O_3) powder to the same depth as that used for the experimental liquids and placed in the furnace. A thermocouple was buried 2 cm deep into the powder, a depth corresponding to that of immersed bobs, and the recorded temperature was used to locate the furnace hotspot and isothermal zone.

The crucible was situated so that the sample was near the bottom of the isothermal zone to ensure that the liquid at the bottom of the crucible was not hotter than the top, which prevented convection. The furnace was then set to various temperatures, spanning the range used in the density experiments (800 - 1500 K). The thermocouple temperature was recorded at each set point and used to create a temperature calibration curve. The thermocouple used in temperature calibration was also tested for accuracy against the melting point of gold; the gold melted within five degrees of the accepted value (1337 K).

2.2.4 Density measurements of liquid NaCl as a standard

To verify the accuracy of the Pt double-bob Archimedean method and the temperature calibration curve employed in this study, the density of liquid NaCl was measured eleven different times between 1102 and 1455 K. These measurements were made before, during and after the density measurements on the sample liquids in Table 2.1 were made.

Table 2.1 The molar composition of the 15 samples used in this study along with their gram formula weights (g.f.w.)

Sample	Li_2CO_3	Na_2CO_3	K_2CO_3	Rb_2CO_3	Cs_2CO_3	$CaCO_3$	$SrCO_3$	$BaCO_3$	g formula wt.
T-25% Ca	0.326	0.236	0.188			0.25			100.082
T-35%Ca	0.283	0.205	0.163			0.35			100.083
T-50%Ca	0.218	0.158	0.125			0.5			100.084
T-10%Sr	0.392	0.284	0.225				0.1		104.836
T-20%Sr	0.348	0.252	0.200				0.2		109.590
T-30%Sr	0.305	0.221	0.175				0.3		114.345
T-50%Sr	0.217	0.162	0.124				0.497	0.001	123.788
T-15%Ba	0.370	.268	0.213					0.15	114.670
T-35%Ba	0.283	0.205	0.163					0.35	134.121
T-50%Ba	0.218	0.158	0.125					0.5	148.710
T-50%Rb				0.5					124.216
Rb_2CO_3				1					230.945
T-50%CaSrBa	0.218	0.158	0.125			0.167	0.167	0.167	111.260
T-50%Cs	0.218	0.158	0.125		0.5				212.950
Cs_2CO_3					1				325.820

2.3 Results

2.3.1 NaCl liquid density

The NaCl liquid density results are listed in Table 2.2 at each temperature of measurement, together with molar volume, which is calculated by dividing the molar mass of NaCl (58.44 g/mol) by density. In Figure 2.1, the liquid molar volume data from this study are plotted against temperature and compared to those reported in Stein et al. (1986), Lange and Carmichael (1987), Liu and Lange (2001, 2006) and Guo et al. (2013).

Figure 2.1 The molar volume of liquid NaCl from this study plotted along with other double-bob Archimedean results from the literature.

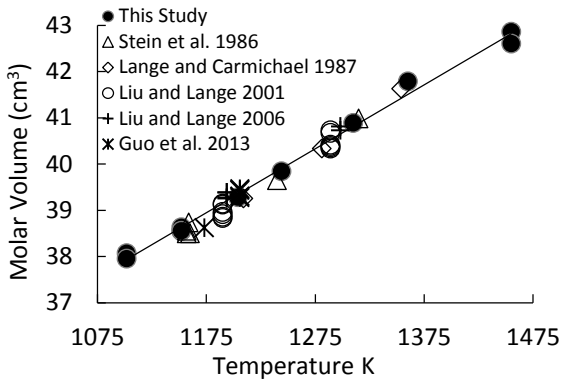

All of these studies employed the double-bob Archimedean method, and the results show excellent inter-laboratory agreement. In addition, the NaCl density measurements performed in this study have significantly extended the temperature range for which double-bob density data is available.

2.3.2 Carbonate liquid densities

The density results for the 15 experimental liquids at each temperature of measurement are reported in Table 2.3. Molar volumes were calculated by dividing the measured density into the gram formula weight (g.f.w.; defined in Table 2.1) of each sample. Molar volumes of all liquids are plotted as a function of temperature in Figure 2.2. Ideally, each density result at each temperature should be based on the average of four (n=4; Table 2.3) density determinations

obtained from four bobs (two large and two small). However, during some experiments, one or two of the four bob measurements failed, often because the bob adhered to the crucible wall during immersion. In some cases, many more bob buoyancy measurements were made, enabling more density determinations, and in Table 2.3, the number of different density measurements at each experimental temperature ranges from one to 13.

Table 2.2 The densities of NaCl liquid and temperatures determined in this study. Also shown are the corresponding molar volumes of NaCl determined by this study at each temperature.

Temp (K)	Density from this study (g/cm^3)	Mol. Volume this study (cm^3/mol)
1102	1.535	38.07
1102	1.540	37.95
1152	1.513	38.63
1152	1.516	38.55
1152	1.516	38.55
1204	1.488	39.28
1244	1.467	39.84
1310	1.429	40.88
1360	1.399	41.79
1455	1.364	42.86
1455	1.372	42.60

Table 2.3 The experimental densities (ρ), molar volumes (Vmeas.) and measurement uncertainties for each density experiment are shown. N indicates the number of independent density measurements obtained during each experiment. Vcalc. is the molar volume given by a fit of the experimental volume data to Eq. 2.4.

Sample	Temp (K)	ρ (g/cm^3)	SD (%)	N	$V_{meas.}$ (cm^3)	$V_{calc.}$ (cm^3)	Difference %
T-25%Ca	813	2.138	0.30	4	46.81	46.52	0.63
T-25%Ca	859	2.123	0.23	4	47.14	47.00	0.31
T-25%Ca	912	2.112	0.30	4	47.39	47.54	-0.32
T-25%Ca	1152	1.992	0.17	4	50.24	50.05	0.39
T-25%Ca	1257	1.948	0.25	4	51.38	51.14	0.47
T-35%Ca	1007	2.110	0.43	4	47.43	47.34	0.20
T-50%Ca	1007	2.201	0.21	2	45.47	45.54	-0.16
T-50%Ca	1054	2.181	0.13	4	45.89	45.98	-0.19
T-50%Ca	1102	2.164	0.25	1	46.25	46.42	-0.36
T-10%Sr	758	2.170	0.08	4	48.31	47.98	0.69
T-10%Sr	859	2.123	0.31	2	49.38	49.11	0.55
T-10%Sr	1257	1.966	0.29	10	53.32	53.52	-0.37
T-20%Sr	1102	2.141	0.16	2	51.19	50.98	0.41

T-20%Sr	1257	2.071	0.30	4	52.92	52.61	0.58
T-20%Sr	1455	2.002	0.20	4	54.74	54.71	0.05
T-30%Sr	960	2.351	0.31	4	48.64	48.72	-0.17
T-30%Sr	1054	2.305	0.42	4	49.61	49.66	-0.12
T-30%Sr	1152	2.248	0.32	2	50.87	50.65	0.42
T-50%Sr	1152	2.524	0.29	2	49.04	48.97	0.15
T-50%Sr	1152	2.540	0.10	4	48.74	48.97	-0.48
T-50%Sr	1257	2.489	0.17	4	49.73	49.91	-0.36
T-50%Sr	1362	2.433	0.47	4	50.88	50.87	0.02
T-50%Sr	1455	2.390	0.09	4	51.79	51.71	0.17
T-15%Ba	850	2.316	0.16	4	49.51	49.56	-0.11
T-15%Ba	960	2.253	0.36	4	50.90	50.80	0.18
T-35%Ba	960	2.643	0.24	7	50.75	50.56	0.36
T-35%Ba	1102	2.553	0.46	7	52.53	52.07	0.89
T-35%Ba	1152	2.546	0.57	13	52.68	52.60	0.15
T-35%Ba	1204	2.534	0.24	4	52.93	53.14	-0.41
T-35%Ba	1257	2.503	0.56	4	53.58	53.70	-0.22
T-50%Ba	1102	2.887	0.05	4	51.51	51.83	-0.61
T-50%Ba	1127	2.852	0.47	4	52.14	52.08	0.13
T-50%Ba	1152	2.855	0.07	2	52.09	52.33	-0.47
T-50%Ba	1257	2.769	0.08	4	53.71	53.39	0.59
T-50%Rb	865	2.618	0.08	4	63.22	63.22	0.01
T-50%Rb	885	2.621	0.32	4	63.15	63.51	-0.57
T-50%Rb	982	2.537	0.17	4	65.24	64.95	0.45
T-50%Rb	1078	2.491	0.07	4	66.44	66.37	0.11
T-50%Rb	1152	2.453	0.42	4	67.47	67.47	0.01
T-50%Rb	1112	2.476	0.20	4	66.85	66.87	-0.04
Rb_2CO_3	1152	2.819	0.23	2	81.92	81.72	0.25
Rb_2CO_3	1257	2.769	0.23	3	83.40	83.60	-0.24
T-50%CaSrBa	1030	2.587	0.20	4	48.02	48.23	-0.44
T-50%CaSrBa	1080	2.556	0.00	1	48.60	48.70	-0.21
T-50%Cs	859	3.085	0.45	4	69.03	69.22	-0.28
T-50%Cs	960	3.009	0.56	4	70.77	70.93	-0.23
T-50%Cs	1112	2.881	0.54	2	73.92	73.51	0.55
Cs_2CO_3	1112	3.461	0.07	4	94.14	94.27	-0.14
Cs_2CO_3	1122	3.438	0.30	4	94.77	94.49	0.29
Cs_2CO_3	1127	3.433	0.39	4	94.91	94.60	0.32
Cs_2CO_3	1163	3.419	0.21	4	95.30	95.41	-0.11
Cs_2CO_3	1214	3.388	0.04	4	96.17	96.54	-0.39

Fig. 2.2 The molar volume of each experimental liquid shown as a function temperature, from this study (solid points) and from Liu and Lange (2003) (empty points). The lines represent the best-fit of the combined experimental data to Eq. 2.3.

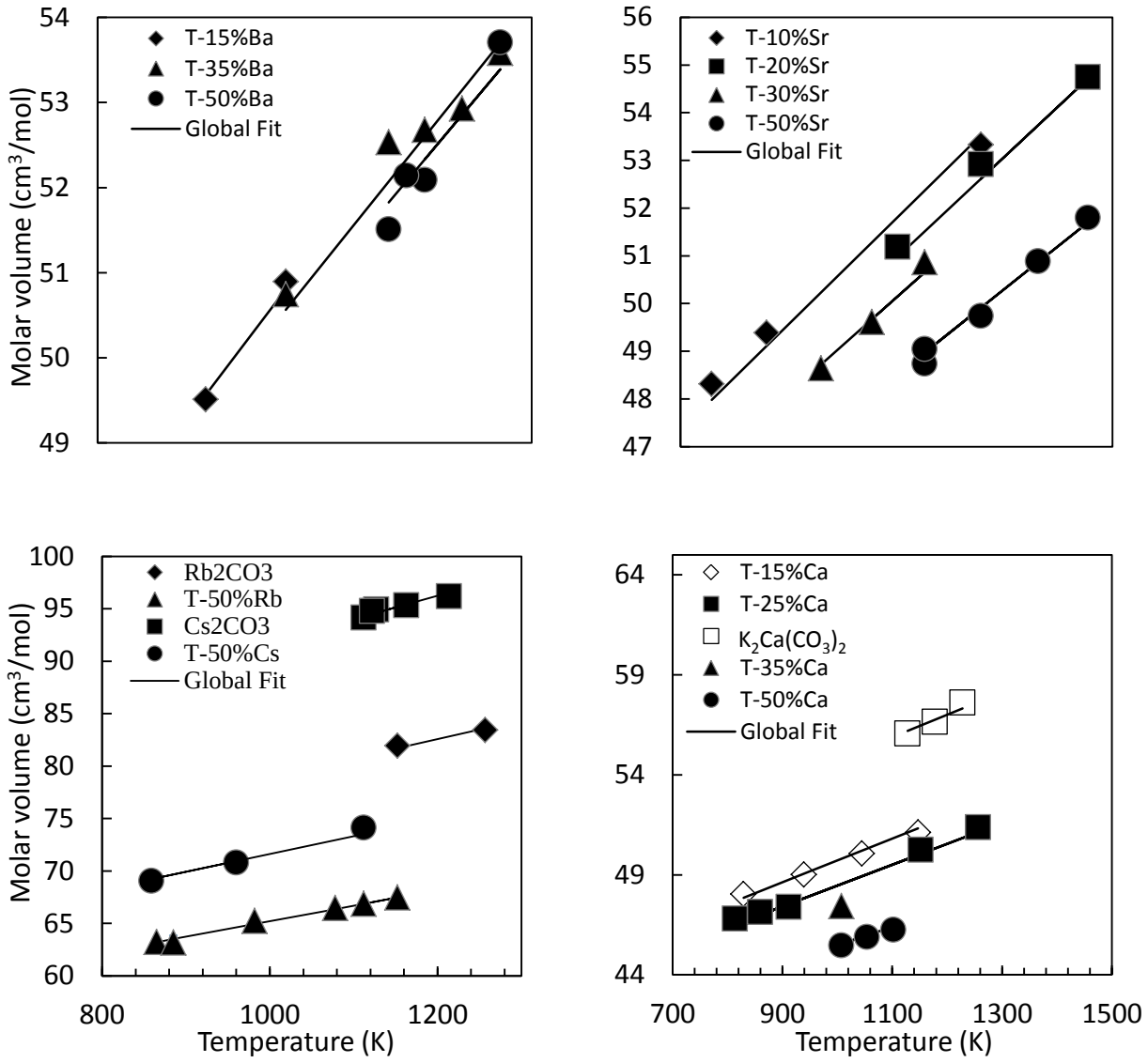

The standard deviation of the measured density for each sample ranges from 0.04 to 0.57 %, and the average is 0.26%, which is identical to the measurement error of Liu and Lange (2003).

A linear fit of the molar volume with temperature was made for each sample liquid with the following equation:

$$V(T) = a_{1100\,K} + b\,(T - 1100\,K) \tag{2.3}$$

where $V(T)$ is the molar volume of the liquid, a is the fitted molar volume of the liquid at 1100 K, b is the thermal expansivity $\frac{\delta V}{\delta T}$ and T is temperature in Kelvin. Table 2.4 gives the fitted

values of a and b for all sample liquids (except T-35%Ca, for which molar volume was obtained at only one temperature; Table 2.3).

Table 2.4 The fitted parameters of linear models of molar volume as a function of temperature for each experimental liquid.

$V = a_{1100\,K} + b\,(T\text{-}1100\,K)$ cm^3/mol			
Sample	$a_{1100\,K}$	$b \cdot 10^3$	Temp. range (K)
T-25%Ca	49.67	10.62	813-1257
T-35%Ca	-	-	1007
T-50%Ca	46.24	8.16	1007-1102
T-10%Sr	51.76	10.01	758-1257
T-20%Sr	51.23	10.04	1102-1455
T-30%Sr	50.22	11.61	960-1152
T-50%Sr	48.35	9.61	1152-1455
T-15%Ba	52.64	12.50	850-960
T-35%Ba	52.17	9.13	960-1257
T-50%Ba	51.55	13.63	1102-1257
T-50%Rb	66.74	15.36	1152-1257
Rb_2CO_3	81.18	14.16	865-1152
T-50%CaSrBa	48.83	11.65	1030-1080
T-50%Cs	73.63	19.43	859-1112
Cs_2CO_3	94.24	17.24	1112-1214

2.3.3 A linear model equation for molar volume

The molar volume data for the 15 liquids in Table 2.3 were combined with those from Liu and Lange (2003) on nine Li_2CO_3-Na_2CO_3-K_2CO_3-$CaCO_3$ liquids in a fit to the following linear volume equation:

$$V^{liq}(X,T) = \sum X_i \left(\overline{V}_{i,1100K} + \frac{\delta \overline{V}_i}{\delta T}[T - 1100\ K]\right). \quad (2.4)$$

In equation 2.4, V^{liq} is the measured molar volume, X_i is the mole fraction of each carbonate component i in each experimental liquid, $\overline{V}_{\mathrm{i,1100K}}$ is the partial molar volume of each carbonate component at 1100 K, and $\frac{\delta \overline{V}_i}{\delta T}$ is the partial molar thermal expansivity of each carbonate component. Fitted values of $\overline{V}_{\mathrm{i}}$ and $\frac{\delta \overline{V}_i}{\delta T}$ for each carbonate component were obtained by multiple

linear regression of Equation 2.4 and reported in Table 2.5. The final adjusted R^2 of the fit is 0.98. The average residual is ± 0.32%, which is close to the average analytical error for density of 0.26%. Most importantly, the residuals show no systematic variation with temperature (Fig. 2.3) or composition (Fig. 2.4). The maximum residual of 0.89% is for a $BaCO_3$-bearing liquid, which is not surprising given the experimental challenges with these liquids. The results from this study show that the molar volume of multicomponent carbonate liquids, including those with more than one alkaline earth carbonate component (e.g, T-50CaSrBa; Table 2.1), mix ideally with respect to composition in the Li_2CO_3-Na_2CO_3-K_2CO_3-Rb_2CO_3-$CaCO_3$-$SrCO_3$-$BaCO_3$ system. Moreover, for the alkali carbonate components, (Rb_2CO_3 and Cs_2CO_3 in this study; Li_2CO_3, Na_2CO_3 and K_2CO_3 in Liu and Lange, 2003), the fitted partial molar volumes (Table 2.5) match those for the pure end-members (Table 2.4).

Table 2.5 The partial molar volumes and partial molar thermal expansivities resulting from a fit of the experimental volumes from this study in combination with molar volume data from Liu and Lange (2003) to a linear mixing model.

$V = V_{i(1100\ K)} + \delta V_i/\delta T\ (T\text{-}1100\ K)$ cm^3/mol		
Component	$V_{i(1100\ K)}$ (cm^3/mol)	$\delta V_i/\delta T$ (10^{-3} cm^3/mol K)
Li_2CO_3	41.22 ± .09	8.83 ± 1.20
Na_2CO_3	53.27 ± .11	12.30 ± 1.11
K_2CO_3	71.59 ± .13	15.68 ± 1.13
Rb_2CO_3	80.78 ± .11	17.98 ± 0.90
Cs_2CO_3	94.00 ± .09	22.28 ± 1.14
$CaCO_3$	40.18 ± .16	6.75 ± 1.52
$SrCO_3$	44.33 ± .22	6.40 ± 1.20
$BaCO_3$	50.99 ± .19	8.65 ± 1.90

Fig. 2.3 The residuals from the fit of the experimental data to Equation 2.3 as a function of temperature. Error bars show the ±2σ measurement error.

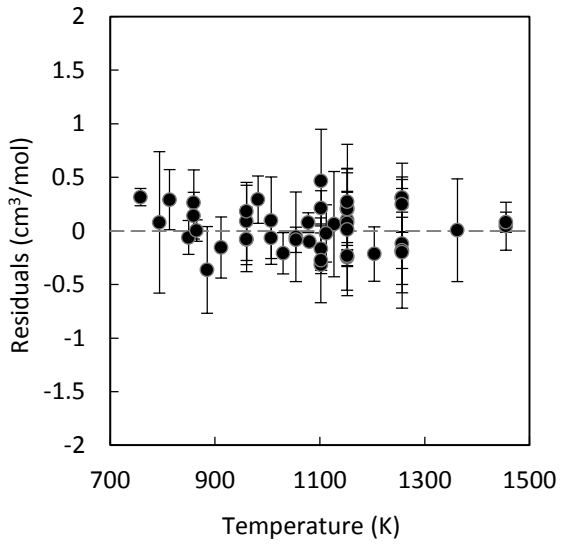

Fig. 2.4 The residuals from the fit of the experimental data to Equation 2.3 for each component shown as a function of mole fraction of the given component. Error bars show the ±2σ measurement error.

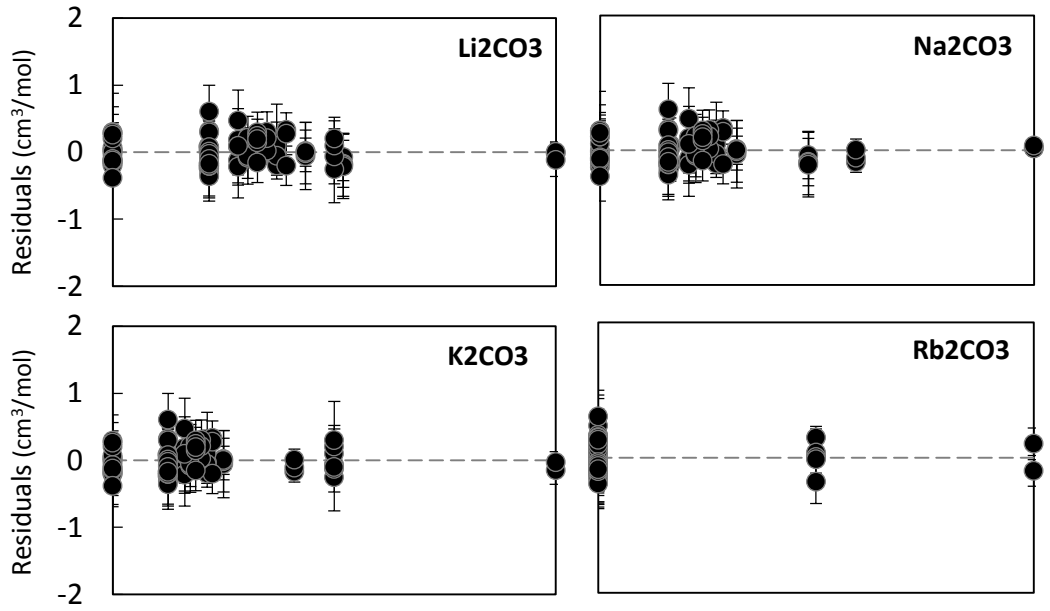

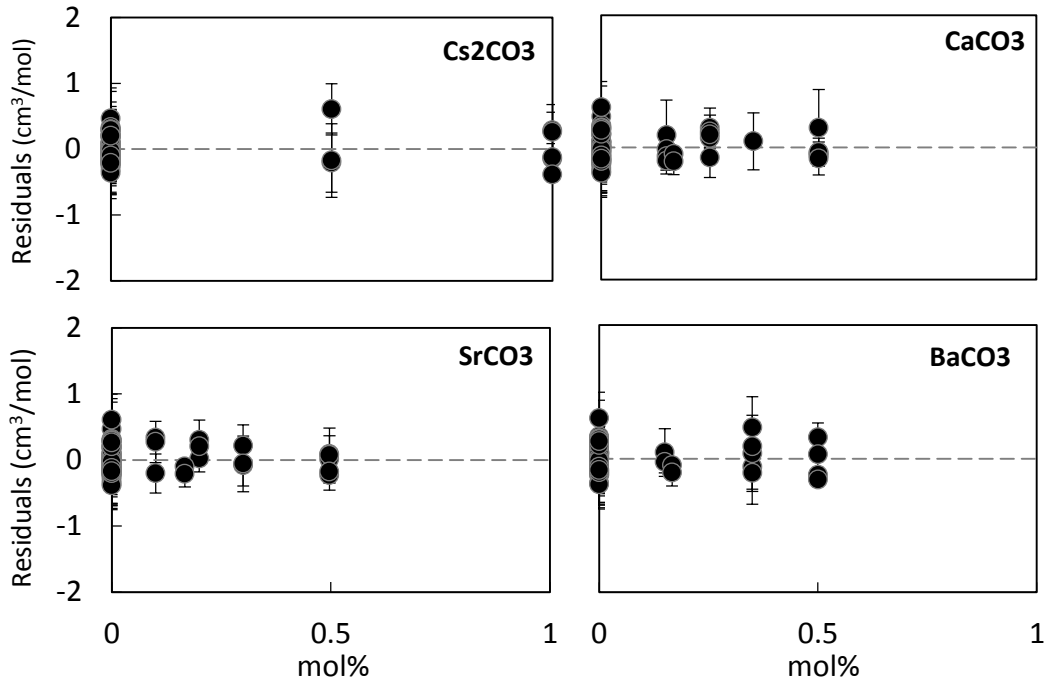

2.3.4 Constant thermal expansion coefficients for alkali vs. alkaline earth carbonate liquids

A plot of the thermal expansion coefficient, $a = \left(1/\overline{V}_i\right) / \left(\P\overline{V}_i/\P T\right)$, for each liquid carbonate component at 1100 K is shown in Figure 2.5 as a function of cation volume. The thermal expansion coefficient appears to be independent of composition, within error, among all five alkali carbonate liquids, with an average value of 22.5 (± 2.1) 10^{-5} K^{-1}, and among all three alkaline earth carbonate liquid components, with an average value of 16.4 (± 2.3) 10^{-5} K^{-1}.

Fig. 2.5 The thermal expansions of each carbonate liquid component at 1100 K plotted against cation volume. The dashed lines show average values for the alkali carbonates ($22.07 \cdot 10^{-5}$) and the alkaline earth carbonates ($16.40 \cdot 10^{-5}$).

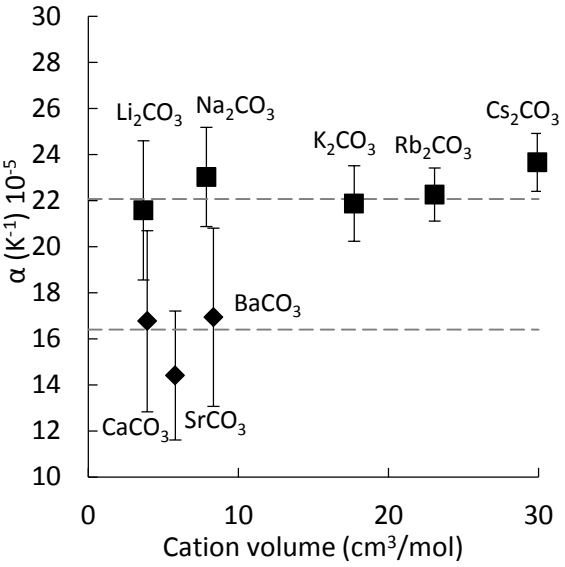

2.3.5 Comparison to results based on the maximum bubble pressure method

The liquid density results from this study are compared to those on Li_2CO_3-Na_2CO_3-K_2CO_3-Rb_2CO_3-Cs_2CO_3-$CaCO_3$-$SrCO_3$-$BaCO_3$ liquids from the literature based on the maximum bubble pressure technique (Kojima et al., 1999, 2003 and 2008), with a reported error of 0.9 %. Although the Kojima et al. density measurements were made on carbonate liquids in the same eight-component system, only two compositions from those three studies match those from this study, namely pure Rb_2CO_3 and Cs_2CO_3. A direct comparison of the density results is made in Figure 2.6; there is general agreement for Rb_2CO_3 liquid, but the density results for Cs_2CO_3 liquid from this study are ~1.8% higher than those measured by Kojima et al. (1999).

Fig. 2.6 The densities of Rb_2CO_3 (diamonds) and Cs_2CO_3 (squares) liquid measured in this study (solid points) compared with density results from Kojima et al., 1999 (empty points) shown as a function of temperature.

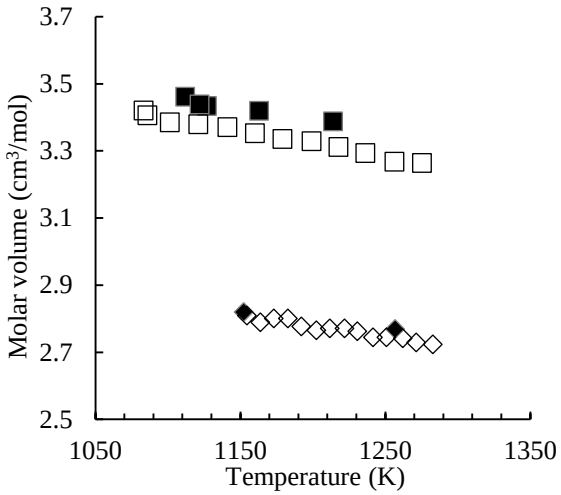

A global comparison of all the density results on the eight-component carbonate liquids from the maximum bubble pressure method, converted to molar volume, to those from the double-bob Archimedean method is made by comparing the results of a fit to the model equation in Eq. 2.4. In Table 2.6, the fitted values for the partial molar volume and thermal expansivity of each of the carbonate components, based on the density data from Kojima et al. (1999, 2003 and 2008), are shown. In a comparison of the results in Tables 2.5 and 2.6, the largest differences are seen for the alkaline earth carbonate components, where the errors on the fitted terms based on the maximum bubble pressure method (Table 2.6) are larger by a factor of two than those based on the double-bob method (Table 2.5). This is consistent with the larger error on density for the maximum bubble pressure method (~0.9%; Kojima et al., 1999, 2003, 2008) compared to that for the double-bob method (~0.3 %; Liu and Lange, 2003; this study). Therefore, although the two sets of density measurements obtained by different techniques are broadly consistent, they were not combined into a final data set. The recommended values to use in the molar volume equation (Eq. 2.3) are those in Table 2.4 and based solely on Pt double-bob Archimedean density measurements.

Table 2.6 The partial molar volumes and partial molar thermal expansivities resulting from a fit of the experimental volumes determined by Kojima et al. (1999, 2003 and 2008) to a linear mixing model.

$V = V_{i(1100\ K)} + \delta V_i/\delta T\ (T\text{-}1100\ K)$ cm^3/mol		
Component	$V_{i(1100\ K)}$ (cm^3/mol)	$\delta V_i/\delta T$ (10^{-3} $cm^3/mol\ K$)
Li_2CO_3	41.58 ± .11	8.41 ± 0.83
Na_2CO_3	53.25 ± .14	12.48 ± 1.14
K_2CO_3	72.01 ± .22	16.55 ± 1.53
Rb_2CO_3	81.47 ± .17	19.33 ± 1.22
Cs_2CO_3	95.69 ± .17	22.61 ± 1.17
$CaCO_3$	39.14 ± .40	7.35 ± 3.41
$SrCO_3$	43.12 ± .39	11.84 ± 3.84
$BaCO_3$	48.40 ± .40	9.09 ± 3.34

2.4 Discussion

2.4.1 A comparison of crystalline and liquid molar volumes with temperature

The newly calibrated volume equation (Eq. 2.4), with the fitted parameters in Table 2.5, can be used to calculate the molar volume of each liquid carbonate component with temperature and compare it to their crystalline molar volume with temperature, for phases where these data are available from X-ray and neutron diffraction studies. This allows for direct comparison of crystal and liquid volumes over a range of temperatures, and how changes in crystal structure and cation coordination affect molar volumes. In Table 2.7, crystalline volumes for each of the eight carbonates (and their polymorphs) at both 298 and 1100 K have been collected from the literature and compared to their respective liquid volumes at 1100 K. For Li_2CO_3 crystal, a volume equation from Liu and Lange (2003) (citing data from A. Kirfel and B. Barbier) has been used:

$$V(T)_{Li2CO3} = 35.2804 + 1.510 \times 10^{-3}T + 1.4402 \times 10^{-6}T^2\ cm^3/mol \qquad (2.5)$$

where T is the temperature in centigrade. Among the alkali carbonates, a comparison of crystalline volumes at 298 K to the liquid at 1100 K reveals a systematic decrease in the liquid to

volume ratio (V_{liq}/V_{xtl}) from Na_2CO_3 (1.28) to Cs_2CO_3 (1.22); the exception to this trend is Li_2CO_3 with a V_{liq}/V_{xtl} ratio of 1.17. Among the alkaline earth carbonates, the similar trend is observed for the orthorhombic $Pmcn$ phases, namely a systematic decline in V_{liq}/V_{xtl} from $CaCO_3$ (1.18) to $BaCO_3$ (1.12).

Table 2.7 Volumes of crystal phases for each carbonate component at both 298 and 1100 K are compared to the liquid volume predicted by our model. V_{liq}/V_{xtl} is the liquid to crystal volume ratio. Crystal space groups are adjacent to their volume.

	$V^{liq}_{1100\,K}$ (cm^3/mol)	$V^{xtl}_{298\,K}$ (cm^3/mol)	V_{liq}/V_{xtl} 298 K	$V^{xtl}_{1100\,K}$ (cm^3/mol)	V_{liq}/V_{xtl} 1100 K
Li_2CO_3	41.22	35.20 $C2/c$[a]	1.17	37.42 $C2/c$[b]	1.10
Na_2CO_3	53.27	41.78 $C2/m$[c]	1.28	48.24 $P6_3/mmc$[d,e]	1.10
K_2CO_3	71.59	56.58 $P2_1/c$[f]	1.27	65.0 $P6_3/mmc$[g,h,i]	1.10
Rb_2CO_3	80.78	65.04 $P2_1/c$[j]	1.24	73.7 $P6_3/mmc$[i]*	1.10
Cs_2CO_3	94.00	76.92 $P2_1/c$[j]	1.22	85.8 $P6_3/mmc$[i]*	1.10
$CaCO_3$	40.18	34.18 $Pmcn$[k]	1.18	36.1 $Pmcn$[k]	1.11
		36.90 $R\bar{3}c$[l]	1.09	37.75 $R\bar{3}m$[m,n]	1.06
$SrCO_3$	44.33	38.98 $Pmcn$[o]	1.14	41.04 $Pmcn$[o]	1.08
				42.75 $R3m$[p,q]	1.04
$BaCO_3$	50.99	45.73 $Pmcn$[o,r]	1.12	48.22 $Pmcn$[o,r]	1.06
				49.66 $R3m$[o,p]	1.03
				49.70 $Fm3m$[o]	1.03

[a]Effenberger and Zemann (1979); Liu and Lange (2003)[b], [c]Dusek et al. (2003); [d]Swaison et al. (1995); [e]Brouns and Visser (1964); [f]Gatehouse and Lloyd (1973); [g]Schneider and Levin (1973); [h]Becht and Struikmans (1976); [i]Dinnebier et al. (2005); [j]Ehrhardt et al. (1980); [k]Antao and Hassan (2010); [l]Markgraf and Reeder (1985), [m]Dove and Powell (1989); [n]Antao et al. (2009); [o]Nie et al. (2017); [p]Lander (1949); [q]Moreau (1964); [r]Antao et al. (2007)
**Value was extrapolated up to 1100 K from high-temperature data.*

At 1100 K, the crystalline alkali carbonates have all transitioned to a hexagonal structure (usually $P6_3/mmc$) and in all cases the V_{liq}/V_{xtl} ratio is ~1.10. For $CaCO_3$, $SrCO_3$ and $BaCO_3$, the $R3m$ or $R\bar{3}m$ phases are stable near 1100 K. $CaCO_3$ undergoes a phase transition from $R\bar{3}c$ to $R\bar{3}m$ at ~1240 K (e.g., Antao et al., 2009; Ishizawa et al., 2013) whereas $SrCO_3$ and $BaCO_3$ undergo a phase change to a hexagonal structure ($R3m$ or $R\bar{3}m$) at ~1173 and ~1073 K, respectively. The orthorhombic to hexagonal phase change is accompanied by a marked increase in volume (4.7%, 3.8% and 2.7% for $CaCO_3$, $SrCO_3$ and $BaCO_3$, respectively). The alkaline

earth carbonates range to lower V_{liq}/V_{xtl} ratios at 1100 K (≥ 1.04) than the 1.10 ratio for all the alkali carbonates. This suggests that the hexagonal alkaline earth carbonate structures (i.e. $R3m$ or $R\bar{3}m$) are more similar to the average liquid structure than are the hexagonal alkali carbonate structures (i.e. $P6_3/mmc$).

Using the General Lattice Utility Program (Gale and Rohl, 2003), pair distribution functions (Cope and Dove, 2007) were calculated in this study for a subset of the crystalline structures for Li_2CO_3, Na_2CO_3, K_2CO_3, $CaCO_3$ and $BaCO_3$. The objective was to obtain coordination numbers for carbonate-carbonate (C-C), metal cation-carbonate (M-C) and metal cation-oxygen (M-O) pairs. These coordination numbers are listed in Table 2.8 and compared with those calculated for the respective liquid carbonates (Tissen and Janssen, 1990; Vuilleumier et al., 2014).

Table 2.8 The coordination numbers of metal cations (i.e. Li, Na, K, Rb, Cs, Ca, Sr, Ba) with oxygen atoms (M-O), metal cations with carbonate groups (M-C) and carbonate groups with other carbonate groups (C-C) for low- and high-temperature crystal phases are compared to coordination numbers in their respective liquids.

	C-C	M-O	M-C
Li_2CO_3 $C2/c$[a]	2	4	4
Li_2CO_3 Liquid[b]	12.5	3.7	3.8
Na_2CO_3 $C2/m$[c]	1	4.5	4
Na_2CO_3 $P6_3/mmc$[d]	5.9	6	5.5
Na_2CO_3 Liquid[b]	12.6	5.2	4.2
K_2CO_3 $P2_1/c$[e]	2	4.5	5
K_2CO_3 Liquid[b]	12.0	6.0	4.4
$CaCO_3$ $Pmcn$[f]	2	9	6
$CaCO_3$ $R\bar{3}c$[g]	6	6	6
$CaCO_3$ $R\bar{3}m$[h]	12	-	6
$CaCO_3$ Liquid[i]	12	7.8	6
$SrCO_3$ $R\bar{3}m$[j]	12	-	6
$BaCO_3$ $R3m$[k]	12	9	6

$BaCO_3$ $Fm3m$[j]	12	-	6

[a]Effenberger and Zemann (1979); [b]Tissen and Janssen (1990);
[c]Arakcheeva et al. (2010); [d]Swaison et al. (1995);
[e]Idemoto et al. (1998); [f]Antao and Hassan (2010);
[g]Markgraf and Reeder (1985); [h]Ishizawa et al. (2013);
[i]Vuilleumier et al. (2014); [j]Strømme (1975);
[k]Antao and Hassan (2007);

The coordination of the metal cation with both oxygen and carbonate for all eight crystalline structures are similar to those for the corresponding liquids (Table 2.8). Instead, the primary structural difference between the crystals and the corresponding liquids is in the carbonate-carbonate (C-C) coordination number, which is 12-fold in all of the carbonate liquids (Tissen and Janssen (1990); Vuilleumier et al. 2014). The low-temperature monoclinic structures for the alkali carbonates and orthorhombic structures for the alkaline-earth carbonates all have C-C coordination numbers of 1 or 2. At high temperature the alkali carbonate structure (e.g., $P6_3/mmc$ for Na_2CO_3) has a C-C coordination number of ~6 while the alkaline-earth carbonate structure (e.g., $R\bar{3}m$) has a C-C coordination number of ~12, similar to that of the liquid. At even higher temperature (>1250 K), the structure for $BaCO_3$ becomes cubic (*Fm3m;* Strømme 1975; Nie et al. 2016)) and the C-C coordination of 12 is maintained. Thus with increasing temperature, the crystalline phases become increasingly "liquid-like", especially for the high-temperature alkaline earth carbonates where a C-C coordination of 12 is attained. The fact that all of the alkali and alkaline-earth carbonate liquids, irrespective of their M-O and M-C coordination numbers, have a shared and constant C-C coordination number of 12 may explain why the alkali and alkaline-earth liquid carbonate components all mix ideally with each other with respect to volume.

2.4.2 Systematic trends of carbonate liquid volume with cation coordination

The partial molar volumes (at 1100 K) of the liquid carbonate components are plotted as a function of cation field strength in Figure 2.7. Cation field strength is defined as $z/(0.126+r)^2$

, where *z* is the formal cation charge, *r* is the crystalline ionic radius of the cation (Shannon and Prewitt, 1969; Shannon, 1976) and the 0.126 term is the ionic radius of the oxygen anion. The ionic radius of the cation depends on its coordination number with oxygen; these coordination environments are different for alkali carbonate versus alkaline-earth carbonate liquids. In first principle molecular dynamics simulations of $CaCO_3$ melt (Vuilleumier et al. 2014), the cations are 7- to 8-fold coordinated by oxygen at ~0.5 GPa. Since coordination increases with pressure, an average coordination of 7-fold for Ca^{2+} and Sr^{2+} and 8-fold for Ba^{2+} (given its larger size) is used in this study to calculate their respective ionic radii. The liquid M-O and M-C coordination numbers in alkali carbonate liquids are distinct from those in alkaline-earth carbonate liquids. Molecular dynamics simulations of Li_2CO_3, Na_2CO_3 and K_2CO_3 point to an oxygen coordination of ~4, ~5 and ~6 for Li^+, Na^+ and K^+, respectively, and a cation-carbonate coordination ~4 for all three alkalis (e.g., Tissen and Janssen, 1990; Habasaki, 1990, Roest et al. 2017). The ~4-fold coordination of Li-O and Li-C has been corroborated by neutron diffraction and XRD studies on Li_2CO_3 liquid (Kohara et al. 1999). Based on these combined studies, for the calculation of cation volume, ionic radii corresponding to an oxygen coordination of 6-fold is used for Rb^+, Cs^+ and K^+, 5-fold for Na^+, and 4-fold for Li^+ (Table 2.9).

Table 2.9 The crystal radius, cation volume and crystal field strength of each carbonate liquid component.

Component	Cation-O Coordination	Crystal Radius (pm)	Cation Volume (cm^3/mol)	Cation Field Strength
Li_2CO_3	4[a]	73	1.96	25.3
Na_2CO_3	5[a]	115	7.58	17.2
K_2CO_3	6[a]	152	17.7	12.9
Rb_2CO_3	6	166	23.1	11.7
Cs_2CO_3	6	181	29.9	10.6
$MgCO_3$*	6	86	1.60	44.5
$CaCO_3$	7[b]	119	4.39	33.3
$SrCO_3$	7	137	6.36	28.9
$BaCO_3$	8	156	9.58	25.2
$FeCO_3$**	6	92	1.96	42.1

[a]Tissen and Janssen (1990) [b]Vuilleumier et al. (2014)

Plots of carbonate liquid volume as a function of field strength (Fig. 2.7) show two distinct trends, one for the alkali carbonate components (Li_2CO_3, Na_2CO_3, K_2CO_3, Rb_2CO_3 and Cs_2CO_3) and another for the alkaline earth carbonate components ($CaCO_3$, $SrCO_3$ and $BaCO_3$). The trend is curved for the alkali carbonate liquids, which cautions against a linear extrapolation of the alkaline earth carbonate trend to estimate the partial molar volume for the $MgCO_3$ and $FeCO_3$ components.

Fig. 2.7 The partial molar volume of each carbonate component from this study at 1100 K as a function of cation volume.

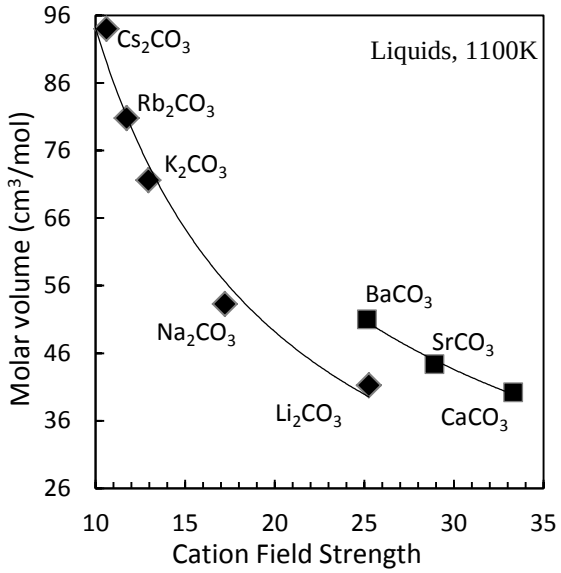

In a second plot (Fig. 2.8), the partial molar volumes of all carbonate components are plotted as a function of cation volume (cm^3/mol), which is defined as $AvN4\pi r^3/3$ where Av is Avogadro's number, N is the stoichiometric number of cations per formula unit (2 for alkalis and 1 for alkaline earths) and r is the crystalline ionic radius. The results lead to two sub-parallel linear trends, with the alkali carbonate liquids falling on one line, and the alkaline-earth carbonate liquids on the other line. A linear fit to each set of liquids (Fig. 2.8) leads to the following equations, both with R^2=0.999:

$$V_{carbonate\ (alkali)} = 1.86\ (\pm\ 0.03) \cdot V_{cation} + 38.3\ (\pm\ 0.6)\ cm^3/mol \quad (2.6a)$$

$$V_{carbonate\ (alkaline\ earth)} = 2.08\ (\pm\ 0.01) \cdot V_{cation} + 31.0\ (\pm\ 0.1)\ cm^3/mol \quad (2.6b)$$

Fig. 2.8 The partial molar volume of the alkali and alkaline earth carbonate liquids at 1100 K as a function of cation volume.

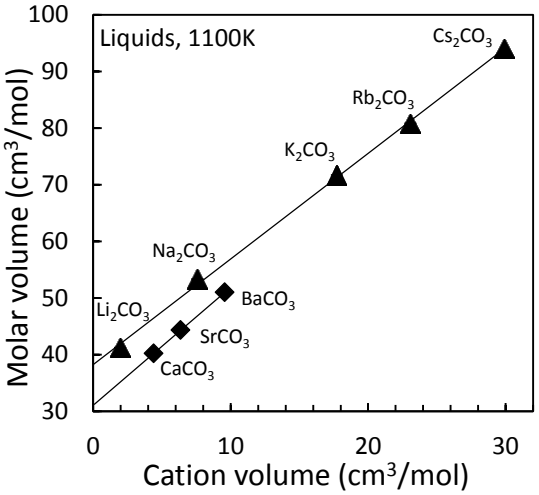

In both Equations 2.6a and 2.6b, $V_{carbonate}$ is the molar volume of the carbonate liquid and V_{cation} is the cation volume as defined above. Table 2.9 lists the calculated cation volumes and field strength for each component in addition to the assumed cation coordination numbers and ionic radii.

The slope intercepts of 38.3 (± 0.6) and 31.0 (± 0.1) cm^3/mol are fitted values (± 1σ) for the partial molar volume of the carbonate ion, $(CO_3)^{2-}$, at 1100 K. The large difference in the partial molar volume of the carbonate ion between the alkali and alkaline-earth carbonate liquids reflects the difference in its M-C (metal cation-carbonate ion) coordination number (four-fold vs. six-fold) (Table 2.9). Thus, the partial molar volume of the carbonate ion is related to the M-C coordination.

2.4.3 Estimates of the partial molar volume of the liquid $MgCO_3$ and $FeCO_3$ components

If it is assumed that both Mg^{2+} and Fe^{2+} are six-fold coordinated by oxygen (slightly lower than the 7-fold coordination inferred for Ca^{2+}, given their smaller size) and six-fold coordinated by carbonate (similar to the case for Ca^{2+}, Sr^{2+} and Ba^{2+}), their cation volumes can be calculated and input into Eq. 2.6b, resulting in partial molar volumes of 34.4 ± 0.1 and 35.1 ± 0.1 cm^3/mol (Fig. 2.9), respectively, for the liquid $MgCO_3$ and $FeCO_3$ components.

Fig. 2.9 The partial molar volumes of alkaline earth carbonate are shown as a function of cation volume from this study along with estimates for the molar volume of MgCO3 based off Dobson et al. (1996) and Kang et al. (2016) and FeCO3 based off Kang et al. (2016). The cation volumes shown assume an octahedral coordination of Mg2+ and Fe2+ cations.

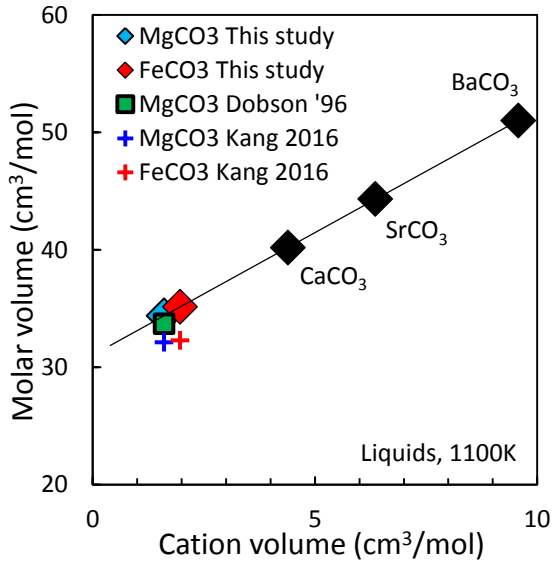

Note that if Mg^{2+} and/or Fe^{2+} are 4-fold (vs. 6-fold) coordinated by oxygen (similar to the case for Li^+ relative to K^+) this leads to smaller ionic radii, smaller cation volumes and smaller partial molar carbonate volumes. However, if Mg^{2+} and/or Fe^{2+} are 4-fold (vs. 6-fold) coordinated by carbonate, then the equation to use is Eq. 2.6a (not 2.6b), which leads to larger calculated partial molar volumes. It is also possible that the actual coordination of Mg^{2+} and Fe^{2+} is non-integer value intermediate between 4- and 6-fold. The key point is that there is a need for high-quality computational simulations of $MgCO_3$ and $FeCO_3$ liquids to constrain their M-O and M-C

coordination numbers, which will allow more accurate estimates of their respective liquid partial molar volumes from the linear trends in Figure 2.8.

2.4.4 Comparison to estimates of liquid V_{MgCO3} and V_{FeCO3} from the literature

Dobson et al. (1996) measured the density of $K_2Mg(CO_3)_2$ liquid density at 773 and 837 K, using the single double-bob Archimedean method, using a corundum bob (~0.5 g) with a Pd wire stem (0.1 mm). They used the same approach to measure the density of $K_2Ca(CO_3)_2$ liquid between 1115 and 1249 K, which was directly compared to Pt double-bob density measurements on the same liquid in Liu and Lange (2003). There is a difference of ~3% in the results, with the corundum single-bob method leading to lower density determinations than those from the Pt double-bob method (Liu and Lange, 2003). Error analysis shows that because of the small mass of the corundum bob (~0.5 g) relative to that for Pt bobs (≤ 26 g), the estimated uncertainty in density using the corundum bob is ~2.5% (Liu and Lange, 2003). With this caveat in mind, an estimate of the partial molar volume of $MgCO_3$ obtained from the two Dobson et al. (1996) density measurements on $K_2Mg(CO_3)_2$ liquid can be made by incorporating them one by one into a fit of Equation 2.4, combined with all the Pt double-bob density results from this study and Liu and Lange (2003). The results lead to V_{MgCO3} values of 31.87 and 32.31 cm^3/mole at 773 and 837 K, respectively. Use of the thermal expansion coefficient of 16.4 (± 2.3) 10^{-5} K^{-1} (i.e., that for the alkaline-earth carbonates; Fig. 2.5) leads to a molar volume of 33.7 cm^3/mol at 1100 K which overlaps within ± 2.5% uncertainty the estimated value for V_{MgCO3} on the basis of Equations 2.6b (assuming 6-fold M-O and M-C coordination).

The molar volumes and thermal expansion coefficients of liquid $MgCO_3$ and $FeCO_3$ have also been estimated by Kang et al. (2016) by fitting thermodynamic properties as to recover the fusion curve data for $MgCO_3$ and $FeCO_3$. Their fitted values for the molar volume of liquid

$MgCO_3$ and $FeCO_3$ (calculated at 1100 K) are 32.1 and 32.3 cm^3/mol, respectively, which are lower than those estimated from Eq.2.6b and may be indirect evidence that the Mg^{2+} and Fe^{2+} cations are in a lower than 6-fold M-O coordination in carbonate liquids. However, the thermal expansion coefficients for the $MgCO_3$ and $FeCO_3$ liquid components in Kang et al. (2016) are those of the crystalline magnesite and siderite phases, which are nearly three times smaller than the average (~16.4 10^{-5} K^{-1}) obtained in this study at 1100 K for the alkaline earth carbonate liquid components. The liquid phase is expected to have a higher thermal expansion coefficient than corresponding mineral phases, because of configurational contributions to thermal expansion that is related to the fact that liquids undergo continual breaking and re-forming of bonds, which permits access to different topologies and modes of expansion that are unavailable to solids (e.g., Lange, 1997). To resolve this issue, high-quality computational simulations of $MgCO_3$ and $FeCO_3$ liquids are needed to constrain their M-O and M-C coordination numbers.

2.5 Conclusions and future work

The results from this study show that multicomponent carbonate liquids mix ideally with respect to volume in the Li_2CO_3-Na_2CO_3-K_2CO_3-Rb_2CO_3-Cs_2CO_3-$CaCO_3$-$SrCO_3$-$BaCO_3$ system at 1 bar. Tight constraints on the partial molar volumes of the alkaline-earth carbonate components ($CaCO_3$, $SrCO_3$ and $BaCO_3$), which are not stable as pure liquids at one bar, are obtained by adding up to 50 mol% of each to the eutectic in the Li_2CO_3-Na_2CO_3-K_2CO_3 system, leading to multicomponent liquids that are stable at one bar over a wide range of temperature (758-1455 K). An area of future work is to extend this strategy to $MgCO_3$- and $FeCO_3$-bearing alkali carbonate liquids and to other thermodynamic property measurements, including 1-bar sound speeds to obtain melt compressibility (e.g., O'Leary et al., 2015) and 1-bar drop calorimetry to obtain the partial molar liquid enthalpies, heats of mixing, and partial molar liquid

heat capacities for multicomponent carbonate liquids that include the alkaline-earth carbonate components.

Another key conclusion is that the partial molar volume of the carbonate ion depends on its coordination with the various alkali- and alkaline-earth metals. In this study, molecular dynamic simulations from the literature were used to constrain the oxygen coordination around the alkali and alkaline-earth metals in carbonate liquids, which controls the size of the ionic radius and thus the cation volume for each metal. When the cation volumes are plotted against the liquid partial molar volume of each respective carbonate component, two distinct linear trends (R^2=0.999) result. The slope intercepts reflect two different partial molar volumes (and thermal expansion coefficients) for the carbonate ion, depending on its coordination with the respective alkali and alkaline-earth metals (i.e., the M-C coordination number). When the M-C is four-fold, both the partial molar volume (~38 cm^3/mol) and its thermal expansion coefficient (~22.1 10^{-5} K^{-1}) are larger than when the M-C is six-fold (~31 cm^3/mol and ~16.4 10^{-5} K^{-1}, respectively). Fortunately, these differences do not preclude linear (ideal) mixing with respect to volume as long as the model equation employs carbonate components (and not oxide components with the carbonate ion). The reason why the liquid partial molar volumes mix ideally at one bar is because all of the liquid carbonate components share the same carbonate-carbonate coordination number of 12, irrespective of their M-C and M-O coordination numbers.

The insights obtained in this study, when computational constraints on M-O and M-C coordination numbers are combined with macroscopic density measurements, show that accurate estimates of the partial molar volume and thermal expansion coefficient of the $MgCO_3$ and $FeCO_3$ components are possible if the M-C and M-O coordination numbers for Mg^{2+} and Fe^{2+} in carbonate melts can be obtained. This underscores the need for high-quality molecular dynamic

simulations on $MgCO_3$- and $FeCO_3$-bearing carbonate melts in order to constrain the volumetric properties of these two relatively abundant carbonate components in the Earth's mantle. Knowledge of the standard state thermodynamic properties of these two important carbonate liquid components will allow thermodynamic models, such as MELTS (Ghiorso et al. 2002), to model partial melting of carbonate-bearing peridotite.

2.6 References

Antao S. M. and Hassan I. (2007) BaCO3: high-temperature crystal structures and the Pmcn→R3m phase transition at 811°C. *Phys. Chem. Miner.* **34**, 573–580.

Antao M. and Hassan I. (2009) The orthorhombic structure of $CaCO_3$, $SrCO_3$, $PbCO_3$ and $BaCO_3$: linear structural trends. *Can. Mineral.* **47**, 1245–1255.

Antao S. M. and Hassan I. (2010) Temperature dependence of the structural parameters in the transformation of aragonite to calcite, as determined from in situ synchrotron powder x-ray-diffraction data. *Can. Mineral.* **48**, 1225–1236.

Arakcheeva A., Bindi L., Pattison P., Meisser N., Chapuis G. and Pekov I. (2010) The incommensurately modulated structures of natural natrite at 120 and 293 K from synchrotron X-ray data. *Am. Min.* ***95***, 574-581.

Becht H. Y. and Struikmans R. (1976) A monoclinic high-temperature modification of potassium carbonate. *Acta Cryst.* **B32**, 3344–3346.

Blundy J. and Dalton J. (2000) Experimental comparison of trace element partitioning between clinopyroxene and melt in carbonate and silicate systems, and implications for mantle metasomatism. *Contrib. to Mineral. Petrol.* **139**, 356–371.

Brouns E. and Visser J. W. (1964) An anomaly in the crystal structure of Na_2CO_3. *Acta Cryst.***17**, 614.

Cope E. R. and Dove M. T. (2007) Pair distribution functions calculated from interatomic potential models using the General Utility Lattice Program. *J. Appl. Cryst.***40**, 589–594.

Dalton J. A. and Wood B. J. (1993) The compositions of primary carbonate melts and their evolution through wallrock reaction in the mantle. *Earth Planet. Sci. Lett.* **119**, 511–525.

Dasgupta R. and Hirschmann M. M. (2006) Melting in the Earth's deep upper mantle caused by carbon dioxide. *Nature* **440**, 659–662.

Dasgupta R. and Hirschmann M. M. (2010) The deep carbon cycle and melting in Earth's interior. *Earth Planet. Sci. Lett.* **298**, 1–13.

Dasgupta R., Hirschmann M. M. and Stalker K. (2006) Immiscible transition from carbonate-rich to silicate-rich melts in the 3 GPa melting interval of eclogite + CO_2 and genesis of silica-undersaturated ocean island lavas. *J. Petrol.* **47**, 647–671.

Dinnebier R. E., Vensky S., Jansen M. and Hanson J. C. (2005) Crystal structures and topological aspects of the high-temperature phases and decomposition products of the alkali-metal oxalates $M_2[C_2O_4]$(M=K, Rb, Cs) *Chem. Eur. J.* **11**, 1119-1129.

Dobson D. P., Jones A. P., Rabe R., Sekine T., Kurita K., Taniguchi T., Kondo T., Kato T., Shimomura O. and Urakawa S. (1996) In-situ measurement of viscosity and density of carbonate melts at high pressure. *Earth Planet. Sci. Lett.* **143**, 207–215.

Dove M. T. and Powell B. M. (1989) Neutron diffraction study of the tricritical orientational order/disorder phase transition in calcite at 1260 K. *Phys. Chem. Minerals* **16**, 503-507.

Dusek M., Chapuis G., Meyer M. and Petricek V. (2003) Sodium carbonate revisited. *Acta Cryst.* **B59**, 337–352.

Effenberger H. and Zemann J. (1979) Verfeinerung der kristallstruktur des lithiumkarbonates, Li_2CO_3. *Z. Kristallogr. Cryst. Mater.* **150**, 133-138.

Ehrhardt V. H., Schweer H. and Seidel H. (1980) Hochdrucksynthesen einiger carbonate mit überkristiischem CO_2. *Z. Anorg. Allg. Chem.* **462**, 185-198.

Gale J. D. and Rohl A. L. (2003) The General Utility Lattice Program (GULP). *Mol. Simul.* **29**, 291–341.

Gatehouse B. M. and Lloyd D. J. (1973) Crystal structure of anhydrous potassium carbonate. *J. Chem. Soc., Dalton Trans.* **0**, 70-72

Ghiorso M. S., Hirschmann M. M., Reiners P. W. and Kress V. C. (2002) The pMELTS: A revision of MELTS for improved calculation of phase relations and major element partitioning related to partial melting of the mantle to 3 GPa. *Geochemistry Geophys. Geosystems* **3**, 36.

Guo X., Lange R. A. and Ai Y. (2013) The density and compressibility of CaO-FeO-SiO_2 liquids at one bar: Evidence for four-coordinated Fe2+ in the CaFeO2 component. *Geochim. Cosmochim. Acta* **120**, 206–219.

Habasaki J. (1990) Molecular dynamics simulation of molten Li_2CO_3 and Na_2CO_3. *Mol. Phys.* **69**, 115-128.

Idemoto Y., Richardson J. W., Koura N., Kohara S. and Loong C. K. (1998) Crystal structure of $(Li_xK_{1-x})_2CO_3$ (x = 0, 0.43, 0.5, 0.62, 1) by neutron powder diffraction analysis. *J. Chem. Phys. Solids* **59**, 363-376.

Ishizawa, N., Setoguchi, H., and Yanagisawa, K. (2013) Structural evolution of calcite at high temperatures : Phase V unveiled. *Sci. Rep.* **3,** 2832.

Kang N., Schmidt M. W., Poli S., Connolly J. A. D. and Franzolin E. (2016) Melting relations in the system $FeCO_3$-$MgCO_3$ and thermodynamic modelling of Fe-Mg carbonate melts. *Contrib. to Mineral. Petrol.* **171**, 1-16.

Kohara S., Suzuya K. and Ohno H. (1999) A reverse Monte Carlo study of molten lithium carbonate. *Plasmas & Ions* **2**, 79–83.

Kojima T., Yanagida M., Tanimoto K., Tamiya Y., Matsumoto H. and Miyazaki Y. (1999) The surface tension and the density of molten binary alkali carbonate systems. *Electrochemistry* **67**, 593-602.

Kojima T., Miyazaki Y., Nomura K. and Tanimoto K. (2003) Density, molar volume, and surface tension of molten Li_2CO_3-Na_2CO_3 and Li_2CO_3-K_2CO_3 containing alkaline earth (Ca, Sr, and Ba) carbonates. *J. Electrochem. Soc.* **150**, E535-E542.

Kojima T., Miyazaki Y., Nomura K. and Tanimoto K. (2008) Density, surface tension, and electrical conductivity of ternary molten carbonate system Li_2CO_3-Na_2CO_3-K_2CO_3 and methods for their estimation. *J. Electrochem. Soc.* **155**, F150.

Lander J. J. (1949) Polymorphism and Anion Rotational Disorder in the Alkaline Earth Carbonates. *J. Chem. Phys.* **17**, 892-901.

Lange R. A. (1997) A revised model for the density and thermal expansivity of K_2O-Na_2O-CaO-MgO-Al_2O_3-SiO_2 liquids from 700 to 1900 K: extension to crustal magmatic temperatures. *Contrib. to Mineral. Petrol.* **130**, 1–11.

Lange R. A. and Carmichael I. S. E. (1987) Densities of Na_2O-K_2O-CaO-MgO-FeO-Fe_2O_3-Al_2O_3-TiO_2-SiO_2 liquids: New measurements and derived partial molar properties. *Geochim. Cosmochim. Acta* **51**, 2931–2946.

Liu Q. and Lange R. A. (2001) The partial molar volume and thermal expansivity of TiO_2 in alkali silicate melts: Systematic variation with Ti coordination. *Geochim. Cosmochim. Acta* **65**, 2379–2393.

Liu Q. and Lange R. A. (2003) New density measurements on carbonate liquids and the partial molar volume of the $CaCO_3$ component. *Contrib. to Mineral. Petrol.* **146**, 370–381.

Liu Q. and Lange R. A. (2006) The partial molar volume of Fe_2O_3 in alkali silicate melts: Evidence for an average Fe^{3+} coordination number near five. *Am. Mineral* **91**, 385–393.

Markgraf S. and Reeder R. (1985) High-temperature structure refinements of calcite and magnesite. *Am. Miner.* **70**, 590–600.

Moreau R. (1964) Etude diffractometrique du carbonate de strontium et du carbonate de baryum entre 20 et 1000°C. *Bull. Soc. Franc. Miner. Crist.* **87**, 547-552.

Nie S., Liu Y., Liu Q., Wang M. and Wang H. (2017) Phase transitions and thermal expansion of $BaCO_3$ and $SrCO_3$ up to 1413K. *Eur. J. Mineral.* **29,** 1–11.

O'Leary M. C., Lange R. A. and Ai Y. (2015) The compressibility of $CaCO_3$-Li_2CO_3-Na_2CO_3-K_2CO_3 liquids: Application to natrocarbonatite and CO_2-bearing nephelinite liquids from Oldoinyo Lengai. *Contrib. to Mineral. Petrol.* **170**, 1-18.

Roest, D.L., Ballone, P., Bedeaux, D., and Kjelstrup, S. (2017) Molecular Dynamics Simulations of Metal / Molten Alkali Carbonate Interfaces. *J. Phys. Chem. C* **121**, 17827-17847.

Schneider S. J. and Levin E. M. (1973) Polymorphism of K_2CO_3. *J. Am. Ceram. Soc*.**56**, 218-219.

Shannon R. D. (1976) Revised effective ionic radii and systematic studies of interatomic distances in halides and chalcogenides. *Acta Cryst.* **A32**, 751-767.

Shannon R. D. and Prewitt C. T. (1969) Effective ionic radii in oxides and fluorides. *Acta Cryst.* **B25**, 925-946.

Stein D. J., Stebbins J. F. and Carmichael I. S. E. (2001) Density of molten sodium aluminosilicates. *J. Am. Ceram. Soc.* **69**, 396–399.

Strømme K. O. (1975) On the crystal structures of the high-temperature forms of strontium and barium carbonate and structurally related compounds. *Acta Chem. Scand.* **29,** 105-110.

Swaison I. P., Dove M. T. and Harris M. J. (1995) Neutron powder diffraction study of the ferroelastic phase transition and lattice melting in sodium carbonate, Na_2CO_3. *J. Phys.: Condens. Matter* **7**, 4395-4417.

Tissen J. T. W. M. and Janssen G. J. M. (1990) Molecular-dynamics simulation of molten alkali carbonates. *Mol. Phys.* **71**, 413-426.

Vuilleumier R., Seitsonen A., Sator N. and Guillot B. (2014) Structure, equation of state and transport properties of molten calcium carbonate (CaCO3) by atomistic simulations. *Geochim. Cosmochim. Acta* **141**, 547–566.

Chapter 3 The compressibility of Li_2CO_3- Na_2CO_3- K_2CO_3- Rb_2CO_3-Cs_2CO_3- $CaCO_3$-$SrCO_3$-$BaCO_3$ liquids: new sound speed measurements, ideal mixing and, systematic trends with composition

3.1 Introduction

Carbonate plays an important role in determining the conditions of partial melting in the mantle. The presence of carbonate in the mantle dramatically lowers and alters the shape of the solidus for peridotite (e.g. Falloon and Green 1989; Dasgupta and Hirschmann 2007; Ghoush et al. 2009) and eclogite-bearing assemblages (e.g. Hammouda 2003; Litasov and Ohtani 2010; Kiseeva et al. 2013), both of which lead to the formation of silica-undersaturated ocean island basalts (Dasgupta et al. 2006). In the presence of carbonate, there may be widespread incipient melting within the upper mantle as deep as 330 km (Dasgupta and Hirschmann 2006). These initial melts will be carbonate-rich and effective metasomatic agents (e.g. Wallace Green and 1988) capable of significantly altering the trace-element composition of the mantle (e.g. Dupuy et al. 1992; Ionov et al. 1993).

Owing to the importance of understanding how carbonate influences melting of the mantle, a wide range of phase-equilibrium experiments have been performed in the literature over a wide range of compositions, temperatures and pressures representative of the carbonated upper mantle (e.g. Dasgupta and Hirschmann 2006; Dasgupta et al. 2004). However, small variations in starting compositions can lead to significant differences in the location of the solidus (e.g. Dasgupta and Hirschmann 2010). High temperature and pressure thermodynamic models (e.g., pMELTS; Ghiorso et al. 2002) have the potential to explore how complex variations in

temperature, pressure and mantle composition can affect partial melting. However, before thermodynamic models like MELTS can incorporate carbonate, they first require standard state thermodynamic data for the relevant carbonate liquid components.

In the mantle, the most abundant carbonate components are $MgCO_3$, $CaCO_3$ and $FeCO_3$ (e.g., Biellman et al., 1993; Dalton and Wood 1993; Dalton and Presnall 1998; Hammouda 2003; Ghosh et al. 2009). Despite their petrologic significance, very little is known about their liquid thermodynamic properties because these three carbonate phases decompose at 1-bar at temperatures well below their melting points. In contrast, the pure alkali carbonates all form stable liquids at 1 bar. Moreover, the eutectic ternary composition $(Li_{.43}, Na_{.31}, K_{.25})_2CO_3$ is stable at temperatures as low as 670 K (Janz et al., 1962, 1979). The low temperature of this ternary composition allows various amounts of alkaline-earth carbonate components to be mixed into it to form stable liquids at 1-bar. For example, Liu and Lange (2003) and O'Leary et al. (2015) applied this approach to measure the density and sound speed (compressibility) of several $CaCO_3$-bearing alkali carbonate liquids at 1 bar. In both studies, they found that the partial molar volume and compressibility of all four carbonate components in the Li_2CO_3-Na_2CO_3-K_2CO_3-$CaCO_3$ system mix ideally.

Following this success, Hurt and Lange (2018) extended the density study of Liu and Lange (2008) to a larger compositional range of liquids in the Li_2CO_3-Na_2CO_3-K_2CO_3-Rb_2CO_3-Cs_2CO_3-$CaCO_3$-$SrCO_3$-$BaCO_3$ system. They also found that the liquid molar volumes (and thermal expansivity) of all eight carbonate components mix ideally. Unfortunately, this strategy of adding alkaline-earth components ($CaCO_3$, $SrCO_3$, $BaCO_3$) to the ternary alkali carbonate melt cannot be extended to $MgCO_3$ or $FeCO_3$-bearing liquids at 1-bar because their decarbonation temperatures are prohibitively low (773 and 743 K respectively, Hurst 1991;

Wang et al 2011). While direct density and sound speed measurements on $MgCO_3$- and $FeCO_3$-bearing liquids at 1-bar are not possible, estimates of their partial molar properties are feasible if clear systematic trends occur as a function of composition in the Li_2CO_3-Na_2CO_3-K_2CO_3-Rb_2CO_3-Cs_2CO_3-$CaCO_3$-$SrCO_3$-$BaCO_3$ system. To this end, Hurt and Lange (2018) showed that the partial molar volume and thermal expansion of the $MgCO_3$ and $FeCO_3$ liquid components could be estimated based on such systematics.

In this study, a similar effort is undertaken with respect to melt compressibility through a study of sound speeds on 13 liquids in the Li_2CO_3-Na_2CO_3-K_2CO_3-Rb_2CO_3-Cs_2CO_3-$SrCO_3$-$BaCO_3$ system, which can be combined to similar measurements made on $CaCO_3$-bearing alkali carbonate liquids (O'Leary et al., 2015). Our objective is to expand the sound speed data set for liquid alkali carbonates to include Rb_2CO_3 and Cs_2CO_3 in order to better constrain systematics across all five alkali (Li, Na, K, Rb, Cs) carbonate liquid components. In addition, sound speed measurements are made on carbonate liquids with ≤ 50 mol% $SrCO_3$ and $BaCO_3$, which can be combined with those of O'Leary et al. (2015) on liquids with ≤ 50 mol% $CaCO_3$, to explore the systematics of liquid compressibility as a function of alkaline-earth carbonate composition. The goal is to use these data and any observed systematic behavior to predict the compressibility of the $MgCO_3$ and $FeCO_3$ liquid components, which in turn can be compared to predictions based on molecular dynamic simulations, as well as direct density measurements at pressure (e.g., sink/float experiments).

3.2 Methods

3.2.1 Sample materials

Seven compositions in the Li_2CO_3- Na_2CO_3- K_2CO_3-$SrCO_3$ quaternary, three in the Li_2CO_3- Na_2CO_3- K_2CO_3-$BaCO_3$ quaternary, and one in the Li_2CO_3-Na_2CO_3-K_2CO_3-Cs_2CO_3

quaternary were synthesized for sound speed measurements. In addition to these 11 liquids, pure Rb_2CO_3 and Cs_2CO_3 were added for a total of 13 liquids in Table 3.1. Samples were synthesized from carbonate reagents with > 99.5% purity. The LOI of each reagent was determined by taking at least 2 aliquots of each reagent, measuring its weight with a mass balance of >0.0001 g precision and drying each aliquot in a 200 °C furnace overnight. The mass of the dried aliquot was re-measured to determine its LOI. The resulting LOI of each reagent was used to calculate the appropriate amounts of each reagent necessary to produce 200 g batches of samples with the desired molar composition. Reagents were weighed out and directly placed into a blender jar and mixed at high speed for several minutes to create a chemically and texturally homogeneous sample. These mixed powders were directly fused into the platinum crucible used for the sound speed measurements, described below.

Table 3.1 The molar compositions of the 13 samples used in this study along with their gram formula weights (g.f.w.).

Sample	Li_2CO_3	Na_2CO_3	K_2CO_3	Rb_2CO_3	Cs_2CO_3	$CaCO_3$	$SrCO_3$	$BaCO_3$	g.f.w
Rb_2CO_3				1					230.945
T-50%Cs	0.218	0.158	0.125		0.5				212.950
Cs_2CO_3					1				325.820
T-10%Sr	0.392	0.284	0.225				0.1		104.836
T-15%Sr	0.370	0.268	0.213				0.15		107.213
T-20%Sr	0.348	0.252	0.200				0.2		109.590
T-25%Sr	0.326	0.236	0.188				0.25		111.978
T-30%Sr	0.305	0.221	0.175				0.3		114.345
T-35%Sr	0.283	0.205	0.163				0.35		116.723
T-50%Sr	0.217	0.162	0.124				0.497	0.001	123.788
T-15%Ba	0.370	.268	0.213					0.15	114.670
T-35%Ba	0.283	0.205	0.163					0.35	134.121
T-50%Ba	0.218	0.158	0.125					0.5	148.710

3.2.2 Sound speed measurements

Sound speed was measured at one bar and high temperature with an ultrasonic frequency-sweep interferometer, which is described in Ai and Lange (2004a,b). Its adaptation for use on carbonate liquids is presented in O'Leary et al. (2015). A brief overview of the technique is

described here. An arbitrary wave generator creates a broadband electronic pulse, which is composed of frequencies spanning ~1-2 MHz. The electronic pulse is converted to an acoustic pulse by a transducer which is mounted on one end of a long (40 cm) alumina ceramic upper rod. The other end of the rod extends into the sample liquid which is held at temperature within a Deltech vertical tube furnace. The sample (~5 g) is contained within a platinum crucible which also serves as the lower rod. Part of the acoustic signal reflects off the end of the rod at the rod-liquid interface, another part is transmitted into the sample liquid and reflects off the bottom of the crucible. Both return reflections are received by the transducer and converted back into an electronic signal. The maxima and minima of the returned signals are evaluated as a periodic function of frequency. The resulting period is related to liquid sound speed by $\Delta f = c/2S$, where Δf is the period of the maxima and minima of the returned signal, c is the sound speed and S is the depth of the liquid which is the distance between the bottom of the alumina rod and the bottom of the platinum crucible.

In this study, the broadband frequency was centered on either 4.5 or 5.5 MHz. Most measurements were made with both frequencies in order to further test for frequency dependence of the sound speed. While frequency dependence may be a concern for silicate melts, the low viscosities of carbonate liquids (e.g., 10^{-2}-10^{-3} Pa-s; Dobson et al. 1996; Kono et al. 2014) indicate that all sound speeds obtained on the samples in this study were relaxed.

3.3 Results

3.3.1 NaCl liquid sound speeds

The accuracy of the ultrasonic frequency-sweep interferometer was tested on pure NaCl liquid before and after measurements were made on the experimental liquids (Table 3.1). The resulting sound speeds for NaCl liquid are plotted in Figure 3.1 and compared to results obtained

from the same ultrasonic frequency-sweep interferometer apparatus (Ai and Lange 2004b) as well as results from the varying-path-length (VPL) method of ultrasonic interferometry (Kress et al. 1988). The NaCl liquid sound speeds measured in this study are within 1% of those measured by the other two studies. Furthermore, our sound speed results on Rb_2CO_3 and Cs_2CO_3 liquid compare well with those of Zhu et al. (1991), which were based on the pulse transmission method (Fig. 3.2).

Figure 3.1 Sound speed results for NaCl liquid from this study agree with those from previous studies using different techniques. The sound speed of liquid NaCl from this study is shown with black circles and compares well to Ai and Lange (2004b) (diamonds) who used the same ultrasonic frequency sweep interferometer and Kress et al. (1988) (empty circles) who used the varying path lengths (VPL) method.

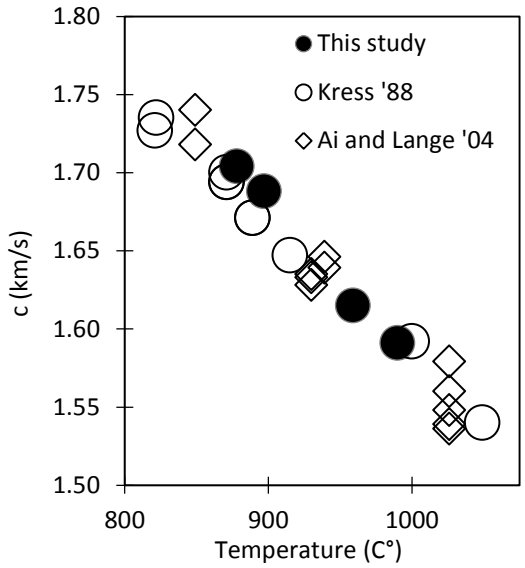

Figure 3.2 The sound speed results on Rb_2CO_3 and Cs_2CO_3 liquid agree (within error) to results from other labs using other techniques. Zhu et al. (1991) used the transmission pulse method to determine the sound speed in pure Rb_2CO_3 (empty diamonds) and Cs_2CO_3 (empty circles). Their results are in agreement, within error, to results from this study. Error bars show 1σ measurement uncertainty.

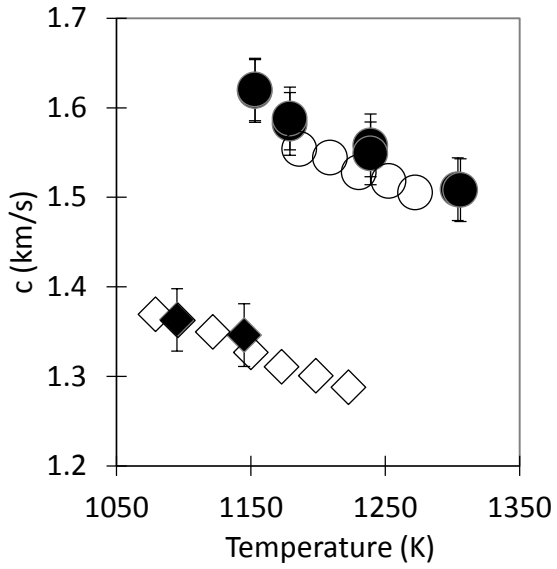

3.3.2 Carbonate liquid sound speed results

Eighty sounds speed measurements were performed on 13 samples in the Li_2CO_3-Na_2CO_3-K_2CO_3-Rb_2CO_3-Cs_2CO_3-$SrCO_3$-$BaCO_3$ system over a temperature range from 739 to 1367 K. The sound speed results for each liquid composition are plotted as a function of temperature in Figure 3.3.

Figure 3.3 The sound speed results from this study shown as a function of temperature for each composition. Sound speeds decrease linearlly with temperature. Alkaline-earth-bearing liquids have significantly (~40%) greater sound speeds than alkalis, implying a smaller compressibility.

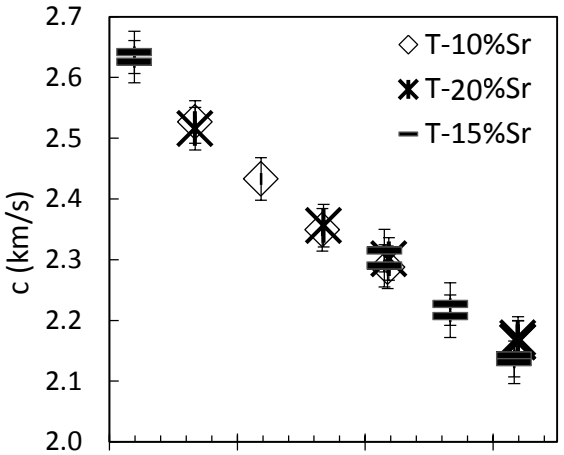
T-10%Sr
T-20%Sr
T-15%Sr
c (km/s)
2.7
2.6
2.5
2.4
2.3
2.2
2.1
2.0

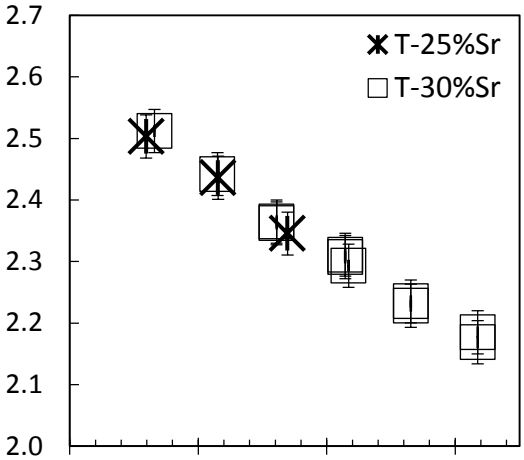
T-25%Sr
T-30%Sr
2.7
2.6
2.5
2.4
2.3
2.2
2.1
2.0

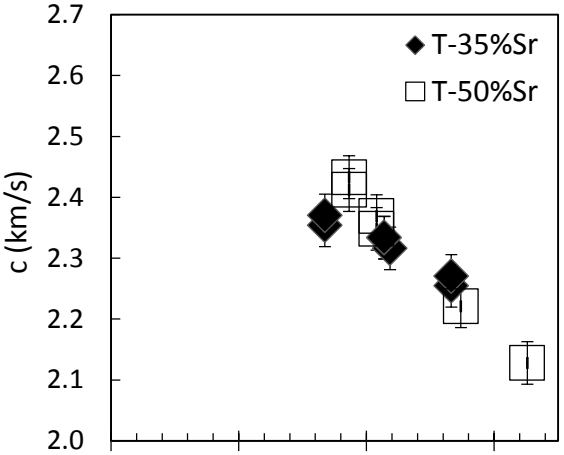
T-35%Sr
T-50%Sr
c (km/s)
2.7
2.6
2.5
2.4
2.3
2.2
2.1
2.0

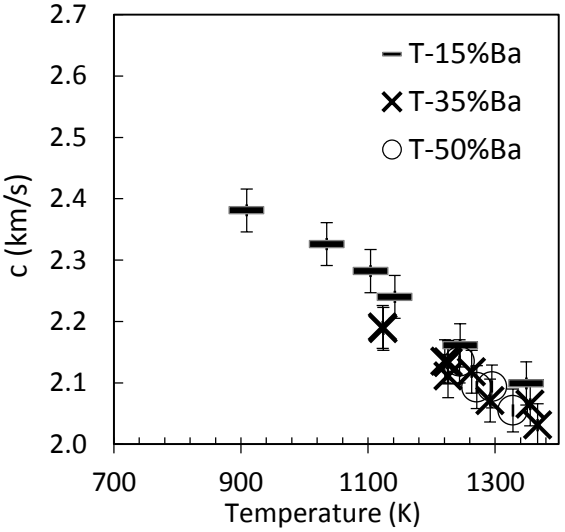
T-15%Ba
T-35%Ba
T-50%Ba
c (km/s)
2.7
2.6
2.5
2.4
2.3
2.2
2.1
2.0
700
900
1100
1300
Temperature (K)

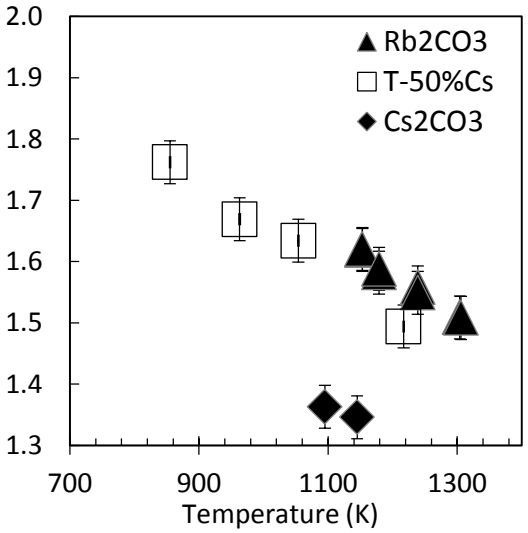
Rb2CO3
T-50%Cs
Cs2CO3
2.0
1.9
1.8
1.7
1.6
1.5
1.4
1.3
700
900
1100
1300
Temperature (K)

The sound speed of each sample liquid at each temperature of measurement was combined with calculations of its liquid density from the results of Hurt and Lange (2018) to calculate the adiabatic compressibility (β_s) from the relation:

$$\beta_s = \frac{1}{\rho c^2} \qquad \text{Eq. 3.1}$$

where ρ is the liquid density and c is the liquid sound speed. Isothermal compressibility (β_T) may be calculated from β_s by the following equation:

$$\beta_T = \beta_S + \frac{TV_T\alpha^2}{C_P} \qquad \text{Eq. 3.2}$$

where T is temperature, V_T is molar volume, α is 1-bar thermal expansion coefficient and C_P is the isobaric heat capacity. V_T and α are both calculated from the carbonate liquid density model of Hurt and Lange (2018). The heat capacity (C_P) for Li_2CO_3, Na_2CO_3 and K_2CO_3 liquids are derived from calorimetric data reported in Janz et al. (1963) and Rolin and Recapet (1964). The C_P for Rb_2CO_3 and Cs_2CO_3 liquids are estimated by extrapolating the trend observed in Li_2CO_3, Na_2CO_3 and K_2CO_3 between their C_P and cation volume (Fig. A.1 in Appendix A). For the alkaline earth carbonate liquids, estimates of their heat capacity are based on the molecular dynamics simulations of Hurt and Wolf (2018a). The $TV_T\alpha^2/C_P$ term constitutes, on average, 13.5% of β_T with a maximum and minimum of 15.5% and 11.1% respectively.

The molar $(\delta V/\delta P)_T$ has also been calculated for each experiment by the relation

$$\frac{\delta V}{\delta P}_T = -V_T\beta_T \qquad \text{Eq. 3.3}$$

The experimental results along with calculations of ρ, β_S, β_T and $\frac{\delta V}{\delta P}_T$ are listed in Table 3.2.

Table 3.2 The measured 1 bar sound speed of each composition is shown with its corresponding temperature. Also shown is the calculated adiabatic compressilbity (βS) isothermal compressibility (βT),

and $\frac{\delta V}{\delta P_T}$. The reported density (ρ) of the sample was calculated from the molar volume model reported in Hurt and Lange (2018).

Sample	T (K)	c (m/s)	ρ (g/cm^3)	β_S (10^{-2} GPa^{-1})	β_T (10^{-2} GPa^{-1})	$\delta V/\delta P$ (10^{-4} bar^{-1} mol^{-1})
Rb_2CO_3	1153	1619	2.826(4)	13.507(360)	15.490(396)	-12.661
Rb_2CO_3	1153	1620	2.826(4)	13.479(360)	15.462(396)	-12.638
Rb_2CO_3	1179	1582	2.809(4)	14.222(388)	16.238(424)	-13.348
Rb_2CO_3	1179	1588	2.809(4)	14.115(388)	16.131(424)	-13.260
Rb_2CO_3	1239	1558	2.773(5)	14.856(413)	16.947(470)	-14.114
Rb_2CO_3	1239	1549	2.773(5)	15.029(413)	17.120(470)	-14.258
Rb_2CO_3	1304	1509	2.735(6)	16.059(450)	18.229(509)	-15.395
Rb_2CO_3	1306	1508	2.734(6)	16.087(452)	18.260(509)	-15.427
T-50%Cs	855	1762	3.080(6)	10.459(247)	12.068(258)	-8.345
T-50%Cs	963	1669	3.000(4)	11.966(300)	13.731(302)	-9.747
T-50%Cs	1054	1634	2.936(2)	12.756(337)	14.647(373)	-10.623
T-50%Cs	1217	1494	2.828(2)	15.840(433)	17.943(432)	-13.509
Cs_2CO_3	1095	1363	3.470(3)	15.511(483)	17.739(533)	-16.655
Cs_2CO_3	1145	1346	3.430(3)	16.094(525)	18.396(602)	-17.477
T-10%Sr	937	2433	2.098(1)	8.052(141)	9.337(154)	-4.666
T-10%Sr	1033	2349	2.054(2)	8.823(153)	10.210(166)	-5.211
T-10%Sr	1135	2288	2.009(3)	9.510(179)	11.001(183)	-5.739
T-15%Sr	739	2641	2.259(4)	6.344(102)	7.367(109)	-3.495
T-15%Sr	739	2626	2.259(4)	6.418(102)	7.441(109)	-3.531
T-15%Sr	1130	2315	2.074(2)	8.997(173)	10.432(186)	-5.393
T-15%Sr	1130	2290	2.074(2)	9.195(173)	10.631(186)	-5.495
T-15%Sr	1233	2227	2.030(2)	9.932(188)	11.465(203)	-6.055
T-15%Sr	1233	2207	2.030(2)	10.113(188)	11.646(203)	-6.150
T-15%Sr	1333	2131	1.989(2)	11.070(209)	12.694(226)	-6.841
T-15%Sr	1333	2142	1.989(2)	10.956(209)	12.581(226)	-6.780
T-20%Sr	834	2516	2.277(4)	6.940(113)	8.030(129)	-3.865
T-20%Sr	1035	2356	2.180(2)	8.263(148)	9.558(159)	-4.804
T-20%Sr	1137	2301	2.134(2)	8.849(173)	10.241(179)	-5.258
T-20%Sr	1339	2164	2.049(2)	10.420(206)	11.994(222)	-6.415
T-20%Sr	1339	2171	2.049(2)	10.354(206)	11.929(222)	-6.380
T-20%Sr	1339	2165	2.049(2)	10.416(206)	11.990(222)	-6.413
T-25%Sr	819	2503	2.350(5)	6.791(103)	7.825(119)	-3.728
T-25%Sr	931	2436	2.295(3)	7.344(131)	8.491(136)	-4.143
T-25%Sr	1039	2345	2.243(2)	8.103(147)	9.355(159)	-4.669
T-30%Sr	832	2512	2.411(6)	6.573(105)	7.581(116)	-3.595
T-30%Sr	930	2442	2.362(4)	7.100(122)	8.203(137)	-3.972
T-30%Sr	1022	2362	2.318(3)	7.734(139)	8.924(154)	-4.403
T-30%Sr	1022	2365	2.318(3)	7.715(139)	8.904(154)	-4.393
T-30%Sr	1129	2311	2.268(2)	8.256(154)	9.542(170)	-4.811
T-30%Sr	1129	2307	2.268(2)	8.284(154)	9.571(170)	-4.825

T-30%Sr	1134	2293	2.266(2)	8.394(153)	9.685(175)	-4.888
T-30%Sr	1231	2228	2.223(2)	9.063(168)	10.438(194)	-5.369
T-30%Sr	1231	2235	2.223(2)	9.005(168)	10.379(194)	-5.339
T-30%Sr	1335	2169	2.178(2)	9.758(189)	11.218(216)	-5.889
T-30%Sr	1335	2185	2.178(2)	9.615(189)	11.076(216)	-5.814
T-35%Sr	1035	2354	2.379(4)	7.588(134)	8.744(153)	-4.291
T-35%Sr	1035	2370	2.379(4)	7.484(134)	8.639(153)	-4.240
T-35%Sr	1128	2333	2.335(3)	7.866(148)	9.102(170)	-4.550
T-35%Sr	1128	2334	2.335(3)	7.861(148)	9.098(170)	-4.547
T-35%Sr	1137	2316	2.331(3)	7.998(153)	9.242(172)	-4.628
T-35%Sr	1233	2255	2.288(2)	8.597(164)	9.921(194)	-5.061
T-35%Sr	1233	2271	2.288(2)	8.477(164)	9.802(194)	-5.000
T-50%Sr	1073	2412	2.568(5)	6.693(128)	7.742(163)	-3.733
T-50%Sr	1073	2433	2.568(5)	6.578(128)	7.627(163)	-3.678
T-50%Sr	1116	2369	2.548(5)	6.994(131)	8.076(170)	-3.926
T-50%Sr	1116	2348	2.548(5)	7.119(131)	8.202(170)	-3.987
T-50%Sr	1248	2221	2.487(4)	8.152(148)	9.333(200)	-4.648
T-50%Sr	1352	2128	2.441(4)	9.047(169)	10.303(216)	-5.228
T-15%Ba	1035	2326	2.221(2)	8.324(128)	9.733(177)	-5.026
T-15%Ba	1104	2282	2.188(2)	8.777(169)	10.258(189)	-5.376
T-15%Ba	1142	2240	2.170(2)	9.183(172)	10.702(192)	-5.655
T-15%Ba	1245	2161	2.124(2)	10.082(198)	11.703(216)	-6.318
T-15%Ba	1349	2099	2.079(3)	10.917(223)	12.636(243)	-6.969
T-35%Ba	1123	2191	2.565(3)	8.121(155)	9.517(209)	-4.976
T-35%Ba	1124	2188	2.565(2)	8.145(162)	9.542(218)	-4.990
T-35%Ba	1221	2135	2.515(3)	8.722(176)	10.210(230)	-5.445
T-35%Ba	1226	2111	2.513(3)	8.931(176)	10.423(247)	-5.564
T-35%Ba	1226	2134	2.513(3)	8.739(176)	10.232(247)	-5.462
T-35%Ba	1226	2133	2.513(3)	8.748(176)	10.240(247)	-5.466
T-35%Ba	1263	2118	2.494(4)	8.937(180)	10.463(248)	-5.626
T-35%Ba	1292	2071	2.480(5)	9.401(179)	10.953(275)	-5.923
T-35%Ba	1355	2065	2.450(6)	9.572(201)	11.180(280)	-6.121
T-35%Ba	1367	2031	2.444(6)	9.918(207)	11.537(282)	-6.331
T-50%Ba	1244	2135	2.792(6)	7.857(163)	9.284(293)	-4.945
T-50%Ba	1271	2093	2.778(7)	8.218(171)	9.668(296)	-5.176
T-50%Ba	1295	2094	2.765(7)	8.248(172)	9.718(315)	-5.226
T-50%Ba	1328	2055	2.748(9)	8.617(181)	10.115(317)	-5.474
T-50%Ba	1438	1993	2.693(12)	9.350(204)	10.940(354)	-6.042

3.3.3 Calculation of experimental uncertainty and error analysis

In order to accurately estimate the uncertainty on the calculated values of β_T for each liquid sample in Table 3.2, the uncertainties in all the liquid properties (sound speed, density,

thermal expansion coefficient, heat capacity) used to calculate this parameter must be propagated. In this study, we employed a bootstrap approach that does not discount correlation of errors into the estimation of total error. The first step was to perform a bootstrap approach to the estimation of error in the calculated density and thermal expansion of each sample liquid in Table 3.2, based on the Hurt and Lange (2018) model equation for carbonate liquids. The residuals from the fit of the carbonate liquid density data set of Hurt and Lange (2018) to a linear mixing model were randomly assigned to their best-fit predicted molar volumes to create 1000 synthetic data sets of molar volumes. A multiple linear regression was performed on each synthetic data set to create 1000 different carbonate liquid volume models. The resulting partial molar volumes and thermal expansivity coefficients were combined in Eq. 3.2 with sound speed measurements from this study and O'Leary et al. (2015) to calculate 1000 synthetic data sets of β_T from each separate carbonate liquid volume model. To account for uncertainty on heat capacity (C_P) values, each of the 1000 synthetic β_T datasets were assigned a C_P value that was randomly drawn from a normal distribution around the mean with an assumed 1σ of 10 KJ/mol. Note that, on average, uncertainty on C_P accounts for only ~4% of total uncertainty. For each of the 1000 synthetic β_T datasets (for all of the data in Table 3.2, together with the data from O'Leary et al., 2015), a standard deviation for β_T for each sample liquid was calculated and is reported in Table 3.2. A similar exercise was applied to the estimated standard deviation for β_S and $(\delta V/\delta P)_T$.

3.3.4 Ideal mixing of β_T

O'Leary et al. (2015) demonstrated that the β_T of liquids in the Li_2CO_3-Na_2CO_3-K_2CO_3-$CaCO_3$ quaternary system mix ideally with respect to their volumes fraction according to the following model equation:

$$\beta_T(X,T) = \sum X_i \frac{\bar{V}_{i.T}}{V_T}\left(\bar{\beta}_{i,1100\,K} + \frac{\delta\bar{\beta}_i}{\delta T}(T - 1100\,K)\right) \qquad \text{Eq. 3.4}$$

where X_i is the mole fraction of each carbonate liquid component *i*, $\bar{V}_{i.T}$ is the partial molar volume of each component *i* at temperature *T*, V_T is the molar volume of the liquid at *T*, $\bar{\beta}_{i,1100\,K}$ is the partial molar compressibility of component *i* at 1100 K and $\frac{\delta\bar{\beta}_i}{\delta T}$ is its temperature dependence. In this study, the same model equation was employed to a fit of all the compressibility data in Table 3.2, together with those from O'Leary et al. (2015), for a total of 24 liquids in the Li_2CO_3-Na_2CO_3-K_2CO_3-Rb_2CO_3-Cs_2CO_3-$SrCO_3$-$BaCO_3$ system.

Using Eq. 3.4, the partial molar compressibility (and its temperature dependence) of each carbonate component was fitted by a multivariable linear regression. The liquid compressibility data from this study (Table 3.2) was combined with those from O'Leary et al. (2015) on 11 $CaCO_3$-Li_2CO_3-Na_2CO_3-K_2CO_3 liquids and fitted to Eq. 3.4. The results are presented in Table 3.3a, with fitted terms (± 1σ) for $\bar{\beta}_{T,i}$ and $\frac{\delta\bar{\beta}_i}{\delta T}$ are listed. The final adjusted R^2 of the model is 0.994. The experimental β_T values are compared to the best-fit model values for each composition as a function of temperature in Fig. 3.4. The average percent residual between the experimental β_T values and those predicted by the model is 1.25%, which is less than the average propagated uncertainty of 2.2% in the experimental β_T values (Table 3.2). This result demonstrates that model equation in Eq. 3.4, which is based on ideal mixing, accurately describes the compositional and temperature dependence to the compressibility of the multi-component carbonate liquids.

Table 3.3a The partial molar compressibilities and their temperature dependencies are shown for each component at 1100 K from derived from a fit of the β_T data to Equation 3.4. The 1σ errors are derived from the standard error on the linear regression fit.

Component	$\bar{\beta}_T$ (1100 K) ± 1σ (10^{-2} GPa $^{-1}$)	$\frac{\delta\bar{\beta}_i}{\delta T}$ ± 1σ (10^{-2} GPa $^{-1}$ K^{-1})
Li_2CO_3	8.91 ± 0.07	0.0059 ± .0008
Na_2CO_3	10.67 ± 0.07	0.0093 ± .0006
K_2CO_3	14.22 ± 0.06	0.0127 ± .0005
Rb_2CO_3	14.65 ± 0.15	0.0175 ± .0011
Cs_2CO_3	17.95 ± 0.10	0.0179 ± .0010
$CaCO_3$	5.97 ± 0.14	0.0079 ± .0011
$SrCO_3$	4.33 ± 0.12	0.0027 ± .0009
$BaCO_3$	5.43 ± 0.26	0.0052 ± .0013

Figure 3.4 Liquid isothermal compressibilites calculated from sound speed measurements are recovered well by an ideal mixing model. Each sound speed measurement is combined with density data from Hurt and Lange (2018) to calculate isothermal compressibilites (β_T) using Eqs. 3.1 and 3.2. Calculated β_T is shown as a function of temperature for each composition. The lines are model values calculated by fitting the calculated isothermal compressibilites with a multiple linear regression to an ideal mixing model (Eq. 3.4). Points approximate the magnitude of 1σ experimental uncertainty.

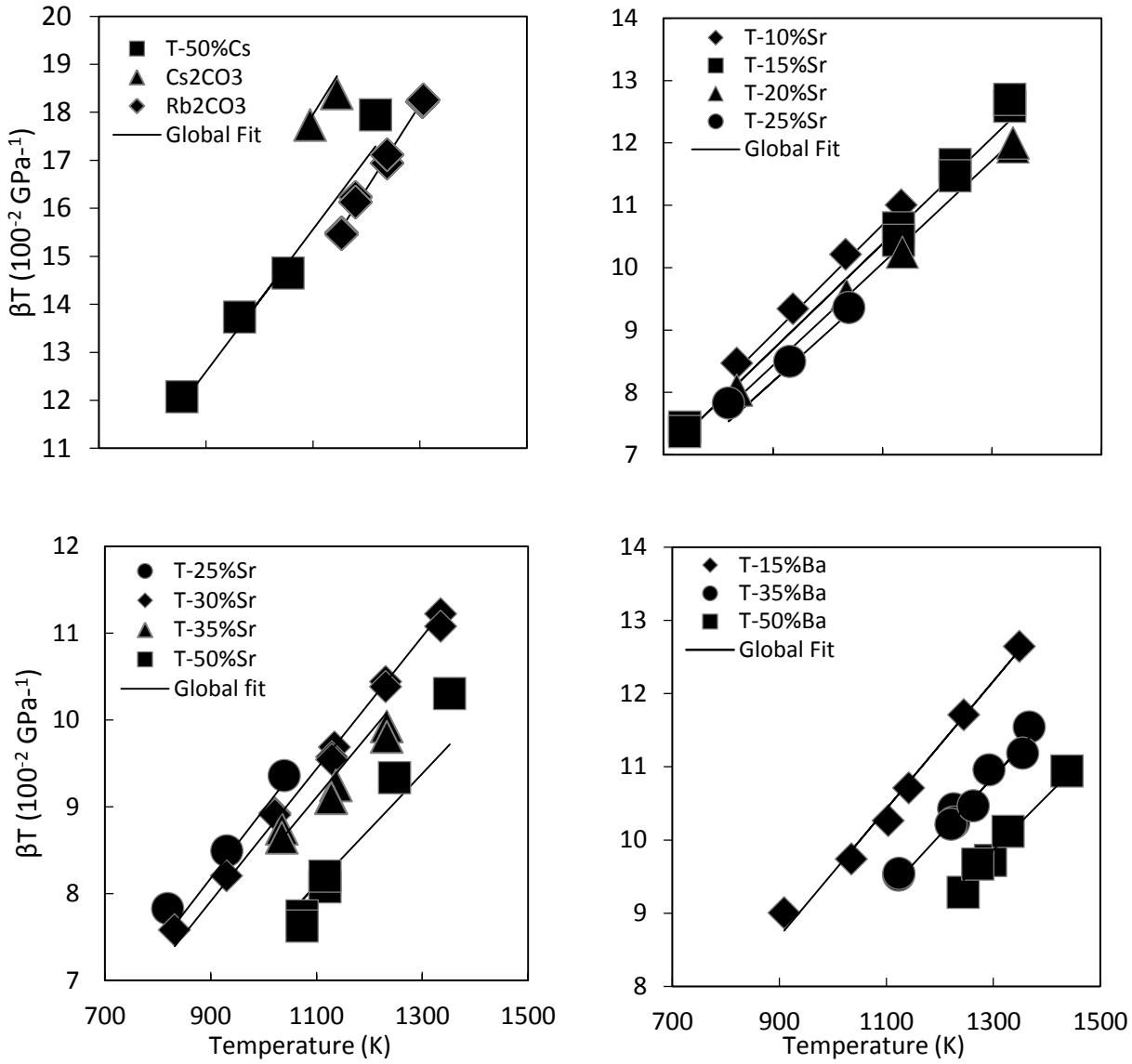

In Table 3.3b, the results of the bootstrap method of propagating the uncertainty from the various datasets used to calculate the experimental values for β_T (Eq. 3.2), reported in Table 3.2, were used to calculate 1000 synthetic β_T datasets, and a multiple linear regression of the model equation (Eq. 3.4) was performed to all of them, which generated 1000 regression results for the fitted $\overline{\beta}_T$ and $\frac{\delta\overline{\beta}_T}{\delta T}$ terms for the eight carbonate components. We took the standard deviation of the 1000 fitted values for each carbonate for the ±1σ values reported in Table 3.3b. These uncertainties are more realistic than those in Table 3.3a, because they incorporate the propagated

uncertainties from the liquid sound speed, density, thermal expansion, and heat capacity values that all contribute to the uncertainty in liquid β_T. The 1σ standard deviations in Table 3.3b range from 1.6% to 9.1% for the $\overline{\beta}_T$ values of K_2CO_3 and $BaCO_3$, respectively, and from 5% to 31% for the $\frac{\delta\overline{\beta}_T}{\delta T}$ terms for K_2CO_3 and $SrCO_3$, respectively. Note that this bootstrap approach was not undertaken in O'Leary et al. (2015), and therefore the fitted errors reported in that study are comparable to those in Table 3.3a, which do not account for the propagated uncertainties in density, thermal expansion and heat capacity.

Table 3.4b The partial molar compressibilities and their temperature dependencies are shown for each component at 1100 K from derived from a fit of the β_T data to Equation 3.4. The 1σ errors are derived from the boot strap method.

Component	$\bar{\beta}_T$ (1100 K) ± 1σ (10^{-2} GPa $^{-1}$)	$\frac{\delta\bar{\beta}_i}{\delta T}$ ± 1σ (10^{-2} GPa $^{-1}$ K^{-1})
Li_2CO_3	8.95 ± 0.35	0.0058 ± .0010
Na_2CO_3	10.64 ± 0.28	0.0094 ± .0007
K_2CO_3	14.23 ± 0.23	0.0127 ± .0006
Rb_2CO_3	14.66 ± 0.35	0.0175 ± .0025
Cs_2CO_3	17.96 ± 0.33	0.0179 ± .0018
$CaCO_3$	5.97 ± 0.50	0.0078 ± .0012
$SrCO_3$	4.37 ± 0.31	0.0026 ± .0008
$BaCO_3$	5.48 ± 0.51	0.0052 ± .0013

A plot of residuals, based on the results of the fit to Eq. 3.4 reported in Table 3.3, as a function of temperature are shown in Figure 3.5, which illustrates there is no structure to these residuals. In Figure 3.6, residuals are plotted as a function of composition for each carbonate component; again, there is no structure to the residuals, which again supports an ideal mixing model with respect to volume fraction (Eq. 3.4).

Figure 3.5 The residuals of the calculated β_T data fitted to an ideal mixing equation (Eq. 3.4) are plotted as a function of temperature and show no structure or dependency.

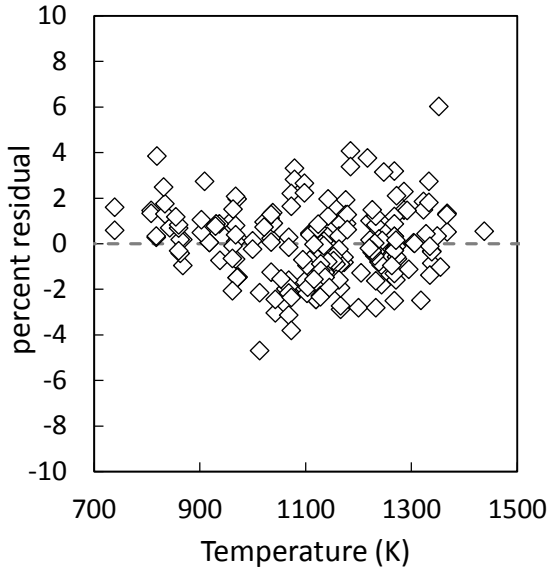

Figure 3.6 The residuals of the model fitting β_T data to an ideal mixing eq. (Eq 3.4) and plotted as a function of volume fraction of each component. The residuals show no structure or dependency on composition.

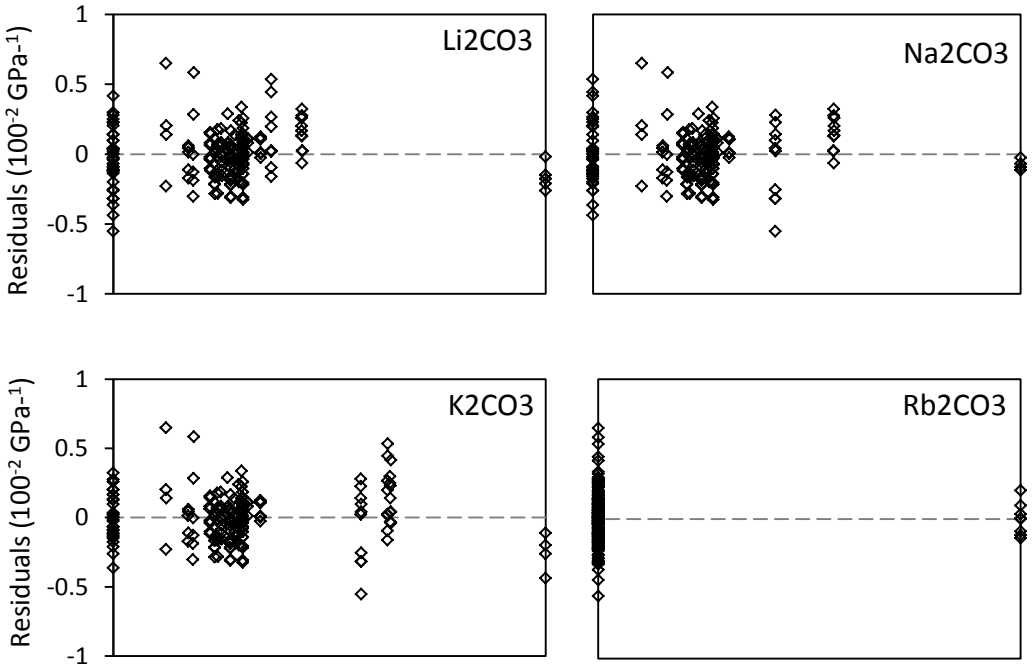

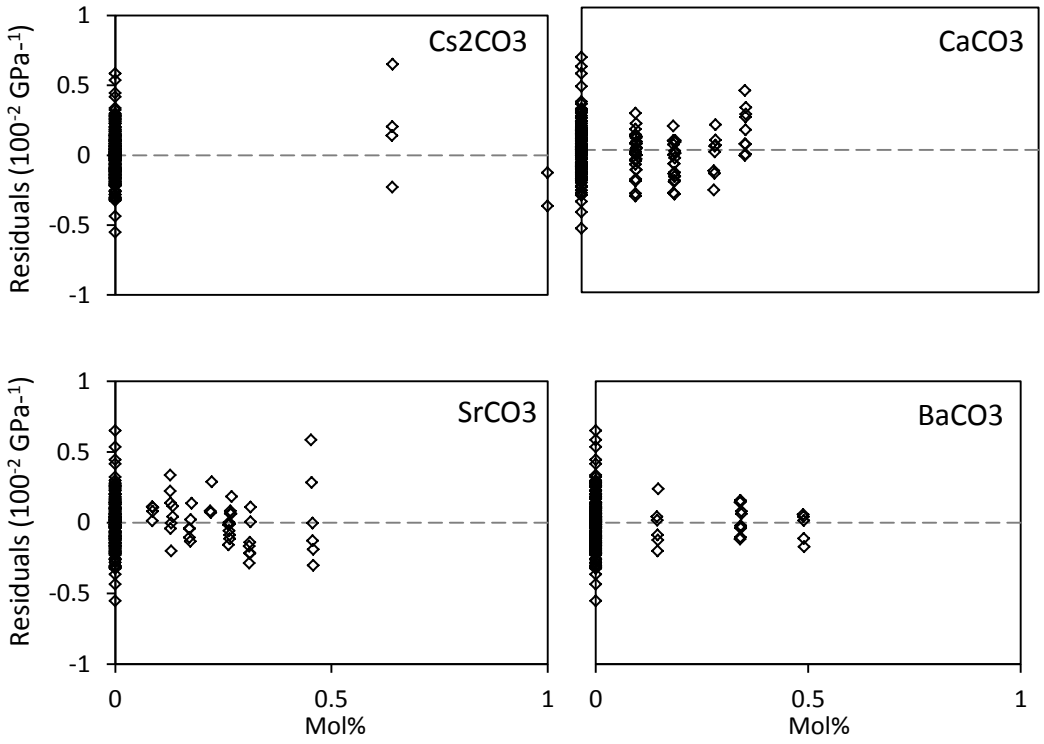

3.3.5 $\left(\frac{\delta V}{\delta P}\right)_T$ results

The pressure dependence of liquid volume, $\left(\frac{\delta V}{\delta P}\right)_T$, may be similarly modeled by an equation that assumes ideal mixing of the carbonate liquid components on the basis of mole fraction:

$$\left(\frac{\delta V}{\delta P}\right)_T (X,T) = \sum X_i \left(\frac{\delta V_{i,1100\,K}}{\delta P} + \frac{\delta^2 \overline{V}_i}{\delta P \delta T}(T - 1100\ K)\right) \quad \text{Eq. 3.5}$$

In Eq. 3.5, $\left(\frac{\delta V}{\delta P}\right)_T$ is the isothermal change in volume with pressure for a given liquid at temperature T, $\frac{\delta V_{i,1100\,K}}{\delta P}$ is the partial molar pressure dependence of volume for each carbonate liquid component i at 1100 K and $\frac{\delta^2 \overline{V}_i}{\delta P \delta T}$ is its linear temperature dependence for each component i. As with βT, a multiple linear regression was used to fit the data in Table 3.2 to Eq. 3.5 and the

resulting fitted terms, $\frac{\delta V_{i,1100\,K}}{\delta P}$ and $\frac{\delta^2 \overline{V}_i}{\delta P \delta T}$, were obtained for each component (Table 3.4). The adjusted R^2 of the fit is 0.994, with an average residual of 1.5%.

The results of this study lead to the same conclusion as that drawn in O'Leary et al. (2015) based on the 4-component Li_2CO_3-Na_2CO_3-K_2CO_3-$CaCO_3$ system, but this time for the 8-component Li_2CO_3-Na_2CO_3-K_2CO_3-Rb_2CO_3-Cs_2CO_3-$SrCO_3$-$BaCO_3$ system. Ideal mixing of carbonate components describes the isothermal compressibility and $\left(\frac{\delta V}{\delta P}\right)_T$ of these liquids well within experimental uncertainty. Figure 3.7 further illustrates this point for Cs_2CO_3, $SrCO_3$ and $BaCO_3$- bearing liquids by highlighting the linear dependence of β_T on volume fraction.

Table 3.4 The partial molar $\frac{\delta \overline{V}_i}{\delta P}$ and $\frac{\delta^2 \overline{V}_i}{\delta P \delta T}$ for each component at 1100 K from a fit of the $\left(\frac{\delta V}{\delta P}\right)_T$ data to equation 3.5. The 1σ errors are estimated from a bootstrap approach.

Component	$\delta \overline{V}_i / \delta P$ (1100 K) ± 1σ (10^{-4} cm^3/bar)	$\delta \overline{V}_i / \delta T \delta P$ ± 1σ (10^{-4} cm^3/bar K)
Li_2CO_3	-3.730 ± 0.152	0.0026 ± 0.0006
Na_2CO_3	-5.681 ± 0.147	-0.0066 ± 0.0005
K_2CO_3	-10.162 ± 0.168	-0.0115 ± 0.0006
Rb_2CO_3	-11.793 ± 0.294	-0.0176 ± 0.0021
Cs_2CO_3	-16.895 ± 0.314	-0.0201 ± 0.0017
$CaCO_3$	-2.431 ± 0.207	0.0039 ± 0.0006
$SrCO_3$	-1.938 ± 0.134	0.0016 ± 0.0005
$BaCO_3$	-2.685 ± 0.264	-0.0038 ± 0.0008

Figure 3.7 Compressibility mixes ideally with respect to volume fraction.The β_T of Cs_2CO_3, $SrCO_3$ and $BaCO_3$-bearing liquids measured along an isotherm and plotted as a function of volume fraction $SrCO_3$ or $BaCO_3$. Solid diamonds show experimental measurements and empty circles show $\bar{\beta}_T$ values derived from the fit to Eq. 3.4.

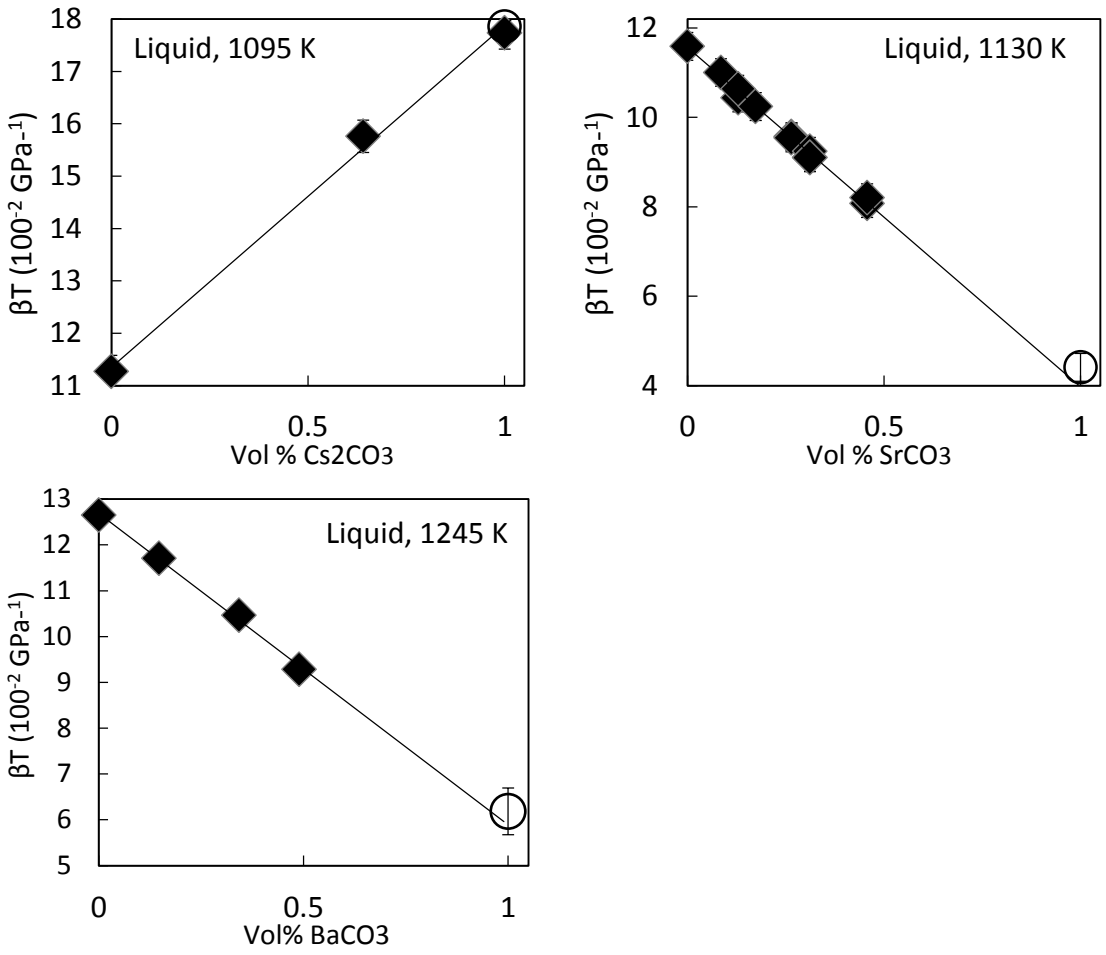

3.4 Discussion

The primary objective of this study is to determine if there are any systematics to the compressibility of carbonate liquids as a function of composition that will enable the partial molar liquid compressibility of the $MgCO_3$ and $FeCO_3$ components to be estimated. By extending the 8-component system explored in this study to these two components, a predictive model for 1-bar liquid compressibility can be applied to naturally occurring carbonate melts in the mantle. To evaluate and test for systematic behavior, plots of liquid β_T for each carbonate component are plotted in various diagrams as a function of different compositional parameters and the results are discussed below.

3.4.1 Liquid compressibility vs. cation field strength and cation volume

The partial molar compressibilities (at 1100 K) of the eight liquid carbonate components are plotted as a function of cation field strength in Figure 3.8. Cation field strength is defined as $z/(0.126+r)^2$, where z is the formal cation charge, r is the crystalline ionic radius of the cation (Shannon and Prewitt, 1969; Shannon, 1976) and the 0.126 term is the ionic radius of the oxygen anion. Because the ionic radius depends on the metal cation-oxygen (M-O), it is necessary to obtain these values from available X-ray and neutron diffraction studies, as well as molecular dynamic simulations. For the alkali carbonate liquids, best estimates of M-O values are ~4 for Li_2CO_3, ~5 for Na_2CO_3, and ~6 for K_2CO_3, Rb_2CO_3, and Cs_2CO_3 (Tissen and Janssen, 1990; Habasaki, 1990; Kohara et al., 1999; Roest et al., 2017). For the alkaline-earth carbonate liquids, M-O values are ~7 for $CaCO_3$ and $SrCO_3$, and ~8 for $BaCO_3$ (Vuilleumier et al., 2014; Hurt and Wolf, 2018b).

Figure 3.8 The partial molar compressibility of each carbonate liquid component at 1100 K derived from a fit to Eq. 3.4, is plotted as a function of cation field strength.

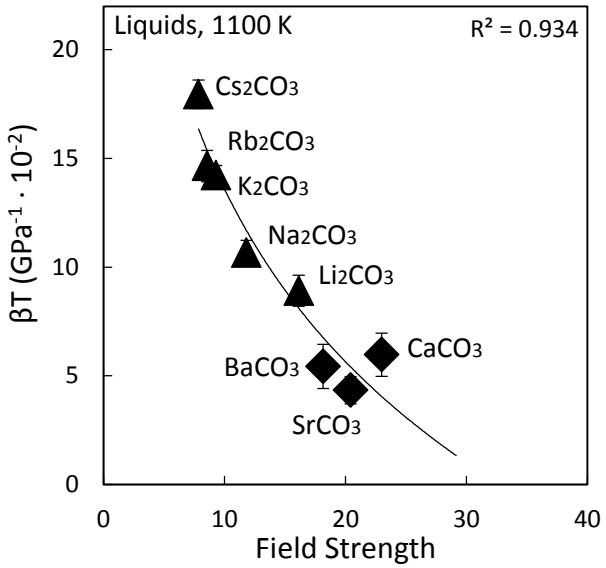

In Figure 3.8, the partial molar carbonate liquid β_T values from Table 3.3 (1100 K) are plotted as a function of field strength. The data show a curved trend, with the highest liquid compressibility associated with the lowest field strength (e.g., Cs_2CO_3). On the basis of this trend, the best estimates of β_T for the liquid $MgCO_3$ and $FeCO_3$ components are values ≤ 3 GPa^{-1} 10^{-2}. If the data are fitted to a linear trend, then the $CaCO_3$ component appears to be an outlier, with a relatively high value for its liquid β_T and estimated values for the liquid compressibility of $MgCO_3$ and $FeCO_3$ are even lower (i.e., highly incompressible).

In a second plot (Fig. 3.9), the partial molar liquid β_T values in Table 3.3 (1100 K) are shown as a function of cation volume (cm^3/mol), which is defined as $AvN4\pi r^3/3$ where Av is Avogadro's number, N is the stoichiometric number of cations per formula unit (2 for alkalis and 1 for alkaline earths) and r is the crystalline ionic radius. The results lead to two distinct trends, one for the alkali carbonate liquids and another for the alkaline earth carbonate liquids. For the alkali carbonate liquids, there is a strong linear relationship ($R^2 = 0.98$) with high cation volumes predictive of high liquid β_T, whereas for the alkaline earth carbonate liquids, there is no clear trend ($R^2 = 0.04$). If the $CaCO_3$ sample is removed from this plot, it is possible that the $SrCO_3$ and $BaCO_3$ samples follow a linear relationship that is sub-parallel to the alkaline carbonate trend. If so, again the β_T for $CaCO_3$ liquid appears to be higher than expected, and the trend described by the two $SrCO_3$ and $BaCO_3$ liquids suggest a relatively low liquid β_T value for the $MgCO_3$ and $FeCO_3$. Alternatively, the alkaline earth carbonate liquid β_T values may all be similar and independent of cation volume, in which case their average may be a predictor of β_T for $MgCO_3$ and $FeCO_3$ liquids. The bottom line is that there is no clear prediction can be made for these two liquid components on the basis of the results in Figure 3.9.

Figure 3.9 The partial molar compressibility of each carbonate liquid component at 1100 K derived from a fit to Eq. 3.4, is plotted as a function of cation volume.

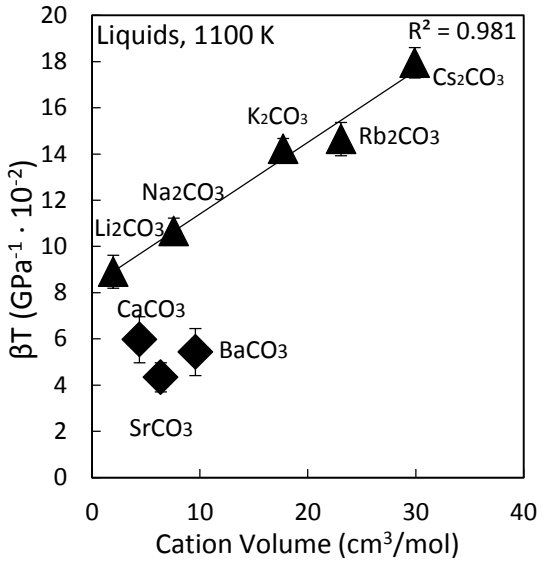

3.4.2 Liquid compressibility vs. liquid molar volume

Another possible relationship to explore is that between liquid compressibility and liquid molar volume. Intuitively, it is expected that liquids with higher molar volumes will be more compressible. In Figure 3.10, plots of the partial molar liquid β_T values (Table 3.3) are shown as a function of partial molar liquid volume from Hurt and Lange (2018). The data fall along two trend lines in a pattern that is nearly identical to what was observed in Figure 3.9 (cation volume). For the alkali carbonate liquids, there is a strong linear relationship ($R^2 = 0.98$) with large liquid molar volumes associated with large liquid β_T, whereas for the alkaline earth carbonate liquids, there is no clear trend ($R^2 = 0.04$). The reason for the similarity in the plots shown in Figures 9 and 10 is that the carbonate liquid molar volumes are strongly correlated with their cation volumes, as discussed at length in Hurt and Lange (2018). Again, the clear conclusion to be drawn from Figure 3.10 is although liquid molar volume appears to strongly

correlate with liquid β_T for the alkali carbonates, there is no correlation among the three alkaline earth carbonate liquids.

Figure 3.10 The partial molar compressibility of each carbonate liquid component at 1100 K derived from a fit to Eq. 3.4, is plotted as a function of molar liquid volume.

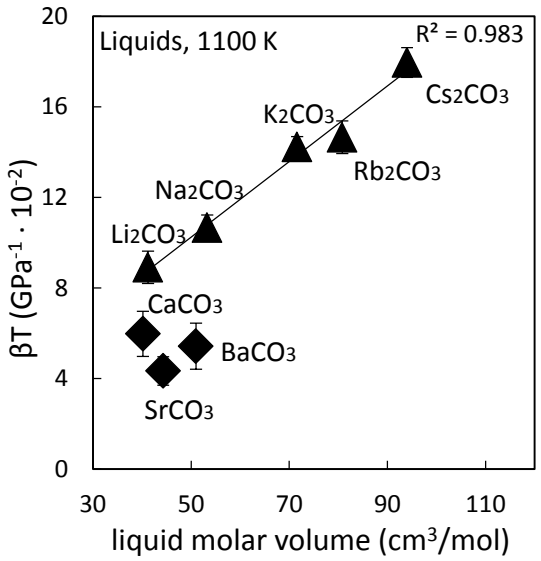

Despite this lack of correlation, a first-order observation that emerges from Figure 3.10 is that the alkali carbonate liquids are systematically more compressible than the alkaline earth carbonate liquids for a given liquid molar volume (for all data shown at 1100 K; Hurt and Lange, 2018). For example, $BaCO_3$ liquid has a partial molar volume (~51.0 cm^3/mol) that is higher than that for Li_2CO_3 (~41.2 cm^3/mol), and yet its partial molar β_T value (5.4 10^{-2} GPa^{-1}) is significantly less than that for Li_2CO_3 (8.9 10^{-2} GPa^{-1}). Understanding why two carbonate liquids with similar molar volumes can have different liquid β_T values requires an examination of the network topology of carbonate liquids, and differences between alkali carbonate and alkaline earth carbonate liquids and their corresponding crystalline phases.

3.4.3 A comparison of alkali carbonate and alkaline earth carbonate liquid structure

Hurt and Lange (2018) explored systematic variations in the liquid molar volumes of alkali and alkaline earth carbonates ($CaCO_3$, $SrCO_3$ and $BaCO_3$) and found that the molar volumes of both groups increase linearly with cation volume but form two separate trends with separate intercepts. They concluded that the partial molar volume of the carbonate ion, $(CO_3)^{2-}$, has a constant value among the alkali carbonate liquids (~38 cm^3) and a different constant value among the alkaline earth carbonate liquids (~31 cm^3/mole). These contrasting partial molar volumes for the carbonate ion reflect the 4-fold metal cation-carbonate (M-C) coordination in alkali carbonate liquids (e.g. Roest et al 2017; Kohara et al 1999; Habaski 1990; Tissen and Janssen 1990) and the 6-fold M-C coordination in alkaline earth carbonate liquids (e.g. Vuilleumier 2014; Hurt and Wolf 2018aa).

At first glance, one might posit that the larger partial molar volume of $(CO_3)^{2-}$ in alkali carbonate liquids may reflect a larger carbonate molecule in the melt compared to alkaline earth carbonate liquids. However, this is the not the case, as M-C distances (a proxy for the size of the carbonate molecule) in alkali carbonate liquids are not appreciably larger than in alkaline earth carbonate liquids. For example, Roest et al. (2017) report M-C distances for alkali carbonate liquids ranging from 2.79 Å for Li_2CO_3 to 3.35 Å for K_2CO_3, whereas Vuilleumier et al. (2014) and Hurt and Wolf (2018a) report M-C distances of of 3.23 Å for $CaCO_3$ liquid. Moreover, molecular dynamic simulations of alkaline earth carbonate liquids suggest that the size of carbonate groups are basically fixed, changing little with temperature, pressure, and state-of-matter (i.e., liquid or solid) (e.g. Vuilleumier et al 2014; Hurt and Wolf, 2018). Therefore, the larger partial molar volume of the carbonate ion, $(CO_3)^{2-}$, in alkali carbonate liquid is not a result of a larger carbonate molecule but instead is caused by difference in how the carbonate ions are arranged (i.e., their network topology) in alkali carbonate and alkaline earth carbonate liquids.

An analogy can be drawn with the 1-bar crystalline polymorphs of SiO_2, all of which are based on silica tetrahedral (Si^{4+} that is 4-fold coordinated by oxygen). The size of the silica tetrahedra does not change among the crystalline polymorphs (e.g., Stixrude and Bukowinski, 1988), but the way the tetrahedra are arranged into different ring structures (i.e., network topology) varies significantly (from 6-membered rings in tridymite to 4-membered rings in coesite), leading to very different molar volumes at similar T-P conditions (e.g., Stixrude and Bukowinski, 1990). It is perhaps not surprising that the partial molar volume of SiO_2 in multicomponent silicate melts matches the value for tridymite (Lange, 1997), which is the SiO_2 polymorph that has the most open network structure and appears to be favored in high-temperature multi-component silicate liquids.

If the network topology controls melt volume, the next question is whether an examination of corresponding crystalline phases for each carbonate component provides a prediction of how much change in topology (and therefore density) can be attained by the liquid under compression. In other words, for a carbonate phase with a large (vs small) volume of fusion at its melting point, it is expected that the liquid will have a relatively large (vs. small) liquid compressibility. If a liquid has a significantly larger molar volume than the corresponding crystal at its congruent fusion temperature, the implication is that the liquid has accessed a significantly different and more open network topology than the crystal. A large liquid β_T is expected because the crystalline phase shows that a more dense and closely-packed topology is possible for that carbonate composition. To further explore this possibility, a comparison of crystalline and liquid molar volumes for each of the carbonate components is required.

3.4.4 Carbonate crystal volumes at high temperature and volumes of fusion

An examination of carbonates crystal structures at high temperatures may provide some insight into liquid compressibility patterns since crystal structures reveal topologies available to the liquid under compression. Alkali carbonate and alkaline earth carbonate crystal volumes are plotted as a function of temperature in Figures 11 and 12, respectively, and compared to their liquid volumes at 1100 and 1500 K, respectively.

Figure 3.11 The molar volumes of alkali carbonate crystal phases of each component have been collected from the literature and are shown as a function of temperature. The molar volume of the liquid from Hurt and Lange (2018) is shown along with the subsequent molar volume of fusion at 1100 K. Dashed lines indicate an extrapolation of the crystal volume.

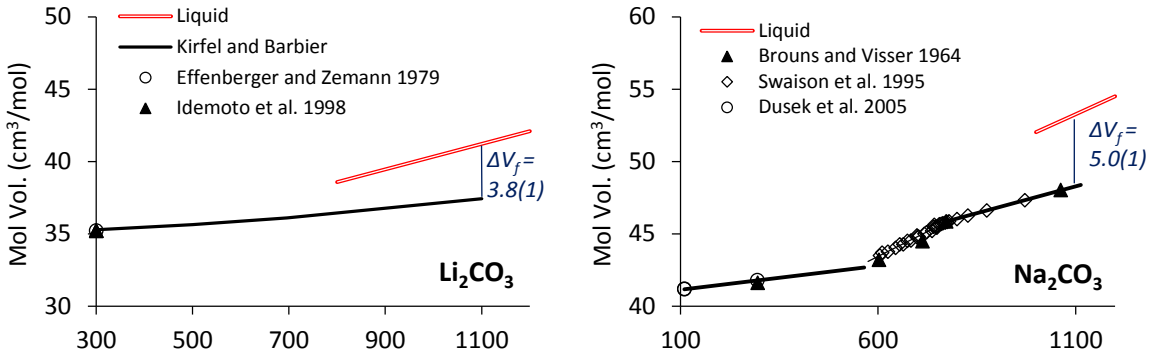

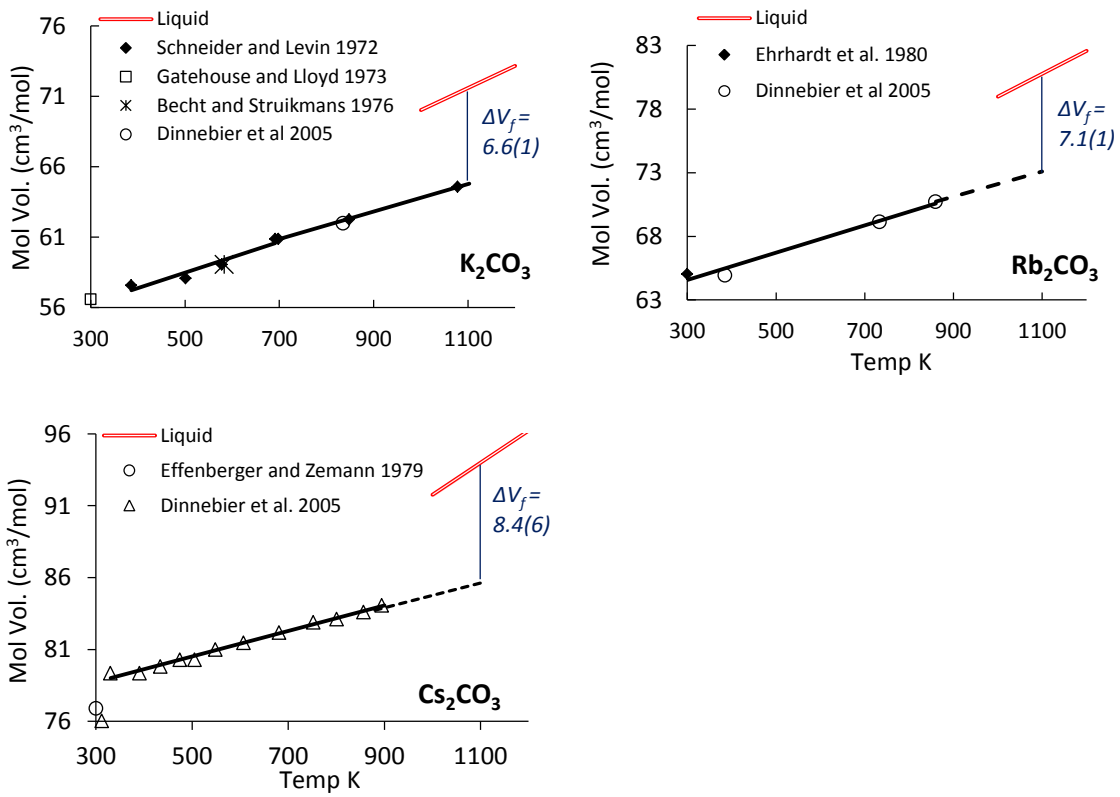

Figure 3.12 The molar volumes of alkaline earth carbonate crystal phases of each component have been collected from the literature and are shown as a function of temperature. The molar volume of the liquid from Hurt and Lange (2018) is shown along with the subsequent molar volume of fusion at 1500 K. Dashed lines indicate an extrapolation of the crystal volume. Note that $MgCO_3$ and $FeCO_3$ are metastable beyond ~773 K, crystal data are from the thermal P-V-T equations-of-state from Litasov et al. (2008) and (2013) (dotted lines).

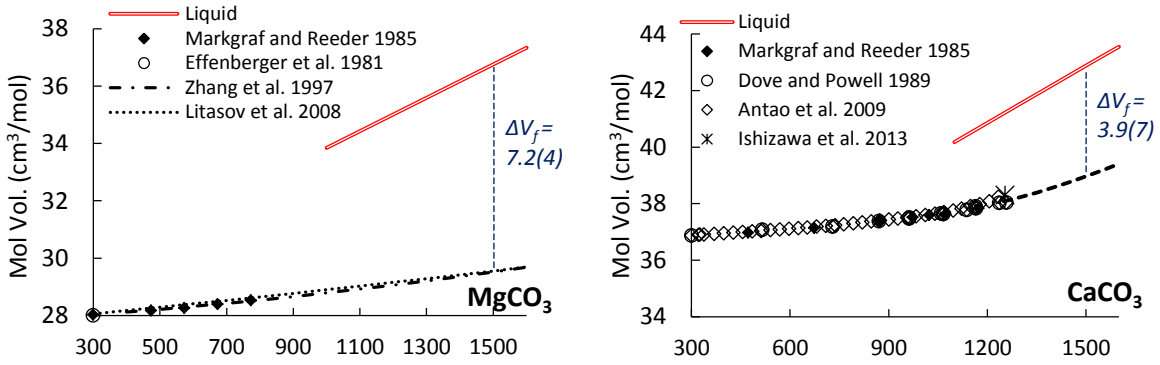

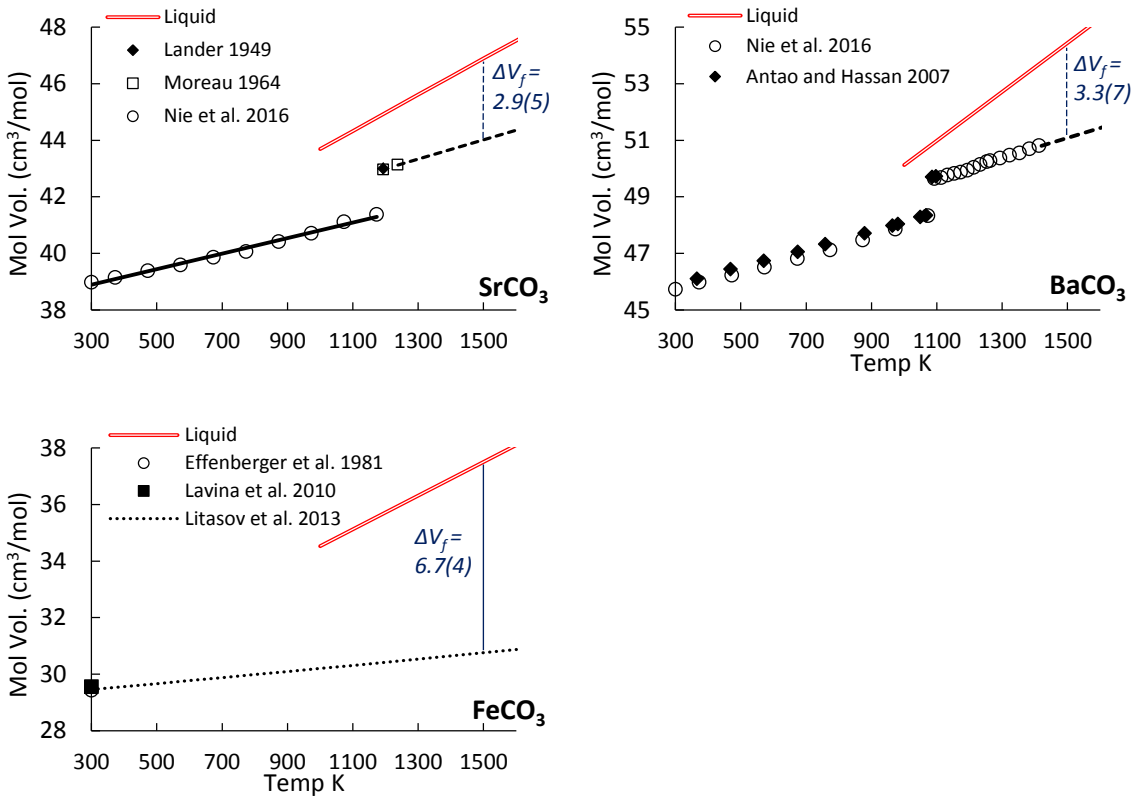

The five alkali carbonates share a remarkable uniformity of crystalline polymorphs. At ambient conditions, the alkali carbonates all assume a monoclinic crystal structure (see Effenberger and Zemann 1979 for Li_2CO_3; Brouns and Visser 1964 for Na_2CO_3; Schneider and Levin 1972 for K_2CO_3 and Dinnebier et al 1980 for Rb_2CO_3 and Cs_2CO_3). They all transition to a hexagonal *P6₃/mmc* phase at higher temperatures with the sole exception of Li_2CO_3, which remains in the *C2/c* space group.

In the case of the alkaline earth carbonates, at ambient conditions, $SrCO_3$ and $BaCO_3$ form *Pmcn* aragonite-structured strontianite and witherite (e.g. Nie et al. 2016). $CaCO_3$ is different in that, at ambient temperatures, the rhombohedral $R\bar{3}c$ calcite phase is stable (rather than aragonite). At high temperature (~1200 K), $SrCO_3$ and $BaCO_3$ transition to a hexagonal *R3m* or $R\bar{3}m$ phase (Lander 1949; Moreau 1964; Strømme 1975; Antao and Hassan 2007) that is similar to the high-temperature phase of $CaCO_3$, Calcite V (e.g. Ishizawa et al 2013). The high

temperature R3m phases of $CaCO_3$, $SrCO_3$ and $BaCO_3$ all exhibit rotational disorder of the carbonate ion (e.g. Strømme 1975). The *Pmcn* → *R3m* phase transition in $SrCO_3$ and $BaCO_3$ is accompanied by a significant increase in molar volume (~3.8% and 2.7% respectively) that is similar in magnitude to the aragonite → calcite phase transition. $SrCO_3$ and $BaCO_3$, which are more stable at high temperatures than $CaCO_3$, further transition to a face-centered cubic (*Fm3m*) phase at 1689 K (Baker 1962) and 1253 K (Nie et al. 2016), respectively, which is accompanied by a subtle (~0.2%) increase in volume. It was noted in Hurt and Lange (2018) that high temperature phases in alkaline earth carbonates (i.e. *Pmcn*→ *R3m*→ *Fm3m*) become progressively more "liquid-like" in terms of their M-O, M-C and C-C coordination numbers. The cubic *Fm3m* phase, for example, has coordination numbers very close to that of the liquid (Hurt and Lange 2018).

A comparison of the high-temperature alkali carbonate crystalline volumes with their corresponding liquid volumes at the same temperature (1100 K) gives their respective volumes of fusion (Figure 3.11). The volumes of fusion increase from 3.8 (± 0.1) cm^3/mol for Li_2CO_3 to 8.4 (± 0.6) cm^3/mol for Cs_2CO_3. A similar comparison can be made between the high-temperature alkaline earth carbonate crystal volumes at 1500 K (above their respective phase transitions and at the upper bound of the experimental sound speed measurements) and their corresponding liquid volumes (Figure 3.12). In this case, the volumes of fusion increase in the order of $SrCO_3$ (2.9 ± 0.5 cm^3/mole) to $BaCO_3$ (3.4 ± 0.7 cm^3/mole) to $CaCO_3$ (3.9 ± 0.7 cm^3/mole), which is the same order found for a progressive increase in liquid compressibility (Table 3.3).

3.4.5 Systematic trends in liquid $(dV/dP)_T$ and β_T with ΔV_{fusion} and $\Delta V_{fusion}/V_{liquid}$

If the volumes of fusion for the respective carbonate phases presage the potential decrease in molar volume with pressure that is possible for each liquid, they can be used as a proxy for $(\delta V/\delta P)_T$ and/or β_T. Because β_T is $(\delta V/\delta P)_T$ divided by molar volume, plots as a function of $\Delta V_{fusion}/V_{liquid}$ are also shown. For the alkali carbonate liquids, plots of $(\delta V/\delta P)_T$ and β_T versus ΔV_{fusion} and $\Delta V_{fusion}/V_{liquid}$ at 1100 K are shown in Figure 3.13. Linear fits to all four sets of data show that the tightest correlation (R^2 = .990) is found when β_T is plotted against ΔV_{fusion}.

Figure 3.13 The partial molar $\frac{\delta V}{\delta P_T}$ of each alkali carbonate liquid component at 1100 K derived from a fit to Eq. 3.5, is plotted as a function of ΔV_{fusion} (a) and $\Delta V_{fusion}/V_{liq}$. (b). The bottom two panels show the partial molar compressibility of each alkali carbonate component at 1100 K as a function of ΔV_{fusion} (c) and $\Delta V_{fusion}/V_{liq}$ (d).

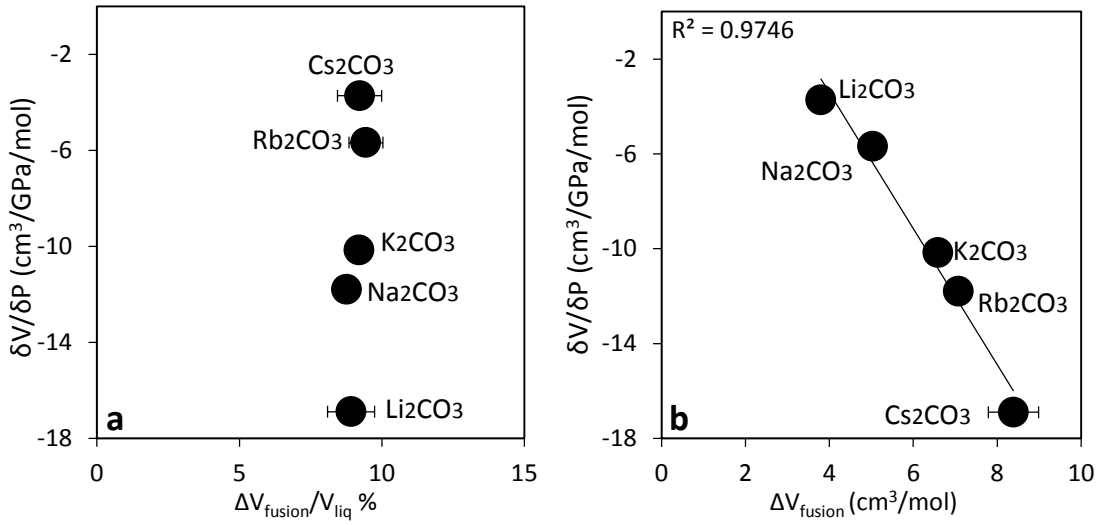

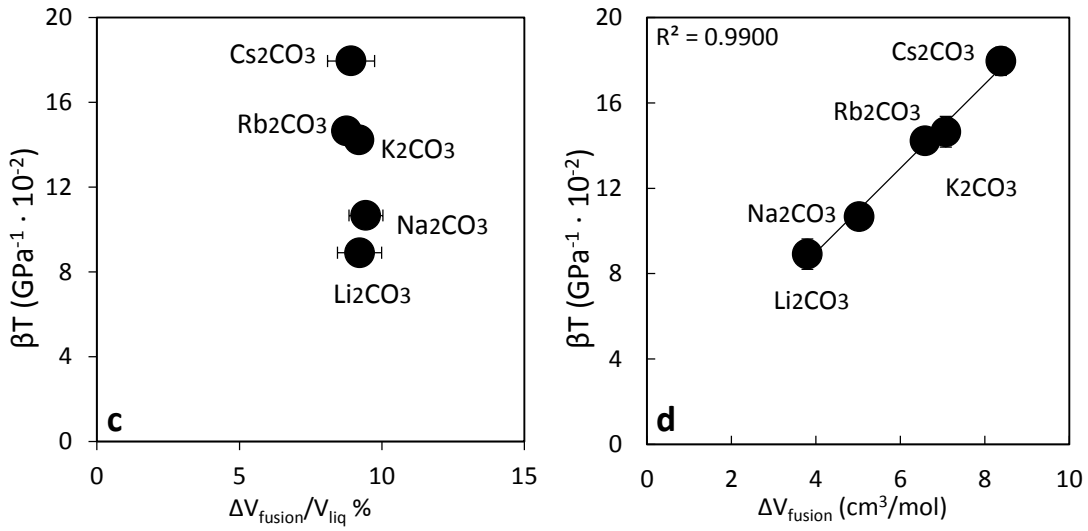

Figure 3.14 The partial molar $\frac{\delta V}{\delta P}_T$ of each alkaline earth carbonate liquid component at 1500 K derived from a fit to Eq. 3.4, is plotted as a function of ΔV_{fusion} (a) and $\Delta V_{fusion}/V_{liq}$. (b). The bottom two panels show the partial molar compressibility of each alkaline earth carbonate component at 1500 K as a function of ΔV_{fusion} (c) and $\Delta V_{fusion}/V_{liq}$ (d).

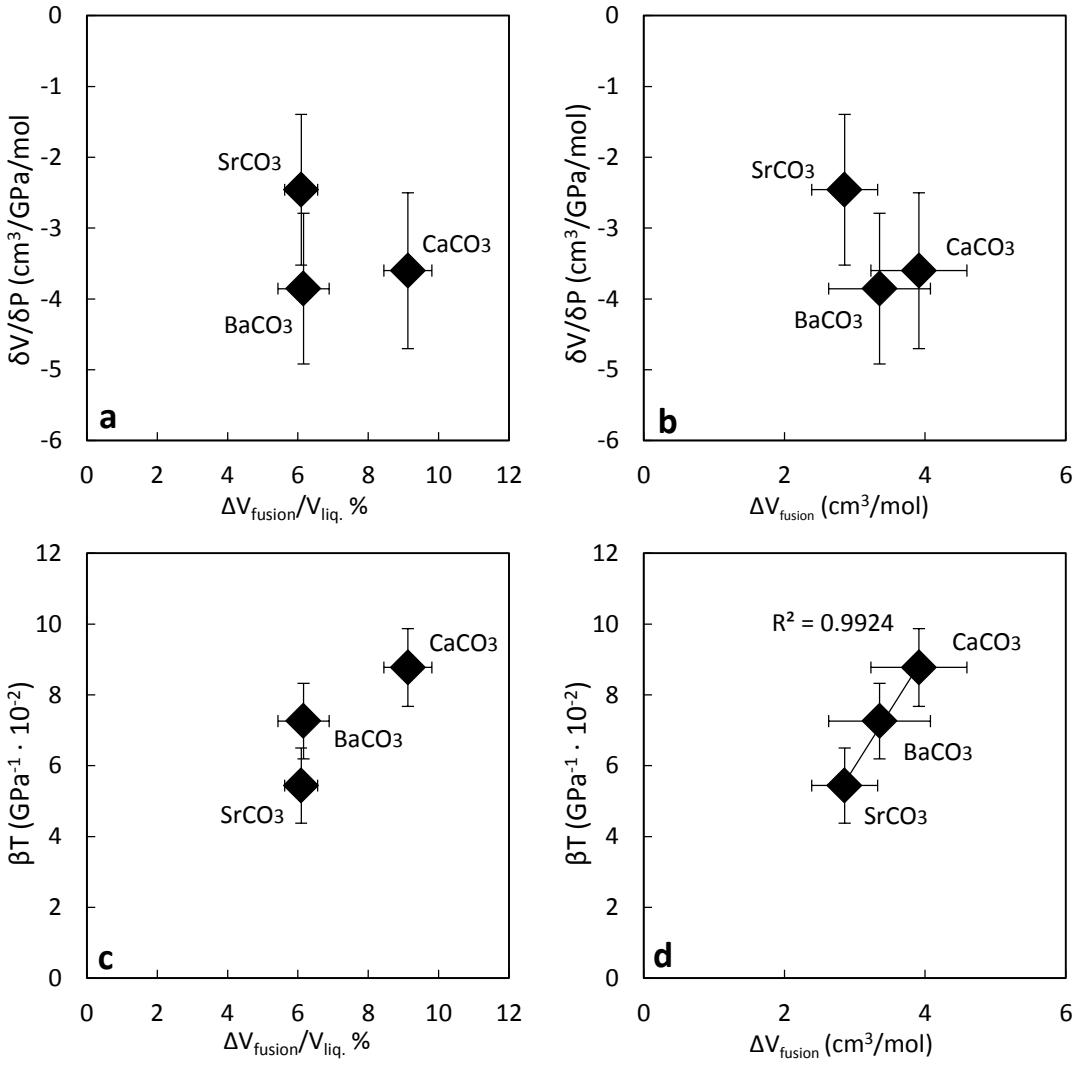

Similar plots and linear fits can be made for the alkaline earth carbonate liquids at 1500 K (Figure 3.14) and again the strongest correlation is between β_T and ΔV_{fusion} (R^2 = .992). These results suggest that one of the best predictors of the magnitude of melt compressibility is the magnitude of the ΔV_{fusion} term, which opens up the opportunity to estimate the partial molar liquid compressibility values for the $MgCO_3$ and $FeCO_3$ components.

3.4.6 Compressibility of $MgCO_3$ and $FeCO_3$ liquid

$MgCO_3$ and $FeCO_3$ are among the most important liquid components for understanding partial melting of the mantle in the presence of carbonate. However, experimental attempts to

study $MgCO_3$-bearing liquids at 1 bar are nearly impossible owing to its low decarbonation temperature (500 °C) (Hurst 1991). Using the relation between compressibility and ΔV_{fusion} (Fig. 3. 14), a broad constraint can be placed on the liquid β_T of these important components. The 1-bar crystalline volumes of magnesite and siderite (extended up to the reference temperature of 1500 K; Table 3.5) are estimated from the work of Litasov et al. (2008) and (2013), and shown in Figure 3.12. These are based on their proposed equation-of-states and allow a best estimate of the molar volume of these two crystalline phases under metastable high-T conditions. Importantly, there is no evidence that a higher-T (higher-volume) crystalline polymorph of $MgCO_3$ exists under any P-T condition within the Earth. For example, magnesite is the stable crystalline phase along its congruent melting curve (~1400 °C at 2.5 GPa; Katsuro and Ito, 190), whereas calcite-V is the stable phase along its congruent melting curve (e.g., Suito et al., 2001).

Table 3.5 The molar volume of the liquid, crystal and ΔV_{fusion} at 1100 K for the alkali carbonates and 1500 K for the alkaline earth carbonates and $FeCO_3$ are shown.

	$V_{1100\,K}^{liq}$ (cm^3/mol)	$V_{1100\,K}^{xtl}$ (cm^3/mol)	ΔV_{fusion} (cm^3/mol)
Li_2CO_3	41.22[a]	37.42[b]	3.80
Na_2CO_3	53.27[a]	48.24[c,d]	5.03
K_2CO_3	71.59[a]	65.0[e,f,g]	6.59
Rb_2CO_3	80.78[a]	73.7[g]*	7.08
Cs_2CO_3	94.00[a]	85.6[g]*	8.4
	$V_{1500\,K}^{liq}$	$V_{1500\,K}^{xtl}$	
$MgCO_3$	36.7[a]	29.6[h]	7.2
$CaCO_3$	42.87[a]	38.96[h,i,j]*	3.91
$SrCO_3$	46.88[a]	44.02[k,l]*	2.86
$BaCO_3$	54.44[a]	51.09[m,n]*	3.35
$FeCO_3$	37.5[a]	30.8[o]	6.7

To calculate ΔV_{fusion}, the liquid volume is also required. The 1-bar, 1500 K liquid volumes for $FeCO_3$ and $MgCO_3$ were estimated in Hurt and Lange (2018) on the basis of linear trends (R^2=.999) among alkaline earth carbonate liquids as a function of cation volume. Hurt and Lange

supplied two volume estimates for both $FeCO_3$ and $MgCO_3$ liquid depending on the coordination of the metal cation with the carbonate molecule. If Mg^{2+} and Fe^{2+} maintain a 6-fold coordination with carbonate (like the other alkaline earth carbonate liquids), then the respective liquid volumes for $MgCO_3$ and $FeCO_3$ are shown in Figure 3.12, together with resulting volumes of fusion of 7.2 (± 0.4) and 6.7 (± 0.4) cm^3/mole, respectively. Note that if a lower (4-fold) M-C coordination (similar to that found among the alkali carbonate liquids) is assumed for Mg^{2+} and $Fe^{2+,}$ even larger ΔV_{fusion} values are obtained.

When the ΔV_{fusion} values of ~7.2 and ~6.7 cm^3/mole for the $MgCO_3$ and $FeCO_3$ components, respectively, are plotted in Figure 3.14, the resulting liquid compressibility values are ~19 and ~18 $GPa^{-1} \cdot 10^{-2}$, respectively, at 1500 K. These remarkably high melt β_T values may be initially unexpected, but make sense given the extremely compact molar volumes of the magnesite and siderite crystalline phases. If the compact topology of these two phases is accessible to the $MgCO_3$ and $FeCO_3$ liquids under compression, then the expectation is that these liquids should have large 1-bar melt β_T values. Needless to say, there are large uncertainties associated with these estimates (± 6 $GPa^{-1} \cdot 10^{-2}$) in Figure 3.14, and the estimated values can be tested through high-quality molecular dynamics simulations and direct density measurements at elevated T-P (via sink/float methods) of these important liquid components.

3.5 Conclusion

The sound speeds of 13 liquids in the Li_2CO_3-Na_2CO_3-K_2CO_3-Rb_2CO_3-Cs_2CO_3-$SrCO_3$-$BaCO_3$ system were measured at 1 bar between 739 and 1367 K and combined with sound speed results from O'Leary and Lange (2015) on 11 liquids in the Li_2CO_3-Na_2CO_3-K_2CO_3-$CaCO_3$ system. Isothermal compressibilities (β_T) were derived from each sound speed measurement and fitted with an ideal mixing model. The model equation recovers the compressibility data to

within ~1.25%, which is smaller than the average experimental uncertainty on β_T values (2.2%), which were calculated with a bootstrap approach. Fitted values for the partial molar compressibility and its temperature dependence were obtained for each of the eight carbonate components and found to match the measured values on the pure components, when available. Isothermal compressibility mixes ideally across the entire compositional and temperature range examined in this study.

Among the alkaline and alkaline earth carbonate liquids, the strongest correlation is between melt compressibility and their respective ΔV_{fusion} $(=V_{liquid}-V_{crystal})$ values. The difference in volume between the liquid and crystal is an accurate predictor of the potential reduction in volume that a liquid can attain (that is a volume similar to the crystal) under pressure. Linear fits to the results on the three alkaline earth carbonate samples ($SrCO_3$, $BaCO_3$ and $CaCO_3$) allow estimates of the liquid compressibility of $MgCO_3$ and $FeCO_3$ to be obtained. The results strongly suggest that their 1-bar compressibility values are far higher than previously assumed. Fortunately, molecular dynamic simulations are well suited to test these predictions.

3.6 References

Ai Y., Lange R. A. (2004a) An ultrasonic frequency-sweep interferometer for liquids at high temperature: 1. Acoustic model. *J. Geophys. Res.* **109**, B12203.

Ai Y., Lange R. A. (2004b) An ultrasonic frequency-sweep interferometer for liquids at high temperature: 2. Mechanical assembly, signal processing, and application. *J. Geophys. Res.* **109**, B12204.

Ai Y., Lange R. A. (2008) New acoustic velocity measurements on $CaO–MgO–Al_2O_3–SiO_2$ liquids: reevaluation of the volume and compressibility of $CaMgSi_2O_6–CaAl_2Si2O_8$ liquids to 25 GPa. *J. Geophys. Res.* **113**, B04203.

Bataleva Y. V., Palyanov Y. N., Sokol A. G., Borzdov Y. M. and Palyanova G. A. (2012) Conditions for the origin of oxidized carbonate-silicate melts: Implications for mantle metasomatism and diamond formation. *Lithos* **128**–**131**, 113–125.

Biellmann C., Gillet P., Guyot F., Peyronneau J. and Reynard B. (1993) Experimental evidence for carbonate stability in the Earth's lower mantle. *Earth Planet. Sci. Lett.* **118**, 31–41.

Cartigny P., Harris J. W. and Javoy M. (1998) Eclogitic diamond formation at Jwaneng: No room for a recycled component. *Science* **280**, 1421–1424.

Dasgupta R., Hirschmann M. M. and Withers A. C. (2004) Deep global cycling of carbon constrained by the solidus of anhydrous, carbonated eclogite under upper mantle conditions. *Earth Planet. Sci. Lett.* **227**, 73–85.

Dasgupta R. and Hirschmann M. M. (2006) Melting in the Earth's deep upper mantle caused by carbon dioxide. *Nature* **440**, 659–662.

Dasgupta R., Hirschmann M. M. and Stalker K. (2006) Immiscible transition from carbonate-rich to silicate-rich melts in the 3 GPa melting interval of eclogite + CO_2 and genesis of silica-undersaturated ocean island lavas. *J. Petrol.* **47**, 647–671.

Dasgupta R. and Hirschmann M. M. (2007) Effect of variable carbonate concentration on the solidus of mantle peridotite. *Am. Mineral.* **92**, 370–379.

Dasgupta R. and Hirschmann M. M. (2010) The deep carbon cycle and melting in Earth's interior. *Earth Planet. Sci. Lett.* **298**, 1–13.

Dobson D. P., Jones A. P., Rabe R., Sekine T., Kurita K., Taniguchi T., Kondo T., Kato T., Shimomura O. and Urakawa S. (1996) In-situ measurement of viscosity and density of carbonate melts at high pressure. *Earth Planet. Sci. Lett.* **143**, 207–215.

Dupuy C., Liotard J. M. and Dostal J. (1992) Zr/hf fractionation in intraplate basaltic rocks: Carbonate metasomatism in the mantle source. *Geochim. Cosmochim. Acta* **56**, 2417–2423.

Falloon T. J. and Green D. H. (1989) The solidus of carbonated, fertile peridotite. *Earth Planet. Sci. Lett.* **94**, 364–370.

Ghiorso M. S., Hirschmann M. M., Reiners P. W. and Kress V. C. (2002) The pMELTS: A revision of MELTS for improved calculation of phase relations and major element partitioning related to partial melting of the mantle to 3 GPa. *Geochemistry Geophys. Geosystems* **3**, 36.

Ghosh S., Ohtani E., Litasov K. D. and Terasaki H. (2009) Solidus of carbonated peridotite from 10 to 20 GPa and origin of magnesiocarbonatite melt in the Earth's deep mantle. *Chem. Geol.* **262**, 17–28.

Hammouda T. (2003) High-pressure melting of carbonated eclogite and experimental constraints on carbon recycling and storage in the mantle. *Earth Planet. Sci. Lett.* **214**, 357–368.

Harmer R. E., Lee C. A. and Eglington B. M. (1998) A deep mantle source for carbonatite magmatism: evidence from the nephelinites and carbonatites of the Buhera district, SE Zimbabwe. *Earth Planet. Sci. Lett.* **158**, 131–142.

Hurst H. J. (1991) The thermal decomposition of magnesite in nitrogen. *Thermochim. Acta* **189**, 91–96.

Hurt S. M. and Lange R. A. (2018) The density of Li_2CO_3-Na_2CO_3-K_2CO_3-Rb_2CO_3-Cs_2CO_3-$CaCO_3$-$SrCO_3$-$BaCO_3$ liquids: New measurements, ideal mixing, and systematic trends with cation coordination. *Geochim. Cosmochim. Acta* (**accepted)**

Ionov D. A., Dupuy C., O'Reilly S. Y., Kopylova M. G. and Genshaft Y. S. (1993) Carbonated peridotite xenoliths from Spitsbergen: implications for trace element signature of mantle carbonate metasomatism. *Earth Planet. Sci. Lett.* **119**, 283–297.

Janz G. J., Neuenschwander E. and Kelly F. J. (1963) High-temperature heat content and related properties for Li_2CO_3, Na_2CO_3, K_2CO_3, and the ternary eutectic mixture. *Trans. Faraday Soc.* **59**, 841.

Kiseeva E. S., Litasov K. D., Yaxley G. M., Ohtani E. and Kamenetsky V. S. (2013) Melting and phase relations of carbonated eclogite at 9-21gpa and the petrogenesis of alkali-rich melts in the deep mantle. *J. Petrol.* **54**, 1555–1583.

Kono Y., Kenney-Benson C., Hummer D., Ohfuji H., Park C., Shen G., Wang Y., Kavner A. and Manning C. E. (2014) Ultralow viscosity of carbonate melts at high pressures. *Nat. Commun.* **5**, 5091.

Kress V. C., Williams Q., Carmichael I. S. E. (1988) Ultrasonic investigation of melts in the system Na_2O-Al_2O_3-SiO_2. *Geochim. Cosmochim. Acta* **52**:283–293.

Lander J. J. (1951) Experimental Heat Contents of SrO, BaO, CaO, BaCO, and SrCO, at High Temperatures. Dissociation Pressures of BaCO, and SrCO,. *J. Am. Chem. Soc.* **73**, 5794–5797.

Litasov K. and Ohtani E. (2010) The solidus of carbonated eclogite in the system CaO-Al2O3-MgO-SiO2-Na2O-CO2 to 32GPa and carbonatite liquid in the deep mantle. *Earth Planet. Sci. Lett.* **295**, 115–126.

Litasov K. D., Fei Y., Ohtani E., Kuribayashi T. and Funakoshi K. (2008) Thermal equation of state of magnesite to 32 GPa and 2073 K. *Phys. Earth Planet. Inter.* **168**, 191–203.

Litasov K. D., Shatskiy A., Gavryushkin P. N., Sharygin I. S., Dorogokupets P. I., Dymshits A. M., Ohtani E., Higo Y. and Funakoshi K. (2013) P-V-T equation of state of siderite to 33GPa and 1673K. *Phys. Earth Planet. Inter.* **224**, 83–87.

Liu Q., Lange R. A. and Ai Y. (2007) Acoustic velocity measurements on Na2O-TiO2-SiO2 liquids: Evidence for a highly compressible TiO_2 component related to five-coordinated Ti. *Geochim. Cosmochim. Acta* **71**, 4314–4326.

O'Leary M. C., Lange R. A. and Ai Y. (2015) The compressibility of $CaCO_3$-Li_2CO_3-Na_2CO_3-K_2CO_3 liquids: Application to natrocarbonatite and CO_2-bearing nephelinite liquids from Oldoinyo Lengai. *Contrib. to Mineral. Petrol.* **170**, 1-18.

Pal'yanov Y. N., Sokol A. G., Borzdov Y. M., Khokhryakov A. F. and Sobolev N. V. (1999) Diamond formation from mantle carbonate fluids. *Nature* **400**, 417–418.

Roest, D.L., Ballone, P., Bedeaux, D. and Kjelstrup, S. (2017) Molecular dynamics simulations of metal / molten alkali carbonate interfaces. *J. Phys. Chem. C* **121**, 17827-17847.

Rolin M. and Recapet J. M. (1964) Contribution a l'étude des proprieties thermódynamiques des carbonates alcalins. III. Courbes d'enthalpeis en function de la temperature et chaleurs de fusion de Na_2CO_3, Li_2CO_3, K_2CO_3 et de leur mélange eutectique ternaire. *Bull Soc. Chim. Fr.* **10**, 2504–2510.

Santillán J. and Williams Q. (2004) A high pressure X-ray diffraction study of aragonite and the post-aragonite phase transition in $CaCO_3$. *Am Mineral.* **89**,1348–1352.

Stixrude L. and Bukowinski M. S. T. (1988) Simple covalent potential models of tetrahedral SiO2: Applications to α-quartz and coesite at pressure. *Phys. Chem. Miner.* **16**, 199–206.

Stixrude L. and Bukowinski M. S. T. (1990) Rings, topology, and the density of tectosilicates. *Am. Mineral.* **75**, 1159–1169.

Wallace M. E. and Green D. H. (1988) An experimental determination of primary carbonatite magma composition. *Nature* **335**, 343-346.

Wang M., Liu Q., Nie S., Li B., Wu Y., Gao J., Wei X. and Wu X. (2015) High-pressure phase transitions and compressibilities of aragonite-structure carbonates: $SrCO_3$ and $BaCO_3$. *Phys. Chem. Miner*. **42**, 517–527.

Zhang J. and Reeder R. J. (1999) Comparative compressibilities of calcite-structure carbonates: Deviations from empirical relations. *Am. Mineral*. **84**, 861–870.

Zhu H., Saito T., Sato Y., Yamamura T., Shimakage K. and Ejima T. (1991) Ultrasonic velocity and absorption coefficient in molten alkali metal nitrates and carbonates. *J. Jpn. Inst. Met.* **55**, 937–944.

Chapter 4 Thermodynamic properties of $CaCO_3$-$SrCO_3$-$BaCO_3$ liquids: a molecular dynamics study using new empirical atomic potentials for alkaline earth carbonates

4.1 Introduction

Carbonate melts play a major role in mantle petrologic processes. Carbonate enters the mantle mostly as $CaCO_3$ (calcite, aragonite or dolomite) through subduction of hydrothermally altered oceanic crust (e.g., Staudigel et al. 1989; Rea and Ruff 1996). Calcium from $CaCO_3$ partitions readily into the silicate phases of the mantle and is replaced by Mg, establishing $MgCO_3$ as a dominant carbonate component of the mantle (Biellmann et al. 1993). Thus, $CaCO_3$ and $MgCO_3$ are the carbonate components of primary concern to mantle petrology. Partial melting of carbonated mantle produces carbonate melts which are effective agents of mantle metasomatism (e.g., Green and Wallace 1988; Yaxley et al. 1991; Dupuy et al. 1992; Ionov et al. 1993; Sleep 2009) owing to their low viscosity (e.g., Dobson et al. 1996; Kono et al. 2014), high mobility (Hunter and McKenzie 1989; Kono et al. 2014), and high enrichment in incompatible elements (Blundy and Dalton, 2000). Additionally, carbonate can dramatically (<550 °C) lower the solidus of peridotite (e.g., Ghosh et al. 2009), potentially enabling widespread low-degree partial melting of upwelling mantle material.

Exploring the role of carbonate in the mantle poses a significant challenge due to the wide range of possible pressures, temperatures, and compositions. Phase equilibria experiments on carbonated peridotite and eclogite at mantle pressures and temperatures have been somewhat successful at constraining the solidus of carbonated mantle rocks; however, small variations in

starting composition have led to significant differences in the location of the solidus in P-T space (e.g., Dasgupta and Hirschmann 2010; Litasov et al. 2013)

Computational thermodynamic models such as MELTS (Ghiorso et al. 2002) offer a potential solution to these complexities, but they require standard state thermodynamic properties of the pure carbonate melt components. In the mantle, the alkaline earth carbonate components $CaCO_3$ and $MgCO_3$ are of particular interest. Many thermodynamic properties are known for the crystal phases (e.g., calcite and magnesite), including thermal expansion (e.g., Markgraf and Reeder 1985), bulk moduli, K'_T (e.g., Redfern and Angel 1999; Ross 1997; Fiquet et al. 2002), and heat capacities (e.g., Jacobs et al. 1981; Berman et al. 1985). However, knowledge of the standard state thermodynamic properties of the respective liquids is limited because alkaline earth carbonates universally decompose at temperatures lower than melting temperatures at 1 bar. For one of the most geologically relevant liquid components, $MgCO_3$, experimental data are especially rare because $MgCO_3$ decomposes at 1 bar at only 500° C (Hurst 1991). Hurt and Lange (2018) offer constraints on the density of $MgCO_3$ liquid at 1 bar by analysis of systematic variations of molar volume and composition in alkaline earth carbonate liquids. However, their estimate depend on the coordination of Mg^{2+} with oxygen and carbonate, which is currently unknown but may be estimated through molecular dynamics (MD) simulations along with the other endmember properties needed for thermodynamic modeling.

Liquid state properties of alkaline earth carbonates are not captured-well by existing atomic potential models. Numerous atomistic classical potential models have been proposed for $CaCO_3$ (e.g., Dove et al. 1992; Pavese et al. 1992; Fisler et al. 2000; Archer et al. 2003 and Vuilleumier et al. 2014). Some of these models (i.e. Dove et al. 1992 and Vuilleumier et al. 2014) have been successfully applied to simulate $CaCO_3$ liquids (e.g., Genge et al. 1995).

However, the classical mechanical models that have been proposed for the remaining alkaline earth carbonates ($MgCO_3$, $SrCO_3$, and/or $BaCO_3$)—Fisler et al, (2000), de Leeuw et al. (2002), Archer et al. (2003) and Raiteri (2015)—were all designed for simulations of crystal or aqueous phases at ambient conditions and are therefore impractical for use in simulating liquids.

We propose a new classical mechanical model for the simulation of alkaline earth carbonate liquids ($MgCO_3$, $CaCO_3$, $SrCO_3$, and $BaCO_3$) that can provide thermodynamic properties both at standard state and at mantle temperatures and pressures as well as liquid structure and mixing properties. This new model is constructed based upon Archer et al. (2003), by recalibrating the potentials to use a simpler rigid-ion formulation appropriate for efficiently simulating melts. We describe modifications to the Archer et al. (2003) model and the general form of the potentials followed by a description of the parameter fitting process. The model is applied to molecular dynamics (MD) simulations of $CaCO_3$-$SrCO_3$-$BaCO_3$ liquids at high temperature and pressure and the results are compared to those predicted by experiments and first principles MD simulations. The model parameters for $MgCO_3$ are also determined and reported, laying the groundwork for a detailed future study of the behavior of $MgCO_3$-bearing melts, which are complex, unique, and especially geologically relevant.

4.2 Training atomic potentials

4.2.1 General description of the model

The goal of this study is to develop a potential set suited to high pressure, high temperature simulations of alkaline earth carbonate liquids (particularly $MgCO_3$) and to verify the model's applicability to $MgCO_3$ liquid by testing it on known liquid properties within the $CaCO_3$-$SrCO_3$-$BaCO_3$ system. An atomistic model is developed for simulations of alkaline earth carbonates

($MgCO_3$, $CaCO_3$, $SrCO_3$, and $BaCO_3$) using rigid ions and partial charges. This model is based upon the model of Archer et al. (2003) for divalent carbonates.

For our rigid ion model, every atom interacts electrostatically with the other atoms through a Coulombic potential:

$$U_{coul} = \sum_{ij} \frac{q_i q_j}{r_{ij}} \qquad \text{Eq. 4.1}$$

where q_i and q_j are the charges on the i^{th} and j^{th} atom and r_{ij} is the distance between them expressed in atomic units. As compared with Archer et al., we reduce the charges on each ion to produce an accurate description of the training data in the absence of a core-shell interaction, as detailed below. Metal cations (Mg, Ca, Sr, and Ba) and oxygen anions interact with surrounding oxygen atoms through a Buckingham potential equation:

$$U_{ij}(r) = Ae^{\left(\frac{-r_{ij}}{\rho}\right)} - \frac{C}{r_{ij}^6} \qquad \text{Eq. 4.2}$$

U_{ij} is the interaction energy between atoms *i* and *j*, and *A*, ρ, and *C* are parameters characterizing the interaction.

Modeling of the carbonate molecules is handled using a combination of 2-body and 3-body potentials to maintain realistic behavior of the trigonal $(CO_3)^{2-}$ anion groups. First, a Morse potential, is used to describe intramolecular carbon-oxygen and oxygen-oxygen interactions (within a given CO_3 group):

$$U(r) = D\left\{\left[1 - e^{[-a(r-r0)]}\right]^2 - 1\right\} \quad \text{Eq. 4.3}$$

where *D*, *a*, and r_0 are parameters describing the depth, inverse-width, and position of the Morse potential well. Additionally, the trigonal planar shape of the CO_3 carbonate molecules is maintained by two harmonic-type potentials. The first is a three-body bond-angle constraint between the carbon atom and each pair of oxygen atoms within the carbonate molecule:

$$U(\theta) = \frac{1}{2} K_1(\theta - 120°)^2. \quad \text{Eq. 4.4}$$

where K_1 is the angular spring constant that maintains near-ideal O-C-O bond angles. An out-of-plane interaction between each carbon atom and the oxygen atoms within a carbonate molecule keeps the carbon atom in-plane with the oxygens and is given by the following equation:

$$U(\Phi) = K_2[1 - \cos(2\Phi)]. \quad \text{Eq. 4.5}$$

where K_2 describes the stiffness of this dihedral angle constraint. These two interactions were retained from the original presentation in Archer et al. (2003). For the three-body interaction, the value of K_1 was fitted, while the value of K_2 for the out-of-plane interaction was retained from Archer et al. (2003).

4.2.2 Fitting potential parameters

To empirically determine the best set of model parameter values, we use lattice dynamics to evaluate the predicted material properties. The optimization is performed using the lattice dynamics and potential fitting algorithm provided by the General Utility Lattice Program (GULP) (see Gale 1996, 1997; Gale and Rohl 2003). The best-fit set of model parameters maximizes the likelihood of the training data, given a reasonable choice of data weight coefficient. GULP minimizes the internal energy of the system to calculate the structure of the given ionic solid along with other physical properties (i.e. elastic constants and bulk moduli). The fitted parameter values are thus determined using weighted least squares regression on the experimentally observed crystal properties.

The fitting procedure is performed in steps, allowing sequential refinement of the parameters as the model is expanded. First only the properties of calcite and aragonite crystals at ambient conditions are fit, obtaining a reasonable rigid ion model for the Ca-endmember minerals. Then the training dataset is expanded to incorporate training mineral data from the full

$MgCO_3$-$CaCO_3$-$SrCO_3$-$BaCO_3$ compositional quaternary at ambient pressures. Figure 4.1a depicts the compositions of the crystal structures used as training data within the $MgCO_3$-$CaCO_3$-$SrCO_3$-$BaCO_3$ system. A preliminary model is obtained by only fitting cation-oxygen Buckingham interactions for Mg-O, Ca-O, Sr-O and Ba-O. The final fitting sequence introduces high-pressure crystal structures of magnesite, calcite, aragonite, strontianite and witherite up to 35 GPa. In this final fitting sequence the full set of parameters is fit simultaneously, to obtain our finished model. Table 4.1 provides the final fitted parameters of our model. The root mean square of the final residuals for the cell parameters only is 0.1358 Å; representing an average error of 1.6%. Figure 4.1b compares compression curves for calcite, aragonite, magnesite, strontianite and witherite up to 10 GPa, as derived from experiments to those calculated by our final model in GULP. The complete list of experimental observables used to fit the potential parameters, their corresponding values calculated by our final model (by both internal and free energy minimization) and the percent residual may be found in Appendix A (Table A.1).

Table 4.1 Fitted pair-potential parameters of our final model. Intermolecular potentials apply only between atoms in different carbonate groups while intramolecular potentials apply to atoms within the same carbonate group. All other potentials apply to the specified atomic interaction, regardless of location.

Functional form	Interaction	Coefficients			
Buckingham (Eq. 4.2)		A (eV)	ρ (Å)	C (eV Å^6)	
	Mg-O	434.025378	0.310286	0.002263	
	Ca-O	4633.366160	0.251064	0.486126	
	Sr-O	19719.288643	0.229122	0.000046	
	Ba-O	6224.146789	0.274170	0.192772	
	O-O	75675.616808	0.196193	0.000095	Intermolecular
Morse (Eq. 4.1)		D (eV)	A (Å^{-1})	r_0 (Å)	
	O-O	2.248065	4.550199	2.19	Intramolecular
	C-O	8.625068	1.166544	1.25	Intramolecular
Three-body (Eq. 4.3)		K_2 (eV/rad^2)	θ_0		
	O-C-O	10.483485	120°		Intramolecular

Torsional (Eq. 4.4)		K (eV)	θ_0	
	O-C-O-O	0.151	0°	Intramolecular
Charges				
	Cation	1.81896400		
	C	1.30022400		
	O	-1.03972933		

Figure 4.1 Mineral training dataset is shown in composition space and compared with performance of fitted atomistic model. Panel a shows a quaternary diagram of the $MgCO_3$-$CaCO_3$-$SrCO_3$-$BaCO_3$ system with points representing the locations of the crystal phases used as training data. **Panel b** compares the compression curves of end member phases as determined from experiments (circles and dotted lines) to curves derived from our model via lattice dynamics in GULP (squares with solid lines). More-detailed information on crystal simulation results may be found in Appendix Table A.1.

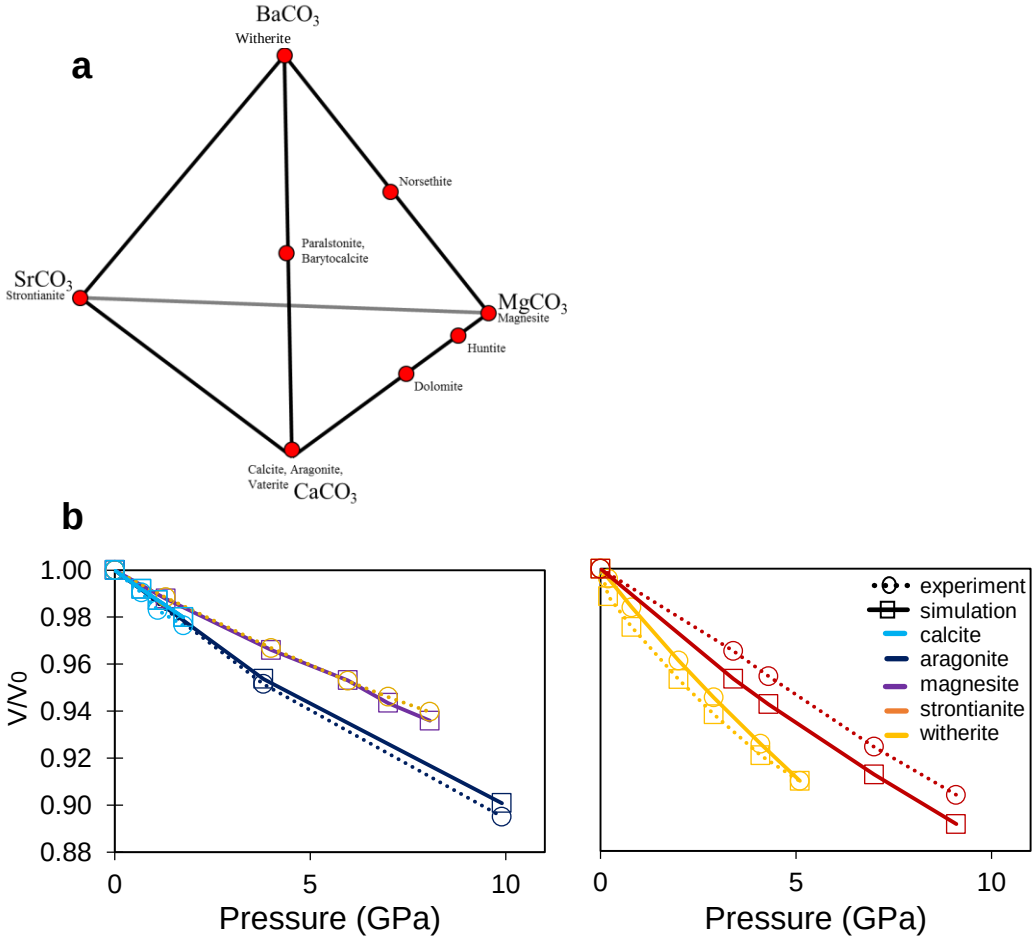

4.2.3 Finite-temperature free energy correction

For the purposes of efficiency and numerical stability the potential fitting algorithm described above minimizes only lattice energies, which effectively assumes a temperature of 0 K. GULP has the capability of fitting properties at finite temperatures by minimizing free energy (Gale, 1998) which would incorporate contributions from phonons including zero point energy and entropy. Unfortunately, potential parameter fitting by free energy optimization requires higher computational resources and is also plagued by numerical instabilities arising from soft phonon modes. This poses a problem because the experimental observables used for fitting were measured at 300 K but treated by the fitting algorithm as if they are 0 K properties.

To work around this problem, we introduce an iterative scaling approach to fit 300 K structures and properties: the fitted properties of each structure are calculated by both lattice energy minimization and free energy relaxation at 300 K in which the cell parameters and atomic positions are allowed to relax between optimization steps according to free energy minimization. The values of cell parameters calculated by lattice energy minimization are divided by the corresponding values calculated by free energy minimization in order to derive a thermal scaling factor. The observed properties are then multiplied by this scaling factor and used to refit the potential parameters by lattice energy minimization. This approach effectively estimates the values of the fitted room-temperature observables based upon 0 K calculations, in order to avoid a temperature-related systematic error.

4.2.4 Applicability of the model to liquids

The model proposed in this study is calibrated on crystal structures and properties at low temperatures. However it is applied to liquids at high temperatures. Despite these differences, this approach remains effective because the potential equations focus on modeling interactions

between atomic pairs (and triples), which depend only on the local structure of the material. Though the vibrational amplitudes and long-range structure can vary widely from solids to liquids, local structural elements are only modestly adjusted by melting. Thus, the liquid structural properties are generally well-represented by the variety of crystal structures present in the training dataset.

To build confidence in these potentials, we verify whether fitted potential interactions of the crystalline training data adequately represent the interatomic distances appropriate to liquids. Figure 4.2 compares the pair distribution functions (pdfs) of atomic pairs for fitted interactions (i.e. O-O, C-O, Mg-O, Ca-O, Sr-O, and Ba-O) of the liquid (as simulated by our model) with those of a sample of crystal structures from the training data. For O-O, C-O, Ca-O, Sr-O, and Ba-O, the interatomic spacing of the training data crystals overlap well with those of the liquids. For Mg-O, however, the overlap is notably less complete. To assess whether our Mg-O potential delivers accurate results at the interatomic spacing representative of simulated $MgCO_3$ liquid, we test our model on a structure that has a cation-oxygen separation distance similar to that predicted for the $MgCO_3$ liquid: magnesite at 82.6 GPa (Fiquet et al. 2002). Though our model is not trained on magnesite above 8.06 GPa, it predicts the crystal lattice dimensions to within the typical model accuracy of 1.6%, suggesting that our Mg-O potential equation is likewise accurate at the Mg-O separation distances predicted for the liquid.

Figure 4.2 Atomic pair distribution functions (PDFs) compare structures of crystals in the training dataset to simulated liquids. Interatomic distances typical of the simulated liquids (shown at 1100 K and 1 bar) are well sampled by the variety of crystals present in the training data. Fitted empirical potentials are thus sampled under geometric conditions similar to their training, consistent with accurate performance. The exception is Mg-O. However, our model accurately predicts the properties of crystalline magnesite at ~83 GPa (dashed line) which has a Mg-O bond length similar to that of the liquid. For the O-O, C-O and Ca-O pairs, the PDF curves shown belong to CaCO3 liquid at 1100 K and 1 bar. The Mg-O, Sr-O and Ba-O curves are derived from simulations of $MgCO_3$, $SrCO_3$ and $BaCO_3$ liquid respectively.

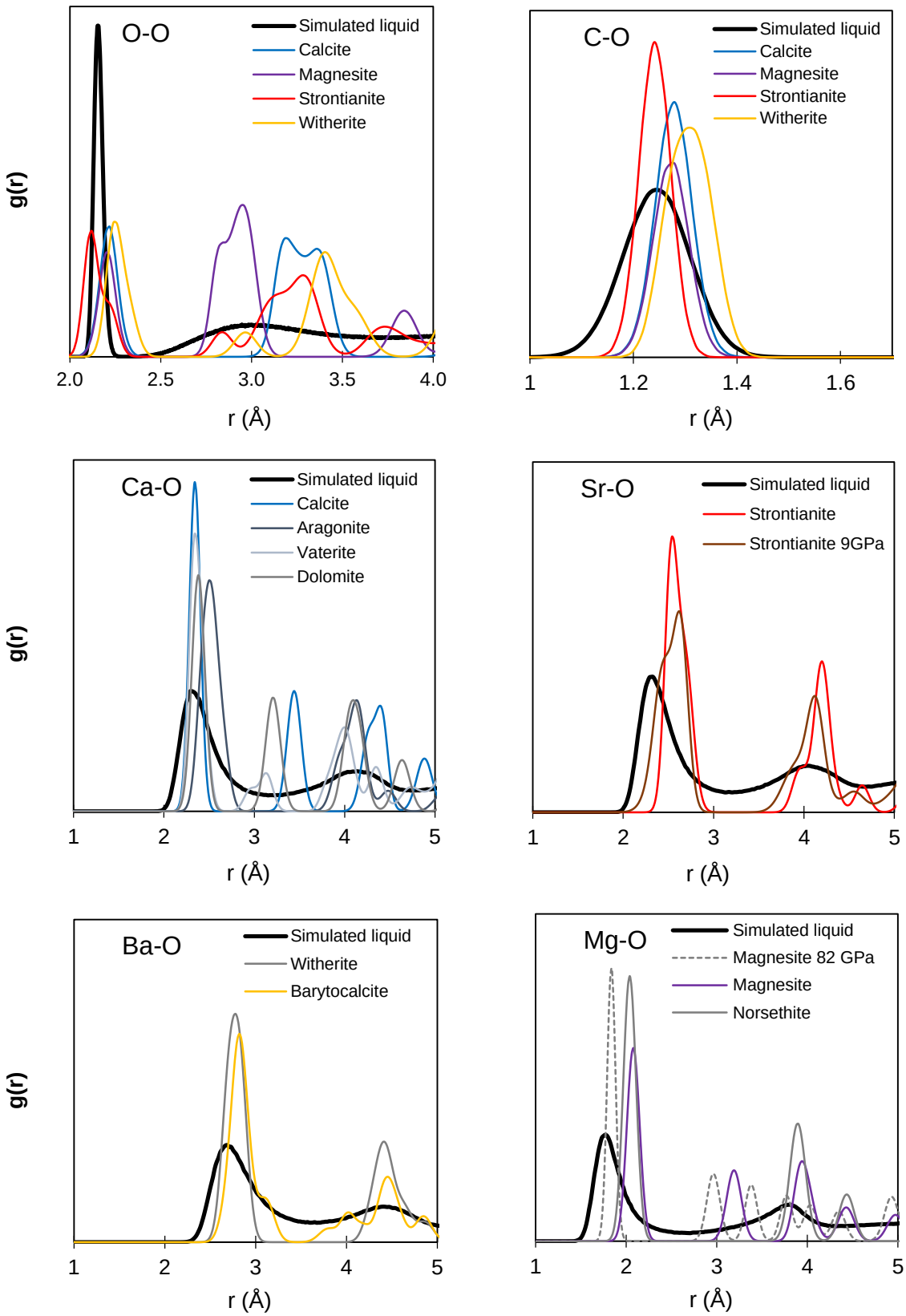
O-O
Simulated liquid
Calcite
Magnesite
Strontianite
Witherite
g(r)
2.0
2.5
3.0
3.5
4.0
r (Å)
C-O
Simulated liquid
Calcite
Magnesite
Strontianite
Witherite
1
1.2
1.4
1.6
r (Å)
Ca-O
Simulated liquid
Calcite
Aragonite
Vaterite
Dolomite
g(r)
1
2
3
4
5
r (Å)
Sr-O
Simulated liquid
Strontianite
Strontianite 9GPa
1
2
3
4
5
r (Å)
Ba-O
Simulated liquid
Witherite
Barytocalcite
g(r)
1
2
3
4
5
r (Å)
Mg-O
Simulated liquid
Magnesite 82 GPa
Magnesite
Norsethite
1
2
3
4
5
r (Å)

We also carry out a similar investigation of the high temperature accuracy of our model, since we did not directly train it on any high-temperature crystal properties. We test our model on various 1 bar, high-temperature crystal structures to demonstrate the model's applicability to high-temperature and high-pressure systems, recovering unit cell parameters with an average percent residual of 1.4%; details are available in the Appendix Table A.2. We conclude that our model is capable of accurately simulating phases outside its training data set at temperatures and pressures relevant to mantle conditions.

4.3 Simulating carbonate liquids

4.3.1 MD simulations

We use our newly fitted potential model to perform atomic molecular dynamics simulations over a wide range of temperatures and pressures using the Large-Scale Atomic/Molecular Massively Parallel Simulator (LAMMPS) (Plimpton 1995). These classical MD simulations use the potential equations to calculate interatomic forces, yielding atomic accelerations from basic Newtonian mechanics.

Interatomic force contributions become progressively weaker as interatomic separation distances increases. To lower computational expense, the approximation threshold for direct atomic interactions is fixed to a cutoff distance of $d_{cut} = 15$ *Å*, where interactions are extremely weak, and the sum of long-range forces is estimated by the Particle-Particle Particle-Mesh (PPPM) solver (Hockney and Eastwood, 1988).

4.3.2 Barostat and thermostat

To simulate various temperatures and pressures, two kinds of standard thermostats and barostats are utilized: the Berendsen (Berendsen et al. 1984) and the Nosé-Hoover (Nosé 1984; Hoover

1985) algorithms. The Berendsen method works by coupling the system to an external isothermal and isobaric bath with an adjustable coupling constant. Though it does not converge precisely to an exact canonical ensemble, it does produce reasonable approximate results and has the clear advantage of rapid equilibration. The Nosé-Hoover method functions by introducing additional dynamical variables in order to guarantee eventual convergence to an exact canonical ensemble, but suffers from long equilibration times and can include persistent unphysical energetic oscillations. We therefore adopt a hybrid approach, where initial rapid equilibration is handled by a Berendsen thermostat/barostat, followed by an accurate production run using the Nosé-Hoover thermostat/barostat for the desired NPT ensemble (with thermostat/barostat updates every 100/1000 timesteps, respectively).

4.3.2 Convergence of MD simulations

In order to maximize the accuracy of simulation results, we test for convergence in terms of both simulation size and duration. We simulate systems across a wide range of system sizes, including: 20, 160, 540, 810, 1280, 2500, 6860, 7290 and 20000 atoms. Simulations including 6860 atoms are found to show convergence of molar volumes to within 0.27 %, and are used for all of our production runs.

To achieve convergence in respect to duration, we run simulations until total energy variation falls below 1 KJ/mol (compared to a temperature-induced energy change of ~400 KJ/mol). We find that, using a timestep of 1 fs (10^{-12} s), an equilibration run (using the Berendsen thermostat and barostat as described above) of 60 ps (10^{-9} s) combined with a production run (using the Nosé-Hoover NPT ensemble as described above) of 60 ps is more than sufficient to achieve convergence of total energy to within acceptable bounds.

Reported simulation uncertainties are estimated by a combination of batch averaging (Grossfield and Zuckerman 2009) and reruns of simulations. Reruns revealed that batch averaging captures most, but not quite all of the simulation uncertainty. Thus, to estimate the total uncertainty for every simulation, we calculate the batch-averaging uncertainty and add an additional uncertainty correction term based on a limited set of repeated simulations, which span the full range of compositions, temperatures and pressures explored in this study.

4.3.3 Calculation of thermodynamic parameters from MD simulations

Volumetric Properties. For each pure endmember composition (i.e. $CaCO_3$, $SrCO_3$, and $BaCO_3$), temperatures in the range of 1100 to 2200 K and pressures between 0 and 30 GPa are simulated. In a few instances, some compositions are simulated at more extreme conditions (i.e. temperature >2200 K and pressures >30 GPa). The molar volumes of the pure endmember liquids predicted by these simulations are depicted in Figure 4.3a as a function of pressure. The molar volumes results are then used to estimate the thermodynamic properties $CaCO_3$, $SrCO_3$, and $BaCO_3$ liquid by fitting to a temperature-dependent 3rd order Birch-Murnaghan equation of state (EOS). For each component, the 1 bar isothermal bulk modulus (K_{T0}), its temperature dependence ($\frac{\delta K_{T0}}{\delta T}$) and pressure dependence (K'), 1 bar molar volume (V_0) and molar thermal expansivity ($\frac{\delta V_0}{\delta T}$) are fitted using least-squares multivariable regression. This model provides pressure (P) as a function of simulated volume (V_{sim}) and simulated temperature (T_{sim}):

$$P(V_{sim}, T_{sim}) = \frac{3K_T(T_{sim})}{2}\left[\left(\frac{V_0(T_{sim})}{V_{sim}}\right)^{\frac{7}{3}} + \left(\frac{V_0(T_{sim})}{V_{sim}}\right)^{\frac{5}{3}}\right]\left\{1 + \frac{3}{4}(K' - 4)\left[\left(\frac{V_0(T_{sim})}{V_{sim}}\right)^{\frac{2}{3}} - 1\right]\right\} \quad \text{Eq. 4.6}$$

where

$$V_0(T_{sim}) = V_0 + \frac{\delta V}{\delta T}(T_{sim} - 1100\ K) \quad \text{Eq. 4.7}$$

and

$$K_T(T_{sim}) = K_{T0} + \frac{\delta K_T}{\delta T}(T_{sim} - 1100\ K) \quad \text{Eq. 4.8}$$

This model recovers the simulated molar volumes within the 1100 – 2300 K temperature range with an average percent residual of only 0.24%, exceeding the training accuracy of the potentials. The compression curves predicted by the fit of the simulation results to a Birch-Murnaghan EOS are shown in Figure 4.3a along with the raw simulated molar volume data as a function of pressure.

Figure 4.3 Panel a. Simulated compression curves for pure alkaline earth carbonate liquids. 2000, 1500, and 1100 K isotherms are shown for each liquid (darker shades denote high temperatures); lines are the fitted equation of state curves using a temperature-dependent 3rd-order Birch Murnaghan EOS (see Eq.4.6 and Table 4.2). Colored points are simulation results. Grey circles represent simulations at temperatures other than the three isotherms, which were also used in fitting parameter values. Panel b. Data residuals for liquid EOS models. Deviation of modeled pressure values from simulation data show little structure as a function of either temperature or pressure for any of the endmember liquid components.

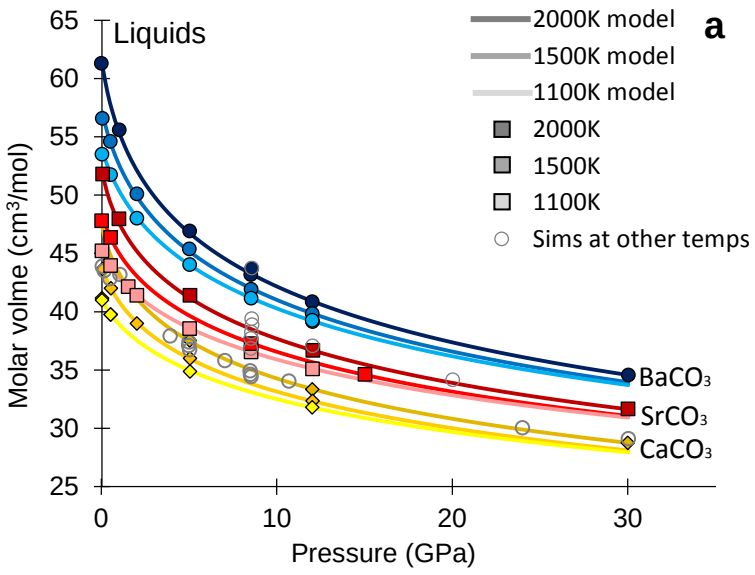

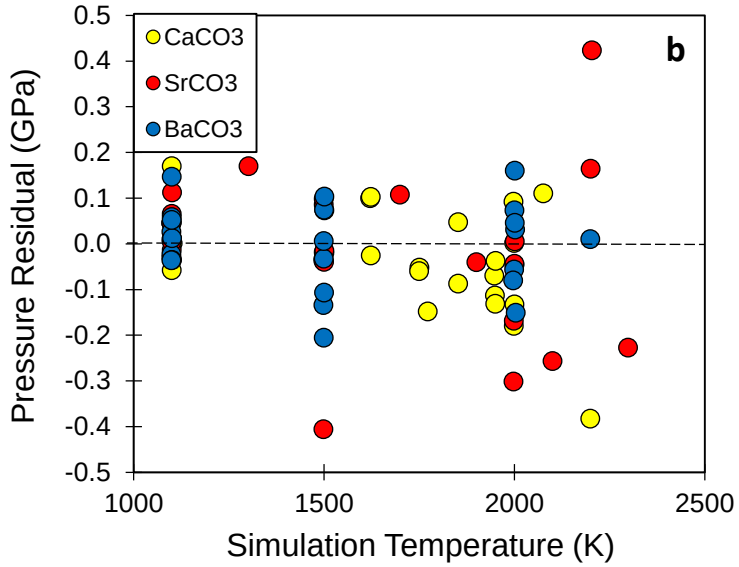

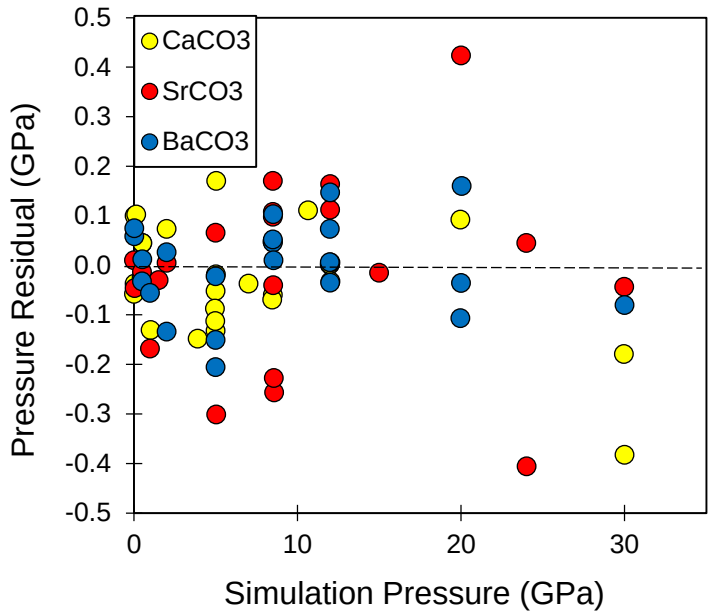

Higher temperature simulations (>2300 up to 3400 K) are also possible using this potential set, but they require the use of higher-order temperature dependent terms for the bulk modulus model given in Eq. 4.8. Since this potential set is designed for application to carbonate liquids in the upper-mantle and crust, we have elected to use the simpler temperature-dependent compression model by restricting to the 1100 – 2300 K temperature range.

Isobaric heat capacity and ΔHfusion. The isobaric heat capacity (C_P) for each composition is estimated from the best-fit linear temperature dependence of the molar enthalpy

(H) for 1 bar simulations over a range of temperatures. A linear model, where the slope represents the heat capacity, $C_P = \frac{\delta H}{\delta T}$, proved adequate to describe H over the entire temperature range (typically 1100 K to 2000 K). The near-constant C_P found in this study is corroborated by heat capacity experiments on alkali carbonate liquids (Janz et al. 1963).

Enthalpies of fusion (ΔH_{fusion}) are required in order to thermodynamically model melting reactions. ΔH_{fusion} may be calculated for $CaCO_3$, $SrCO_3$, and $BaCO_3$ by simulating a various crystal liquidus phases and their respective liquids at their 1 bar fusion temperature and taking the difference in enthalpy. Note that an accurate calculation of ΔH_{fusion} involves the simulation of high-temperature crystals and their phonon modes. Since this model is developed primarily for liquids, accurate calculation of phonon modes is not prioritized.

4.4 Results

4.4.1 MD simulation results

The pair-potential model described above is used to simulate 15 liquids in the $CaCO_3$-$SrCO_3$-$BaCO_3$ ternary at temperatures from 1100 – 3400 K and pressures from 0 to 43 GPa. The full simulation results are tabulated in the Appendix Table A.3.

4.4.2 The thermodynamic properties of alkaline earth liquids

The thermodynamic properties for the pure liquid components $CaCO_3$, $SrCO_3$, and $BaCO_3$ at 1100 K and 1 bar have been estimated by modeling the simulation data with Eq. 4.6. The thermodynamic property parameters (i.e. molar volume (V_{1100K}), thermal expansivity ($\delta V/\delta T$), compressibility ($\beta_{T,\ 1100K}$) and its linear temperature dependence ($\delta \beta T/\delta T$), and the pressure dependence of compressibility (K') of $CaCO_3$, $SrCO_3$ and $BaCO_3$ liquids) are determined by least-squares minimization using the temperature-dependent compressibility

model (see Eq.4.6). The fitted properties are provided in Table 4.2 alongside experimental constraints proposed by Hurt and Lange (2018) and Hurt et al. (2018). Note that, as explained above, only simulations with temperature ≤ 2300 K are included in the fitting of thermodynamic parameters.

Table 4.2 Fitted EOS models for each pure liquid endmember. The simulation data of the pure components at temperatures < 2300 K were used to fit the thermodynamic property parameters of a Birch-Murnaghan 3rd order EOS (see Eq. 4.6, 4.7 and 4.8). C_P was estimated by fitting a line to simulated enthalpy as a function of temperature for the pure components at ~1 bar; the slope of the line $\frac{\delta H}{\delta T}\Big|_P$ was taken as C_P. ΔH_{fusion} is the difference between the simulated enthalpy of the crystal and the liquid at the prospective melting temperature.

Property	$CaCO_3$		$SrCO_3$		$BaCO_3$	
	Sim.	*Exp.*	*Sim.*	*Exp.*	*Sim.*	*Exp.*
$V_{1100\ K}$ (cm^3/mol)	41.02(9)	40.18(16)	45.29(8)	44.33(22)	53.83(10)	50.99(19)
$\delta V/\delta T$ (cm^3/mol/K)·10^{-3}	6.60(27)	6.75(152)	7.17(36)	6.40(120)	8.34(69)	8.65(190)
$\beta_{T,1100\ K}$ (GPa^{-1})·10^{-2}	6.63(29)	5.97(50)	7.22(38)	4.33(31)	9.10(32)	5.43(51)
$\delta\beta_T/\delta T$ (GPa^{-1} K^{-1}) ·10^{-5}	7.17(28)	7.85(106)	7.70(54)	2.67(94)	7.73(52)	5.17(133)
K'	10.28(38)	-	11.66(69)	-	8.73(50)	-
C_P (J/mol/K)	164(3)	-	163(2)	-	155(2)	-
ΔH_{fusion} KJ/mol	aragonite→ liq.(1500 K) 44(1)	-	strontianite→ liq. (1773 K) 55(1)	-	witherite→ liq. (1823K) 54(1)	-
	calcite→ liq.(1500 K) 68(1)	-		-	R3m $BaCO_3$→ liq.(1700 K) 23(1)	-

Figure 4.3a depicts the raw simulated molar volumes as a function of pressure for each pure component ($CaCO_3$, $SrCO_3$, and $BaCO_3$) along with the 1100 K, 1500 K, and 2000 K isotherms calculated from the best-fit compression model (see parameter values in Table 4.2). As shown by the model residuals in Figure 4.3b, the fitted thermodynamic properties recover

well the simulated molar volumes across the applicable temperature and pressure range. Figure 4.3b demonstrates that there is no correlation or structure to the residuals as a function of either temperature or pressure, confirming that Eq.4.6 is an adequate model to describe the liquid simulation data.

Figure 4.4 shows the molar volumes of $CaCO_3$, $SrCO_3$, and $BaCO_3$ liquids predicted by applying our fitted thermodynamic properties to a 3rd order Birch-Murnaghan EOS at 1100 K from 0 to 15 GPa. These predictions are compared to estimates based on the liquid molar volume and compressibility experiments of Hurt and Lange (2018) and Hurt et al. (2018) respectively. The experimental fields show the 1σ range of molar volumes predicted for these liquids at 1100 K by applying the experimentally-estimated thermodynamic properties to a 3rd order Birch-Murnaghan EOS. The uncertainties are estimated via a standard Monte Carlo approach. For each pure liquid component, 10^3 random volumes are chosen within a pertinent range. Those volumes are combined with random draws of the experimentally determined thermodynamic properties (i.e. V_{1100K} and $K_{T,\,1100K}$) from a normal distribution constructed from their experimental 1σ uncertainties. Parameter values are assumed uncorrelated. Though K' has not yet been directly experimentally determined for any of the alkaline-earth carbonate liquids, we estimate a reasonable range of values based on previous experimental and simulations studies. Vuilleumier et al. (2015) and Zhang and Liu (2014) predicted a K' value of 8.2 and 7.0 respectively for $CaCO_3$ liquid. Fusion curve analysis studies of K_2CO_3 predicted a K' of K_2CO_3 liquid of 13.7 (Liu et al. 2007) and 14.4 ± 1.1 (Wang et al. 2016). Our own study predicts K' values between 8.73 and 11.66. Based on all these estimates, we adopt a broad range for K' represented by a uniform distribution between 7 and 12.

Figure 4.4 Simulated compression curves for each carbonate melt component agree well with experimental predictions. Colored circles are volumes of individual simulations and black lines are values

predicted by the fitted EOS model. The colored fields show the predicted molar volumes and their range of uncertainty based on experimental constraints provided in Hurt and Lange (2018) and Hurt et al. (2018).

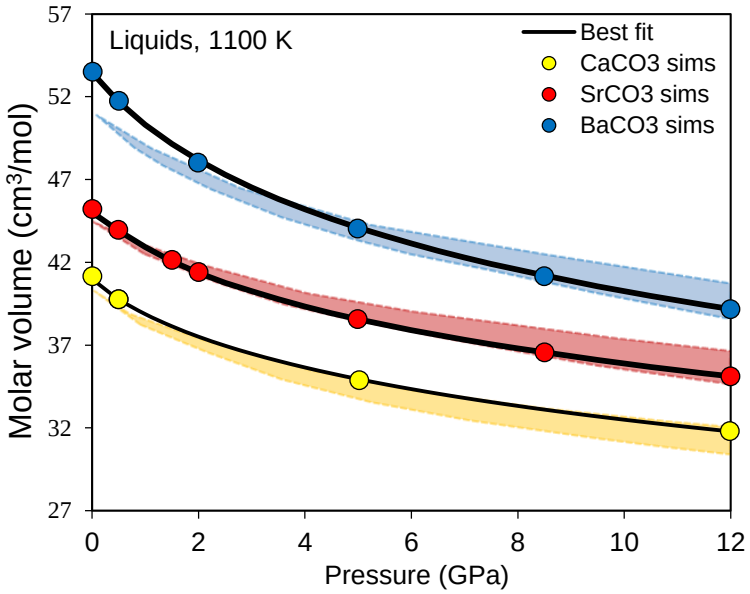

The reference temperature of 1100 K is chosen for this study because it is the temperature at which experiments on alkaline earth carbonate-bearing liquids are best constrained. Note these experimental estimates are based on partial molar quantities of mixed alkali-alkaline earth carbonate liquids and are predicated on the assumption that $CaCO_3$, $SrCO_3$ and $BaCO_3$ mix ideally with alkali carbonate liquids over their entire compositional range. Also note that 1100 K is actually below the true fusion temperature of the pure compounds and thus the low-temperature simulations actually represent metastable liquids, but it nevertheless represents a useful metastable reference state, since it is most directly probed by the experiments, which are stable at such temperatures because of significant freezing-point depression at their near-eutectic composition.

4.5 Discussion

4.5.1 Analysis of model accuracy for alkaline earth carbonate liquids

$CaCO_3$ liquid. At 1100 K and pressures >1 GPa our simulated molar volumes of $CaCO_3$ liquid agree (within uncertainty) to experimental estimates from Hurt and Lang (2018) and Hurt et al. (2018). At 1 bar, where the experimental uncertainties are smallest, our model predicts a molar volume 2.1% larger than the experimental value and continues to make predictions near the upper bound of experimental uncertainty. At 12 GPa, our predicted volume of $CaCO_3$ liquid converges to that of aragonite. Estimates of $CaCO_3$ liquid thermal expansivity ($\delta V/\delta T$), and $\delta\beta_T/\delta T$ agree well with experimental determinations (to within 8.7%). Our simulations suggest a larger compressibility than experiments, 6.63(29) versus $5.97(50)\cdot10^{-2}$ GPa^{-1}, which is probably a reflection of its inflation of 1 bar volumes.

$SrCO_3$ and $BaCO_3$ liquid. Our simulations of $SrCO_3$ and $BaCO_3$ liquid volume at 1100 K generally fall within experimental uncertainty. However, like $CaCO_3$, 1 bar molar volume estimates start larger than what is suggested by experiments (2.2 % larger for $SrCO_3$ and 5.6% for $BaCO_3$). At high-pressure (> 1 GPa for SrCO3 and >2 GPa for $BaCO_3$) our compression curve enters the experimentally-constrained field and trends towards the lower bound of experimental uncertainty. The $SrCO_3$ and $BaCO_3$ simulations generally make volume predictions that agree well with experimental estimates (at least at pressures > 1GPa), however, since the simulated volumes trend from the upper to lower bound of experimental uncertainty going from 0-15 GPa, the estimated compressibility is far greater than what is predicted by experiments. For $SrCO_3$ the compressibility is $7.22(38)\cdot10^{-2}$ GPa^{-1} from simulations versus $4.33(31)\cdot10^{-2}$ GPa^{-1} from experiments and $9.10(32)\cdot10^{-2}$ GPa^{-1} from simulations versus $5.43(51)\cdot10^{-2}$ GPa^{-1} from experiments for $BaCO_3$. Like $CaCO_3$ our estimate of thermal expansivity ($\delta V/\delta T$) agrees with experimental estimates to within its experimental uncertainty for both components.

The volumes predicted by our model appear to be accurate at high pressure but the 1 bar volumes are over-estimated. The elevated compressibility of these two components is due to the inaccurately high 1 bar volumes. Still, using the derived thermodynamic properties together in a 3rd-order Birch-Murnaghan EOS returns reasonably accurate volumes at pressure, particularly at pressures >1 GPa.

4.5.2 $CaCO_3$ liquid: comparison to first-principles MD

Liquid structure and Pair distribution functions. Vuilleumier et al. (2014) studied the properties of $CaCO_3$ melt using first principles MD simulations (FPMD). We compare the pair distribution function (PDF) curves predicted by our model to the first-principles derived curves of Vuilleumier et al. (Figure 4.5). For nearly all atomic pairs, these curves are in remarkable near-complete agreement with each other, despite their complete independence. The only notable exception to this match is for the nearest-neighbor O-O pair (representing intramolecular oxygen atoms). Our model predicts a much narrower peak than Vuilleumier et al., implying a stiffer O-O interaction within the carbonate groups. The O-O PDF curves predicted by Vuilleumier are probably more realistic, since they are also in better agreement with O-O pdf curves for carbonate crystals (see O-O panel of Figure 4.2), where our model also under-predicts peak width. An added consequence of these narrow O-O peaks is that our model predicts distinct separation of first and second nearest-neighbors among O-O pairs. This is in contrast to the results of Vuilleumier et al. (2014), where the first minimum in the PDF has a small but nonzero value, implying that different carbonate groups in Vuilleumier's melt can come closer to each other (to within the O-O nearest neighbor distances of ~2.6 Å) than our simulated melt. This may suggest a greater repulsion among carbonate groups in our simulated melt compared to Vuilleumier's model. Despite issues with the O-O interaction, our model successfully predicts all

other aspects of liquid structure and recovers the properties of both carbonate crystals and liquids.

Figure 4.5 PDF curves for liquid $CaCO_3$. Predicted liquid structure from this study (solid lines) is compared to those calculated by First Principles MD (dashed lines, Vuilleumier et al., 2014) at three different temperature-density states. The two models show remarkably strong agreement everywhere, except for the nearest neighboring oxygens peak, where our empirical MD simulations predict narrower peaks, corresponding to an overly stiff O-O bond.

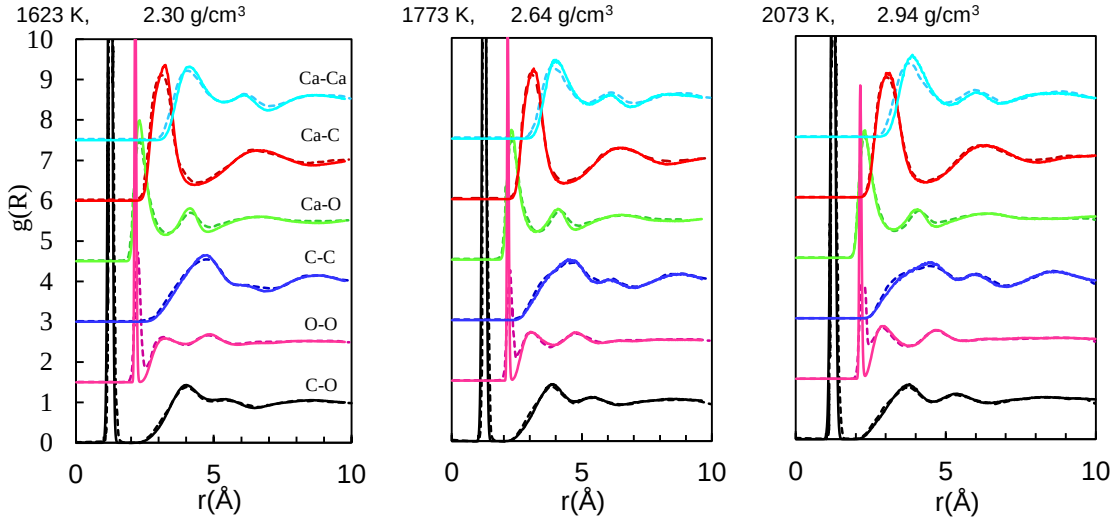

Liquid molar volume as a function of pressure. Vuilleumier et al. (2014) used the PDF curves generated by their FPMD simulations to fit a simplified empirical pair-potential. The resultant model was used in classical MD simulations to estimate the thermodynamic properties of $CaCO_3$ liquid. Zhang and Liu (2015) also produced a FPMD study of $CaCO_3$ liquid and developed an equation of state. The FPMD results from both Vuilleumier et al. (2014) and Zhang and Liu (2015) are compared to results from this study along with experimental constraints from Hurt and Lange (2018) and Hurt et al. (2018) in Table 4.3.

Table 4.3 The thermodynamic properties of $CaCO_3$ liquid at 1100 K and 1 bar derived from our simulations compared to properties proposed by two FPMD studies and experimental estimates.

Property	This study	Vuilleumier et al. (2014)	Zhang and Liu (2015)	Experimental ± 1σ
	MD	FPMD	FPMD	

$V_{1100\ K}$ (cm^3/mol)	41.02(9)	40.8	42.8	40.21(15)[a]
$\delta V/\delta T$ (cm^3/mol/K)·10^{-3}	6.60(27)	7.67	5.84	6.90(145)[a]
$\beta_{T,1100\ K}$ (GPa^{-1})·10^{-2}	6.63(29)	6.83	6.98	5.96(50)[b]
$\delta\beta_T/\delta T$ (GPa^{-1} K^{-1}) ·10^{-5}	7.17(30)	5.12	3.81	7.85(106)[b]
K'	10.28(38)	8.2	6.982	-
C_P (J/mol/K)	164(3)	145	144	-
ΔH_{fusion} (aragonite → liquid)	44(1) (1500 K)	-	67.48 (1500 K)	-

[a]Hurt and Lange 2018
[b]Hurt et al. 2018

Three compression curves are shown in Figure 4.6a representing $CaCO_3$ liquid at 1100 K from 0-15 GPa. The volumetric compression curves at 1100 K are shown for this study (black), Zhang and Liu (blue), and Vuilleumier (green). Also shown is the 1σ experimental field (derived from Monte Carlo sampling as described above). Over most of the pressure range, our model predicts volumes bracketed by the two FPMD studies. At 1 bar, our model agrees with predictions based on Vuilleumier, but converges with Zhang and Liu at high pressure. As shown in Fig 4.6a, at pressures >7 GPa, the EOS from Vuilleumier predicts molar volumes for $CaCO_3$ liquid that are lower than aragonite, while our model and the one proposed by Zhang and Liu converge to the crystalline volumes. Additionally, FPMD results of $CaCO_3$ liquid at 2000 K from Li et al. (2017) are also shown on Figure 4.3b and are generally ~5% greater than the upper 1σ limit on the experimental field. In general, our model returns molar volumes that are in good agreement with predictions made by experiments and/or FPMD.

Figure 4.6 Comparison of compression properties of $CaCO_3$ liquid across simulation studies. Panel a shows predicted compression curves of $CaCO_3$ liquid at 1100 K. Comparison of our model (black line) and two FPMD studies: Zhang and Liu (2015) (blue line) and Vuilleumier et al. (2015) (green line). The

colored field shows compression behavior determined from experimental constraints and its uncertainty. The red dashed line shows the molar volume of aragonite based on Ono et al. (2005). **Panel b** shows high-temperature compression of $CaCO_3$ liquid. Compression curves from our best-fit liquid EOS model are shown along the 1750 K and 1950 K isotherms (red lines). The same isotherms are shown from an early empirical MD study (Genge et al., 1995) and a 2000 K FPMD simulation from Li et al. (2017). For comparison, the colored field shows the feasible region determined from experiments at 1850 K.

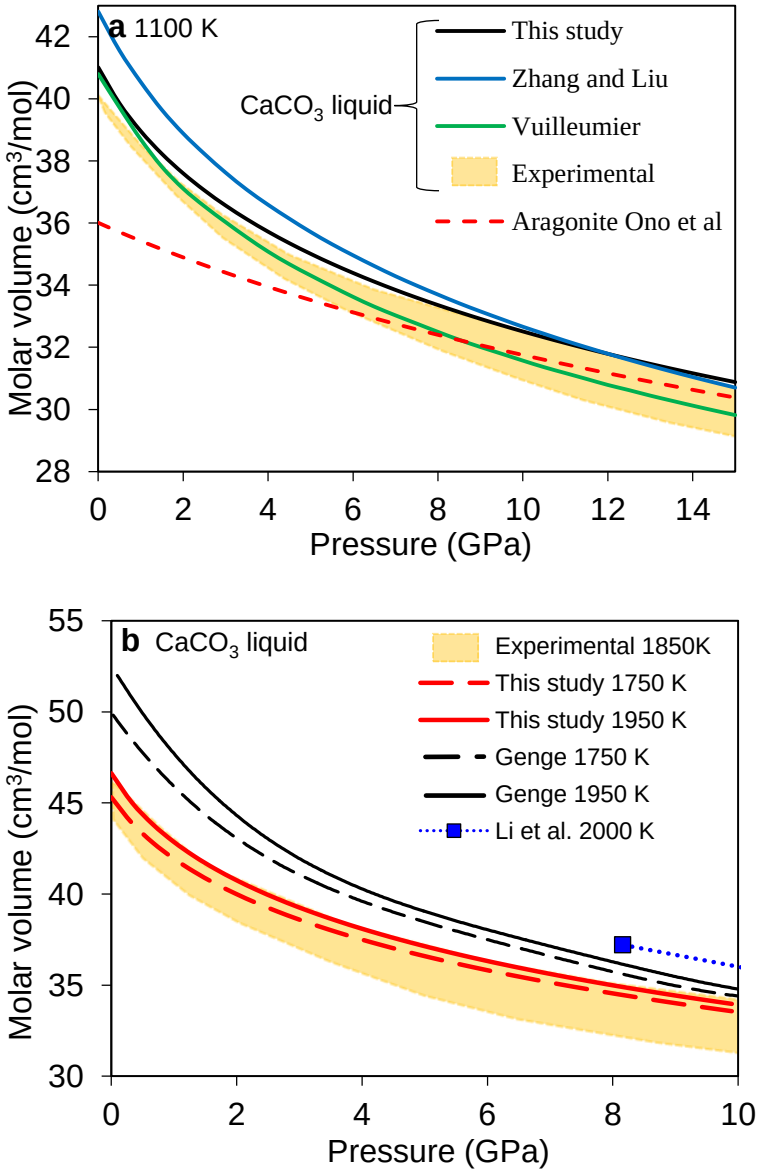

Thermodynamic properties. The compressibility predicted by our model is comparable to first-principle-derived estimates. However, our model predicts values for thermal expansivity ($\delta V/\delta T$) and ($\delta \beta_T/\delta T$) that are in better agreement with experimental constraints than both the Zhang and Liu (2015) and Vuilleumier et al. (2014) models. Our estimate of $CaCO_3$ liquid

isobaric heat capacity is 164(3) J/K/mol, which is higher than the estimates from Vuilleumier et al. (2014) and Zhang and Liu (2015) of 145 and 144 J/K/mol respectively. K' is also estimated to be higher (10.28) than what either the Vuilleumier (8.2) or Zhang and Liu (6.982) suggest. For properties that are experimentally constrained (i.e. V_{1100K}, $(\delta V/\delta T)$, β_T and $\delta\beta_T/\delta T$) our proposed thermodynamic properties are either comparable to estimates from first-principle calculations or in agreement with experiments.

4.5.3 Comparison to an empirical pair-potential MD study

Raiteri et al. (2015) developed a potential set for the simulation of alkaline-earth carbonates ($MgCO_3$, $CaCO_3$, $SrCO_3$ and $BaCO_3$) in aqueous environments. Their model does an excellent job recovering crystal structures at ambient conditions. However, we applied the Raiteri et al. model to the crystals at high pressures (up to 83 GPa) and found significant deviations from experimental results especially among the unit cell parameters of aragonite-group structures and magnesite. Application of the Raiteri et al. model to $CaCO_3$ melt at 2000 K up to 10 GPa suggests that it's is not a good fit for carbonate melt simulations; the 1 bar liquid volume is too low by ~15% and thermal expansion and compressibility are both too low by a factor of ~3 compared to experimental projections.

Genge et al. (1995) used a modified version of the Dove et al. (1992) classical potential model to study $CaCO_3$ melt via molecular dynamics. To directly compare our models, we plotted $CaCO_3$ liquid molar volume as predicted by our proposed EOS along the 1750 K and 1950 K isotherms from 0 to 10 GPa (Figure 4.6b). These are compared to $CaCO_3$ molar volume curves and simulation volumes reported in Genge et al. (1995). Also plotted is the 1σ field of $CaCO_3$ liquid molar volume at 1850 K predicted by Hurt and Lange (2018) and Hurt et al. (2018). At pressures <5 GPa, the Genge et al. (1995) study significantly overestimates the molar volume of

$CaCO_3$ liquid in respect to experimental estimates. In contrast, our model predicts volumes in agreement with experimental constraints (within the bounds of uncertainty) over the entire pressure and temperature range.

4.5.4 Liquid structure and structural evolution with T and P

The structures of $CaCO_3$, $SrCO_3$, and $BaCO_3$ liquid predicted by this model are all similar, differing only in terms of average atomic separation distances; the coordination numbers of atomic pairs (which is the average number of atoms of type *i* that immediately surround atoms of type *j*) are fairly consistent among $CaCO_3$, $SrCO_3$, and $BaCO_3$ liquids. Coordination numbers for atomic pairs were derived from pdf curves, *g(r),* for each simulated liquid. The equation for determining average coordination number of atomic pair *i* and *j* (CN_{ij}) is given by:

$$CN_{ij} = 4\pi \int_0^{r_1} r^2 g(r) \rho \, dr \quad \text{Eq. 4.9}$$

where *r* is the atomic separation distance in Å; r_1 is the maximum cutoff radius located at the first minimum in the PDF, representing the edge upper edge of the first nearest-neighbor peak; ρ is the average atomic number density of atom *j* with units of $\frac{atoms}{Å^3}$.

At 1100 K and 1 bar, the coordination numbers of O-O and C-O pairs are 2.0 and 3.0 respectively, as expected, and do not change over the entire studied PT range. The C-C coordination is approximately closest-packing (10.9). The cation-O coordination increases systematically with atomic period from 6.9 for Ca-O to 7.3 for Sr-O and 7.7 for Ba-O. The cation-C coordination (which may be thought of as cation coordination with the carbonate molecule) is the same for each component and is approximately octahedral (5.9). These coordination numbers are in excellent agreement with Vuilleumier et al. (2014) and are similar to that of *Fm3m* $BaCO_3$, the high-temperature, 1 bar polymorph of witherite (Strømme 1975).

Increased pressure and temperature both clearly affect liquid structure. With increasing temperature (2000 K) and ambient pressure, these coordination numbers remain relatively unchanged with the exception of the C-C pair. At this higher temperature, the first and second coordination shells of the C-C pairs merge and the coordination number increases to 16. As expected, pressure has a more dramatic effect on liquid structure. At 12 GPa and 1100 K, the C-C coordination decreases slightly to 10.5 while the cation-O coordination increases to 7.7, 8.9 and 9.8 for Ca-O, Sr-O and Ba-O respectively. The cation-C coordination also increases from 5.9 to 6.9.

In terms of atomic separation distances, compressing the liquid from ambient pressure to 30 GPa decreases the average cation-O nearest-neighbor distance by only ~5% while the average distance between carbonate groups decreases by ~8%. The most dramatic change to atomic spacing brought on by increasing pressure occurs between the cation and carbonate molecule; average spacing between the cation and C decreases ~11% at 30 GPa. Atomic spacing within CO_3 molecules changes very little (~0.1%) with pressure, temperature and composition. This corroborates the conclusion of Hurt and Lange (2018) that the partial molar volume of $(CO_3)^{2-}$ is constant within $CaCO_3$-$SrCO_3$-$BaCO_3$ liquids. Cation-O distances (a proxy for cation size) and carbonate ion size vary only modestly. The simulations indicate that changes in liquid volume are primarily achieved by more/less efficient packing of metal cations and carbonate groups.

4.5.5 Mixing behavior

We used our model to simulate various compositional mixtures within the $CaCO_3$-$SrCO_3$, $CaCO_3$-$BaCO_3$ and $SrCO_3$-$BaCO_3$ binaries at 1100 K and 1 bar, 1500 K and 1 bar, and 1100 K and 12 GPa to assess whether molar volumes and enthalpies mix linearly over these pressure and temperature ranges. Figure 4.7a shows the percent volume of mixing of the various mixtures

along the compositional binaries at various PT conditions as a function of mole fraction. Error bars represent the 1σ uncertainty on the simulated molar volume. In all cases, the V_{mix} is less than ±0.5% and averages ±0.23%, which is fully consistent with the average simulation uncertainty on volumes of ±0.21% . Thus, at these PT conditions, the model predicts ideal mixing (i.e. *Vmix* ≈ *0*) which is consistent with experimental observations (Hurt and Lange 2018). Simulations of the 50-50 mol% binary liquids at 12 GPa imply that $CaCO_3$, $SrCO_3$ and $BaCO_3$ mix ideally at high pressure and thus $\delta V/\delta P$ mixes ideally according to mol fraction and β_T mixes ideally according to volume fraction.

Figure 4.7 Ideal mixing of volumes and enthalpy is demonstrated for binary mixtures in liquid $SrCO_3$-$CaCO_3$-$BaCO_3$ system. In panel a, the volume of mixing (V_{mix}) of simulated binary liquids at 1100 and 2000 K and pressures of 0 and 12 GPa are plotted as a function of mol% B (fraction of the lighter component). The volume of mixing never exceeds the 1σ simulation uncertainty on molar volume. In panel **b**, enthalpy of mixing (H_{mix}) is shown for the same simulated liquids and in almost every instance is within the 2σ uncertainty of 0 with only 1 in 20 simulations falling more than 2σ away from zero, consistent with statistical expectation.

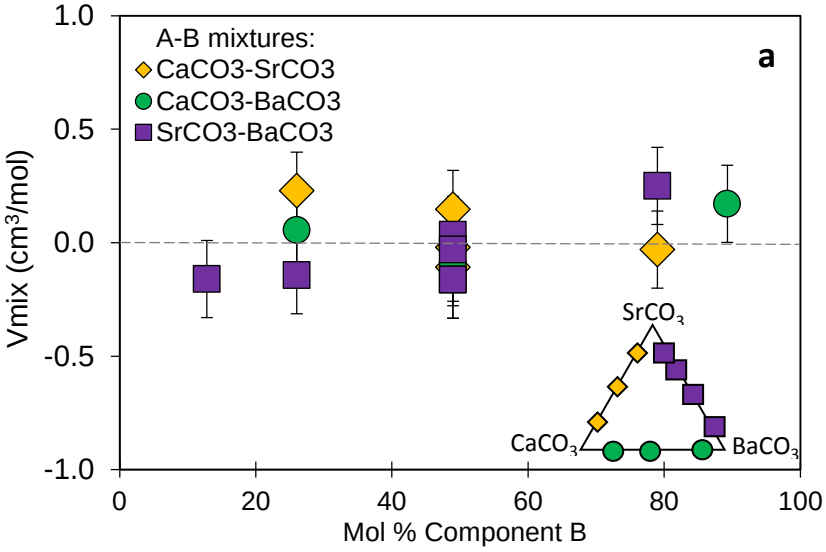

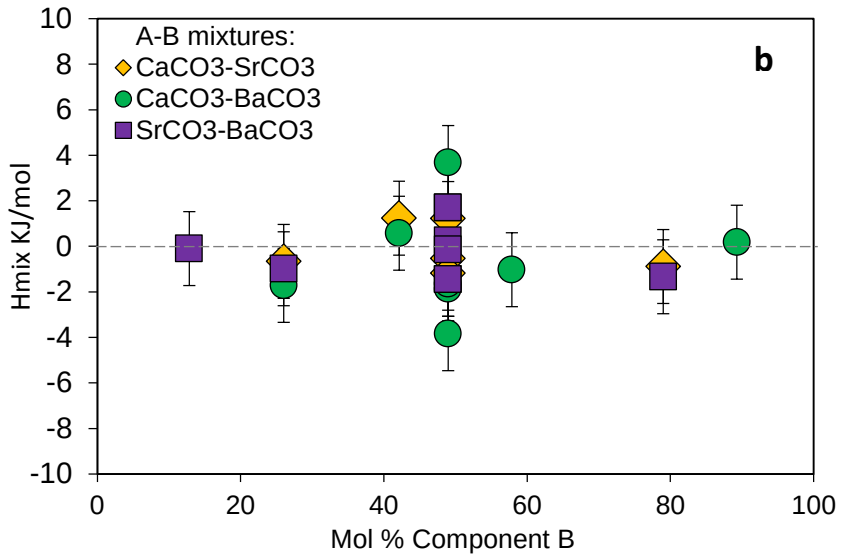

In regards to enthalpy, the simulations along the binary systems from 1100 – 2000 K and 0 – 12 GPa exhibit ideal mixing (i.e. $\Delta H_{mix} \approx 0$) to within 0.1% in respect to mole fraction (Figure 4.7b). The average value of ΔH_{mix} is ±1.2 KJ/mol, which agrees with the average 1σ simulation uncertainty for binary mixtures of ±1.5 KJ/mol, thus demonstrating that the variance in ΔH_{mix} is explained by uncertainty. Since enthalpy mixes ideally across a temperature range (i.e. 1100-2000 K in this case), its temperature derivative (isobaric heat capacity), must also mix ideally according to mole fraction. This, indeed, is corroborated by simulations of binary mixtures over a temperature range which demonstrates ideal mixing of heat capacity according to mole fraction.

4.6 Implications

Thermodynamic modeling the partial melting of carbonate-bearing mantle requires the pure, standard state thermodynamic properties and mixing properties of the alkaline earth carbonate liquid components. These liquid components are nearly impossible to study experimentally owing to their instability at 1 bar. MD simulations can supply constraints on the

properties of these components. We have developed a pair potential model for the simulation of alkaline earth carbonate liquids ($MgCO_3$, $CaCO_3$, $SrCO_3$, and $BaCO_3$), enabling us to predict their structure and thermodynamic properties over a range of mantle-relevant conditions. Our model is capable of accurately reproducing the experimentally-determined density and compressibility of liquids in the $CaCO_3$-$SrCO_3$-$BaCO_3$ system, thus lending confidence to its predictions of properties for which there are no direct experimental constraints (i.e. C_P, ΔH_{fusion} and K' of $CaCO_3$, $SrCO_3$, and $BaCO_3$ liquid), and paving the way for future work on $MgCO_3$ liquid. The proposed thermodynamic properties for $CaCO_3$, $SrCO_3$ and $BaCO_3$ liquids also lays the necessary groundwork for improved thermodynamic modeling of melting reactions for multi-component carbonated mantle.

Thermodynamic models such as MELTS rely not only on knowledge of standard state properties of pure components but also mixing behaviors. Our simulations predict linear additivity of molar volume, heat capacity and compressibility for $CaCO_3$-$SrCO_3$-$BaCO_3$ liquids across a broad range of compositions and P-T conditions that are experimentally inaccessible. Apart from thermodynamic modeling, mixing behavior results are essential for correct interpretation of density and compressibility experiments; because pure alkaline earth carbonate liquids are unstable at 1 bar, experimental constraints are necessarily derived from measurements on mixtures of alkaline-earth carbonates and alkali carbonates (e.g., Liu and Lange 2003; O'Leary et al. 2015; Hurt et al. 2018; Hurt and Lange 2018). This experimental approach requires the assumption that molar volume and compressibility mix ideally across the entire compositional spectrum which is not fully verifiable with experimental data alone. Our simulations provide theoretical support to this assumption, suggesting that a host of liquid

properties in the $CaCO_3$-$SrCO_3$-$BaCO_3$ system mix ideally across a broad compositional and P-T range.

Correct interpretation of experimental density and compressibility results for alkaline earth carbonate liquids also relies on knowledge of liquid structure. Our MD simulations have revealed the commonality of $CaCO_3$-$SrCO_3$-$BaCO_3$ liquid structures, namely an octahedral coordination of metal cations with carbonate molecules and an approximately cubic coordination of the metal cation with oxygen atoms at 1 bar. Knowledge of these coordination numbers is crucial for assessing systematic variation among alkaline earth carbonate properties because many properties vary as a function of metal cation radius (Wang et al. 2015; O'Leary et al. 2015; Hurt et al. 2018; Hurt and Lange 2018) which, in turn, varies as a function of its coordination environment. Some estimates of $MgCO_3$ liquid properties also depend on metal cation coordination (Hurt et al. 2018 and Hurt and Lange 2018). Hurt et al. (2018) and Hurt and Lange (2018), also conjectured that the partial molar compressibility and volume of the carbonate ion in melt depends on the coordination of carbonate with metal cations. Our simulations of $CaCO_3$-$SrCO_3$-$BaCO_3$ liquid allow the relationship between partial molar properties of the carbonate ion and coordination environment to be assessed.

4.7 References

Arapan S. and Ahuja R. (2010) High-pressure phase transformations in carbonates. *Phys. Rev. B* **82**, 184115.

Archer T. D., Birse S. E. A., Dove M. T., Redfern S. A. T., Gale J. D. and Cygan R. T. (2003) An interatomic potential model for carbonates allowing for polarization effects. *Phys. Chem. Miner.* **30**, 416–424.

Berendsen H. J. C., Postma J. P. M., van Gunsteren W. F., DiNola a and Haak J. R. (1984) Molecular dynamics with coupling to an external bath. *J. Chem. Phys.* **81**, 3684–3690.

Berman R. G. (1988) Internally consistent thermodynamic data for minerals in the system Na_2O-K_2O-CaO-MgO-FeO-Fe_2O-SiO_2-TiO_2-H_2O-CO_2. *J. Petrol.* **29**, 445–552.

Biellmann C., Gillet P., Guyot F., Peyronneau J. and Reynard B. (1993) Experimental evidence for carbonate stability in the Earth's lower mantle. *Earth Planet. Sci. Lett.* **118**, 31–41.

Blundy J. and Dalton J. (2000) Experimental comparison of trace element partitioning between clinopyroxene and melt in carbonate and silicate systems, and implications for mantle metasomatism. *Contrib. to Mineral. Petrol.* **139**, 356–371.

Chen P. F., Chiao L. Y., Huang P. H., Yang Y. J. and Liu L. G. (2006) Elasticity of magnesite and dolomite from a genetic algorithm for inverting Brillouin spectroscopy measurements. *Phys. Earth Planet. Inter.* **155**, 73–86.

Dalton J. and Presnall D. C. (1998) Carbonatitic melts along the solidus of model lherzolite in the system CaO-MgO-Al_2O_3-SiO_2-CO_2 from 3 to 7 GPa. *Contrib. to Mineral. Petrol.* **131**, 123–135.

Dandekar D. P. and Ruoff A. L. (1968) Temperature dependence of the elastic constants of calcite between 160° and 300° K. *J. Appl. Phys.* **39**, 6004-6009.

Dasgupta R. and Hirschmann M. M. (2006) Melting in the Earth's deep upper mantle caused by carbon dioxide. *Nature* **440**, 659–662.

De Villiers J. P. R. (1971) Crystal structures of aragonite, strontianite, and witherite. *Am. Mineral.* **56**, 758–767.

de Leeuw N. H., Harding J. and Parker S. (2002) Molecular dynamics simulations of the incorporation of Mg 2+ , Cd 2+ and Sr 2+ at calcite growth steps: Introduction of a SrCO 3 potential model. *Mol. Simul.* **28**, 573–589.

Dickens B. and Bowen J. S. (1971) The crystal structure of $BaCa(CO_3)_2$ (barytocalcite). *J. Res. Natl. Bur. Stand. A. Phys. Chem.* **75**, 197–203.

Dobson D. P., Jones A. P., Rabe R., Sekine T., Kurita K., Taniguchi T., Kondo T., Kato T., Shimomura O. and Urakawa S. (1996) In-situ measurement of viscosity and density of carbonate melts at high pressure. *Earth Planet. Sci. Lett.* **143**, 207–215.

Dollase W. A. and Reeder R. J. (1986) Crystal structure refinement of huntite, $CaMg_3(CO_3)_4$, with X-ray powder data. *Am. Mineral.* **71**, 163–166.

Dove M. T., Winkler B. and Leslie M. (1992) A new interatomic potential model for calcite: applications to lattice dynamics studies, phase transition, and isotope fractionation. *Am. Mineral.* **77**, 244–250.

Dupuy C., Liotard J. M. and Dostal J. (1992) Zr/hf fractionation in intraplate basaltic rocks: Carbonate metasomatism in the mantle source. *Geochim. Cosmochim. Acta* **56**, 2417–2423.

Effenberger, H (1980) Die kristallstruktur des minerals paralstonite, $BaCa(CO_3)_2$. *Neu. Jb. Mineral, Mh.* 353-363.

Effenberger H. and Zemann J. (1985) Single crystal X-ray investigation of norsethite, BaMg(CO3)2: One more mineral with an aplanar carbonate group. *Zeitschrift fur Krist. - New Cryst. Struct.* **171**, 275–280.

Fiquet G., Guyot F. and Itie J. P. (1994) High-pressure X-ray diffraction study of carbonates: $MgCO_3$, $CaMg(CO_3)_2$, and CaCO3. *Am. Mineral.* **79**, 15–23.

Fisler D. K., Gale J. D. and Cygan R. T. (2000) A shell model for the simulation of rhombohedral carbonate minerals and their point defects. *Am. Mineral.* **85**, 217–224.

Gale J. D. (1996) Empirical potential derivation for ionic materials. *Philos. Mag. B* **73**, 3–19.

Gale J. D. (1997) GULP: a computer program for the symmetry-adapted simulation of solids. *J. Chem. Soc. Faraday Trans.* **93**, 629–637.

Gale J. D. (1998) Analytical Free Energy Minimization of Silica Polymorphs. *J. Phys. Chem. B* **102**, 5423–5431.

Gale J. D. and Rohl A. L. (2003) The General Utility Lattice Program (GULP). *Mol. Simul.* **29**, 291–341.

Genge M. J., Price G. D. and Jones A. P. (1995) Molecular dynamics simulations of $CaCO_3$ melts to mantle pressures and temperatures: implications for carbonatite magmas. *Earth Planet. Sci. Lett.* **131**, 225–238.

Ghiorso M. S., Hirschmann M. M., Reiners P. W. and Kress V. C. (2002) The pMELTS: A revision of MELTS for improved calculation of phase relations and major element partitioning related to partial melting of the mantle to 3 GPa. *Geochemistry Geophys. Geosystems* **3**, 36.

Ghosh S., Ohtani E., Litasov K. D. and Terasaki H. (2009) Solidus of carbonated peridotite from 10 to 20 GPa and origin of magnesiocarbonatite melt in the Earth's deep mantle. *Chem. Geol.* **262**, 17–28.

Green D.H., Wallace M.E. (1988) Mantle metasomatism by ephemeral carbonatite melts. *Nature* **336**, 459–462.

Grossfield A. and Zuckerman D. M. (2009) Chapter 2 Quantifying Uncertainty and Sampling Quality in Biomolecular Simulations. *Annu. Rep. Comput. Chem.* **5**, 23–48.

Hearmon R.F.S. (1946) The elastic constants of anisotropic minerals. *Rev. Mod. Phys.* **18**, 409-440.

Hockney R.W., Eastwood J.W. (1988) Computer simulations using particles. Institute of Physics Publishing, London, pp. 267-304.

Hoover W. G. (1985) Canonical dynamics: equilibrium phase-space distributions. *Phys. Rev. A* **31**, 1695.

Hunter R. H. and McKenzie D. (1989) The equilibrium geometry of carbonate melts in rocks of mantle composition. *Earth Planet. Sci. Lett.* **92**, 347–356.

Hurst H. J. (1991) The thermal decomposition of magnesite in nitrogen. *Thermochim. Acta* **189**, 91–96.

Hurt S.M., Lange R.A. and Ai, Y. (2015) The density and compressibility of $BaCO_3$-$SrCO_3$-$CaCO_3$-K_2CO_3-Na_2CO_3-Li_2CO_3 liquids: new measurements and a systematic trend with cation field strength. *AGU Fall Meeting Abstracts*. *(Data available upon request)*

Hurt S.M., Lange R.A. and Ai, Y. (2018) The compressibility of Li2CO3- Na2CO3- K2CO3- Rb2CO3-Cs2CO3- CaCO3-SrCO3-BaCO3 liquids: new sound speed measurements, ideal mixing and, systematic trends with composition. **(in preparation)**.

Hurt S. M. and Lange R. A. (2018) The density of Li_2CO_3-Na_2CO_3-K_2CO_3-Rb_2CO_3-Cs_2CO_3-$CaCO_3$-$SrCO_3$-$BaCO_3$ liquids: New measurements, ideal mixing, and systematic trends with cation coordination. *Geochim. Cosmochim. Acta* **(accepted)**.

Ionov D. A., Dupuy C., O'Reilly S. Y., Kopylova M. G. and Genshaft Y. S. (1993) Carbonated peridotite xenoliths from Spitsbergen: implications for trace element signature of mantle carbonate metasomatism. *Earth Planet. Sci. Lett.* **119**, 283–297.

Jacobs G. K., Kerrick D. M. and Krupka K. M. (1981) The high-temperature heat capacity of natural calcite ($CaCO_3$). *Phys. Chem. Miner.* **7**, 55–59.

Janz G. J., Neuenschwander E. and Kelly F. J. (1963) High-temperature heat content and related properties for Li2CO3, Na2CO3, K2CO3, and the ternary eutectic mixture. *Trans. Faraday Soc.* **59**, 841.

Kono Y., Kenney-Benson C., Hummer D., Ohfuji H., Park C., Shen G., Wang Y., Kavner A. and Manning C. E. (2014) Ultralow viscosity of carbonate melts at high pressures. *Nat. Commun.* **5**, 5091.

Li Z., Li J., Lange R., Liu J. and Militzer B. (2017) Determination of calcium carbonate and sodium carbonate melting curves up to Earth's transition zone pressures with implications for the deep carbon cycle. *Earth Planet. Sci. Lett.* **457**.

Liu L., Chen C., Lin C. and Yang Y. (2005) Elasticity of single-crystal aragonite by Brillouin spectroscopy. *Phys. Chem. Miner.* **32**, 97–102.

Liu Q., Tenner T. J. and Lange R. A. (2007) Do carbonate liquids become denser than silicate liquids at pressure? Constraints from the fusion curve of K_2CO_3 to 3.2 GPa. *Contrib. to Mineral. Petrol.* **153**, 55–66.

Markgraf S. and Reeder R. (1985) High-temperature structure refinements of calcite and magnesite. *Am. Mineral.* **70**, 590–600.

Martinez I., Zhang J. and Reeder R.J. (1996) In situ X-ray diffraction of aragonite and dolomite at high pressure and high temperature: evidence for dolomite breakdown to aragonite and magnesite. *Am. Mineral.* **81**:611-624.

Nie S., Liu Y., Liu Q., Wang M. and Wang H. (2017) Phase transitions and thermal expansion of $BaCO_3$ and $SrCO_3$ up to 1413K. *Eur. J. Mineral.*, 1–11.

Nosé S. (1984) A unified formulation of the constant temperature molecular dynamics methods. *J. Chem. Phys.* **81**, 511.

Palaich S. E. M., Heffern R. A., Hanfland M., Lausi A., Kavner A., Manning C. E. and Merlini M. (2016) High-pressure compressibility and thermal expansion of aragonite. *Am. Mineral.* **101**, 1651–1658.

Plimpton S. (1995) Fast parallel algorithm for short-range molecular dynamics. *J. Comput. Phys.***117,** 1-42.

Raiteri P., Demichelis R. and Gale J. D. (2015) Thermodynamically Consistent Force Field for Molecular Dynamics Simulations of Alkaline-Earth Carbonates and Their Aqueous Speciation. *J. Phys. Chem. C* **119**, 24447–24458.

Rea D. K. and Ruff L. J. (1996) Composition and mass flux of sediment entering the world's subduction zones: Implications for global sediment budgets, great earthquakes, and volcanism. *Earth Planet. Sci. Lett.* **140**, 1–12.

Redfern S.A.T. and Angel R.J. (1999) High-pressure behavior and equation of state of calcite, CaCO3. *Contrib. to Mineral. Petrol.* **134**, 102–106.

Ross N. L. (1997) The equation of state and high-pressure behavior of magnesite. *Am. Mineral.* **82**, 682–688.

Sleep N. H. (2009) Stagnant lid convection and carbonate metasomatism of the deep continental lithosphere. *Geochemistry, Geophys. Geosystems* **10**.

Staudigel H., Hart S. R., Schmincke H. U. and Smith B. M. (1989) Cretaceous ocean crust at DSDP Sites 417 and 418: Carbon uptake from weathering versus loss by magmatic outgassing. *Geochim. Cosmochim. Acta* **53**, 3091–3094.

Steinfink H, Sans FJ (1959) Refinement of the crystal structure of dolomite. *Am. Mineral.*, **44**, 679-682.

Stromme K. O. (1975) On the crystal structure of high-temperature forms of strontium and barium carbonate and structurally related compounds. *Acta Chem. Scand. A* **29**, 105–110.

Vuilleumier R., Seitsonen A., Sator N. and Guillot B. (2014) Structure, equation of state and transport properties of molten calcium carbonate (CaCO3) by atomistic simulations. *Geochim. Cosmochim. Acta* **141**, 547–566.

Wang J. and Becker U. (2009) Structure and carbonate orientation of vaterite ($CaCO_3$). *Am. Mineral.* **94**, 380–386.

Wang M., Liu Q., Nie S., Li B., Wu Y., Gao J., Wei X. and Wu X. (2015) High-pressure phase transitions and compressibilities of aragonite-structure carbonates: $SrCO_3$ and $BaCO_3$. *Phys. Chem. Miner.* **42**, 517–527.

Wang M., Liu Q., Inoue T., Li B., Pottish S., Wood J., Yang C. and Tao R. (2016) The K_2CO_3 fusion curve revisited: New experiments at pressures up to 12 GPa. *J. Mineral. Petrol. Sci.* **111**, 241–251.

Yaxley G. M., Crawford A. J. and Green D. H. (1991) Evidence for carbonatite metasomatism in spinel peridotite xenoliths from western Victoria, Australia. *Earth Planet. Sci. Lett.* **107**, 305–317.

Ye Y., Smyth J. R. and Boni P. (2012) Crystal structure and thermal expansion of aragonite-group carbonates by single-crystal X-ray diffraction. *Am. Mineral.* **97**, 707–712.

Zhang J. and Reeder R. J. (1999) Comparative compressibilities of calcite-structure carbonates: Deviations from empirical relations. *Am. Mineral.* **84**, 861–870.

Zhang Z. and Liu Z. (2015) High pressure equation of state for molten CaCO3 from first principles simulations. *Chinese J. Geochemistry* **34**, 13–20.

Chapter 5 The novel topology and thermodynamic properties of $MgCO_3$ liquid from molecular dynamic simulations: implications for the density of primary carbonatite melts

5.1 Introduction

Carbonate plays an important role in partial melting of the mantle. It dramatically lowers the solidus of the mantle peridotite (e.g. Dasgupta and Hirschmann 2006) and eclogite (e.g. Hammouda 2003), up to ~600 °C (Dasgupta and Hirschmann 2007), producing low degree partial melts (0.03-0.3%) of carbonatite liquid (e.g. Green and Wallace 1998; Dalton and Wood 1993; Dasgupta and Hirschmann 2006) which are highly mobile owing to their ultralow viscosities (e.g. Hunter and McKenzie 1989; Dobson et al. 1996; Kono et al. 2014). Carbonatite melts in the mantle are efficient agents of metasomatism (e.g. Green and Wallace 1988; Dupuy et al. 1992; Yaxley et al. 1991; Rudnick et al. 1993; Pokhilenko et al. 2015) and are important for the petrogenesis of ocean island basalts (e.g. Dasgupta et al. 2006) and investigations of the deep carbon cycle (e.g. Dasgupta and Hirschmann 2010).

$MgCO_3$ is one of the most geologically relevant carbonate liquid components. Carbonate enters the mantle through subduction of hydrothermally altered oceanic crust (e.g., Staudigel et al. 1989; Rea and Ruff 1996). Calcium from $CaCO_3$ partitions readily into the silicate phases of the mantle and is replaced by Mg which establishes $MgCO_3$ as a dominant carbonate mantle component (Biellmann et al. 1993). Investigations into the composition of primary carbonatite melts produced by partial melting of carbonated mantle eclogite and peridotite show that $MgCO_3$ along with $CaCO_3$ and $FeCO_3$ are the major components of interest (Dalton and Wood 1993; Dalton and Presnall 1998; Hammouda 2003; Ghosh et al 2009).

Carbonated mantle systems have been extensively studied via phase equilibrium experiments (e.g. Wendlandt and Mysen 1980; Dalton and Wood 1993; Dalton and Presnall 1998; Hammouda 2003; Ghosh et al 2009; Litasov and Ohtani 2010; Dasgupta et al 2013). While such experiments are immensely valuable, they have limitations. For example, small variations in the starting composition can result in significant variations in the location of the solidus in P-T space (Dasgupta and Hirschmann 2010). This proves problematic given the significant compositional heterogeneity of carbonated mantle, both in its silicate and carbonate phases. The compositional complexity is further compounded by the wide ranges of temperatures and pressures at which partial melting may occur. A phase equilibrium experiment cannot be performed for every relevant composition, temperature and pressure. Furthermore, phase equilibrium experiments often scale up temperature and pressure together, making it difficult to determine the extent to which variations in phase equilibria are due to temperature versus pressure effects.

Thermodynamic modeling software such as MELTS (Ghiorso et al. 2002) or Thermo-Calc (Andersson et al 2002) can help resolve these issues but they rely on knowledge of the standard state thermodynamic properties of the pure carbonate melt components. For the most important carbonate crystal phases (e.g. magnesite and calcite), the standard state properties are well known, including thermal expansion (e.g. Markgraf and Reeder 1985), bulk moduli, K'_T (e.g. Redfern and Angel 1999; Ross 1997; Fiquet et al. 2002), and heat capacities (e.g. Jacobs et al. 1981; Berman et al. 1985). However, knowledge of the standard state thermodynamic properties of the respective liquids is limited because alkaline earth carbonates and $FeCO_3$ decompose at temperatures lower than their 1 bar melting temperatures. In spite of the difficulties posed by decarbonation, some properties of the $CaCO_3$ component have been

determined experimentally: the molar volume and thermal expansion of $CaCO_3$ liquid have been determined by density experiments on mixed alkali carbonate melts containing variable amounts $CaCO_3$ at 1 bar and high temperatures (Hurt and Lange, 2018). Similarly, O'Leary et al (2015) performed sound speed measurements on mixtures of $CaCO_3$ and alkali carbonate melt to constrain the compressibility (β_T) and $\delta\beta_T/\delta T$ of the liquid $CaCO_3$ component. However, there is a near total paucity of standard state thermodynamic data for $MgCO_3$ liquid. This is due to its very low (500° C) 1 bar decarbonation temperature (Hurst 1991), which makes experiments on $MgCO_3$-bearing liquids near impossible at 1 bar.

At present, MD simulations provide the only plausible path for obtaining the complete set of endmember properties needed to incorporate carbonates into a thermodynamic modeling framework like MELTS. The classical pair potential model presented in Hurt and Wolf (2018a) is designed specifically for simulations of alkaline earth carbonate liquids. Their model is used in this study to simulate liquids in the $MgCO_3$-$CaCO_3$-$SrCO_3$-$BaCO_3$ quaternary system from 773 to 2373 K up to 20 GPa. The simulations supply crucial constraints on the standard state thermodynamic properties of pure $MgCO_3$ liquid which are difficult or impossible to determine experimentally. Apart from thermodynamic properties, the simulations explore liquid structure and mixing behavior in the $MgCO_3$-$CaCO_3$-$SrCO_3$-$BaCO_3$ quaternary system. The local structure of carbonate liquids can be characterized by the coordination of the metal cations with neighboring oxygens and carbonate molecules. In the recent experimental studies of Hurt and Lange (2018) and Hurt et al. (2018) the molar volume and compressibility of $MgCO_3$ is estimated by systematic variations with the alkali and alkaline earth carbonates; their estimates, however, depend on liquid structure, namely the coordination of Mg^{2+} with the carbonate groups. These coordination numbers, which are obtainable via MD simulations, are thus necessary for

correctly interpreting the systematic trends in experimental density and compressibility measurements among alkali and alkaline earth carbonate liquids and will allow meaningful estimates of the $MgCO_3$ and $FeCO_3$ liquid components to be made based on systematics. Mixing behavior is also required for interpretation of experimentally derived density and compressibility data; currently our knowledge of alkaline earth carbonate liquid thermodynamic properties rests on experiments on mixtures (since pure components are unstable), which assumes that ideal mixing is complete across the entire compositional spectrum. Though necessary, this assumption is not experimentally verifiable, but it can be directly tested through MD simulations. These mixing properties are also essential for thermodynamic models such as MELTS, which combine pure standard state and mixing properties to predict the behavior of intermediate composition liquids.

In order to assess whether carbonate melts (especially those rich in Fe) are buoyant throughout the upper mantle and transition zone, simulations are also performed on $CaCO_3$-$MgCO_3$ binary compositions from 1.5 to 17.5 GPa and 1423 to 1873 K along various pressure-temperature paths approximating that of subducting slabs. The simulation composition, temperature and pressure are representative of near-solidus carbonatite melts formed by low-degree partial melting of carbonated eclogite and peridotite. This is done in order to estimate the density of primary carbonatite melts as a function of depth and determine whether some compositions of carbonate melt are sufficiently dense to enter the lower mantle under certain conditions.

5.2 Methods

An empirically-derived pair-potential model for the simulation of alkaline earth carbonate liquids using rigid ions and partial charges was developed through the General Utility Lattice

Program (GULP) (Gale, 1997; Gale and Rohl, 2003). A complete description and assessment of this model is available in (Hurt and Wolf, 2018) where it was applied to the simulation of liquids in the $CaCO_3$-$SrCO_3$-$BaCO_3$ system. This model is now applied to molecular dynamic (MD) simulations of $MgCO_3$ liquid using the Large-scale Atomic/Molecular Massively Parallel Simulator (LAMMPS) (Plimpton, 1995).

42 different liquid compositions were simulated within the $MgCO_3$-$CaCO_3$-$SrCO_3$-$BaCO_3$ quaternary over a temperature range of 773-2373 K and up to 20 GPa. MD simulations were performed with a timestep of 1 fs for $1.2 \cdot 10^5$ timesteps (120 ps). Each simulation began with an equilibration phase of 60 ps using the canonical (NVE) ensemble with the Berendsen barostat and thermostat (Berendsen et al., 1984) which equilibrates quickly and smoothly but deviates slightly from the canonical ensemble. A second equilibration phase of 40 ps was performed under the NPT ensemble using the Nosé-Hoover barostats and thermostats (Nosé, 1984; Hoover, 1985). A third phase of 20 ps continues the NPT ensemble and constitutes the final production run.

Every simulation was checked to ensure that total energy had converged to within 0.02% of total energy and volume to within 0.27 %. This level of volume convergence is achieved with a simulation size of 6860 atoms. Every simulation began with the initial atomic positions and velocities corresponding to $CaCO_3$ liquid at 2.275 g/cm^3 density and 1623 K.

5.3 Results

5.3.1 Structure of $MgCO_3$ liquid versus $CaCO_3$, $SrCO_3$ and $BaCO_3$ liquids at 1100 K and 1 bar

In Hurt and Wolf (2018a) this model was used to simulate $CaCO_3$, $SrCO_3$ and $BaCO_3$ liquids in the range of 1100 – 3400 K and up to 43 GPa and an analysis of $CaCO_3$-$SrCO_3$-$BaCO_3$ liquid structure was performed. It was found that $CaCO_3$, $SrCO_3$ and $BaCO_3$ share a nearly

identical liquid structure differing only in terms of average atomic separation distances, this simulation result, in combination with the observation of broad congruencies and systematic variations in the properties of $CaCO_3$-$SrCO_3$-$BaCO_3$ liquids (e.g. Hurt and Lange 2018; Hurt and Wolf 2018a) led to the conclusion that similarities in properties among $CaCO_3$, $SrCO_3$ and $BaCO_3$ liquids are related to their near-identical liquid structure. These studies emphasized the relationship between metal cation coordination with carbonate groups (M-C) (where M stands for the cations Mg, Ca, Sr or Ba) and oxygen atoms (M-O) and thermodynamic properties. In this study, the liquid structure and coordination environment of $MgCO_3$-bearing liquids have been investigated to determine whether $MgCO_3$ shares the same liquid structure as the remaining alkaline-earth carbonates.

Liquid structure may be characterized by pair distribution functions (pdf) which, for a particular pair of atoms i and j gives the frequency distribution atom j normalized to its average atomic density as a function of interatomic separation distance (r) in Å. The liquid structures are further characterized by the coordination numbers of particular atomic pairs. Coordination numbers are calculated from the pdf curves ($g(r)$). The equation for determining average coordination number of atomic pair i and j (CN_{ij}) is given by:

$$CN_{ij} = 4\pi \int_0^{r_1} r^2 g(r) \rho \, dr \quad \text{Eq. 5.1}$$

where r is the atomic separation distance in Å; $r_1$is the maximum cutoff radius located at the first minimum in the PDF, representing the edge upper edge of the first nearest-neighbor peak; ρ is the average atomic number density of atom j with units of $\frac{atoms}{Å^3}$.

At 1100 K and 0 GPa, $CaCO_3$, $SrCO_3$ and $BaCO_3$ liquids share similar coordination numbers for the M-O, C-C and M-C pairs, as depicted in Fig. 5.1. There are some minor

variations between them. For instance, Ca-O, Sr-O and Ba-O coordination numbers vary systematically, with Ca-O at 6.9, Sr-O at 7.3 and Ba-O at 7.7. C-C and M-C are the same for each liquid at 10.9 and 5.9 respectively. Thus, carbonate molecules are arranged near-closest packing, metal cations are in near-octahedral coordination with carbonate groups and near-cubic with oxygen atoms.

$MgCO_3$ liquid does not share the same coordination environment. The Mg-O and Mg-C coordination is tetrahedral. The C-C coordination is slightly greater in $MgCO_3$ (11.6) compared to $CaCO_3$-$SrCO_3$-$BaCO_3$ liquids (10.9), but still reflects nearly closest-packing (12). For all liquids at all temperatures and pressures, the C-O coordination is 3 and O-O is 2 as expected. Figure 5.1 shows pdf curves of $MgCO_3$, $CaCO_3$, $SrCO_3$ and $BaCO_3$ liquids for the C-C, M-O and M-C pairs at 1100 K and 1 bar. As evident, the curves are nearly the same for $CaCO_3$, $SrCO_3$ and $BaCO_3$, but $MgCO_3$ liquid assumes a different form for each pair.

Figure 5.1 Liquid structure of $MgCO_3$ is distinct from $CaCO_3$, $SrCO_3$ and $BaCO_3$. Pair distribution functions at 0 bar and 1100 K generated from simulations for $MgCO_3$, $CaCO_3$, $SrCO_3$ and $BaCO_3$ liquids. The X-O, C-C and X-C pairs are shown where X is the cation (Mg, Ca, Sr or Ba). To facilitate comparison, the interatomic separation distance (r) has been normalized to the position of the first peak (r_0).

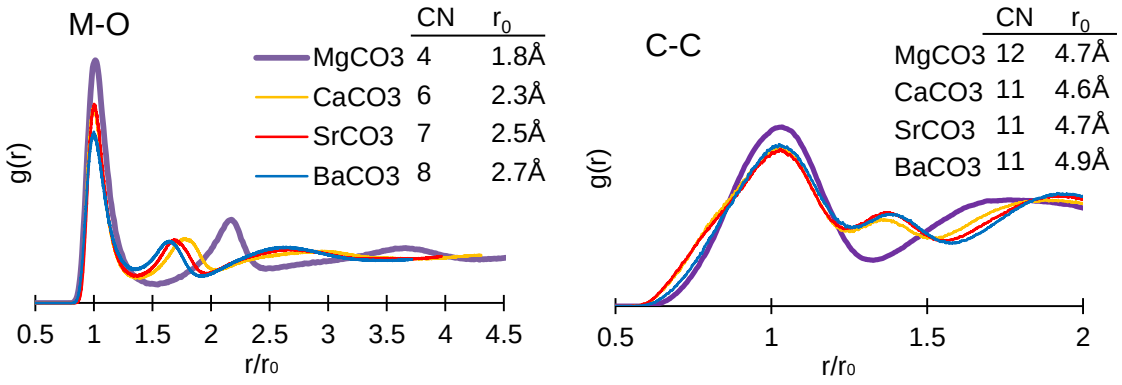

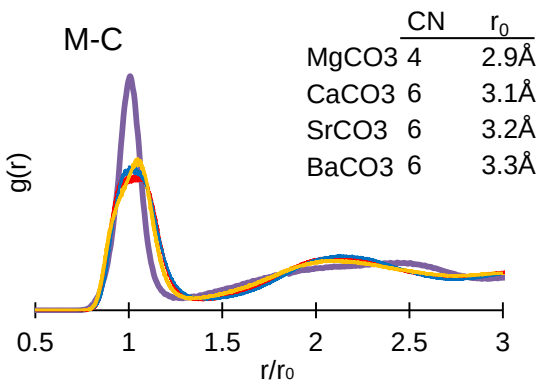

5.3.2 The evolution of $MgCO_3$ liquid structure with pressure

To determine whether the unique structure of $MgCO_3$ liquid persists at high pressure, simulations of pure $MgCO_3$ liquid representing isothermal compression, were analyzed at 1100 K between 0 and 12 GPa. M-C and M-O coordination numbers were calculated at each pressure and shown in Fig. 5.2.

As pressure increases, the Mg-O coordination number increases linearly from 4 (at 1 bar) to 5.6 (at 12 GPa). M-O coordination number varies systematically among the alkaline earth carbonates. At 12 GPa, the coordination number of the Ba-O pair is ~10, ~9 for Sr-O, ~8 for Ca-O and ~6 for Mg-O. Thus, at pressure, the Mg-O coordination number falls in-line with the alkaline earth systematic trend (Fig. 5.2). For the M-C coordination numbers, $CaCO_3$-$SrCO_3$-$BaCO_3$ liquids average around 6 at 1 bar and then increase modestly to ~6.8 by 12 GPa. The Mg-C coordination starts off at 4 at 1 bar and converges rapidly to values consistent with the other alkaline earth carbonates. Simulations indicate that the liquid structure of $MgCO_3$ becomes progressively more like that of the other alkaline earth carbonates with pressure, becoming indistinguishable by 12 GPa.

Figure 5.2 The structure of MgCO3 liquid becomes more like $CaCO_3$-$SrCO_3$-$BaCO_3$ liquids at high pressure. The evolution of coordination of M-O and M-C pairs is shown for pure $MgCO_3$, $CaCO_3$, $SrCO_3$ and $BaCO_3$ liquids as a function of pressure up to 12 GPa. In $MgCO_3$, the coordination of M-O and M-C pairs liquid starts off at 4 at 1 bar and approach ~6 at 12 GPa.

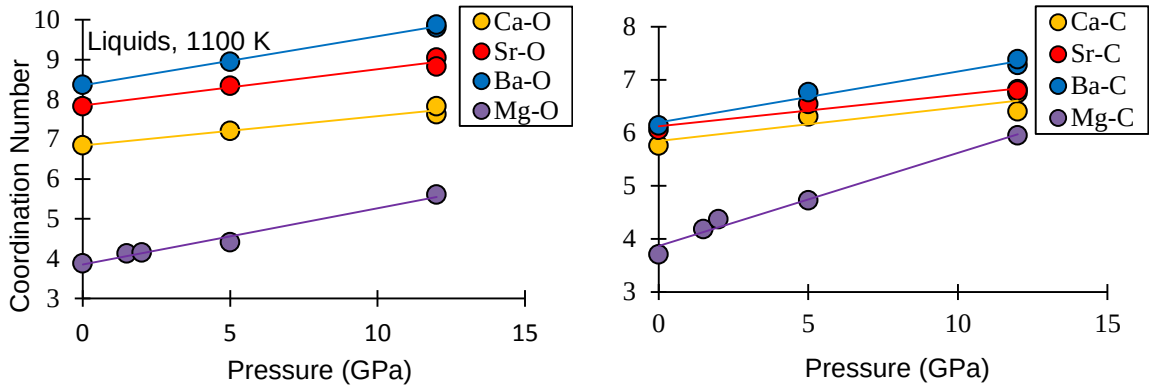

5.3.3 The thermodynamic properties of $MgCO_3$

In Hurt and Wolf (2018a), this model was used to simulate $CaCO_3$, $SrCO_3$ and $BaCO_3$ liquids and calculate their thermodynamic properties over a range of geologically relevant temperatures and pressures. Their simulations predicted nearly parallel compression curves, 1 bar molar volumes that increase systematically with cation radius and congruent thermal expansion coefficients. Many of these predictions, namely systematic variation in molar volume and congruent thermal expansions, are corroborated by the experiments of Hurt and Lange (2018) and Hurt et al. (2018).

To investigate whether the properties of $MgCO_3$ liquid follow the trends observed among $CaCO_3$, $SrCO_3$ and $BaCO_3$, the thermodynamic properties of $MgCO_3$ liquid have been calculated from the simulations. The complete simulation results, including composition, temperature, pressure, molar volume, total energy and enthalpy are listed in Table A.4 (Appendix A). The simulated molar volumes of $MgCO_3$ liquid are used to fit the parameters of a temperature-dependent 4th order Birch-Murnaghan equation of state (EOS) (Angel 2000):

$$P = 3K_{T,0}f_E(1+2f_E)^{5/2}\left\{1+\frac{3}{2}(K'-4)f_E+\frac{3}{2}\left[K_{T,0}K''+(K'-4)(K'-3)+\frac{35}{9}\right]f_E^2\right\} \quad \text{Eq. 5.2}$$

where $K_{T,0}$ is the isothermal bulk modulus at 1 bar and simulation temperature (T) and K' and K'' are 2nd and 3rd order pressure dependence terms which are all fitted parameters. $K_{T,0}$ is a function of temperature according to:

$$K_{T,0}(T) = K_{Tr,0} + \frac{\delta K_0}{\delta T}(T - 1100\ K) \quad \text{Eq. 5.3}$$

$(\frac{\delta K_0}{\delta T})$ is the fitted 1bar temperature dependence of the bulk modulus and $K_{T,0}$ is the fitted 1 bar bulk modulus at the reference temperature. The Eulerian finite strain, $f_{E,}$ is defined as:

$$f_E = \left[\left(V_{T,0}/V_{T,P}\right)^{2/3} - 1\right]/2 \quad \text{Eq. 5.4}$$

$V_{T,P}$ is the simulation volume at T and pressure (P). $V_{T,0}$ is the volume at 1 bar and T and can be calculated from the fitted 1 bar volume at 1100 K ($V_{Tr,0}$) and the fitted thermal expansion (α). $V_{T,0}$ thus becomes:

$$V_{T,0} = V_{Tr,0}e^{\alpha(T-1100\ K)} \quad Eq.\ 5.5$$

The parameter α is the fitted thermal expansion coefficient and is temperature independent. The full set of fitted parameters for this EOS is given in Table 5.1. This Birch-Murnaghan EOS model recovers the simulated molar volumes in the 1100 – 2000 K temperature range up to 20 GPa with a root-mean square of volume residuals of 0.27 cm^3/mol. The 1100 K compression curve predicted by the fit of the simulation results to a Birch-Murnaghan EOS is shown in Figure 5.3 along with the raw simulated molar volume data as a function of pressure up to 12 GPa. Also shown are the simulated compression curves of $CaCO_3$, $SrCO_3$ and $BaCO_3$ liquids. Clearly, the model predicts a curve for $MgCO_3$ that is radically different from the other three alkaline earth carbonate components. The 1 bar molar volume is near that of $SrCO_3$ and decreases dramatically with pressure, implying a 1 bar compression far-exceeding that of the other alkaline earth

carbonate liquids. The compression curve rapidly flattens out and at pressures > 5 GPa where it begins to parallel the other alkaline earth carbonates. This behavior is consistent with the conclusions drawn from liquid structure evolutions: at 1 bar $MgCO_3$ liquid assumes a markedly different coordination environment than the other alkaline earth carbonates, but with increasing pressure it gradually comes into conformity with them.

Table 5.1 The thermodynamic properties of $MgCO_3$ liquid as derived from the simulations. These are fitted parameters of a 4th order Birch-Murnaghan EOS (Eq. 5.2) that have been fitted to the simulations of $MgCO_3$ liquid from 773 to 2000 K up to 20 GPa by the least squares method. $V_{Tr,0}$ is the molar volume at 1100 K and 1 bar; α is the thermal expansion; $K_{Tr,0}$ is the bulk modulus at 1 bar and 1100 K and $\delta K_0/\delta T$ is its temperature dependence; K' and K'' are 3rd and 4th order pressure dependence terms. The root mean square of the pressure residuals of the fit is 0.06 GPa and of the volume residuals is 0.27 cm^3/mol.

Property	Best Fit (1σ)
$V_{Tr,0}$ (cm^3/mol)	44.21(9)
α ($10^{-4} \cdot K^{-1}$)	1.07(14)
$K_{Tr,0}$ (GPa)	6.15(15)
$\delta K_0/\delta T$ ($10^{-3} \cdot$ GPa/K)	-1.37(35)
K'	2.41(1)
K''	3.16(1)

Figure 5.3 Compression curve of $MgCO_3$ liquid strongly deviates from other alkaline-earth carbonates. In panel a, simulated molar volumes at 1100 K as a function of pressure for $MgCO_3$, $CaCO_3$, $SrCO_3$ and $BaCO_3$ liquid are depicted. The black lines represent best-fit Birch-Murnaghan equations of state (3rd order for $CaCO_3$, $SrCO_3$ and $BaCO_3$ and 4th order for $MgCO_3$) for each liquid. As evident, $CaCO_3$, $SrCO_3$ and $BaCO_3$ form near-parallel curves that increase systematically from Ca to Ba. $MgCO_3$ liquid does not follow the trend. Panel b shows the same compression curves in terms of density.

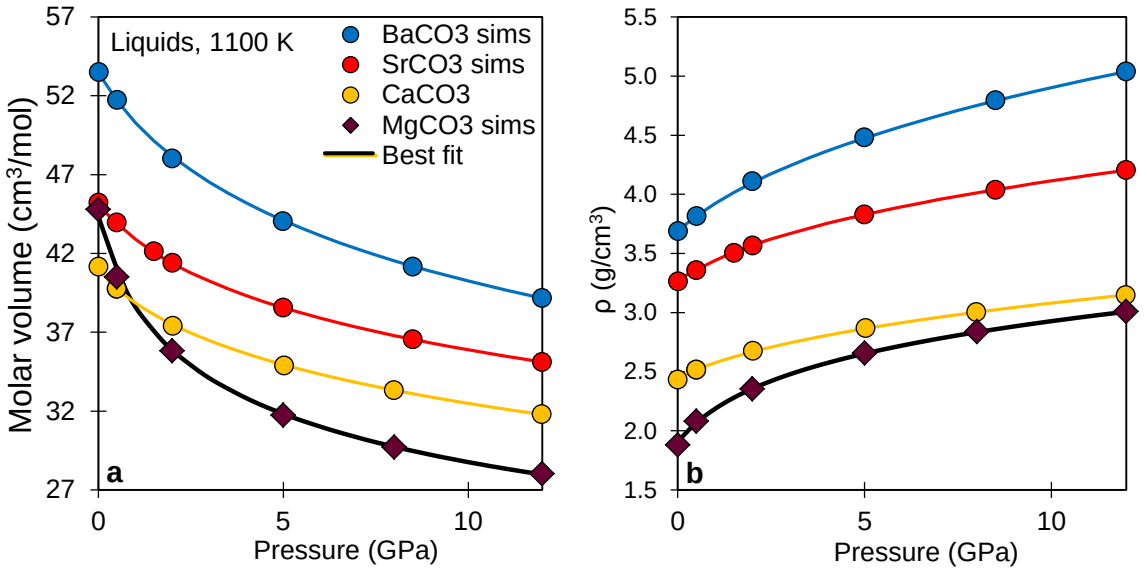

5.3.4 Non-ideal mixing within the $MgCO_3$-$CaCO_3$-$SrCO_3$-$BaCO_3$ quaternary system at 1 bar

Knowledge of mixing behavior within $MgCO_3$-bearing systems is important for a few reasons: currently knowledge of alkaline earth carbonate liquid thermodynamic properties rests on experiments on mixtures (since pure components are unstable) (e.g. Liu and Lange 2003; O'Leary et al. 2015; Hurt and Lange 2018; Hurt et al. 2018). These studies necessarily assume that the properties of the various components mix ideally across the entire compositional spectrum. Unfortunately, this assumption is not fully experimentally verifiable due to decarbonation of alkaline carbonate components, but it can be directly tested through MD simulations. Mixing properties are also essential for thermodynamic models such as MELTS, which combine pure standard state and mixing properties to predict the behavior of intermediate composition liquids.

In Hurt and Wolf (2018a) this model was applied to simulate liquids in three binary systems: $CaCO_3$-$SrCO_3$, $CaCO_3$-$BaCO_3$ and $SrCO_3$-$BaCO_3$. It was found that molar volumes and molar isobaric heat capacities and compressibility all mix ideally across a wide range of temperatures and pressures. To test whether such ideal mixing behavior extends to $MgCO_3$-

bearing liquids, simulations of mixed liquids are performed in the $MgCO_3$-$CaCO_3$-$SrCO_3$-$BaCO_3$ quaternary system at 1 bar and 1100 K. In the case of molar volume, ideality of mixing is assessed by calculating volume of mixing (ΔV_{mix}) for each binary (i.e. $MgCO_3$-$CaCO_3$, $MgCO_3$-$SrCO_3$ and $MgCO_3$-$BaCO_3$) liquid. V_{mix} is given by:

$$\Delta V_{mix} = V - \sum V_i X_i \quad \text{Eq. 5.6}$$

Where V is the molar volume of the binary liquid and ΣV_i is the sum of the product of the molar volume of component i (V_i) and its mole fraction (X_i) in the mix at the specified temperature and pressure. ΔV_{mix} is 0 in the case of ideal mixing (e.g. as is the case within the $CaCO_3$-$SrCO_3$-$BaCO_3$ liquid system).

Ideal mixing of enthalpies is also assessed for each simulated liquid within the $MgCO_3$-bearing binaries (at 1100 K and 1bar) with an analogous equation for enthalpy of mixing (ΔH_{mix}), where ΔH_{mix} is given by:

$$\Delta H_{mix} = H - \sum H_i X_i \quad \text{Eq. 5.7}$$

H is the simulated enthalpy of mixing for the binary liquid and H_i is the enthalpy of the pure component i. The mixed simulation results are listed in Table A.5 (Appendix A) which lists the composition, volume (V), enthalpy, ideal volume ($\Sigma V_i X_i$), ideal enthalpy ($\Sigma H_i X_i$), ΔV_{mix} and ΔH_{mix}.

The ΔV_{mix} and ΔH_{mix} values can be modeled with a sub-regular mixing equation:

$$\Delta Z_{mix} = (w_0 + w_1 X) \cdot X[1 - X] \quad \text{Eq. 8}$$

Where ΔZ_{mix} is the mixing property for either volume or enthalpy, X is mole fraction of $MgCO_3$, and w0 and w1 are constants which have been fitted by the least squares method to simulation results. The values of fitted w_0 and w_1 at 1100 K and 1 bar for all three binaries for ΔV_{mix} and ΔH_{mix} are given in Table A.6 (Appendix A). Fig. 5.4a depicts ΔV_{mix} and Fig. 5.4b

ΔH_{mix} for each simulated mixture as a function of $MgCO_3$ mol % along with the fitted sub-regular mixing model values (Eq. 5.8). Fig. 5.4a shows departures from ideal mixing in respect to molar volumes especially for liquids along the $SrCO_3$-$MgCO_3$ or $CaCO_3$-$MgCO_3$ binaries where the magnitude of ΔV_{mix} is as high as -0.87(11) cm^3/mol. Volumes of mixing are nearly all predicted to be negative. While the magnitude of ΔV_{mix} is approximately the same within the $CaCO_3$-$MgCO_3$ and $SrCO_3$-$MgCO_3$ binaries, it is markedly reduced for $BaCO_3$-$MgCO_3$ liquids. For all binaries, the mixing behavior is slightly asymmetric; the magnitude of ΔV_{mix} reaches a maximum at 60-75 mol. % $MgCO_3$. The non-ideal mixing of volumes in Mg-CO_3-bearing liquids means that volumetric derivative properties such as compressibility do not mix ideally either.

Figure 5.4 Non-ideal mixing dominates volumetric and enthalpic properties in $MgCO_3$-bearing systems at 1 bar, unlike $CaCO_3$-$SrCO_3$-$BaCO_3$ mixtures**.** do not mix ideally in MgCO3-bearing systems at 1 bar. The ΔVmix (a) and ΔHmix (b) of $MgCO_3$-bearing binary liquids at 1100 K and 1 bar are shown; non-zero values indicate non-ideal mixing.. Both The ΔV_{mix} and ΔH_{mix} are, for the most part, negative and reach a minimum at $MgCO_3$ molar concentrations of 0.6 to 0.8. Points are simulation results and lines are best-fits of the simulations to sub-regular mixing equations (Eq. 5.8). Note that, for ΔH_{mix}, simulated total energy values were used instead of enthalpy because they are equal at 0 GPa and because simulated enthalpy has larger errors than total energy due to fact that enthalpy calculations fold in fluctuations on both pressure and volume.

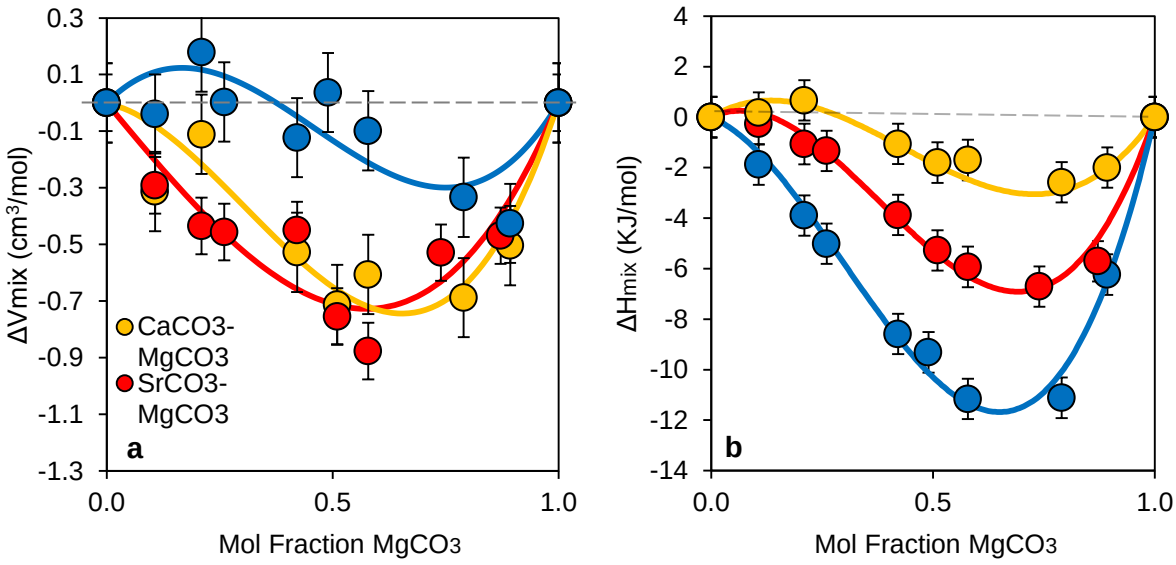

The case of enthalpy of mixing (ΔH_{mix}) is closely analogous. Unlike liquids in the $CaCO_3$-$SrCO_3$-$BaCO_3$ system enthalpy does not mix ideally among $MgCO_3$-bearing mixtures. Figure 5.4b shows ΔH_{mix} as a function of $MgCO_3$ mole percent for the $CaCO_3$-$MgCO_3$, $SrCO_3$-$MgCO_3$ and $BaCO_3$-$MgCO_3$ binaries. ΔH_{mix} is negative for every mixture except $CaCO_3$-$MgCO_3$ with low (< 0.5) mole fractions of $MgCO_3$. The magnitude of ΔH_{mix} increases systematically from $CaCO_3$ (which reaches a maximum of 3.1 KJ/mol), to $BaCO_3$, (with a maximum of ~12 KJ/mol). Within each binary, the magnitude of ΔH_{mix} peaks at 60-75 mol% $MgCO_3$. Interestingly, the $BaCO_3$-$MgCO_3$ system exhibits the lowest ΔV_{mix} but the highest ΔH_{mix}; this suggests that the mechanism responsible for non-ideal mixing in volumetric properties, is not the same as the one driving non-ideal mixing in enthalpic properties.

It was noted in Hurt and Wolf (2018a) that simulations predict isobaric heat capacities to mix ideally according to mole fraction in the $CaCO_3$-$SrCO_3$-$BaCO_3$ liquids. Simulations of $MgCO_3$-bearing binary liquids from 1100 to 2000 K and 1 bar allowed calculation of the isobaric heat capacity. For $CaMg(CO_3)_2$, $SrMg(CO_3)_2$ and $BaMg(CO_3)_2$, the heat capacity is estimated to be 146, 140 and 139 J/mol respectively while ideal mixing would predict values of 157, 157 and 153 respectively. Heat capacities are thus systematically lower than expected for $MgCO_3$-bearing-systems.

5.3.5 The mechanism behind non-ideal mixing in $MgCO_3$-bearing liquids

As noted above, liquid properties (e.g. molar volume, compressilbity, enthalpy and heat capacity) do not mix ideally in the $MgCO_3$-binary compositions as they do in the $CaCO_3$-$SrCO_3$-$BaCO_3$ liquid system. The non-ideality of mixing in $MgCO_3$-bearing liquids should be evident in the pdf curves of mixtures (i.e. there should be some noticeable difference between the pdf

curves of pure $MgCO_3$ compared to an $MgCO_3$-bearing mixture). Such a difference would point to a mechanism driving non-ideal mixing behavior.

Within the $MgCO_3$-$CaCO_3$-$SrCO_3$-$BaCO_3$ quaternary there are six binaries. Various compositions within each binary were simulated at 1100 K and 1 bar and pdf curves were calculated for every atomic pair. The full range of pdf curves for M-O, M-C and C-C pairs for each binary composition is available in Fig. A.2 (Appendix A). The striking uniformity of pdf curves demonstrates that M-O, M-C and C-C pairs in binary liquids retain the same structure and coordination as in the pure liquids. This means that, at 1 bar, Mg^{2+} maintains its 4-fold coordination with carbonate and oxygen irrespective of composition. Similarly, if small amounts of $CaCO_3$, $SrCO_3$ and $BaCO_3$ are mixed into $MgCO_3$ liquid, Ca^{2+}, Sr^{2+} and Ba^{2+} maintain their octahedral coordination with carbonate. While the Mg-O and Mg-C coordination in mixtures is the same as in pure $MgCO_3$ liquid (i.e. Mg^{2+} maintains a coordination of 4 with carbonate and oxygen atoms) there are some notable differences between the pdf curves of pure and mixed $MgCO_3$. An interesting but less important change is that, in $MgCO_3$-bearing binary liquids, the C-C interaction transforms into a weighted average of the two end members (Fig. A.3 in Appendix A).

The key structural difference between pure and mixed $MgCO_3$ liquids is shown to be metal cation ordering. In pure $MgCO_3$ liquid at 1 bar, the 1st Mg-M (i.e. Mg-Mg) coordination sphere partially overlaps with the 2nd coordination sphere. The first sphere contains 3 metal cations at an average distance of 3.7 Å. The 2nd sphere has an additional 9 atoms at an average distance of 5.3 Å. When $MgCO_3$ is mixed with another carbonate, Mg^{2+} mostly vacates the first coordination sphere surrounding other Mg^{2+} ions and is preferentially replaced by other metal cations (i.e. Ca^{2+}, Sr^{2+}or Ba^{2+}). Figure 5.5 shows Mg-Mg pdf curves in pure $MgCO_3$ and

$MgCa(CO_3)_2$ along with Mg-Ca in $MgCa(CO_3)_2$ and demonstrates that the first coordination shell in pure $MgCO_3$ disappears in the mixed compounds and is replaced by Ca^{2+}. This kind of cation ordering was not observed in $CaCO_3$-$SrCO_3$-$BaCO_3$ liquids. Such ordering in $MgCO_3$-bearing mixtures can explain why some properties of $MgCO_3$-bearing liquids do not mix ideally, while $CaCO_3$-$SrCO_3$-$BaCO_3$ liquids do. This is likely related to the ordering in the calcite-dolomite-magnesite series where ordering of cations generates the highly order dolomite structure in order to accommodate cations of mixed sizes with minimal lattice strain (Vinograd 2006). Since V_{mix} is nearly always negative, cation ordering apparently allows the liquid to pack space more efficiently.

Figure 5.5 Mg-Mg pdf curve in pure $MgCO_3$ liquid are significantly altered upon mixing due to Mg^{2+} vacating the 1st coordination shell in favor of Ca^{2+}, Sr^{2+} or Ba^{2+} ions. The pdf curves were generated from simulations of pure $MgCO_3$ liquid and a mixture, $CaMg(CO_3)_2$, at 1100 K and 1 bar. The first coordination shell (CN: 3) in pure $MgCO_3$ disappears in the mixture and is filled with Ca^{2+}. This same effect occurs in $MgCO_3$ mixtures with the other cations (Sr^{2+} and Ba^{2+}). This likely results from an energetic penalty for Mg^{2+} to be surrounded by other Mg^{2+} ions; the preferential ordering induced by surrounding the Mg-CO_3 tetrahedral complexes with the (Ca, Sr, Ba)$^{2+}$ octahedral complexes thus might be favored as it relaxes stresses in the atomic structure.

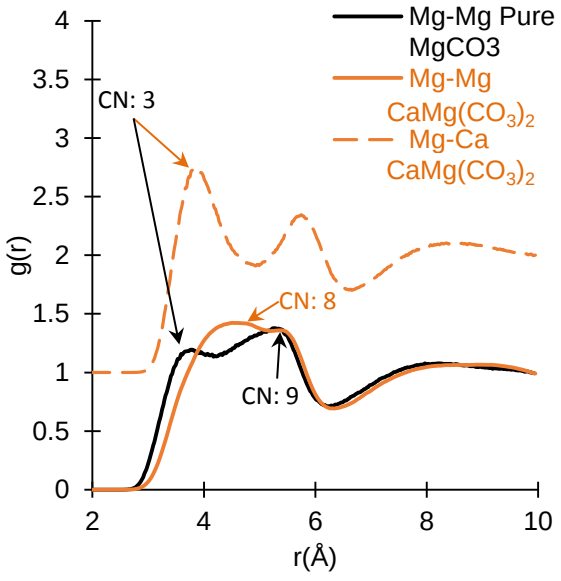

5.3.6 Ideal mixing within the $MgCO_3$-$CaCO_3$-$SrCO_3$-$BaCO_3$ quaternary system at high pressure

Since the simulated compression curve and liquid structure of $MgCO_3$ liquid are both similar to that of the other alkaline earth carbonate liquids at high (12 GPa) pressure, simulations of binary mixtures $CaMg(CO_3)_2$, $SrMg(CO_3)_2$ and $BaMg(CO_3)_2$ were performed at 1100 K up to 12 GPa to assess whether volumes and enthalpy mix ideally at pressure. The values of ΔV_{mix} calculated from the resulting simulations are -0.02(3), -0.13(3) and -0.11(3) cm^3/mol for $CaMg(CO_3)_2$, $SrMg(CO_3)_2$ and $BaMg(CO_3)_2$ respectively. These ΔV_{mix} values are dramatically smaller than at 1 bar (which range between -0.34 and -0.91 cm^3/mol). Fig. 5.6 shows ΔV_{mix} (normalized to ΔV which is the volume difference between $CaCO_3$ and $MgCO_3$ liquid) at 1100 K as function of pressure. It is necessary to normalize ΔV_{mix} to ΔV because the molar volume of the MgCO3-CaCO3 binary mixture is always bracketed by the volume of the pure endmembers, therefore, at pressures where pure CaCO3 and MgCO3 are close in volume, ΔV_{mix} will appear small, normalizing to the volume difference between the endmembers corrects for this. As evident, ΔV_{mix} approaches 0 (ideal mixing) with increasing pressure.

In the previous section, it was noted that Mg-Mg is the only pair to manifest a notable difference in the pdf curves between pure and mixed $MgCO_3$ liquid (Fig. 5.5). The pdf curve shows metal cation ordering that provides a mechanistic explanation for non-ideality in mixing of at least some of the properties in $MgCO_3$-bearing liquids. Since ΔV_{mix} diminishes to nearly 0 at 12 GPa, we might expect to see little difference between Mg-Mg pdf curves in pure $MgCO_3$ versus an $MgCO_3$ mixture at that pressure. The inset on Figure 5.6 shows, in fact, that the difference between pure and mixed $MgCO_3$ liquids vanishes at 12 GPa. This provides a powerful corroboration that metal cation ordering does, in fact, explain non-ideal mixing in volumetric properties among $MgCO_3$-bearing liquids.

Figure 5.6 Mixing of molar volumes of $CaCO_3$ and $MgCO_3$ liquid approach ideality with increasing pressure due to a progressively diminishing of cation ordering effect. V_{mix} is shown normalized to $\Delta V_{Ca\text{-}Mg}$ (which is the difference between pure $CaCO_3$ and $MgCO_3$ liquid at the given pressure) as a function of pressure. As pressure increase the magnitude of non-ideality approaches 0. The insert shows liquid Mg-Mg pdf curves of pure $MgCO_3$ (solid lines) compared to $CaMg(CO_3)_2$ (dotted lines) at 1 bar, 2 and 12 GPa. The disparity between the two curves reflects the degree of cation ordering in the liquid. As pressure increase the mixed $CaMg(CO_3)_2$ curve conforms to that of pure $MgCO_3$.

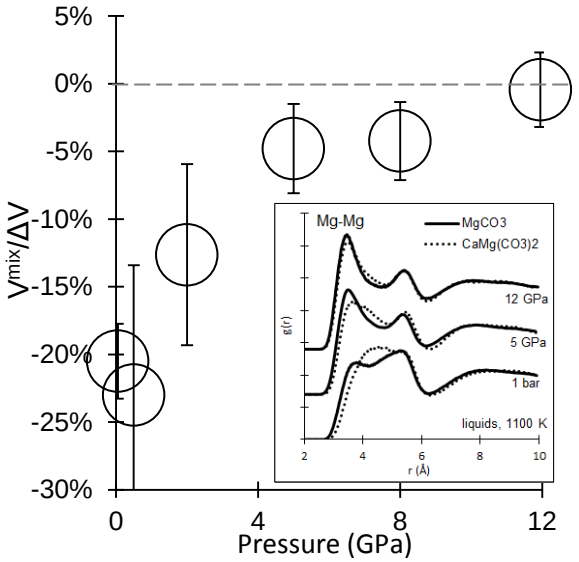

In contrast the simulations indicate that non-ideal mixing of enthalpy does not diminish at high pressure like ΔV_{mix}. At 12 GPa, the ΔH_{mix} for the three binary compositions was calculated to be -2.9, -8.2 and -11.7 KJ/mol for $CaMg(CO_3)_2$, $SrMg(CO_3)_2$ and $BaMg(CO_3)_2$ respectively which is even greater in magnitude than their respective 1 bar values. This would suggest that cation ordering in $MgCO_3$-bearing liquids is not directly responsible for non-ideal mixing of enthalpies.

5.3.7 Simulation of primary carbonatite melts

The simulation results presented above highlight the novel topology of $MgCO_3$ liquid and provide estimates of its thermodynamic properties and mixing behavior which is important for future integration of the $MgCO_3$ liquid component into thermodynamic modeling software such as MELTS or Thermo-Calc. However, the pair potential model can also be directly applied to

geologic systems by providing property estimates of natural carbonatite liquids at relevant temperatures and pressures. In order to estimate the density of primary carbonatite melts generated by low-degree partial melting of carbonated mantle, simulations are performed in the $CaCO_3$-$MgCO_3$ liquid system. To ensure that the simulations accurately represent natural systems, the simulated compositions, temperatures and pressures are based on the results of phase equilibrium experiments from the literature focused on carbonated mantle partial melting. To constrain the composition of carbonatite melts produced by partial melting of the carbonated mantle, Dalton and Wood (1993) and Dalton and Presnall (1998) conducted phase equilibrium experiments on carbonated peridotite systems at pressures ranging from 1.5 to 7 GPa and temperatures from 1423 to 1703 K. Hammouda (2003) and Ghosh et al. (2009) conducted similar experiments for carbonated eclogite in the 6-17.5 GPa pressure range. The carbonate melt compositions produced were > 92 wt. % $CaCO_3$ and $MgCO_3$ for the peridotite-derived melts and > 88 wt. % for the eclogite-derived. The remaining composition is mostly $FeCO_3$ and SiO_2. We estimate the densities of the primary carbonate melts of Dalton and Wood (1993), Dalton and Presnall (1998), Hammouda (2003) and Ghosh et al. (2009) by simplifying them to $CaCO_3$-$MgCO_3$ binary compositions and simulating them at their respective temperature and pressure conditions. The simulated $CaCO_3$-$MgCO_3$ melts range in density between 2.49 to 3.11 g/cm^3 at 1.5 and 17.5 GPa respectively. Since the $FeCO_3$ component is omitted in these simulations, the actual density would be expected to be somewhat higher. An approximate correction to the simulated densities may be made by assuming $FeCO_3$ has the same molar volume as the $CaCO_3$-$MgCO_3$ binary melt and integrating it into the density calculation. The density may be further corrected by accounting for the SiO_2 liquid component of the carbonatite melt by using the volumetric data from Lange and Carmichael (1987) and Kress et al. (1988) and assuming the

SiO_2 volume mixes ideally into the carbonate melt. Table 5.2 gives the simulated melt composition, gram formula weight, molar volume and simulated density along with the $FeCO_3$-SiO_2-corrected density.

Table 5.2 Simulated densities of $CaCO_3$-$MgCO_3$ binary liquids approximating the compositions of carbonatite liquid produced by phase equilibrium experiments of carbonated mantle of Dalton and Wood (1993), Dalton and Presnall (1998) Hammouda (2003) and Ghosh et al. (2009). The pressures and temperatures of the simulations reflect those of the phase equilibrium experiments. Corrected density is the simulated density corrected for the small concentrations of $FeCO_3$ and SiO_2 present in the liquid produced in the original phase equilibrium experiment.

$MgCO_3$ (mol%)	Press. (GPa)	Temp. (K)	Gram formula wt.	Sim.Vol. (cm^3/mol)	Sim. ρ (g/cm^3)	Corrected ρ (g/cm^3)
Dalton and Wood (1993)						
13.6	1.5	1423	98.22	39.19	2.506	2.507
17.4	1.5	1423	97.69	39.23	2.490	2.497
22.5	2.2	1523	96.95	38.28	2.532	2.545
28.7	2.5	1523	96.05	37.76	2.544	2.558
31.6	2.8	1573	95.63	37.47	2.552	2.573
35.1	3.0	1573	95.11	37.09	2.564	2.585
Dalton and Presnall (1998)						
40.9	3.0	1518	93.64	36.59	2.559	2.561
44.0	3.5	1543	93.15	35.94	2.592	2.592
45.8	4.0	1563	92.86	35.44	2.620	2.618
49.2	5.0	1603	92.33	34.54	2.673	2.669
50.9	6.0	1653	92.05	33.77	2.726	2.717
55.5	7.0	1703	91.33	33.03	2.765	2.756
Hammouda (2003)						
10.5	6.0	1523	98.43	34.91	2.820	2.871
10.9	7.0	1273	98.36	33.61	2.927	2.957
10.8	10.0	1373	98.38	32.23	3.052	3.086
14.1	10.0	1473	97.86	32.47	3.014	3.068
Ghosh et al (2009)						
87.1	12.5	1873	86.35	29.53	2.925	3.071
86.8	13.5	1823	86.40	29.12	2.967	3.096
61.1	15.0	1873	90.45	29.62	3.053	3.133
76.1	17.5	1833	88.08	28.30	3.112	3.182

5.4 Discussion

5.4.1 Comparison of $MgCO_3$ to alkali and alkaline earth carbonate liquids

MD simulations of $MgCO_3$ liquid indicate that, at ambient pressure (where $MgCO_3$ liquid is unstable) Mg^{2+} assumes a 4-fold coordination with both the carbonate molecule and oxygen

much like alkali carbonate liquids, Li_2CO_3, $NaCO_3$ and K_2CO_3 (e.g. Roest et al. 2017; Kohara et al. 1999). This stands in contrast to $CaCO_3$-$SrCO_3$-$BaCO_3$ liquids in which metal cations are in 6-fold coordination with carbonate and 7- to 8-fold coordination with oxygen (Hurt and Wolf 2018aa). Although $MgCO_3$ is an alkaline-earth carbonate like $CaCO_3$, $SrCO_3$, and $BaCO_3$ its liquid structure is more similar to that of the alkali carbonates particularly Li_2CO_3; this is well-illustrated by the comparison of pdf curves of $MgCO_3$ liquid from this study, with those generated by FPMD for Li_2CO_3 liquid (Roest et al. 2017, Figure 5.7). This resemblance in liquid structure (and physical properties) is not unprecedented. It's predicted by the Mg-Li diagonal relationship in which the compounds of certain elemental pairs (Li-Mg, Be-Al, B-Si and C-P) that are diagonally adjacent, share some properties in common (e.g., Feinstein 1984).

Figure 5.7 The liquid structure of $MgCO_3$ is similar to that of Li_2CO_3. The liquid pdf curves of $MgCO_3$ from our simulations (solid lines) are compared to those of Li_2CO_3 generated by FPMD simulations from Roest et al. 2017 (dotted lines) at 1200 K and 15 kbar. $CaCO_3$ liquid at 1200 K and 15 kbar is shown for comparison (grey dashed line). $MgCO_3$ liquid is more like Li_2CO_3 than $CaCO_3$

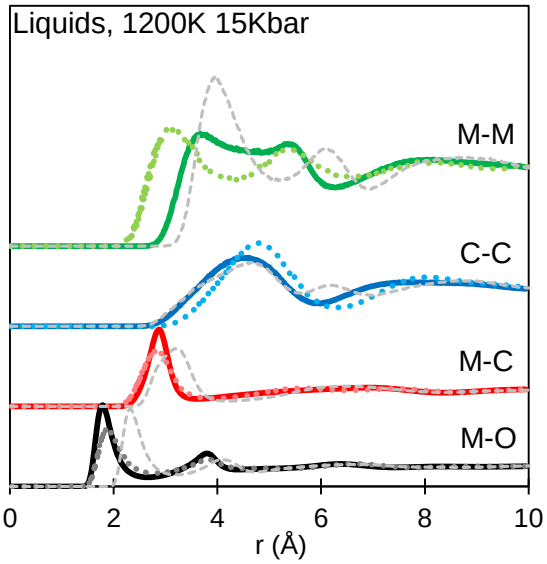

Since the liquid structure of $MgCO_3$ is more "alkali-like" than "alkaline-earth-like" it's expected that its properties should be similar to that of the alkali carbonate liquids (particularly

Li_2CO_3). Alkali carbonates are generally more voluminous than their alkaline earth counterparts not only because of the additional metal cation per formula unit but because the partial molar volume of $(CO_3)^{2-}$ is greater, ~38 cm^3/mol versus 31 cm^3/mol (Hurt and Lange 2018). Applying the molar volume systematic trend equation for alkali carbonate liquids from Hurt and Lange (2018) yields a 1 bar $MgCO_3$ liquid volume of ~40 cm^3/mol at 1100 K. The fitted Birch-Murnaghan EOS model (Eq. 5.2) predicts a 1 bar $MgCO_3$ liquid volume of 44.21(9) cm^3/mol at 1100 K. It's likely that the actual volume is somewhat lower since the model typically slightly overestimates 1 bar volumes. For $CaCO_3$, $SrCO_3$ and $BaCO_3$ liquids the model requires a -0.35, -0.33 and -0.75 GPa pressure correction respectively to bring simulated 1 bar volumes into agreement with the experimental projections of Hurt and Lange (2018). An analogous -0.6 GPa pressure correction would bring the $MgCO_3$ simulations into agreement with the predictions from Hurt and Lange (2018).

Chapter 3 provides analogous systematic trend equations for the compressibility of alkali and alkaline earth carbonate liquids based on a positive linear relationship between liquid compressibility and volume of fusion. Their model equation predicts a compressibility of ~20 · 10^{-2} GPa^{-1} for $MgCO_3$ liquid at 1100 K, assuming it fits into the alkali carbonate trend and ~16 10^{-2} GPa^{-1} if it fits into the alkaline-earth trend. Given the similarity of the $MgCO_3$ liquid structure to Li_2CO_3, the alkali carbonate trend might actually provide a better prediction. If a -0.6 GPa pressure correction is applied, our $MgCO_3$ liquid simulations predict a compressibility (β_T) of 12.2 · 10^{-2} GPa^{-1} at 1100 K. These estimates of $MgCO_3$ liquid compressibility differ dramatically from other alkaline earth carbonate liquids (i.e. $CaCO_3$, $SrCO_3$ and $BaCO_3$) which have 1 bar, 1100 K compressibilities between 4.33 - 5.97 · 10^{-2} GPa^{-1}. The other alkaline earths

have a more compact liquid structure (chapter 2) that is closer in volume to that of their respective high-temperature crystal phases and thus the liquid has a lower compressibility.

5.4.2 Comparison to previous studies of $MgCO_3$ liquid thermodynamic properties

As noted above, the structure of $MgCO_3$ liquid becomes more like the remaining alkaline earth carbonates as it is subjected to progressively higher pressures. By 12 GPa, the M-O and M-C coordination numbers of $MgCO_3$ liquid converge to values in line with $CaCO_3$, $SrCO_3$, and $BaCO_3$ liquid (Fig. 5.2). This pressure-induced transformation of liquid structure is also evident in the compression curve of $MgCO_3$ liquid which begins to parallel the other three alkaline earth carbonate liquids at pressures >5 GPa (Fig. 5.3). This unique topology of $MgCO_3$ liquid results in a dramatically more buoyant, compressible melt than proposed by previous studies.

The standard state thermodynamic properties of $MgCO_3$ liquid have been previously estimated by Kang et al. 2016 by fitting a thermodynamic model to the congruent melting curve of $MgCO_3$ which is bracketed by four experimentally determined points (~1858 K at 3 GPa and 1883 K at 3.6 GPa from Irving and Wyllie 1975 and 2183 K at 8 GPa and 2363 K at 15 GPa from Katsura and Ito 1990). This approach arrives at a molar volume of $MgCO_3$ liquid of ~32 cm^3/mol and a compressibility of $2.6 \cdot 10^{-2}$ GPa^{-1} at 1100 K and 1 bar. The $MgCO_3$ properties proposed by Kang et al. differ markedly from our simulation results. However, Kang et al. makes takes a problematic approach to calculating the standard state thermodynamic properties for $MgCO_3$ liquid. The estimates of standard state thermodynamic properties of $MgCO_3$ (and $FeCO_3$ as well) liquid proposed by Kang et al. were calculated by fusion curve analysis. The fusion curve of $MgCO_3$ is currently bracketed by 4 experimental points (and only 3 for $FeCO_3$). However, 5 thermodynamic parameters are fitted based on only 4 experimental observations.

Since, the number of fitted parameters exceeds the number of constraining observations, an alternative set of thermodynamic properties could recover the observables just as well.

The problem is under-constrained and we can see some of the resulting issues in the fitted thermodynamic properties proposed by Kang et al. (2016); for example, the thermal expansions of $MgCO_3$ and $FeCO_3$ liquid are the same the thermal expansion of their respective crystal phases. Liquid thermal expansion is generally expected to be greater than that of the crystal (Lange 1997). $CaCO_3$, $SrCO_3$ and $BaCO_3$ liquids, for example, have a thermal expansion ~3 times greater than their respective crystal phases (Hurt and Lange 2018). Kang et al also give a temperature dependence of compressibility ($\delta\beta_T/\delta T$) of $MgCO_3$ liquid that is lower, by an order of magnitude, than those of $CaCO_3$, $SrCO_3$ and $BaCO_3$ liquids (Hurt et al. 2018). For these reasons, we recommend the standard state $MgCO_3$ liquid thermodynamic properties derived from this study.

5.4.3 The density of primary carbonatite melts

Natural carbonatite liquids are effective agents of mantle metasomatism and scavengers of trace elements (e.g. Blundy and Dalton 2000). The mobility and ascent rates of primary carbonatite melts are thus a question of geologic concern. Ascent rate is related to melt viscosity, which has been measured at pressure (e.g. Kono et al. 2014), and density. The densities of some important carbonate liquid components (e.g. $CaCO_3$) at pressure have been constrained by 1 bar liquid density experiments (e.g. Liu and Lange, 2003; Hurt and Lange 2018) and liquid sound speed measurements (e.g. O'Leary et al. 2015; Hurt et al. in prep). However, primary carbonatite melts generated in the mantle by low-degree partial melting contain significant amounts of $MgCO_3$ (Dalton and Wood 1993; Dalton and Presnall1998; Ghosh et al. 2009); the density of this component is almost totally unknown but is estimated by simulations in this study. Using the

compositions of low-degree primary carbonatite melts generated in phases equilibrium experiments of carbonated peridotite (Dalton and Wood 1993; Dalton and Presnall1998) and eclogite (Hammouda 2003; Ghosh et al. 2009) simulations at temperature and pressure are performed by simplifying experimental compositions to $CaCO_3$-$MgCO_3$ binary liquids. The simulated liquid densities were corrected to account for the small (1-12 mol %) concentrations of $FeCO_3$ and SiO_2 in the melt. The simulated densities are summarized in Table 2 and are depicted in Figure 5.8. According to the simulations, primary carbonatite melts maintain a significant density contrast with the surrounding mantle rocks. Even the densities of melts from Hammouda (2003) which represent a cold slab subduction PT path (and are relatively enriched in denser $CaCO_3$ and $FeCO_3$ components) never approach that of the silicate mantle rocks. Given the ultralow viscosity of these kinds of liquids (e.g. Dobson et al. 1996; Kono et al. 2014), any positive density contrast will swiftly drive liquid ascent meaning any degree of carbonate melt will quickly escape from a descending slab, thus inhibiting the subduction and storage of carbonate into the lower mantle.

Figure 5.8 The densities of primary carbonatite melts maintain a high positive density contrast with the surrounding mantle. The simulated densities of $MgCO_3$-$CaCO_3$ binary liquids representing primary carbonatite melts corrected for $FeCO_3$ and SiO_2 concentration are shown as a function of depth. The simulation temperatures, pressures and compositions are based on the phase equilibrium experiments of Dalton and Wood (1993) (squares), Dalton and Presnall (1998) (triangles), Hammouda (2003) (diamonds) and Ghosh et al. (2009) (circles). Coloring reflects simulation temperature. Mantle density as a function of depth is taken from PREM (Dziewonski and Anderson, 1981).

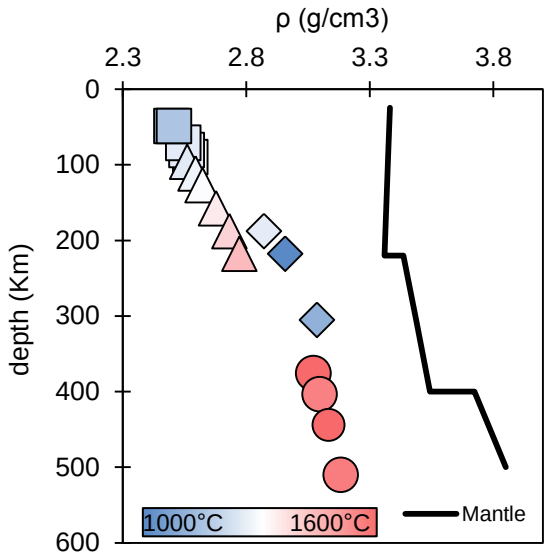

The only common carbonate component heavy enough to potentially affect a density crossover is $FeCO_3$. Kang and Schmidt (2017) studied the melting of subducted banded iron formation (BIF) and they concluded that partial melting of BIF-bearing oceanic crust could produce ferrocarbonatite liquids dense enough to stagnate or even sink in certain parts of the mantle. While $FeCO_3$ liquid was not directly simulated in this study, it's possible that $FeCO_3$ shares the volumetric properties of $MgCO_3$ since Fe^{2+} and Mg^{2+} have similar ionic radii and molar volume tracks well with ionic radius (chapter 2). In this case, we may use our $MgCO_3$ liquid properties as a proxy for $FeCO_3$. Under this assumption, the $FeCO_3$ concentration necessary for affecting a density cross over can be calculated as a function of depth for a hypothetical carbonatite in the $MgCO_3$-$CaCO_3$-$FeCO_3$ system. For the purposes of this calculation it will be assumed that the molar volumes of all three components mix ideally and that $X^{Mg} = X^{Ca}$. The $MgCO_3$ and $FeCO_3$ liquid volumes at temperature and pressure are approximated from the simulations of this study while the $CaCO_3$ liquid volume is calculated from the1 bar density data of Liu and Lange (2018) in combination with the $CaCO_3$ compressibility results of O'Leary et al. (2015). This calculation shows that, even assuming

conditions most favorable for a density crossover (i.e. a P-T path representing cold-slab-subduction), the requisite $FeCO_3$ concentration would exceed 60 wt.% (37 mol.% FeO) which is far outside the compositional bounds suggested by phase equilibrium experiments on carbonated mantle compositions which generally fall below 10 wt.%.

The same calculation can be performed assuming the $MgCO_3$ and $FeCO_3$ liquid thermodynamic properties suggested by Kang et al. (2015 and 2016). Kang et al. offers a suite of $FeCO_3$ liquid standard state thermodynamic properties, however, their solutions were derived from a $FeCO_3$ fusion curve analysis that was ultimately based on only three experimental points and thus the seven model parameters outnumbered the observed constraints meaning that their solution is non-unique. In any case, the densities of $FeCO_3$ and $MgCO_3$ liquid proposed by Kang et al are decidedly denser than what is indicated by the simulations of this study. If Kang et al. are correct, a hypothetical carbonatite in the $MgCO_3$-$CaCO_3$-$FeCO_3$ system, could eliminate the density contrast with 29-41 wt. % $FeCO_3$ (18-25 wt. % FeO). While this concentration of iron is not observed in phase equilibria experiments, it has been observed in ferrocarbonatite dykes of unambiguous magmatic origin (Thompson et al. 2002). Assuming the volumetric properties proposed by Kang et al. (2016), such ferrocarbonatites liquids would be in equilibrium or negatively buoyant in the mantle from ~200 km to the transition zone which is in accordance with the conclusions of Kang and Schmidt (2017) in regards to ferrocarbonatite melts produced by partial melting of subducted BIF. However, our simulations suggest that $FeCO_3$ and $MgCO_3$ liquid components are much more voluminous than previously thought; even an iron-rich ferrocarbonatite melt would remain buoyant throughout the entire mantle.

Figure 5.9 If $FeCO_3$ liquid assumes a low-density (4-fold) liquid structure it will remain buoyant throughout the entire upper mantle and transition zone. The density of a ferrocarbonatite liquid, $(Fe_{.28}Mg_{.21}Ca_{.28})CO_3$ see Thompson et al. 2002 shown as a function of depth along a carbonated peridotite solidus PT path. The red points are calculated with our model and assume that $FeCO_3$ has the same liquid

structure as $MgCO_3$ characterized by a four-fold coordination of Fe^{2+} with CO_3 groups; $FeCO_3$ liquid component is thus given the same molar volume as $MgCO_3$.The yellow points show the ferrocarbonatite liquid density calculated from the thermodynamic properties for $FeCO_3$ and $MgCO_3$ liquid proposed in Kang et al. (2016) in combination with the $CaCO_3$ liquid partial molar volume calculated from our model.

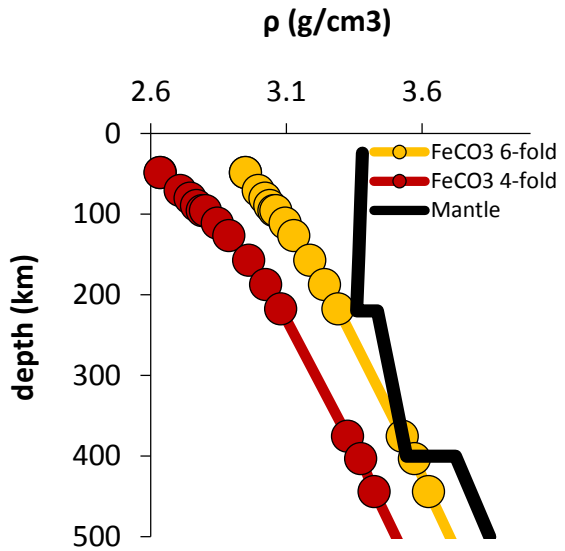

5.5 Conclusions

We perform classical MD simulations of $MgCO_3$-bearing liquids using the pair potential model of Hurt and Wolf (2018a) at mantle pressures and temperatures. We find that $MgCO_3$ liquid assumes a novel topology characterized by four-fold coordination of Mg^{2+} with both the carbonate molecule and O^{2-}. Such a structure is markedly different from that of the other alkaline earth carbonate liquids in which the metal cation is in 6-fold coordination with the carbonate molecule and 7-8 fold coordination with oxygen atoms. The liquid structure of $MgCO_3$ bears significant resemblance to that of Li_2CO_3, which is predicted by the diagonal relationship for Li and Mg compounds. Our simulations further suggest that the thermodynamic properties of $MgCO_3$ are more like Li_2CO_3 than other alkaline earth carbonate liquids; this results in a dramatically more buoyant and compressible liquid than previous studies have suggested. The voluminous structure and subsequent low density of $MgCO_3$-bearing liquids bolsters the density

contrast of $MgCO_3$-bearing carbonatite melts in the mantle increasing their already significant rates of ascent and preventing ferrocarbonatite melts from achieving a density crossover with the surrounding mantle.

The simulations have further suggested that $MgCO_3$ molar volume, thermal expansivity, compressilbity, enthalpy and heat capacity do not mix ideally with $CaCO_3$-$SrCO_3$-$BaCO_3$ liquids. Non-ideal mixing of volumetric properties stems from localized metal cation ordering around the Mg^{2+} ion. It is energetically favorable to surround tetrahedral Mg-CO_3 complexes with octahedral Ca, Sr, Ba-carbonate complexes. This effect gradually diminishes with pressure; by 12 GPa, $MgCO_3$ molar volume mixes near-ideally with $CaCO_3$-$SrCO_3$-$BaCO_3$ liquids. On the other hand, non-ideal mixing of enthalpy $MgCO_3$-beaing systems persists even at high pressure.

The novel topology of $MgCO_3$ liquid indicated by our simulations opens questions on another important component in mantle-derived carbonatite melts: $FeCO_3$. Given the similar ionic radii of Fe^{2+} and Mg^{2+}, it's possible that Fe^{2+} also assumes a 4-fold coordination with $(CO_3)^{2-}$ and O^{2-} in $FeCO_3$ liquid. Multi-angle energy dispersive X-ray diffraction experiments on $MgCO_3$ and $FeCO_3$ melts are needed in order to verify the liquid structure of these important carbonate components.

5.6 References

Andersson J.O., Helander T., Höglund L., Shi P.F., and Sundman B., (2002). Thermo-Calc and DICTRA, Computational tools for materials science. *Calphad*. **26**, 273-312.

Berendsen H. J. C., Postma J. P. M., van Gunsteren W. F., DiNola a and Haak J. R. (1984) Molecular dynamics with coupling to an external bath. *J. Chem. Phys.* **81**, 3684–3690.

Berman R. G. and Brown T. H. (1985) Heat capacity of minerals in the system Na_2O-K_2O-CaO-MgO-FeO-Fe_2O_3-Al_2O_3-SiO_2-TiO_2-H_2O-CO_2: representation, estimation, and high temperature extrapolation. *Contrib. to Mineral. Petrol.* **89**, 168–183.

Biellmann C., Gillet P., Guyot F., Peyronneau J. and Reynard B. (1993) Experimental evidence for carbonate stability in the Earth's lower mantle. *Earth Planet. Sci. Lett.* **118**, 31–41.

Blundy J. and Dalton J. (2000) Experimental comparison of trace element partitioning between clinopyroxene and melt in carbonate and silicate systems, and implications for mantle metasomatism. *Contrib. to Mineral. Petrol.* **139**, 356–371.

Dalton J. a and Presnall D. C. (1998) Carbonatitic melts along the solidus of model lherzolite in the system CaO-MgO-Al_2O_3-SiO_2-CO_2 from 3 to 7 GPa. *Contrib. to Mineral. Petrol.* **131**, 123–135.

Dalton J. A. and Wood B. J. (1993) The compositions of primary carbonate melts and their evolution through wallrock reaction in the mantle. *Earth Planet. Sci. Lett.* **119**, 511–525.

Dasgupta R. and Hirschmann M. M. (2006) Melting in the Earth's deep upper mantle caused by carbon dioxide. *Nature* **440**, 659–662.

Dasgupta R. and Hirschmann M. M. (2007) Effect of variable carbonate concentration on the solidus of mantle peridotite. *Am. Mineral.* **92**, 370–379.

Dasgupta R. and Hirschmann M. M. (2010) The deep carbon cycle and melting in Earth's interior. *Earth Planet. Sci. Lett.* **298**, 1–13.

Dasgupta R., Mallik A., Tsuno K., Withers A. C., Hirth G. and Hirschmann M. M. (2013) Carbon-dioxide-rich silicate melt in the Earth's upper mantle. *Nature* **493**, 211-222.

Dobson D. P., Jones A. P., Rabe R., Sekine T., Kurita K., Taniguchi T., Kondo T., Kato T., Shimomura O. and Urakawa S. (1996) In-situ measurement of viscosity and density of carbonate melts at high pressure. *Earth Planet. Sci. Lett.* **143**, 207–215.

Dupuy C., Liotard J. M. and Dostal J. (1992) Zr/hf fractionation in intraplate basaltic rocks: Carbonate metasomatism in the mantle source. *Geochim. Cosmochim. Acta* **56**, 2417–2423.

Feinstein H. I. (1984) Diagonal relationships—Descriptive or theoretical? *J. Chem. Educ.***61**, 128.

Fiquet G., Guyot F., Kunz M., Matas J., Andrault D. and Hanfland M. (2002) Structural refinements of magnesite at very high pressure. *Am. Mineral.* **87**, 1261–1265.

Gale J. D. (1997) GULP: a computer program for the symmetry-adapted simulation of solids. *J. Chem. Soc. Faraday Trans.* **93**, 629–637.

Gale J. D. and Rohl a L. (2003) The General Utility Lattice Program (GULP). *Mol. Simul.* **29**, 291–341.

Ghiorso M. S., Hirschmann M. M., Reiners P. W. and Kress V. C. (2002) The pMELTS: A revision of MELTS for improved calculation of phase relations and major element partitioning related to partial melting of the mantle to 3 GPa. *Geochemistry Geophys. Geosystems* **3**, 36.

Ghosh S., Ohtani E., Litasov K. D. and Terasaki H. (2009) Solidus of carbonated peridotite from 10 to 20 GPa and origin of magnesiocarbonatite melt in the Earth's deep mantle. *Chem. Geol.* **262**, 17–28.

Green D. H., Wallace M. E. (1988) Mantle metasomatism by ephemeral carbonatite melts. *Nature* **336**, 459–462.

Hammouda T. (2003) High-pressure melting of carbonated eclogite and experimental constraints on carbon recycling and storage in the mantle. *Earth Planet. Sci. Lett.* **214**, 357–368.

Hoover W. G. (1985) Canonical dynamics: Equilibrium phase-space distributions. *Phys. Rev. A* **31**, 1695–1697.

Hunter R. H. and McKenzie D. (1989) The equilibrium geometry of carbonate melts in rocks of mantle composition. *Earth Planet. Sci. Lett.* **92**, 347–356.

Hurst H. J. (1991) The thermal decomposition of magnesite in nitrogen. *Thermochim. Acta* **189**, 91–96.

Hurt S.M., Lange R.A. and Ai, Y. (2018) The compressibility of Li_2CO_3- Na_2CO_3- K_2CO_3-Rb_2CO_3-Cs_2CO_3- $CaCO_3$-$SrCO_3$-$BaCO_3$ liquids: new sound speed measurements, ideal mixing and, systematic trends with composition. **(in preparation)**.

Hurt S. M. and Lange R. A. (2018) The density of Li_2CO_3-Na_2CO_3-K_2CO_3-Rb_2CO_3-Cs_2CO_3-$CaCO_3$-$SrCO_3$-$BaCO_3$ liquids: New measurements, ideal mixing, and systematic trends with cation coordination. *Geochim. Cosmochim. Acta* **(accepted)**.

Hurt S. M. and Wolf A. S. (2018) Thermodynamic properties of $CaCO_3$-$SrCO_3$-$BaCO_3$ liquids: a molecular dynamics study using new empirical atomic potentials for alkaline earth carbonates. *Phys. Chem. Miner*. **(in review)**.

Irving A. J. and Wyllie P. J. (1975) Subsolidus and melting relationships for calcite, magnesite and the join $CaCO_3$-$MgCO_3$ 36 kb. *Geochim. Cosmochim. Acta* **39**, 35–53.

Jacobs G. K., Kerrick D. M. and Krupka K. M. (1981) The high-temperature heat capacity of natural calcite ($CaCO_3$) *Phys. Chem. Miner.* **7**, 55–59.

Katsura T. and Ito E. (1990) Melting and subsolidus phase relations in the $MgSiO_3$-$MgCO_3$ system at high pressures: implications to evolution of the Earth's atmosphere. *Earth Planet. Sci. Lett.* **99**, 110–117.

Kono Y., Kenney-Benson C., Hummer D., Ohfuji H., Park C., Shen G., Wang Y., Kavner A. and Manning C. E. (2014) Ultralow viscosity of carbonate melts at high pressures. *Nat. Commun.* **5**, 5091.

Lange R. A. (1997) A revised model for the density and thermal expansivity of K_2O-Na_2O-CaO-MgO-Al_2O3-SiO_2 liquids from 700 to 1900 K: extension to crustal magmatic temperatures. *Contrib. to Mineral. Petrol.* **130**, 1–11.

Lange R. A. and Carmichael I. S. E. (1987) Densities of Na_2O-K_2O-CaO-MgO-FeO-Fe_2O_3-Al_2O_3-TiO_2-SiO_2 liquids: New measurements and derived partial molar properties. *Geochim. Cosmochim. Acta* **51**, 2931–2946.

Kang N. and Schmidt M. W. (2017) The melting of subducted banded iron formations. *Earth Planet. Sci. Lett.* **476**, 165–178.

Kang N., Schmidt M. W., Poli S., Connolly J. A. D. and Franzolin E. (2016) Melting relations in the system $FeCO_3$-$MgCO_3$ and thermodynamic modelling of Fe-Mg carbonate melts. *Contrib. to Mineral. Petrol.* **171**, 1-16.

Katsura T. and Ito E. (1990) Melting and subsolidus phase relations in the $MgSiO_3$-$MgCO_3$ system at high pressures: implications to evolution of the Earth's atmosphere. *Earth Planet. Sci. Lett.* **99**, 110–117.

Kohara S. (1999) A reverse Monte Carlo study of molten lithium carbonate. *Plasmas & Ions* **83**, 79–83.

Kress V. C., Williams Q. and Carmichael I. S. E. (1988) Ultrasonic investigation of melts in the system Na_2O-Al_2O_3-SiO_2. *Geochim. Cosmochim. Acta* **52**, 283–293.

Litasov K. and Ohtani E. (2010) The solidus of carbonated eclogite in the system CaO-Al_2O_3-MgO-SiO_2-Na_2O-CO_2 to 32GPa and carbonatite liquid in the deep mantle. *Earth Planet. Sci. Lett.* **295**, 115–126.

Litasov K. D., Shatskiy A., Ohtani E. and Yaxley G. M. (2013) Solidus of alkaline carbonatite in the deep mantle. *Geology* **41**, 79–82.

Liu Q. and Lange R. A. (2003) New density measurements on carbonate liquids and the partial molar volume of the CaCO3 component. *Contrib. to Mineral. Petrol.* **146**, 370–381.

Markgraf S. and Reeder R. (1985) High-temperature structure refinements of calcite and magnesite. *Am. Miner.* **70**, 590–600.

Nosé S. (1984) A unified formulation of the constant temperature molecular dynamics methods. *J. Chem. Phys.* **81**, 511.

O'Leary M. C., Lange R. A. and Ai Y. (2015) The compressibility of $CaCO_3$-Li_2CO_3-Na_2CO_3-K_2CO_3 liquids: Application to natrocarbonatite and CO_2-bearing nephelinite liquids from Oldoinyo Lengai. *Contrib. to Mineral. Petrol.* **170**, 1-18.

Plimpton S. (1995) Fast parallel algorithm for short-range molecular dynamics. *J. Comput. Phys.***117,** 1-42.

Rea D. K. and Ruff L. J. (1996) Composition and mass flux of sediment entering the world's subduction zones: Implications for global sediment budgets, great earthquakes, and volcanism. *Earth Planet. Sci. Lett.* **140**, 1–12.

Redfern S. A. T. and Angel R. J. (1999) High-pressure behaviour and equation of state of calcite, CaCO3. *Contrib. to Mineral. Petrol.* **134**, 102–106.

Roest D. L., Ballone P., Bedeaux D. and Kjelstrup S. (2017) Molecular dynamics simulations of metal/molten alkali carbonate interfaces. *J. Chem. Phys. C.***121**, 17827-17847.

Ross N. L. (1997) The equation of state and high-pressure behavior of magnesite. *Am. Mineral.* **82**, 682–688.

Rudnick R. L., McDonough W. F. and Chappell B. W. (1993) Carbonatite metasomatism in the northern Tanzanian mantle: petrographic and geochemical characteristics. *Earth Planet. Sci. Lett.* **114**, 463–475.

Sharygin I. S., Litasov K. D., Shatskiy A., Golovin A. V., Ohtani E. and Pokhilenko N. P. (2015) Melting phase relations of the Udachnaya-East Group-I kimberlite at 3.0-6.5GPa: Experimental evidence for alkali-carbonatite composition of primary kimberlite melts and implications for mantle plumes. *Gondwana Res.* **28**, 1391–1414.

Staudigel H., Hart S. R., Schmincke H. U. and Smith B. M. (1989) Cretaceous ocean crust at DSDP Sites 417 and 418: Carbon uptake from weathering versus loss by magmatic outgassing. *Geochim. Cosmochim. Acta* **53**, 3091–3094.

Thompson R., Smith P., Gibson S., Mattey D. and Dickin A. (2002) Ankerite carbonatite from Swartbooisdrif, Namibia: the first evidence for magmatic ferrocarbonatite. *Contrib. to Mineral. Petrol.* **143**, 377–396.

Vinograd V. L., Winkler B., Putnis A., Gale J. D. and Sluiter M. H. F. (2006) Static lattice energy calculations of mixing and ordering enthalpy in binary carbonate solid solutions. *Chem. Geol.* **225**, 304–313.

Wendlandt R. F. and Mysen B. O. (1980) Melting phase relations of natural peridotite + CO2 as a function of degree of partial melting at 15 and 30 kbar. *Am. Mineral.* **65**, 37–44.

Yaxley G. M., Crawford A. J. and Green D. H. (1991) Evidence for carbonatite metasomatism in spinel peridotite xenoliths from western Victoria, Australia. *Earth Planet. Sci. Lett.* **107**, 305–317.

Chapter 6 Conclusion

Carbonate phases play an important role in partial melting of the mantle. Carbonate can lower the solidus of peridotite by as much as 600° (Dasgupta and Hirschmann 2007). Near-solidus melts of carbonated mantle are carbonatitic (e.g. Dalton and Wood 1993), such melts are efficient agents of metasomatism (e.g., Wallace and Green 1988) due to their high affinity for incompatible elements (e.g., Dasgupta et al. 2009) and high mobility (e.g., Hunter and McKenzie). Carbonate liquid metasomatism is essential to the petrogenesis of alkalic ocean-island basalts, silica-undersaturated lavas (e.g., Dasgupta et al. 2006) and kimberlites (e.g., Pokhilenko et al. 2015). Low-degree partial melting of carbonated mantle is also responsible for surficial carbonatites (e.g., Harmer et al. 1998). Though carbonatites are relatively rare, they nonetheless serve as important economic deposits of rare-earth elements (e.g., Nikiforov et al. 2014). Carbonate melts also play a crucial role in the deep carbon cycle (e.g., Dasgupta and Hirschmann 2010) especially in regards to carbon storage in the lower mantle (e.g., Thomson et al. 2016).

Carbonate liquid in the mantle is produced by low-degree partial melting of CO_2-rich mantle rocks (e.g., peridotite and eclogite) (e.g., Dalton and Wood 1993; Hammouda 2003). The solidus of carbonated peridotite and eclogite has been extensively studied by phase equilibrium experiments (e.g., Falloon and Green 1989; Dalton and Wood 1993; Dalton and Presnall 1998; Hammouda 2003; Yaxley and Brey 2004; Dasgupta et al. 2006; Dasgupta and Hirshmann 2007; Brey et al. 2008; Ghosh et al 2009; Litasov and Ohtani 2010; Dasgupta et al. 2013). However,

small variations in starting composition of phase equilibrium experiments lead to large differences in the location of the solidus in P-T space (e.g., Dasgupta and Hirschmann 2010; Litasov et al. 2013).

Thermodynamic modelling software such as MELTS (Ghiorso et al. 2002) could resolve these issues, but requires the standard state thermodynamic properties of pure carbonate liquid components. $MgCO_3$ (and $FeCO_3$ to a lesser extent) are the carbonate liquid components of primary interest (e.g., Dalton and Wood 1993) to mantle partial melting. Currently there are no reliable constraints available in the literature on the standard thermodynamic properties of $MgCO_3$ or $FeCO_3$ liquid. This is due to the extremely low, 1 bar decarbonation temperature of $MgCO_3$ and $FeCO_3$ which inhibits formation of stable $MgCO_3$/$FeCO_3$-bearing liquids.

This dissertation provides some of the first estimates on the standard state thermodynamic properties of $MgCO_3$ liquid and (and $FeCO_3$ liquid by proxy). Estimates are made by a two-pronged approach. The first approach is an analysis of systematic variations in the volumetric properties of alkali and alkaline earth carbonate liquids. The second approach involves the development of an empirically-derived potential set for classical mechanics molecular dynamic simulations of $MgCO_3$ liquid.

An analysis of systematic variations in the 1 bar molar volumes of alkali and alkaline earth carbonate liquids (chapter 2) reveals a strong positive, linear trend between liquid molar volumes and cation volume (calculated from the ionic radius of the metal cation in each liquid). Alkali and alkaline earth liquids form two separate trends with two separate intercepts; because the intercept represents a metal cation volume of 0 it is taken as the partial molar volume of carbonate in the liquid. Alkali carbonate liquids have a more voluminous partial molar $(CO_3)^{2-}$ volume (38.3 ± 0.6 cm^3/mol) compared to alkaline earths (31.0 ± 0.1 cm^3/mol).

Differences in the partial molar volume of carbonate in the liquid arise from differences in structure. Alkali and alkaline earth carbonate liquids differ in their coordination of the metal cation with the carbonate; alkali metals assume a 4-fold coordination with carbonate (e.g., Roest et al. 2017) while alkaline earth metals are in 6-fold (see chapter 4). If Mg^{2+} and Fe^{2+} are in 6-fold coordination with carbonate, they would have a molar volume of 34.4(1) and 35.1(1) cm^3/mol respectively at 1100 K. However, molecular dynamic simulations (see chapter 5) suggest that, due to the small ionic radius of Mg^{2+}, it assumes a 4-fold coordination with carbonate and a liquid structure similar to alkali carbonate melts. Thus, the alkali trend would provide a better estimate of $MgCO^3$ molar volume at 1 bar giving an 1100 K volume of 40.0(6) cm^3/mol (which is comparable to the volume suggested by MD simulation results presented in chapter 5. Similarly, if Fe^{2+} in $FeCO_3$ liquid assumes a 4-fold coordination like Mg^{2+}, the molar volume of $FeCO_3$ liquid could be surprisingly voluminous (40.4 ± 0.6 cm^3/mol).

Analysis of systematic variations in the 1 bar compressibilities of alkali and alkaline earth liquids reveal that ΔV_{fusion} is an effective predictor of liquid compressibility. Assuming the $MgCO_3$ liquid volumes suggested in chapter 2, and assuming there is no metastable 1 bar high-temperature phase transitions in magnesite (there is no evidence for this), MgCO3 has the greatest ΔV_{fusion} among the alkaline earth carbonates. According to the strong correlation between β_T and ΔV_{fusion} its compressibility would be significantly larger than the other alkaline earth carbonate liquids. If Mg^{2+} in $MgCO_3$ liquid is in 6-fold coordination, the compressibility of $MgCO_3$ melt would be ~18(6) $10^{-2} \cdot GPa^{-1}$ at 1500 K. However, MD simulations (chapter 5) suggests Mg^{2+} is in 4-fold coordination with carbon, thus it may be more appropriate to use the trend for alkali carbonate liquids, giving an estimated compressibility of 22(2) $10^{-2} \cdot GPa^{-1}$ at

1100 K. In any case, the compressibility of $MgCO_3$ liquid is estimated to be dramatically greater than $CaCO_3$.

The strong relationship between liquid properties and liquid structure illustrated in chapters 2 and 3, underscore the need for computational MD studies of carbonate melts. Chapter 4 of this dissertation presents a new empirically-derived potential set for classical mechanical simulations of alkaline earth carbonate ($MgCO_3$, $CaCO_3$, $SrCO_3$, $BaCO_3$) liquids. While potential sets applicable to $CaCO_3$ liquid have been previously developed (e.g., Dove et al. 1992; Vuilleumier et al. 2014), there is no potential set well-suited to molecular dynamic simulations of $MgCO_3$ liquid currently available in the literature. To verify the model's applicability to alkaline earth liquids, various properties pure and mixed liquids in the $CaCO_3$-$SrCO_3$-$BaCO_3$ system were estimated by employing the potential set model to molecular dynamic simulations over a temperature and pressure range representative of the crust and upper mantle. The model generally over-estimates 1 bar molar volumes (2% for $CaCO_3$ and $SrCO_3$, 5% for $BaCO_3$), but at high pressure (>0.5 GPa for $CaCO_3$ and $SrCO_3$ and >2 GPa for $BaCO_3$) simulated volumes converge to values consistent with the experimental constraints presented in chapters 1 and 2 (i.e. 1 bar molar volumes, thermal expansion and compressibilities). The success of the model at recovering the known properties of $CaCO_3$, $SrCO_3$ and $BaCO_3$ liquids lends credibility to its simulations of $MgCO_3$ liquid (for which there are no direct experimental constraints).

Liquid structures and coordination environments for $CaCO_3$-$SrCO_3$-$BaCO_3$ liquids are also reported in chapter 4. The simulations point to a remarkable congruency in liquid structure for the $CaCO_3$, $SrCO_3$ and $BaCO_3$ melts. The biggest structural difference between these liquids and the alkali carbonates is the coordination of the metal cation with $(CO_3)^{2-}$ groups. Ca^{2+}, Sr^{2+}

and Ba^{2+} are in 6-fold coordination with carbon and the alkalis (Li^{+}, Na^{+} and K^{+}) are in 4-fold (e.g., Roest et al. 2017).

The simulations of $CaCO_3$-$SrCO_3$-$BaCO_3$ liquids also provide valuable constraints on mixing behavior. Molar volume, compressibility, enthalpy and heat capacity all mix ideally across the entire studied compositional, pressure and temperature range. This both corroborates experimental observations on mixing behavior and extends it to new properties (i.e. enthalpy and heat capacity) and new PT conditions.

Chapter 5 the potential set model to molecular dynamic simulations of pure and mixed $MgCO_3$ liquids. The simulations indicate that, at 1 bar, $MgCO_3$ liquid adopts a novel topology characterized by an "alkali-like" 4-fold coordination of Mg^{2+} with the $(CO_3)^{2-}$ groups. Like the alkali liquids, the simulated $MgCO_3$ liquid structure has a high partial molar volume of $(CO^3)^{2-}$; it is more voluminous and compressible than expected by systematic trends in the properties of alkaline earth carbonate liquids. The simulations suggest that the structure and properties of $MgCO_3$ liquid are more like the alkali carbonates than alkaline earths. Furthermore, the simulations show that in mixtures of $MgCO_3$ with $CaCO_3$, $SrCO_3$ or $BaCO_3$, Mg^{2+} preferentially surrounds itself with different metal ions (i.e. Ca^{2+}, Sr^{2+} or Ba^{2+}). This ordering of cations in the liquid results in non-ideal mixing of volumetric properties and a consistently negative ΔV_{mix} (meaning that MgCO3-bearing mixed liquids pack space more efficiently). As pressure increases, the structure of $MgCO_3$ liquid becomes more like the other alkaline earth carbonates—the cation ordering effect gradually diminishes with pressure (disappearing by 12 GPa) and $MgCO_3$ begins to mix near-ideally with other alkaline earth liquid components. However, non-ideal mixing in enthalpic properties (i.e. enthalpy and heat capacity) is significant ($\Delta H_{mix} > 10$ KJ/mol) both at 1 bar and at high pressure (to at least 12 GPa). Future experimental work

attempting to estimate the volumetric or enthalpic properties of pure $MgCO_3$ liquid from partial molar properties in an $MgCO_3$-bearing mixture should take special care to ensure those properties mix ideally.

6.1 Implications for $FeCO_3$ liquid and buoyancy of carbonatites in the mantle

$MgCO_3$ is a major component of carbonatitic melts produced by near-solidus partial melting of carbonated mantle (e.g., Dalton and Presnall 1998). The density of pure $CaCO_3$ liquid has often been employed in the literature as a proxy for carbonatite melt (e.g., Hammouda and Laporte 2000; Kono et al. 2014). However, this work predicts a relatively high molar volume and compressibility for $MgCO_3$ liquid which means that $MgCO_3$-rich carbonatite melts are significantly more buoyant than pure $CaCO_3$ liquid. The $MgCO_3$ component, which may constitutes up to 75 mol% of the carbonatite melt (Ghosh et al. 2009), has a significantly smaller density than $CaCO_3$ (ranging from 22% less dense at 1 bar, to 5% less dense at 12 GPa). Its low density could help explain the high ascent rates of primary carbonatite and kimberlite melts (e.g., Russell et al. 2012).

As demonstrated in chapter 2, many carbonate liquid properties (e.g., molar volume) track with ionic radius. Mg^{2+} has a similar ionic radius as Fe^{2+} (0.71 for Mg^{2+} and 0.77 for Fe^{2+} in four-fold coordination) therefore it's possible that $FeCO_3$ liquid shares many volumetric properties with $MgCO_3$ (i.e. 1 bar molar volume, compressibility and thermal expansion). In such case, the property predictions of $MgCO_3$ liquid presented here would serve as a proxy for $FeCO_3$.

$FeCO_3$ is the only common carbonate liquid component with the potential to affect a density crossover with the mantle (i.e. negative or neutral buoyancy). Some workers have posited that $FeCO_3$-rich carbonate melts (i.e. ferrocarbonatites) could sink or stagnate in the upper

mantle due to a negative buoyancy or equilibrium (Kang and Schmidt 2017). However, If $FeCO_3$ assumes the voluminous and compressible liquid structure of $MgCO_3$ proposed here, then even the most iron-rich ferrocarbonatites would be buoyant throughout the entire upper mantle and transition zone.

While considerations of buoyancy and ascent rates for mantle carbonatites hold some important implications for mobility and storage of carbon in the mantle, the true utility of the standard state thermodynamic properties of carbonate melt lies in their potential application to thermodynamic modelling software such as MELTS (Ghiorso et al. 2002). A self-consistent set of standard state thermodynamic properties for pure $MgCO_3$ (and $FeCO_3$) liquid, would allow thermodynamic models to simulate the full range of partial melting of the mantle in the presence of carbonate. In the mantle there are various mantle silicate compositions (e.g., lherzolite, peridotite and eclogite), variable carbonate compositions and a wide range of relevant temperatures and pressures. As important as phase equilibrium experiments are, they cannot possibly cover the full range of compositions, pressures and temperatures of interest. Integration of carbonate liquid components into thermodynamic modelling software is the end-goal for fundamental property determinations such as these. This would ultimately allow the effects of carbonate in the mantle to be more fully explored.

6.2 Future directions

The most pressing need now, in light of the $MgCO_3$ liquid properties presented here, is an analysis of the magnesite ($MgCO_3$) fusion curve. Currently, the temperature of fusion of $MgCO_3$ is known at four PT points (~1858 K at 3 GPa and 1883 K at 3.6 GPa from Irving and Wyllie 1975 and 2183 K at 8 GPa and 2363 K at 15 GPa from Katsura and Ito 1990). The thermodynamic properties for $MgCO_3$ liquid proposed here (chapter 5) can be combined with

those of magnesite (which are well known, e.g., Litasov et al. 2008) and its fusion curve can be calculated and compared to the four known data points. More experimental constraints on the $MgCO_3$ (and $FeCO_3$) fusion curve would improve this comparison and also allow for a full-fledged fusion curve analysis. A sufficient number of experimental constraints on the $MgCO_3$ fusion curve would also allow the standard state thermodynamic properties of $MgCO_3$ liquid to be independently calculated. The minimum number of experimental constraints must exceed the number of estimated properties. A full set of standard state thermodynamic properties must include: $V_{0,ref}$ (the 1 bar molar volume at reference temperature), α (the 1 bar thermal expansion and possibly an additional linear temperature-dependence term), $K_{0,ref}$ (the 1 bar bulk modulus at reference temperature), $\delta K_0/\delta T$ (1 bar temperature –dependence of bulk modulus), K' (the pressure-dependence of bulk modulus), C_P (the isobaric heat capacity of the liquid), ΔH_{fusion} (the latent heat of fusion) and T_{fusion} (the temperature of fusion). Thus, a minimum of 9 experimental constraints on the $MgCO_3$ fusion curve must be available to independently estimate the properties of $MgCO_3$ liquid—more constraints would significantly shrink errors on such property estimates. Such constraints need also be sensitive to the relevant parameters.

Sink-float experiments are also an important next-step. This dissertation has compared three different possibilities for the volumetric properties of $MgCO_3$ liquid. The first model is based on systematics and assumes Mg^{2+} is in 6-fold coordination with carbonate groups, making it similar to the other alkaline-earth carbonate liquids and thus the stiffest and most compact of the three proposals. The second model is also based on systematics and assumes Mg^{2+} is in 4-fold coordination with the carbonates and is thus more similar to the alkali carbonate liquids. The final model is based on MD simulations of the potential set model from chapter 4 and is the most buoyant. The $MgCO_3$ liquid densities predicted by the three models at 1858 K (the lowest

temperature of congruent melting for $MgCO_3$) from 3-5 GPa are compared in Fig. 6.1. The density prediction from MD is very close to the one from 4-fold systematics. However, the density contrast between MD/4-fold systematics and 6-fold systematics is large enough at these pressures to successfully differentiate between various models with sink-float experiments.

Figure 6.1 The densities of $MgCO_3$ liquid at 1858 K from 3-5 GPa predicted by the various models presented in this dissertation. The blue line is based on constraints from systematics and assumes Mg^{2+} is in 6-fold coordination with the carbonate groups. The red line is also based on systematics but assumes Mg^{2+} is in 4-fold coordination with carbonate molecules (similar to alkali carbonate liquids). The black line is the density predicted by the equation of state based on MD simulations presented in chapter 5 (which suggests that Mg-C coordination is 4-fold). The density contrast is large enough that sink-float experiments could successfully differentiate between 6-fold and 4-fold models.

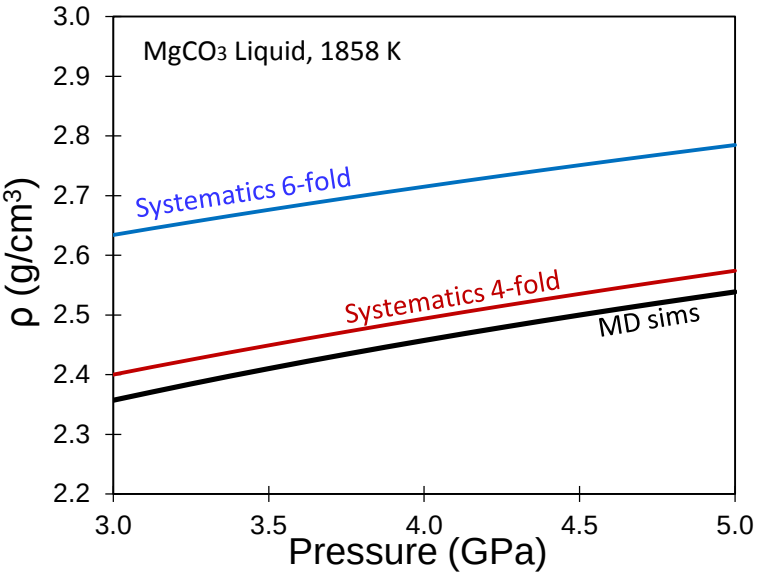

Sink/float experiments are ideal for this liquid (Knoche and Luth 1996) since the fusion temperature at 3-3.6 GPa is known (Irving and Wyllie 1975), the viscosity of the liquid is very low (e.g., Kono et al. 2014) and there are already broad constraints on liquid density.

Another experiment that could provide valuable insights into the structure of $MgCO_3$ and $FeCO_3$ melt is multi-angle energy dispersive X-ray diffraction. This technique can obtain liquid pdf curves at high pressure from which metal cation coordination with oxygen could be calculated. A determination of metal cation-carbon coordination would indicate which of the

systematic trends (described in chapters 2 and 3) apply to $FeCO_3$ melt. Unfortunately, the elements are too light in $MgCO_3$ liquid to yield an accurate reading, however a constraint on Fe-O coordination in $FeCO_3$ liquid could hold implications for the coordination environment in $MgCO_3$ melt given the similar ionic radius.

6.3 References

Brey G. P., Bulatov V. K., Girnis A. V. and Lahaye Y. (2008) Experimental melting of carbonated peridotite at 6-10 GPa. *J. Petrol.* **49**, 797–821.

Dalton J. and Presnall D. C. (1998) Carbonatitic melts along the solidus of model lherzolite in the system CaO-MgO-Al_2O_3-SiO_2-CO_2 from 3 to 7 GPa. *Contrib. to Mineral. Petrol.* **131**, 123–135.

Dalton J. A. and Wood B. J. (1993) The compositions of primary carbonate melts and their evolution through wallrock reaction in the mantle. *Earth Planet. Sci. Lett.* **119**, 511–525.

Dasgupta R., Hirschmann M. M. and Stalker K. (2006) Immiscible transition from carbonate-rich to silicate-rich melts in the 3 GPa melting interval of eclogite + CO_2 and genesis of silica-undersaturated ocean island lavas. *J. Petrol.* **47**, 647–671.

Dasgupta R. and Hirschmann M. M. (2007) Effect of variable carbonate concentration on the solidus of mantle peridotite. *Am. Mineral.* **92**, 370–379.

Dasgupta R. and Hirschmann M. M. (2010) The deep carbon cycle and melting in Earth's interior. *Earth Planet. Sci. Lett.* **298**, 1–13.

Dasgupta R., Hirschmann M. M., McDonough W. F., Spiegelman M. and Withers A. C. (2009) Trace element partitioning between garnet lherzolite and carbonatite at 6.6 and 8.6 GPa with applications to the geochemistry of the mantle and of mantle-derived melts. *Chem. Geol.* **262**, 57–77.

Dasgupta R., Mallik A., Tsuno K., Withers A. C., Hirth G. and Hirschmann M. M. (2013) Carbon-dioxide-rich silicate melt in the Earth's upper mantle. *Nature* **493**, 211-222.

Falloon T. J. and Green D. H. (1989) The solidus of carbonated, fertile peridotite. *Earth Planet. Sci. Lett.* **94**, 364–370.

Ghiorso M. S., Hirschmann M. M., Reiners P. W. and Kress V. C. (2002) The pMELTS: A revision of MELTS for improved calculation of phase relations and major element partitioning related to partial melting of the mantle to 3 GPa. *Geochemistry Geophys. Geosystems* **3**, 36.

Ghosh S., Ohtani E., Litasov K. D. and Terasaki H. (2009) Solidus of carbonated peridotite from 10 to 20 GPa and origin of magnesiocarbonatite melt in the Earth's deep mantle. *Chem. Geol.* **262**, 17–28.

Hammouda T. (2003) High-pressure melting of carbonated eclogite and experimental constraints on carbon recycling and storage in the mantle. *Earth Planet. Sci. Lett.* **214**, 357–368.

Harmer R. E., Lee C. A. and Eglington B. M. (1998) A deep mantle source for carbonatite magmatism: evidence from the nephelinites and carbonatites of the Buhera district, SE Zimbabwe. *Earth Planet. Sci. Lett.* **158**, 131–142.

Hunter R. H. and McKenzie D. (1989) The equilibrium geometry of carbonate melts in rocks of mantle composition. *Earth Planet. Sci. Lett.* **92**, 347–356.

Irving A. J. and Wyllie P. J. (1975) Subsolidus and melting relationships for calcite, magnesite and the join $CaCO_3$-$MgCO_3$ 36 kb. *Geochim. Cosmochim. Acta* **39**, 35–53.

Kang N. and Schmidt M. W. (2017) The melting of subducted banded iron formations. *Earth Planet. Sci. Lett.* **476**, 165–178.

Katsura T. and Ito E. (1990) Melting and subsolidus phase relations in the $MgSiO_3$-$MgCO_3$ system at high pressures: implications to evolution of the Earth's atmosphere. *Earth Planet. Sci. Lett.* **99**, 110–117.

Knoche R. and Luth R. W. (1996) Density measurements on melts at high pressure using the sink/float method: Limitations and possibilities. *Chem. Geol.* **128**, 229–243.

Kono Y., Kenney-Benson C., Hummer D., Ohfuji H., Park C., Shen G., Wang Y., Kavner A. and Manning C. E. (2014) Ultralow viscosity of carbonate melts at high pressures. *Nat. Commun.* **5**, 1-7.

Litasov K. D., Fei Y., Ohtani E., Kuribayashi T. and Funakoshi K. (2008) Thermal equation of state of magnesite to 32 GPa and 2073 K. *Phys. Earth Planet. Inter.* **168**, 191–203.

Litasov K. and Ohtani E. (2010) The solidus of carbonated eclogite in the system CaO-Al_2O_3-MgO-SiO_2-Na_2O-CO_2 to 32 GPa and carbonatite liquid in the deep mantle. *Earth Planet. Sci. Lett.* **295**, 115–126.

Litasov K. D., Shatskiy A., Ohtani E. and Yaxley G. M. (2013) Solidus of alkaline carbonatite in the deep mantle. *Geology* **41**, 79–82.

Nikiforov A. V, Öztürk H., Altuncu S. and Lebedev V. A. (2014) Kizilcaören ore-bearing complex with carbonatites (northwestern Anatolia, Turkey): Formation time and mineralogy of rocks. *Geol. Ore Depos.* **56**, 35–60.

Pokhilenko N. P., Agashev A. M., Litasov K. D. and Pokhilenko L. N. (2015) Carbonatite metasomatism of peridotite lithospheric mantle: Implications for diamond formation and carbonatite-kimberlite magmatism. *Russ. Geol. Geophys.* **56**, 280–295.

Russell J. K., Porritt L. A., Lavallé Y. and Dingwell D. B. (2012) Kimberlite ascent by assimilation-fuelled buoyancy. *Nature* **481**, 352–356.

Thomson A. R., Walter M. J., Kohn S. C. and Brooker R. A. (2016) Slab melting as a barrier to deep carbon subduction. *Nature* **529**, 76–79.

Wallace M. E. and Green D. H. (1988) An experimental determination of primary carbonatite magma composition. *Nature* **335**, 343-346.

Yaxley G. M. and Brey G. P. (2004) Phase relations of carbonate-bearing eclogite assemblages from 2.5 to 5.5 GPa: Implications for petrogenesis of carbonatites. *Contrib. to Mineral. Petrol.* **146**, 606–619.

APPENDIX

Figure A.1 The isobaric heat capacities of Li_2CO_3, Na_2CO_3 and K_2CO_3 as a function of cation volume. The trend is extrapolated to Rb_2CO_3 and Cs_2CO_3 to give an estimate of their C_P for use in Eq. 3.2.

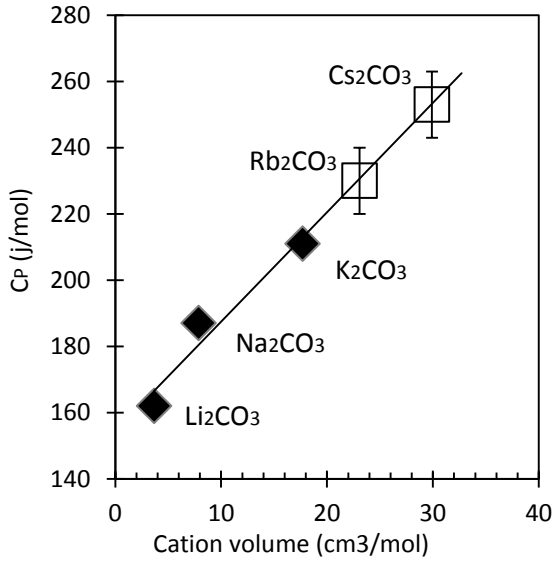

Table A.1 Crystal structure training data: Experimentally measured data for crystals structures used to fit potential parameters are shown along with the corresponding values predicted by the final model by both internal energy (0 K) and free energy (300 K) optimization. Free energy accounts for energy contributions from zero point energy, entropy, and phonons. The percent residual is the difference between adjusted experimental value and the predicted value at 0 K. Atomic positions were also used in fitting but are omitted here. Unit cell volume is provided for convenience, but was not explicitly used in fitting.

Structure	Parameter description	Experimental (300 K)	Adjusted Exp. (0 K)	Calculated (300 K)	Calculated (0 K)	Percent residual
Calcite 0 GPa						
$CaCO_3$	Cell Parameters (Å)					
$R\bar{3}c$	a,b	4.989[a]	4.977	4.922	4.910	-1.3
	c	17.044[a]	16.891	17.097	16.944	0.3
	Cell Volume ($Å^3$)	367.4	362.4	358.7	353.8	-2.4
	Elastic Constants (GPa)					
	C_{11}	145.7[b]	153.0	175.4	184.2	20.4
	C_{33}	85.3[b]	88.4	89.9	93.2	5.4
	C_{44}	33.4[b]	34.7	39.8	41.4	19.2
	C_{12}	55.9[b]	60.3	58.3	62.9	4.3
	C_{13}	53.5[b]	58.5	55.9	61.1	4.5
	C_{14}	-20.5[b]	-22.8	18.2	20.2	-188.8
	Bulk Modulus (GPa)	67[a]	71	82	87	22.4
Calcite 0.68 GPa						
	Cell Parameters (Å)					
	a,b	4.985[a]	4.974	4.914	4.903	-1.4
	c	16.903[a]	16.755	17.002	16.853	0.6
	Cell Volume ($Å^3$)	363.8	359.0	355.6	350.9	-2.3
Calcite 1.10 GPa						
	Cell Parameters (Å)					
	a,b	4.977[a]	4.966	4.910	4.899	-1.3
	c	16.834[a]	16.688	16.945	16.798	0.7
	Cell Volume ($Å^3$)	361.1	356.4	353.8	349.2	-2.0
Calcite 1.75 GPa						
	Cell Parameters (Å)					
	a,b	4.965[a]	4.955	4.904	4.894	-1.2
	c	16.801[a]	16.656	16.860	16.714	0.4
	Cell Volume ($Å^3$)	358.7	354.2	351.1	346.7	-2.1
Magnesite 0 GPa						
$MgCO_3$	Cell Parameters (Å)					
$R\bar{3}c$	a,b	4.636[b]	4.612	4.564	4.540	-1.6
	c	15.017[b]	14.845	15.160	14.986	1.0
	Cell Volume ($Å^3$)	279.5	273.4	273.5	267.5	-2.1
	Elastic Constants (GPa)					

	C_{11}	260.3[c]	289.9	231.6	257.9	-11.0
	C_{12}	82.9[c]	85.4	99.9	102.9	20.5
	C_{13}	59.6[c]	71.0	34.9	41.6	-41.4
	C_{14}	-20.1[c]	-4.0	-3.5	-0.7	-82.6
	C_{33}	153.7[c]	167.8	153.2	167.3	-0.3
	C_{44}	59.7[c]	65.4	39.5	43.3	-33.8
	Bulk Modulus (GPa)	107[a]	119	101	112	-5.6
Magnesite 1.3 GPa						
	Cell Parameters (Å)					
	a,b	4.618[a]	4.596	4.549	4.527	-1.5
	c	14.952[a]	14.796	15.052	14.895	0.7
	Cell Volume ($Å^3$)	276.1	270.6	269.7	264.3	-2.3
Magnesite 4.0 GPa						
	Cell Parameters (Å)					
	a,b	4.592[a]	4.572	4.523	4.503	-1.5
	c	14.784[a]	14.649	14.859	14.723	0.5
	Cell Volume ($Å^3$)	270.0	265.2	263.3	258.6	-2.5
Magnesite 5.96 GPa						
	Cell Parameters (Å)					
	a,b	4.578[a]	4.560	4.506	4.488	-1.6
	c	14.679[a]	14.555	14.737	14.613	0.4
	Cell Volume ($Å^3$)	266.4	262.1	259.1	254.9	-2.7
Magnesite 6.99 GPa						
	Cell Parameters (Å)					
	a,b	4.568[a]	4.551	4.497	4.480	-1.6
	c	14.590[a]	14.471	14.678	14.558	0.6
	Cell Volume ($Å^3$)	263.7	259.5	257.1	253.0	-2.5
Magnesite 8.06 GPa						
	Cell Parameters (Å)					
	a,b	4.561[a]	4.545	4.489	4.473	-1.6
	c	14.519[a]	14.405	14.622	14.507	0.7
	Cell Volume ($Å^3$)	261.6	257.7	255.2	251.4	-2.4
Aragonite 0 GPa						
$CaCO_3$	Cell Parameters (Å)					
Pmcn	a	4.9596[d]	4.949	4.9988	4.9880	0.8
	b	7.9644[d]	7.853	8.0663	7.9531	1.3
	c	5.7416[d]	5.675	5.6961	5.6301	-0.8
	Cell Volume ($Å^3$)	226.79	220.5	229.68	223.35	1.3
	Elastic Constants (GPa)					
	C_{11}	85.0[e]	92.2	89.5	97.1	5.3
	C_{22}	159.6[e]	173.6	201.1	218.8	26.0
	C_{33}	87.0[e]	93.9	103.7	111.9	19.2
	C_{44}	42.7[e]	46.2	45.2	48.9	5.9

	C_{55}	41.3[e]	46.2	39.8	44.5	-3.6
	C_{66}	25.6[e]	28.8	26.2	29.5	2.3
	Bulk Modulus (GPa)	68.9[f]	79.5	64.3	74.2	-6.7
Aragonite 3.8 GPa						
	Cell Parameters (Å)					
	a	5.602[g]	5.537	5.551	5.487	-0.9
	b	7.846[g]	7.765	7.920	7.838	0.9
	c	4.913[g]	4.904	4.962	4.953	1.0
	Cell Volume ($Å^3$)	215.9	210.8	218.2	213.0	1.1
Aragonite 9.9 GPa						
	Cell Parameters (Å)					
	a	5.429[g]	5.378	5.356	5.306	-1.3
	b	7.711[g]	7.685	7.747	7.721	0.5
	c	4.8511[g]	4.839	4.924	4.9116	1.5
	Cell Volume ($Å^3$)	203.1	200.0	204.3	201.2	0.6
Aragonite 19.5 GPa						
	Cell Parameters (Å)					
	a	5.216[g]	5.170	5.132	5.087	-1.6
	b	7.580[g]	7.579	7.635	7.634	0.7
	c	4.7749[g]	4.760	4.8718	4.8571	2.0
	Cell Volume ($Å^3$)	188.8	186.5	190.9	188.6	1.1
Aragonite 27.9 GPa						
	Cell Parameters (Å)					
	a	5.076[g]	5.045	4.975	4.929	-2.3
	b	7.504[g]	7.497	7.094	7.615	1.6
	c	4.7168[g]	4.700	4.975	4.8118	2.4
	Cell Volume ($Å^3$)	179.7	177.8	175.6	180.6	1.6
Aragonite 34.8 GPa						
	Cell Parameters (Å)					
	a	4.948[g]	4.921	-	4.817	-2.1
	b	7.507[g]	7.500	-	7.618	1.6
	c	4.663[g]	4.647	-	4.817	3.7
	Cell Volume ($Å^3$)	173.21	171.5	-	176.8	3.1
Dolomite 0.03 GPa						
$CaMg(CO_3)_2$	Cell Parameters (Å)					
$R\bar{3}$	a,b	4.804[h]	4.784	4.752	4.732	-1.1
	c	15.997[h]	15.840	15.906	15.750	-0.6
	Cell Volume ($Å^3$)	319.7	313.8	311.1	305.4	-2.7
	Elastic Constants (GPa)					
	C_{11}	204.1[c]	220.0	213.4	230.0	4.6
	C_{12}	68.5[c]	73.0	71.2	75.9	3.9
	C_{13}	45.8[c]	51.8	49.5	56.0	8.1

	C_{14}	20.6[c]	27.5	6.6	8.8	-68.0
	C_{15}	6.7[c]	7.2	-15.4	-16.5	-329.9
	C_{33}	97.4[c]	103.7	112.1	119.4	15.1
	C_{44}	39.1[c]	41.8	39.5	42.2	1.0
	Bulk Modulus (GPa)	90.7[h]	98.3	92.3	100	1.8
Strontianite 0 GPa						
$SrCO_3$	Cell Parameters (Å)					
Pmcn						
	a	5.0914[d]	5.060	-	5.1073	0.9
	b	8.3519[d]	8.192	-	8.3626	2.1
	c	5.9901[d]	5.889	-	5.9933	1.8
	Cell Volume ($Å^3$)	254.72	244.1	-	255.98	4.9
	Bulk Modulus (GPa)	62[i]	78	-	70	-10.3
Strontianite 1.0 GPa						
	Cell Parameters (Å)					
	a	5.0659[i]	5.041	-	5.0966	1.1
	b	8.3940[i]	8.322	-	8.3406	0.2
	c	5.9604[i]	5.891	-	5.9317	0.7
	Cell Volume ($Å^3$)	253.46	247.1	-	252.15	2.0
Strontianite 1.7 GPa						
	Cell Parameters (Å)					
	a	5.0592[i]	5.036	-	5.0900	1.1
	b	8.3806[i]	8.321	-	8.3277	0.1
	c	5.9367[i]	5.872	-	5.8893	0.3
	Cell Volume ($Å^3$)	251.71	246.0	-	249.64	1.5
Strontianite 2.3 GPa						
	Cell Parameters (Å)					
	a	5.0514[i]	5.028	-	5.0847	1.1
	b	8.3714[i]	8.318	-	8.3183	0.0
	c	5.9209[i]	5.859	-	5.8534	-0.1
	Cell Volume ($Å^3$)	250.38	245.1	-	247.58	1.0
Strontianite 3.4 GPa						
	Cell Parameters (Å)					
	a	5.0376[i]	5.016	5.0249	5.0758	1.2
	b	8.3275[i]	8.284	8.3835	8.3047	0.3
	c	5.8595[i]	5.802	5.5191	5.7883	-0.2
	Cell Volume ($Å^3$)	245.81	241.1	232.50	243.99	1.2
Strontianite 4.3 GPa						
	Cell Parameters (Å)					
	a	5.0286[i]	5.007	5.0909	5.0691	1.2
	b	8.3053[i]	8.262	7.5154	8.2968	0.4
	c	5.8199[i]	5.763	6.1664	5.7354	-0.5
	Cell Volume	243.06	238.4	235.93	241.22	1.2

	($Å^3$)					
Strontianite 5.7 GPa						
	Cell Parameters (Å)					
	a	5.0202[i]	5.000	5.1137	5.0595	1.2
	b	8.2959[i]	8.266	8.5510	8.2899	0.3
	c	5.8114[i]	5.758	5.4773	5.6538	-1.8
	Cell Volume ($Å^3$)	242.03	238.0	239.5	237.14	-0.3
Strontianite 7.0 GPa						
	Cell Parameters (Å)					
	a	4.9972[i]	4.977	5.0714	5.0513	1.5
	b	8.2354[i]	8.237	8.2871	8.2889	0.6
	c	5.7209[i]	5.654	5.6447	5.5786	-1.3
	Cell Volume ($Å^3$)	235.44	231.8	237.23	233.57	0.8
Strontianite 8.2 GPa						
	Cell Parameters (Å)					
	a	4.9783[i]	4.996	5.0262	5.0440	1.0
	b	8.1927[i]	8.167	8.3172	8.2916	1.5
	c	5.6911[i]	5.627	5.5721	5.5098	-2.1
	Cell Volume ($Å^3$)	232.12	229.6	232.94	230.44	0.4
Strontianite 9.1 GPa						
	Cell Parameters (Å)					
	a	4.9707[i]	4.952	-	5.0387	1.8
	b	8.1789[i]	8.161	-	8.2957	1.6
	c	5.6622[i]	5.613	-	5.4589	-2.8
	Cell Volume ($Å^3$)	230.20	226.8	-	228.18	0.6
Witherite 0 GPa						
$BaCO_3$	Cell Parameters (Å)					
Pmcn	a	5.3193[d]	5.298	5.3323	5.3109	0.2
	b	8.9056[d]	8.853	8.8651	8.8129	-0.5
	c	6.4353[d]	6.351	6.5692	6.4832	2.1
	Cell Volume ($Å^3$)	304.85	297.9	310.54	303.44	1.9
	Bulk Modulus (GPa)	48[i]	52	46	50	-4.2
Witherite 0.2 GPa						
	Cell Parameters (Å)					
	a	5.2864[i]	5.275	5.3191	5.3077	0.6
	b	8.9371[i]	8.865	8.8770	8.8054	-0.7
	c	6.4363[i]	6.347	6.5560	6.4652	1.9
	Cell Volume ($Å^3$)	304.08	296.8	309.56	302.16	1.8
Witherite 0.8 GPa						
	Cell Parameters (Å)					
	a	5.2750[i]	5.260	-	5.2988	0.7
	b	8.9107[i]	8.888	-	8.7850	-1.2

	c	6.3821[i]	6.357	-	6.4115	0.9
	Cell Volume ($Å^3$)	299.98	297.2	-	298.46	0.4
Witherite 2.0 GPa						
	Cell Parameters (Å)					
	a	5.2447[i]	5.236	5.2924	5.2841	0.9
	b	8.8894[i]	8.838	8.8030	8.7524	-1.0
	c	6.2842[i]	6.209	6.3818	6.3050	1.6
	Cell Volume ($Å^3$)	292.98	287.3	297.32	291.60	1.5
Witherite 2.9 GPa						
	Cell Parameters (Å)					
	a	5.2299[i]	5.216	-	5.2753	1.1
	b	8.8445[i]	8.826	-	8.7349	-1.0
	c	6.2331[i]	6.211	-	6.2246	0.2
	Cell Volume ($Å^3$)	288.32	285.9	-	286.82	0.3
Witherite 4.1 GPa						
	Cell Parameters (Å)					
	a	5.2158[i]	5.210	5.2724	5.2661	1.1
	b	8.8059[i]	8.769	8.7574	8.7209	-0.6
	c	6.1585[i]	6.089	6.1843	6.1149	0.4
	Cell Volume ($Å^3$)	282.86	278.194	285.54	280.83	0.9
Witherite 5.1 GPa						
	Cell Parameters (Å)					
	a	5.2088[i]	5.204	5.2652	5.2603	1.1
	b	8.7873[i]	8.705	8.8002	8.7173	0.1
	c	6.1052[i]	6.082	6.0431	6.0201	-1.0
	Cell Volume ($Å^3$)	279.44	275.498	280.01	276.06	0.2
Huntite						
$Mg_3Ca(CO_3)_4$	Cell Parameters (Å)					
$R32$	a,b	9.5027[j]	9.478	9.3648	9.3406	-1.5
	c	7.8212[j]	7.731	7.7781	7.6881	-0.6
	Cell Volume ($Å^3$)	611.6	601.453	590.7	580.9	-3.4
Vaterite						
$CaCO_3$	Cell Parameters (Å)					
$P6_522$ [k]	a,b	7.290[k]	7.257	7.2360	7.203	-0.7
	c	25.302[k]	25.209	24.640	24.549	-2.6
	Cell Volume ($Å^3$)	1164	1149.411	1117	1103	-4.0
Paralstonite $CaBa(CO_3)_2$						
$P321$	Cell Parameters (Å)					
	a,b	8.692[l]	8.640	8.725	8.673	0.4
	c	6.148[l]	6.067	6.182	6.101	0.6
	Cell Volume ($Å^3$)	402.3	392.233	407.6	397.4	1.3
Barytocalcite						

$BaCa(CO_3)_2$	Cell Parameters (Å)					
$P\,2_1/m$ [m]	a	8.092[m]	7.891	8.335	8.128	3.0
	b	5.2344[m]	5.245	5.214	5.225	-0.4
	c	6.544[m]	6.433	6.605	6.493	0.9
	Cell Volume ($Å^3$)	266.4	256.824	275.4	265.5	3.4
	β (°)	106.05[m]	105.322	106.4	105.67	0.3
Norsethite						
$BaMg(CO_3)_2$	Cell Parameters (Å)					
$R32$	a,b	5.022[n]	5.015	5.007	5.000	-0.3
	c	16.770[n]	16.478	16.696	16.405	-0.4
	Cell Volume ($Å^3$)	366.3	358.923	362.5	355.2	-1.0

[a]Zhang and Reeder, 1999; [b]Dandekar and Ruoff, 1968; [c]Chen et al., 2006; [d]Ye et al., 2012; [e]Hearmon, 1946; [f]Liu et al., 2005; [g]Palaich et al, 2016; [h]Martinez et al., 1996; [i]Wang et al., 2015; [j]Dollase and Reeder, 1986; [k]Wang and Becker, 2009; [l]Effenberger, 1986; [m]Dickens and Bowen, 1971; [n]Effenberger and Zemann, 1985

Table A.2 Mineral Test Data: Cell parameters and unit cell volumes of various crystal structures that were not used as model training data are shown. Also shown are the corresponding values calculated by our model through free energy optimization or MD in GULP. The percent residual is the percent difference between experimental and predicted values; the average percent residual is 1.41% which is on par with the training data demonstrating the applicability of the model to high temperature and high pressure phases.

	Cell Parameters	Experimental values (Å)	Predicted values (Å)	Percent residual
Magnesite 82.6 GPa	a,b	4.2783[a]	4.2329	-1.07%
	c	12.5461[a]	12.6452	0.79%
	Volume ($Å^3$)	198.88	196.21	-1.34%
Magnesite 773 K	a,b	4.650[b]	4.574	-1.63%
	c	15.186[b]	15.222	0.24%
	Volume ($Å^3$)	284.38	275.84	-3.00%
Calcite 1173 K	a,b	4.975[b]	4.941	-1.69%
	c	17.585[b]	17.760	1.00%
	Volume ($Å^3$)	376.9	375.4	-0.40%
Strontianite 1173 K	a	5.1419[c]	5.2248	1.61%
	b	8.503[c]	8.460	-0.51%
	c	6.29[c]	6.08	-3.32%
	Volume ($Å^3$)	269	275	-2.26%
Witherite 1073 K	a	5.3338[c]	5.3155	-0.34%
	b	8.9400[c]	8.9119	-0.31%
	c	6.7323[c]	6.7115	-0.31%
	Volume ($Å^3$)	321.28	317.93	-1.04%
$R3m$ $BaCO_3$ 1086 K	a	5.2212[c]	5.3923	3.28%
	c	10.4921[c]	9.9652	-5.02%
	Volume ($Å^3$)	247.70	250.94	1.31%
Pmmn Post-aragonite $BaCO_3$ 70 GPa	a	4.255[d]	4.360	2.46%
	b	4.895[d]	4.952	1.16%
	c	4.255[d]	4.232	-0.54%
	Volume ($Å^3$)	88.62	91.36	3.09%
Pmmn Post-aragonite $SrCO_3$ 14.5 GPa	a	4.652[d]	4.644	-0.17%
	b	5.043[d]	5.084	0.82%
	c	4.309[d]	4.294	-0.35%
	Volume ($Å^3$)	101.1	101.4	0.29%

[a] Fiquet et al. (2002)
[b] Markgraf and Reeder (1985)
[c] Nie et al. (2017)
[d] Arapan and Ahuja (2010)

Table A.3 The details of individual MD simulations of liquids are listed. Since absolute energies have little meaning in a simulation, the reported total energy and enthalpy are normalized relative to $CaCO_3$ at 1100 K and 0 GPa.

Temp (K)	Pressure (GPa)	Mol. Vol. (cm^3/mol)	Tot. Energy (kJ/mol)	Enthalpy (kJ/mol)
$CaCO_3$ Simulations				
1101(1)	0.00(2)	41.00(6)	0.0(5)	0.0(12)
1100(1)	0.01(1)	41.15(6)	0.6(5)	1.4(8)
1101(1)	0.50(1)	39.87(7)	-1.7(5)	19.1(10)
1101(1)	0.50(1)	39.87(7)	-1.7(5)	19.1(10)
1100(1)	5.02(1)	34.89(5)	-6.3(5)	169.0(7)
1100(1)	12.01(2)	31.77(5)	7.7(5)	389.6(9)
1103(1)	11.99(2)	31.80(5)	7.1(5)	388.5(9)
1498(1)	0.03(2)	43.66(7)	67.1(6)	68.7(14)
1501(2)	0.51(3)	42.02(8)	63.7(6)	85.3(15)
1501(1)	2.00(2)	38.98(7)	56.4(6)	134.4(10)
1499(2)	5.02(2)	35.99(6)	51.7(6)	232.5(13)
1498(2)	12.01(1)	32.34(6)	56.2(5)	444.8(7)
1621(1)	0.03(4)	43.89(11)	84.9(6)	86.5(18)
1623(16)	0.13(35)	43.52(0)*	83.8(19)	89.7(19)
1623(2)	0.47(4)	42.83(8)	84.0(6)	104.1(21)
1630(9)	0.39(15)	41.54(10)	79.2(22)	95.3(52)
1750(1)	0.96(3)	42.15(7)	100.2(6)	140.7(16)
1751(2)	5.00(3)	36.73(6)	88.2(5)	271.9(13)
1750(2)	8.50(3)	34.43(6)	87.8(5)	380.4(12)
1772(18)	3.89(45)	37.91(0)*	94.0(22)	241.6(21)
1852(2)	4.94(3)	37.11(6)	103.7(6)	287.3(14)
1853(1)	8.47(4)	34.63(6)	101.9(6)	395.4(17)
1950(2)	1.02(2)	43.19(7)	130.7(6)	174.9(13)
1949(2)	4.97(3)	37.39(6)	117.8(6)	303.9(15)
1951(2)	7.01(2)	35.80(6)	116.1(6)	367.0(12)
1948(2)	8.45(3)	34.94(6)	116.1(5)	411.4(14)
2000(2)	0.03(3)	47.40(11)	147.9(6)	149.6(19)
2001(2)	5.00(3)	37.55(6)	124.7(6)	312.4(16)
1999(2)	11.99(3)	33.34(6)	125.8(6)	525.5(14)
1998(2)	19.97(2)	30.76(6)	138.2(6)	752.5(9)
1999(2)	29.98(2)	28.75(5)	166.0(5)	1027.9(9)
2076(22)	10.65(53)	34.04(0)*	134.7(24)	497.4(23)
2197(2)	23.98(4)	30.06(6)	173.4(6)	894.2(15)
3398(3)	12.01(6)	35.80(6)	313.1(7)	743.3(26)
3401(3)	43.02(5)	28.14(5)	383.0(7)	1593.5(16)
**denotes NVT ensemble*				
$SrCO_3$ Simulations				
1099(1)	0.01(1)	45.26(6)	107.0(5)	107.7(11)
1100(1)	0.49(1)	43.97(6)	104.4(5)	126.0(8)
1099(1)	1.51(2)	42.14(6)	100.6(5)	164.2(10)
1100(1)	2.00(1)	41.41(6)	99.0(5)	182.1(8)
1100(1)	5.00(2)	38.56(6)	98.4(5)	291.3(10)
1100(1)	8.50(2)	36.56(5)	105.0(5)	416.1(12)

	1101(1)	12.01(4)	35.10(5)	113.6(5)	535.3(18)
	1099(1)	24.00(1)	32.01(5)	158.1(5)	926.5(6)
	1302(2)	8.49(1)	36.84(5)	129.6(6)	442.7(7)
	1499(1)	-0.02(2)	47.76(8)	171.8(6)	171.0(13)
	1501(1)	0.50(2)	46.35(7)	168.9(6)	192.0(12)
	1500(2)	8.50(2)	37.27(5)	155.2(5)	472.3(10)
	1501(2)	14.99(1)	34.63(5)	170.9(5)	690.2(15)
	1498(2)	24.02(2)	32.33(5)	202.2(5)	978.9(12)
	1700(2)	8.49(4)	37.71(6)	182.7(5)	503.2(17)
	1900(2)	8.52(3)	38.26(6)	211.3(6)	537.5(16)
	2000(2)	0.04(3)	51.81(8)	253.2(6)	255.3(18)
	1999(2)	0.97(2)	47.96(7)	242.9(6)	289.9(14)
	1998(2)	5.02(2)	41.40(6)	227.2(6)	435.3(12)
	2001(2)	12.02(2)	36.68(5)	228.8(5)	669.8(12)
	2001(2)	29.99(3)	31.67(5)	280.5(6)	1230.6(13)
	2100(2)	8.57(3)	38.88(6)	240.6(6)	573.9(14)
	2200(2)	12.01(2)	37.06(6)	256.1(6)	701.2(12)
	2204(2)	20.00(2)	34.15(5)	272.0(6)	955.1(11)
	2299(2)	8.55(3)	39.40(6)	267.9(6)	604.8(14)
	3398(3)	11.95(5)	39.46(6)	417.0(7)	888.7(20)
			$BaCO_3$ Simulations		
	1100(1)	0.01(1)	53.53(7)	255.9(5)	256.7(10)
	1101(1)	0.51(1)	51.74(7)	252.6(5)	279.0(10)
	1099(1)	1.99(1)	48.02(6)	247.2(5)	343.1(11)
	1100(1)	4.99(1)	44.04(5)	247.3(5)	467.4(10)
	1100(1)	8.50(2)	41.16(5)	256.0(5)	606.1(14)
	1101(1)	11.99(1)	39.26(5)	268.3(5)	739.2(8)
	1100(1)	12.00(1)	39.17(5)	269.0(5)	739.3(7)
	1099(1)	20.00(1)	36.23(5)	306.5(5)	1031.0(7)
	1501(1)	0.02(2)	56.57(8)	318.0(6)	319.2(15)
	1499(2)	0.49(3)	54.61(8)	314.4(6)	341.1(20)
	1498(2)	1.99(2)	50.11(7)	306.7(6)	406.8(14)
	1499(2)	4.98(1)	45.38(6)	303.3(5)	529.5(9)
	1501(1)	8.51(2)	41.91(5)	307.3(5)	664.1(11)
	1500(1)	11.99(3)	39.85(5)	317.3(5)	795.1(17)
	1500(2)	19.97(2)	36.63(5)	351.6(5)	1083.2(11)
	2002(2)	-0.03(3)	61.30(10)	395.6(6)	394.2(22)
	1999(2)	0.98(4)	55.58(8)	383.8(6)	438.6(23)
	2004(2)	4.99(2)	46.92(6)	372.6(5)	607.1(14)
	2001(2)	8.49(3)	43.20(6)	375.0(6)	741.9(18)
	2001(2)	11.98(2)	40.84(6)	383.2(6)	872.7(14)
	2001(3)	20.05(2)	37.28(5)	410.2(7)	1157.7(12)
	1997(2)	30.02(2)	34.58(5)	455.5(6)	1493.5(11)
	2199(2)	8.54(5)	43.72(6)	401.8(6)	775.3(26)
	3002(1)	29.98(4)	35.68(6)	580.1(5)	1649.9(19)
Mol% $CaCO_3$			**$CaCO_3$-$SrCO_3$ Binary Simulations**		
26.02	1101(1)	0.00(2)	43.92(8)	78.7(5)	78.8(10)
48.98	1100(1)	0.00(1)	43.03(7)	53.8(5)	54.1(6)
79.01	1100(1)	-0.03(1)	41.93(7)	22.4(5)	21.2(6)
48.98	1099(1)	12.00(1)	33.50(7)	60.2(5)	462.2(6)
48.98	1501(2)	0.02(3)	45.86(8)	120.9(5)	121.9(16)

48.98	1999(1)	0.04(6)	49.57(10)	201.0(6)	203.0(29)
Mol% $CaCO_3$		**$CaCO_3$-$BaCO_3$ Binary Simulations**			
26.02	1101(1)	0.00(1)	50.21(9)	188.0(5)	188.2(11)
42.13	1101(1)	0.03(2)	48.38(10)	147.6(5)	149.0(15)
48.98	1100(1)	0.00(1)	47.42(8)	128.9(5)	128.9(13)
57.88	1098(1)	0.00(2)	46.29(10)	106.9(6)	106.9(13)
89.29	1099(1)	0.00(2)	42.17(8)	27.2(5)	27.2(14)
48.98	1100(1)	12.00(1)	35.57(7)	138.9(5)	565.8(11)
48.98	1501(2)	-0.03(1)	50.34(9)	194.0(5)	192.7(12)
48.98	1999(2)	-0.03(3)	54.37(11)	272.1(6)	270.7(22)
Mol% $SrCO_3$		**$SrCO_3$-$BaCO_3$ Binary Simulations**			
12.83	1100(1)	0.01(1)	52.63(8)	237.1(5)	237.7(10)
26.02	1101(1)	-0.01(2)	51.52(6)	217.6(5)	217.1(12)
48.98	1100(1)	0.00(1)	49.33(6)	182.8(6)	183.1(10)
48.98	1101(1)	0.01(1)	49.44(7)	183.5(5)	184.1(12)
79.01	1100(1)	0.00(2)	46.75(6)	137.6(5)	136.9(11)
48.98	1100(1)	12.00(1)	37.21(5)	192.8(5)	639.5(8)
48.98	1499(2)	0.01(3)	52.42(7)	246.9(6)	247.8(19)
48.98	2002(2)	-0.03(3)	56.76(9)	326.1(6)	324.4(18)

Table A.4 The complete simulation results are shown below. Total energy and Enthalpy are relative to their respective values for $MgCO_3$ at 1100 K and 0 GPa. 1 σ error on temperature is 2 K, 0.02 GPa for pressure, 0.1 cm^3/mol for volume, 0.2 KJ for total energy and 0.9 KJ for enthalpy.

	Temp. (K)	Press. (GPa)	Mol. Vol. (cm^3/mol)	Tot. Energy (KJ/mol)	Enthalpy (KJ/mol)
			Pure $MgCO_3$		
	773	0.00	43.10	-49	-49
	1100	0.00	44.48	0	0
	1499	0.00	46.46	61	61
	2000	0.00	47.98	136	136
	1099	0.49	40.52	-2	17
	900	1.99	35.39	-32	-
	1101	2.01	35.84	-2	70
	1500	2.02	36.85	58	132
	1869	2.98	35.89	112	219
	2273	3.58	35.97	170	299
	1101	4.99	31.74	2	160
	1101	5.00	31.74	3	161
	1501	5.00	32.66	61	224
	1100	8.00	29.71	8	245
	2274	8.05	31.96	173	430
	1099	12.01	28.03	17	353
	1500	11.99	28.67	72	416
	1099	15.01	27.14	25	432
	2000	14.95	28.41	147	571
	2373	15.00	28.95	197	631
Mol frac. $MgCO_3$			***$CaCO_3$-$MgCO_3$ Simulations***		
0.11	1100	0.00	41.06	196	195
0.12	1424	1.49	39.19	239	298
0.14	1424	1.49	39.28	236	294
0.15	1423	1.54	39.23	232	291
0.15	1372	9.98	32.23	223	544
0.17	1423	1.46	39.14	227	284
0.2	1523	2.21	38.28	235	319
0.21	1099	0.00	43.06	43	43
0.21	1101	0.00	41.62	174	173
0.22	1523	2.20	38.35	230	314
0.22	1523	2.20	38.35	230	314
0.26	1523	2.49	37.76	222	316
0.28	1573	2.83	37.47	224	329
0.29	1525	2.52	37.70	216	310
0.32	1573	2.84	37.33	217	322
0.32	1572	3.03	37.09	216	328
0.35	1518	2.98	36.71	200	309
0.35	1573	3.01	36.99	208	319
0.35	1572	3.01	36.88	208	318
0.4	1544	3.50	36.12	191	317
0.41	1519	2.98	36.59	187	296
0.42	1100	-0.01	41.94	126	125
0.44	1543	3.50	35.94	184	309

0.46	1563	4.00	35.44	183	324
0.51	1100	-0.01	42.06	105	104
0.51	1100	-0.01	42.06	105	104
0.51	1998	0.01	46.60	249	249
0.51	1100	0.50	40.05	104	124
0.51	1100	2.00	36.41	102	174
0.51	1799	2.98	37.15	207	317
0.51	1800	2.99	37.16	207	318
0.51	1573	4.98	34.42	176	347
0.51	1099	4.99	33.13	103	268
0.51	1603	5.02	34.54	181	354
0.51	1655	5.98	33.77	184	386
0.51	1100	8.00	31.33	108	358
0.51	1100	12.00	29.86	117	475
0.56	1703	7.03	33.03	183	414
0.58	1102	0.00	42.41	91	90
0.61	1873	14.97	29.62	205	648
0.76	1834	17.48	28.30	174	668
0.79	1099	0.00	43.06	43	43
0.87	1873	12.48	29.53	150	518
0.87	1821	13.54	29.12	145	538
$SrCO_3$-$MgCO_3$ Simulations					
0.11	1100	0.01	44.89	291	291
0.21	1100	0.00	44.66	257	256
0.26	1101	-0.01	44.60	240	239
0.42	1099	0.01	44.48	185	185
0.49	1100	11.99	31.51	172	549
0.51	1100	0.00	44.11	154	154
0.51	2000	0.03	48.71	299	300
0.58	1100	-0.01	43.93	131	131
0.74	1100	0.01	44.15	78	78
0.87	1100	0.00	44.11	36	36
$BaCO_3$-$MgCO_3$ Simulations					
0.11	1100	0.00	52.52	422	421
0.26	1101	0.00	51.18	346	346
0.42	1099	0.01	49.59	266	266
0.49	2000	-0.02	53.57	373	372
0.49	1099	12.00	33.60	247	650
0.58	1100	0.00	48.19	189	188
0.79	1099	0.00	46.04	89	88
0.89	1100	0.01	45.02	45	45

Table A.5 The volume and enthalpy results of MgCO3-bearing binary simulations at 1100 K and 1 bar are shown below. Ideal volumes and enthalpies and ΔV_{mix} *and* ΔH_{mix} calculated according to Eq. 7 and 8 are also listed.

Comp. Mol%$MgCO_3$	Mol. Vol. (cm^3/mol)	Ideal Vol. (cm^3/mol)	ΔV_{mix} (cm^3/mol)	Enthalpy (KJ/mol)	Ideal H (KJ/mol)	ΔH_{mix} (KJ/mol)
			$CaCO_3$-$MgCO_3$			
0.0	41.00	41.00	0.00	218.9	218.9	0.0
10.7	41.06	41.37	-0.31	195.7	195.5	0.2
21.0	41.62	41.73	-0.11	173.6	173.0	0.7
42.1	41.94	42.47	-0.53	125.6	126.7	-1.1
51.0	42.06	42.78	-0.71	105.4	107.2	-1.8
57.9	42.41	43.01	-0.61	90.5	92.2	-1.7
79.0	43.06	43.75	-0.69	43.4	46.0	-2.6
89.3	43.60	44.11	-0.50	21.5	23.5	-2.0
100.0	44.48	44.48	0.00	0.0	0.0	0.0
			$SrCO_3$-$MgCO_3$			
0.0	45.26	45.26	0.00	326.0	326.0	0.0
10.7	44.89	45.18	-0.29	290.8	291.1	-0.3
21.0	44.66	45.10	-0.44	256.5	257.6	-1.1
26.0	44.60	45.06	-0.46	239.9	241.2	-1.3
42.1	44.48	44.93	-0.45	184.8	188.7	-3.9
51.0	44.11	44.86	-0.76	154.4	159.7	-5.3
57.9	43.93	44.81	-0.88	131.4	137.3	-5.9
74.0	44.15	44.68	-0.53	78.1	84.8	-6.7
87.2	44.11	44.58	-0.47	36.1	41.8	-5.7
100.0	44.48	44.48	0.00	0.0	0.0	0.0
			$BaCO_3$-$MgCO_3$			
0.0	53.53	53.53	0.00	475.0	475.0	0.0
10.7	52.52	52.56	-0.04	422.2	424.1	-1.9
21.0	51.81	51.63	0.18	371.4	375.3	-3.9
26.0	51.18	51.17	0.00	346.4	351.4	-5.0
42.1	49.59	49.71	-0.12	266.3	274.9	-8.6
49.0	49.13	49.09	0.04	233.0	242.3	-9.3
57.9	48.19	48.29	-0.10	188.9	200.1	-11.2
79.0	46.04	46.38	-0.33	88.6	99.7	-11.1
89.3	45.02	45.45	-0.43	44.7	50.9	-6.2
100.0	44.48	44.48	0.00	0.0	0.0	0.0

Table A.6 Gives the coefficients fitted to Eq. 1 to describe both ΔVmix and ΔHmix calculated by our simulations of liquids in each of the three binaries at 1100 K and 1 bar.

	ΔV_{mix}	(cm^3/mol)	ΔH_{mix}	(KJ/mol)
	W_0	W_1	W_0	W_1
$CaCO_3$-$MgCO_3$	0.48	-6.78	10.43	-35.51
$SrCO_3$-$MgCO_3$	-1.74	-3.77	8.38	-62.56
$BaCO_3$-$MgCO_3$	1.89	-6.47	6.28	-92.95

Figure A.2 PDF curves for M-O, C-C and M-C pairs in pure liquids are unchanged by mixing**.** The coordination of M^{2+} with oxygen atoms and carbonate groups is unaffected by the composition of the liquid. The carbon-carbon pdf curve changes when Mg^{2+} is introduced into the mix but remains a weighted average of the two endmember components (Fig. A.3).

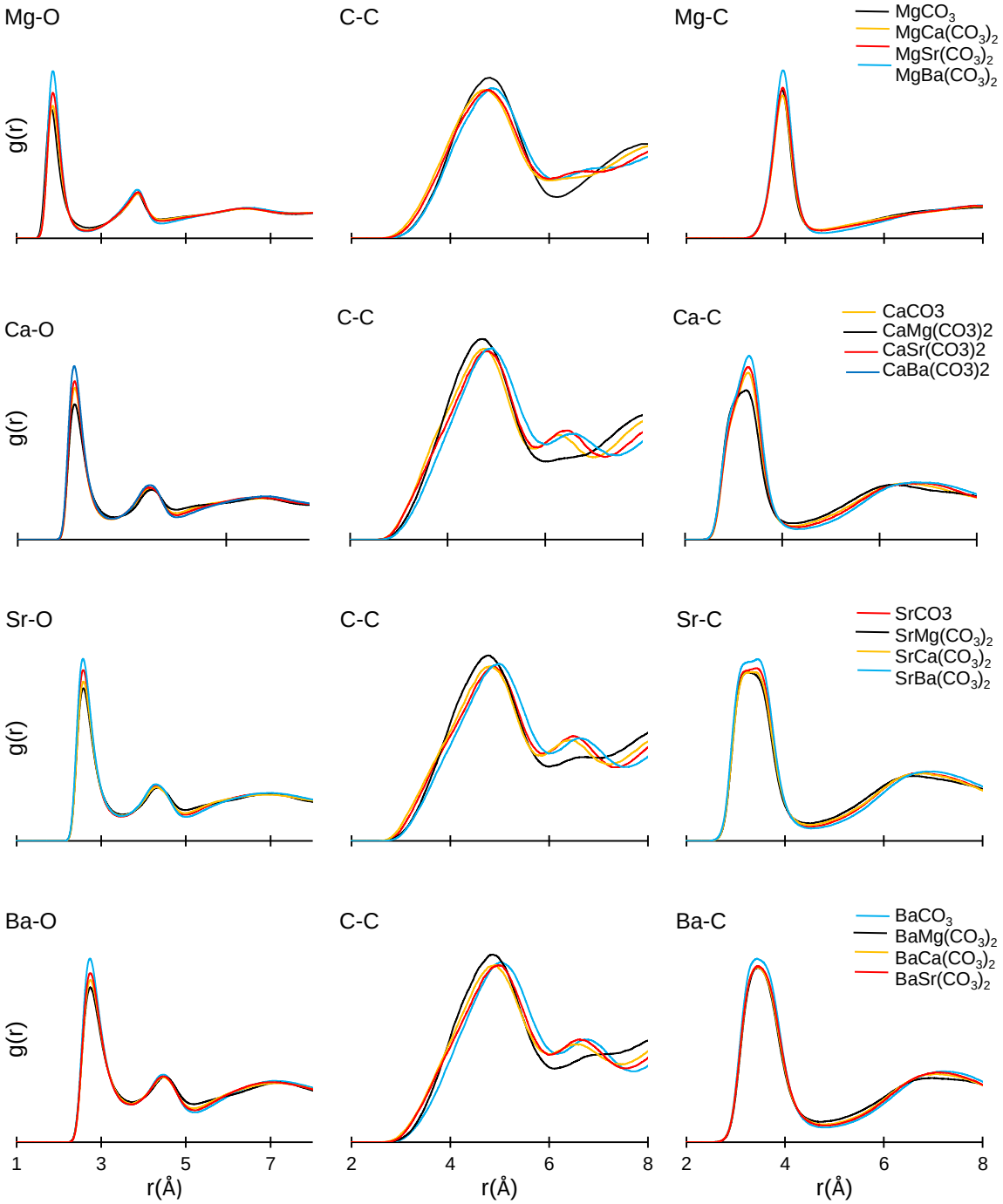

Figure A.3 Structural packing of carbonate molecules varies systematically for Mg-bearing carbonate mixtures. Shown below are pdf curves from simulations of C-C pairs (at 1100 K and 0 bar) for pure $MgCO_3$ liquid (purple line), pure $CaCO_3$ (yellow line) liquid and an intermediate binary composition, $CaMg(CO_3)_2$ (orange line). The black line is the C-C pdf curve of $CaMg(CO_3)_2$ calculated from the composition-weighted average of the two end members which nearly perfectly predicts the simulated structure; this demonstrates that carbonate packing is not responsible for deviations from ideality in $CaCO_3$-$MgCO_3$ mixtures.